UNIVERSITY OF SOUTHAMPTON

Thin Film Amorphous Silicon Cells by Inductive PECVD, with a View Towards Flexible Substrates

by

Owain D. Clark

A thesis submitted in partial fulfillment for the
degree of Doctor of Philosophy

in the
Faculty of Engineering, Science and Mathematics
School of Electronics and Computer Science

June 2009

UNIVERSITY OF SOUTHAMPTON

ABSTRACT

FACULTY OF ENGINEERING, SCIENCE AND MATHEMATICS
SCHOOL OF ELECTRONICS AND COMPUTER SCIENCE

Doctor of Philosophy

by Owain D. Clark

A range of amorphous silicon based films and solar cells have been fabricated using an inductively coupled PECVD reactor in order to investigate how the deposition conditions influenced their properties. Complete cells were deposited onto rigid and flexible substrates, and homogeneous thin films were grown to investigate their optical and electrical properties separately from the influence of whole devices.

Initial photoconductivity measurements performed on intrinsic amorphous silicon showed that it was suitable for photovoltaic applications ($10^{-4}\Omega^{-1}cm^{-1}$), complete single junction pin superstrate cells were then fabricated. The deposition conditions were altered to optimise cell efficiency, and the impact of substrate temperature, RF power, gas flow rate, system pressure, and substrate choice was commented on. The best cell produced was grown at 250C and was 8.05% efficient, after reversal of its structure to nip an efficiency of 5.77% was observed.

The deposition temperature was lowered to 200C, and the properties of doped and intrinsic amorphous silicon films were investigated using measurements of the dark conductivity variation with temperature and spectroscopic ellipsometry. Optimum growth conditions were determined for each type of film and an nip cell was deposited using them resulting in an efficiency of 4.59%. The requirement of a carefully selected intrinsic region thickness in order to achieve effective collection of generated carriers was considered.

Lastly the process was transfered from rigid glass to flexible polished stainless steel and Kapton substrates, requiring inversion of the cell orientation. A $1cm^2$ cell on a steel substrate was found to be functional under illumination and was 0.27% efficient. A $1cm^2$ cell was deposited onto Kapton but was only measured under dark conditions. It was concluded that the rear contact topography and defect density is of significant importance when dealing with flexible substrates and that sputtering rather than evaporation would have been a more suitable technique to fabricate it.

Declaration of Authorship

I, OWAIN CLARK, declare that the thesis entitled

THIN FILM AMORPHOUS SILICON CELLS BY INDUCTIVE PECVD WITH A VIEW TOWARDS FLEXIBLE SUBSTRATES

and the work presented in the thesis are both my own, and have been generated by me as the result of my own original research. I confirm that:

- this work was done wholly or mainly while in candidature for a research degree at this University;
- where any part of this thesis has previously been submitted for a degree or any other qualification at this University or any other institution, this has been clearly stated;
- where I have consulted the published work of others, this is always clearly attributed;
- where I have quoted from the work of others, the source is always given. With the exception of such quotations, this thesis is entirely my own work;
- I have acknowledged all main sources of help;
- where the thesis is based on work done by myself jointly with others, I have made clear exactly what was done by others and what I have contributed myself;
- parts of this work have been published as:

O. D. Clark, M. Thwaites, and D. M. Bagnall. Towards thin film amorphous silicon Micro-morph cells on flexible substrates. In *PVSAT4*, pages 97–100, Bath, 2008.

M. Banakar, O. D. Clark, and D. M. Bagnall. Variable angle spectroscopic ellipsometry used to optimise thin film silicon and ITO layers. In *PVSAT5*, pages 151–154, Wrexham, 2009.

Signed:.....

Date:.....

Contents

Nomenclature

In order of appearance:

PV	PhotoVoltaic
W	Watt
c-Si	crystalline Silicon
CIGS	Copper Indium Gallium Selenide
CIS	Copper Indium Selenide
ITO	Indium Tin Oxide
CdTe	Cadmium Telluride
a-Si:H	amorphous Hydrogenated Silicon
CVD	Chemical Vapour Deposition
μc-Si	microcrystalline Silicon
PECVD	Plasma Enhanced Chemical Vapor Deposition
a-Si	unhydrogenated amorphous Silicon
XPS	Xray Photoemission Spectroscopy
h	Planck's constant
ω	frequency (radians)
E	Energy (J) (also Electric field)
Ψ	work function (eV)
E_f	Fermi energy (eV)
UPS	UV Photoemission Spectroscopy
eV	electron Volts
E_u	Urbach energy (eV)
E_c	conduction band edge (eV)
E_v	valence band edge (eV)
μ_0	free carrier mobility
μ_d	drift carrier mobility
q	charge (Coulombs)
k	momentum (also extinction coefficient and Boltzmann's coefficient)
E_g	optical gap (eV)
E_m	mobility gap (eV)
ESR	Electron Spin Resonance

RF	Radio Frequency
PVD	Physical Vapour Deposition
nc-Si	nano crystalline Silicon
pc-Si	proto crystalline Silicon
DC	Direct Current
E_a	Activation energy
σ_{RT}	room temperature conductivity
LESR	Light induced Electron Spin Resonance
$\alpha(\lambda)$	absorption coefficient
a-Ge:H	Hydrogenated amorphous Germanium
a-SiGe:H	Hydrogenated amorphous Silicon Germanium
a-SiC:H	Hydrogenated amorphous Silicon Carbide
TCO	Transparent Conducting Oxide
PEN	PolyEthylene Naphthalate
e-beam	electron beam
slm	standard litres per minute
MFC	Mass Flow Controller
sccm	standard cubic centimetres per minute
IPA	IsoPropAnol
R_{TCO}	parasitic TCO Resistance (Ω)
R_{shunt}	shunt Resistance (Ω)
R_s	series Resistance (Ω)
I_{pl}	Photocurrent (A)
I_D	ideal diode forward current (A)
υ	Diode ideal factor
I_s	diode reverse saturation current (A)
J_{01} and J_{02}	double diode model current prefactors (A)
V_{oc}	open circuit Voltage (V)
I_{sc}	short circuit Current (A)
FF	Fill Factor
V_{mp}	maximum power Voltage (V)
I_{mp}	maximum power Current (A)
η	Cell efficiency (%)
AM1.5	Air Mass 1.5
NREL	National Renewable Energy Laboratory
ECN	Energy research Center of the Netherlands
c	speed of light
$\tilde{n}$	Complex refractive index
n	Real refractive index
MSE	Mean Square Error
PET	PolyEthylene Terephthalate

Acknowledgements

Whilst there are many people who I owe thanks to over the years that it took me to complete this thesis, firstly I would like to express my gratitude to Professor Darren Bagnall for guiding me through my Ph.D. The route has been unconventional to say the least. With the loss of the department's original offices and cleanroom facilities to fire came substantial upheaval in my original research topic. Without Darren's support and the arrangements he made so that I could relocate to another facility and complete my research, I might never have finished the project.

Secondly I would like to thank everyone at PlasmaQuest Ltd. who made me feel welcome and a part of their team for so long. A special mention goes to Mike Thwaites, Peter Hockley, Barry Holton, James Dutson, and Andrew Yeadon. I certainly learnt a large amount of information in a relatively small time whilst working with you.

There are too many colleagues at the University of Southampton to mention individually, but special thanks goes to Stuart Boden, Tristan Temple, Robert Maunder, and Matthew Bennett for all the time spent both in and out of work. Every member of the Nano-Group department deserves thanks for making it a great department to be part of.

I would also like to thank all of my friends for their patience in listening to me talk about electronics, in particular Paul Harmsworth, Rebecca Coath, Melanie Hodgkinson, Gemma Parsons, Matthew Mcconville, Tadge Channer, and Suzanne Channer. I am sure that there are many more people to be mentioned and I am grateful to you all.

Lastly I would like to thank my family for making all of this possible, without your continued support over the last 27 years it certainly would not have been.

The work presented in this thesis was funded by EPSRC grant number GR/S86341/01. (SUPERGEN - PV Materials for the 21st Century)

Chapter 1

Introduction

The world is currently dependent on fossil fuels and other sources of non-renewable energy to meet its demands. These reserves are finite resources and as such the need to reduce our dependency on them is widely agreed on, to the point where ideally energy generation could be self sustaining over the whole planet. In 1956 Hubbert [1] famously predicted that peak oil (the peak of oil production) would occur in the time interval between 1965 and 1970. Peak oil did not happen during Hubbert's predicted timeline but at some point it is an inevitability. In addition to the issue of peak oil production, the price of crude oil has risen extremely sharply in the last decade (see Figure 1.1) due to a combination of economic and political factors and this trend shows no signs of reversing as of 2008. Because of the current high price of crude oil, renewable energy sources are now far more economically favourable than they were in the 20th century and are becoming a viable alternative to traditional methods of electricity generation based on fossil fuels and uranium.

Renewable energy can be harvested from many natural sources including tidal waves, wind, geothermal heat, sunlight, hydroelectricity, biomass, and biofuels. Many advances in all of these fields have been made to the point where by 2006, 18.4% of global electricity generation was provided by renewable sources. Excluding large hydroelectric from this figure 3.4% (or 220GW) of electricity generated globally was provided by renewable sources in 2007. This is an increase of 50% over the same figure from 2004 and demonstrates the impressive growth rate of installed renewable generation capacity over the last 5 years. A breakdown of energy generation by type into renewable and non renewable sources for 2007 is shown in Figure 1.2.

The PV (PhotoVoltaic) global market is the fastest growing of all renewables. At present wind provides more electricity globally with an estimated 95GW generated in 2007 compared to only 10MW from installed PV, but the growth rate of installed wind power capacity was less than 30% whilst the PV market grew at a rate of over 60% from 2002 to 2006 [2]. This is largely because global PV growth has been encouraged by generous

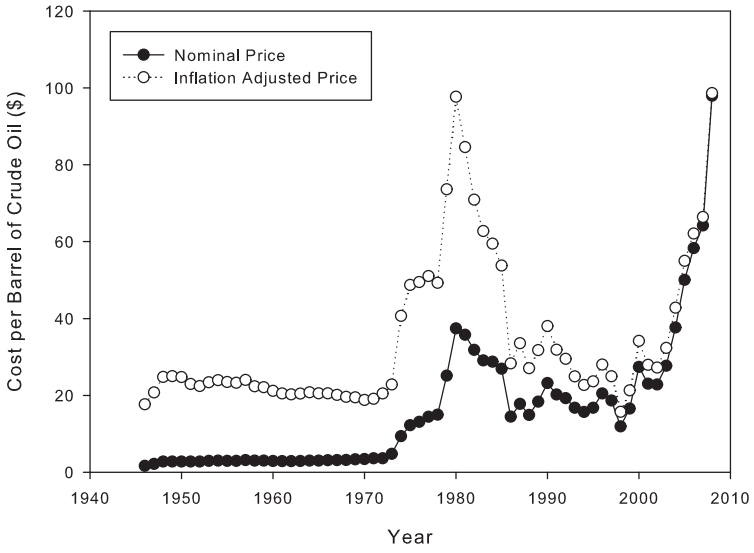

FIGURE 1.1: The price of crude oil per barrel in US dollars averaged over 12 months, both nominal and adjusted for inflation from 1946 to 2008. Oil price data is taken from www.ioga.com, and adjusted using the Consumer Price Index (CPU-U). The large peak around 1980 is due to the formation of OPEC and the price of crude returning to its free market point after American price controls in the 1970s

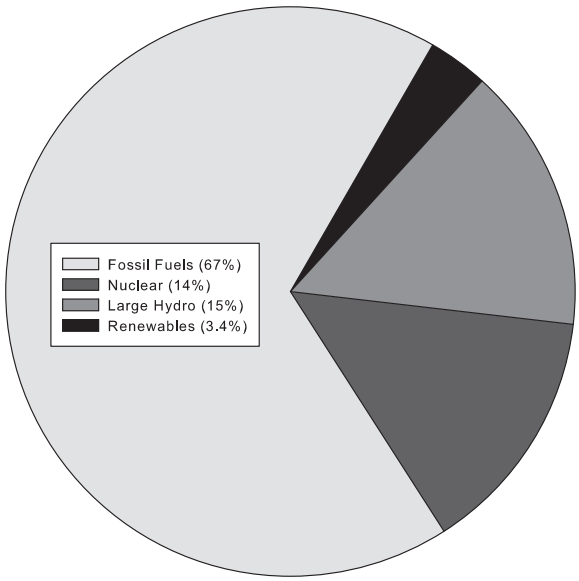

FIGURE 1.2: Electricity generation by source in 2007 [2]. The majority of electricity from renewable sources was supplied by large hydroelectric plants, defined as having a generation capacity of at least 10MW. Other renewable sources accounted for 3.4% of global electricity generation

goverment subsidies for residential installations, particularly Japan and Germany in the early 1990s (although the USA was the first to offer a national feed-in tarriff in 1978). Many more countries and states such as Spain and California have since begun their own subsidy programs.

The installed and forecast global capacity for PV capacity production in MW from 2006 to 2012 is shown in Figure 1.3. It is expected that the PV capacity installed during 2010 will be roughly four times greater than the amount installed in 2007. A target set by the European Commission for 2007 is to generate 20% of all required energy for its member states from renewable sources by 2020. The United Kingdom has set its own individual target (along with all other EU member states) of generating 15% of its energy from renewable sources by 2020. In 2005 the actual figure was less than 5%. 64 countries worldwide now have targets for renewable energy production, including 22 developing countries and it is likely that PV will play a significant part in this.

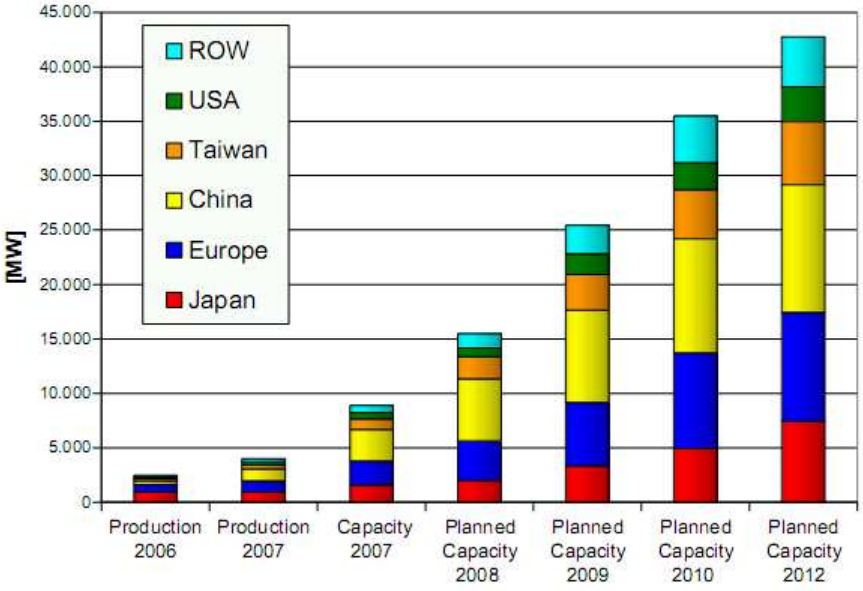

FIGURE 1.3: Actual and forecast installed global PV capacity from 2006 to 2012 per year. Figure reproduced from [3]

One of the most important figures for any energy source is the cost per Watt (W) of generating it. It is generally accepted that PV would be competitive with fossil fuels if energy could be generated at 2$/W or less, which is close to the cost of coal based energy. If this figure could be lowered to 1$/W then PV could compete with non-renewable sources without government subsidies. Measuring a true figure of cost per Watt for solar panels is difficult as there are many associated costs. Primarily there are the costs of researching and producing the panel itself, the cost of building and running a plant to fabricate it, and secondly the cost of installing and maintaining the panel at its final destination. The average PV cost per Watt was 4$/W in 1996, falling to 3$/W in 2003. It is forecast that this figure will fall to 3$/W in 2005, and 1$/W in 2010 if present trends continue [4]. (First Solar has claimed that it has achieved 0.98$/W for the fourth

quarter of 2008 with a 735 MW production capacity[1]). It will take several years for recently commissioned or completed plants to produce reliable data, but research into more efficient cells with lower production costs in parallel with continuing government subsidies to support further development of the industry should ensure that the cost per Watt of PV energy does continue to fall.

The first solar cells were developed in 1954 at Bell Labs by G.L. Pearson, C.S. Fuller, and D.M. Chapin [5]. They consisted of small strips of doped single crystal silicon, and were 6% efficient. Crystalline silicon (c-Si) was the material that drove the first generation of solar cell development as it was a familiar material to the microelectronics industry, and its bandgap of 1.12eV was well suited to the solar spectrum. The disadvantage to c-Si based solar cells is the substrate cost. Due to the expense required to produce single crystalline wafers by the Czochralski process, over 40% of a module's cost is attributable to the cost of the starting silicon wafers [6]. 200μm of silicon is also lost as kerf from every wafer cut from a process ingot of c-Si further increasing the module cost per Watt. Modern commercial PV modules based on c-Si substrates tend to be in the range of 15% to 20% efficient.

The second generation of solar cells is based on thin film technology. The light absorbing layers of such cells are on the order of 1μm thick as opposed to 200-400μm thick c-Si wafers. The absorbing thin film is deposited onto a large area substrate, which means that module fabrication can become the focus of a production line instead of individual wafers that have to be assembled further. The substrate itself can be cheap, glass is popular as a supporting substrate and even flexible polymers are a possibility for low temperature deposition. Use of flexible substrates also makes a "roll to roll" process a possibility, where a moving substrate undergoes continual deposition and is cut to assemble modules afterwards. Thin film modules are typically half as efficient as their crystalline equivalents, but relatively greater reductions in module fabrication and production costs offset this loss to lower the cost per Watt compared to a first generation design. There are 3 major competing thin film technologies that have currently given rise to commercial modules. (Dye sensitised cells are not discussed as they are still regarded as being in the developmental stage.)

CIGS (Copper Indium Gallium Selenide) is a solid solution of CIS (Copper Indium Selenide) and copper gallium selenide. Depending on the ratio of the two compounds in the final material, it possesses a direct bandgap that can be varied from 1eV to 1.7eV. An absorbing layer of 1μm is typically used in devices, and is often deposited onto a molybdenum coated glass substrate. The deposition of CIGS is complicated and usually involves co-evaporation of the metals followed by an anneal with selenide present as a gas. The deposition process can be difficult to scale up to large deposition areas whilst maintaining homogeneity of the thin film. One fear for long term development of CIGS technology is that indium is a rare metal and is currently in demand for the

[1] `http://firstsolar.com/company_overview.php`

manufacture of ITO (Indium Tin Oxide). Despite these problems CIGS has produced the best efficiencies of any thin film technology so far, with close to 20% measured under laboratory conditions [7]. The production of CIGS based modules is primarily based in the USA, Global Solar has an 85MW plant in Texas whilst Nanosolar is planning a plant capable of 430MW of production in California and a smaller future plant based in Germany. Several more plants are planned or have already been built in Europe with most intending to ramp up production to full output in 2008-2009 (see table 1.1).

CdTe (Cadmium Telluride) is a poly-crystalline direct bandgap absorber with a bandgap of 1.4eV to 1.5eV which is perfectly suited to absorbing the solar spectrum. When combined with a layer of cadmium sulfide a heterojunction is formed making a solar cell. An efficiency of 16.5% has been demonstrated in the laboratory [8]. The only commercial producers of CdTe cells are First Solar who plan a manufacturing capacity of 1097MW by the end of 2009, and Calyxo which plans to ramp up production in 2009 at a new 60MW plant in Malaysia along with its existing 25MW plant in Germany. There are some concerns relating to the amount of cadmium used to manufacture CdTe modules as it is a controlled substance under the European RoHS (Restrictions of Hazardous Substances) legislation due to its toxicity. However solar modules are currently exempted from this legislation.

A-Si:H (Amorphous Hydrogenated Silicon) is the last of the 3 dominant thin film technologies. A-Si:H is a disordered network of silicon and hydrogen atoms that is usually deposited from a silane precursor onto a heated substrate. The bandgap is near 1.7eV, and as such a-Si:H does not readily absorb light above approximately 700nm in wavelength. The absorption of short wavelength light is strong making a-Si:H cells suitable candidates for indoor applications as well as outdoor. The deposition process is very flexible and by varying process conditions the grain size of the material can be altered from truly amorphous to nano, micro, or polycrystalline. Taken to extremes, high temperature processing such as thermal CVD (Chemical Vapour Deposition) allows thin film growth of single crystal silicon from the gas phase. A-Si:H is often deposited at temperatures of 200-300C or lower which allows deposition onto flexible polymer substrates that could not support CIGS or CdTe processing.

Problems with a-Si:H include instability under light soaking which can decrease initial device efficiency by up to 30%, and a low hole mobility. A-Si:H based modules are usually 8%-10% efficient, and one of the biggest manufacturers is Sharp who plan to ramp up to 160MW of production in Japan by the end of 2008 with a tandem a-Si:H/μc-Si (microcrystalline Silicon) cell design. Other major manufacturers include Sontor (another subsidiary of Q-Cells) and Ersol. A more comprehensive list of current and emerging thin film fabrication plants divided by their cell type is presented in table 1.1.

Figure 1.4 shows a breakdown of the installed and planned world PV production divided into first and second generation technology. Thin film production capacity is growing

Company	Annual output (MW)	Completion date	Cell type
Avancis gmbh	20	2008	CIS
Global Solar	85	2008	CIGS
Johanna solar technology gmbh	30	2008	CIGS
Nanosolar	430	2008-9	CIGS
Odersun	30	2008	CIS
Solibro	45+90	2009	CIGS
Sulfercell	5	2008	CIS
Würth solar gmbh	30	2008	CIS
Calyxo	25+60	2008-9	CdTe
First Solar	1097	2009	CdTe
Ersol	100	2008	a-Si:H
Inventux	33	2008	a-Si:H
Schott Solar	33	2008	a-Si:H
Sharp	100	2008	a-Si:H
Sontor	25+100	2008-9	a-Si:H
VHF Flexcell	250	2008	a-Si:H

TABLE 1.1: Annual capacity in MW of current and planned thin film fabrication plants

every year and the trend is expected to continue. Research into thin film based cells is currently driving the reduction in cost per Watt of PV. It remains to be seen if any of the main second generation technologies will become a clear market leader, but it is more likely that the market will remain shared as each approach brings its own advantages and disadvantages. The focus on development now that second generation cells are in mass production is on further refinements. Third generation thin film cell features include advancements in PV materials and expansion to multiple junction designs to enhance light absorption through spectral splitting.

A-Si:H is a current thin film technology because as a material it is better understood than CdTe or CIGs, and because it is possible to deposit it using a low temperature process. It is well placed to become a third generation PV technology with further refinements to cell design and material deposition. Third generation concepts such as multiple junction cells are already in development, and research into lowering deposition requirements is also ongoing. One advantage of a-Si:H over CIGS is the potential for low temperature deposition onto cheap and flexible polymer substrates which has been shown to be possible. It is unlikely that a-Si:H will ever be able to challenge CIGS on the basis of efficiency, but looking at the larger picture of cost per Watt for both technologies process improvements could give a-Si:H the edge in the future.

Supergen is a program (2004-2012) funded by the EPSRC to develop research into renewable technologies in the UK. One arm of the program is a consortium of 6 universities formed specifically to investigate concepts that could lead to a reduction in the cost per Watt of PV power. Part of the contribution from the University of Southampton to the project is to develop the field of thin film research in the UK, and this was achieved

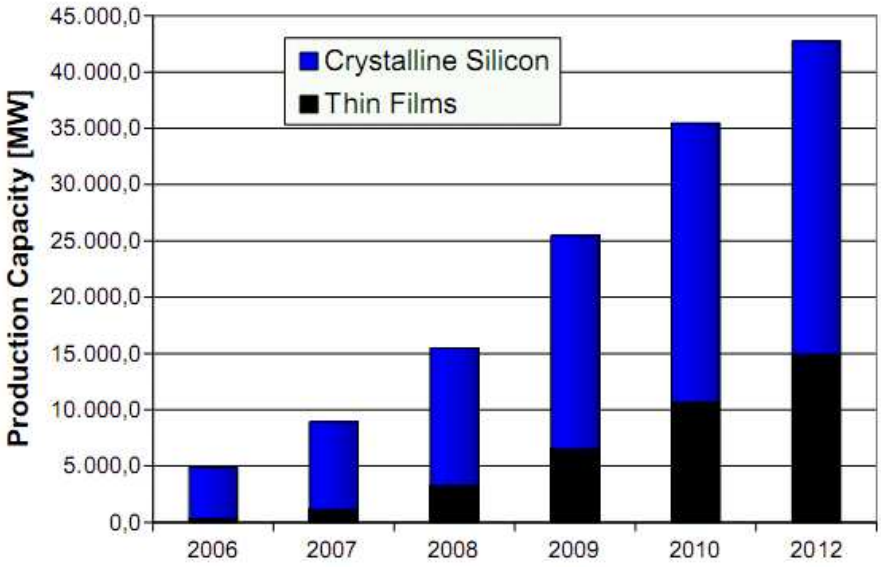

FIGURE 1.4: Current and predicted world PV production separated by first and second generation technologies from 2006 to 2012. Figure reproduced from [3]

through a partnership with the commercial company Plasma Quest Ltd. Plasma Quest Ltd provided a PECVD reactor which was restored to operational use and used to develop a low temperature deposition process for a-Si:H, which could subsequently be transferred to a flexible substrate. The PECVD (Plasma Enhanced Chemical Vapor Deposition) reactor was designed by Plasma Quest Ltd and as such is unique to this project.

Practical work for the project was divided into 3 phases. Firstly a process unconstrained by limits on deposition parameters was developed to deposit the most efficient single junction a-Si:H cell possible. This work provided familiarity with the fabrication and analysis equipment that was used throughout the project whilst working to meet the Supergen aim of a 10% efficient thin film device.

Following the conclusion of this, phase work was moved to focus on the analysis of individual thin films deposited at a lower than optimum temperature using analysis equipment developed specifically for this purpose. Thin films that could also be used to extend a single junction cell to a tandem design that could take advantage of spectral splitting were also investigated. The resulting deposition trends observed from thin film analysis were used to create a low temperature deposition process for a single junction cell that could be transferred to a flexible substrate. Finally various flexible substrates were trialled as part of this process and conclusions were drawn about the most promising methods by which third generation flexible thin film a-Si:H cells could be fabricated.

Chapter 2

Background and literature survey

2.1 The discovery of a-Si:H

Since research into the electronic properties and applications of a-Si:H began in the 1950s and 1960s, it has become widely known as a promising material for PV applications. Early research methods of producing a-Si (unhydrogenated amorphous Silicon) such as sputtering and evaporation did not utilise hydrogen and suffered from a very high density of electronic defects. This prevented observation of semiconducting action.

A-Si:H was first produced by the decomposition of silane via application of an electrical plasma, and the subsequent deposition of the species that resulted onto a heated substrate. This method is known as PECVD and is still widely in use. The reactor used was inductive, as was the reactor used to produce a-Si:H for this project. This is a departure from the norm in that modern PECVD reactors are usually capacitative to enable large area deposition. The pros and cons of each approach to plasma generation are discussed in section 3.2.

Chittick et al. [9] deposited a-Si:H onto substrates heated from 25 to 650C. Material resistivity was measured and decreased from $10^{14}\Omega$cm for room temperature deposited films to less than $10^{5}\Omega$cm for substrate temperatures of 500C or greater. The films were found to be photoconductive with the greatest ratio of dark to light conductivity being roughly 3 orders of magnitude for intrinsic a-Si:H grown using a substrate temperature of 300C. A smeared absorption edge was noted from 0.75μm to 1.5μm which is now known to relate to the density of states of a-Si:H and accounts for absorption in the 0.8eV to 1.65eV range (see section 2.3). Finally the metastability of a-Si:H was commented upon, with the resistivity of a sample exposed to air increasing and eventually settling over a period of time.

Walter Spear saw the potential of this new material and arranged for Chittick's reactor to be moved to the University of Dundee. Working with Pete Le Comber he continued to

perform much of the early work on the characterisation of a-Si:H, including its transport properties and the possibility that it could be doped in the same manner as c-Si with group III and V elements (see section 2.5).

2.2 The atomic structure of c-Si and a-Si:H

C-Si and a-Si:H exhibit similar properties despite their structural differences. The structure of c-Si is a regular lattice of silicon atoms which possesses long range order, and a-Si:H is comprised of a random network of silicon and hydrogen atoms. There is a large probability of finding silicon atoms at a repeating distance in a c-Si lattice. The same is true for a-Si:H for several interatomic distances, but soon after the 3D nature of the random network comes into effect and the 1D interatomic spacing becomes increasingly erratic.

A random network has the ability to include atoms on an ad-hoc basis as it forms because they are no longer constrained to lattice points. This property makes a comparison to c-Si theory difficult as it is no longer clear what constitutes a defect in an a-Si:H random network. A point defect in c-Si is most commonly a vacancy, an interstitial, or an extrinsic defect. These defects are not applicable to a-Si:H as it has no defined structure to deviate from. Instead it is useful to define a defect as an atom that is over or under co-ordinated in terms of the bonding of its outer electron shell. Figure 2.1 shows point defects expected in a c-Si lattice and equivalent under co-ordinated point defects in a-Si:H. A silicon atom will form four chemical bonds to neighboring atoms ideally, but it would be under co-ordinated if it formed three or less.

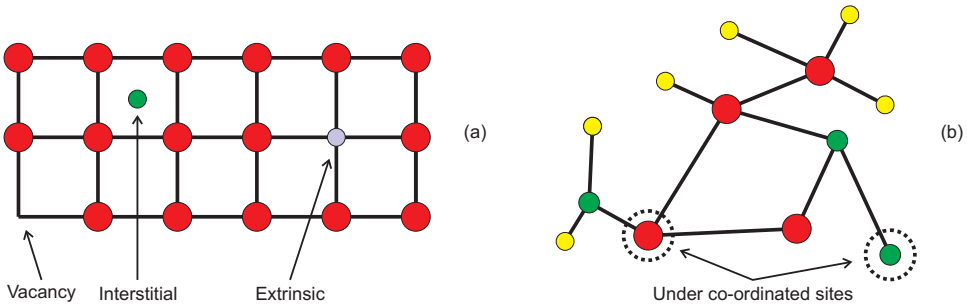

FIGURE 2.1: Point defects in c-Si (a), and a-Si (b)

An under co-ordinated atom in a-Si:H represents a dangling bond which may be neutral or charged with a hole or electron. It is also possible for an atom to have more than one dangling bond in an a-Si:H lattice. In a perfect network of a-Si:H every dangling bond would be terminated with a hydrogen atom, but a fraction of unpassivated bonds will always remain. Hydrogenation of a-Si reduces this fraction to an extent that a-Si:H becomes useful as an electronic material. The random nature of an a-Si:H network has both positive and negative effects on its behavior as a semiconductor. It allows it to be

a more efficient absorber of light beneath 700nm than c-Si, but yet also degrades carrier transport properties due to the existence of deep gap energy states related to dangling bonds. All of these effects can be related to the density of states of a-Si:H.

2.3 The density of states

The a-Si:H density of states is typically probed by optical spectroscopy. Jackson et al. [10] used XPS (Xray Photoemission Spectroscopy) to observe the valence band density of states and the inverse technique to observe the conduction band density of states. XPS uses a photon of energy $h\omega$ to excite an electron from a valence state to the conduction band, (where h is Planck's constant and w is the photon frequency). Assuming no scattering and that the electron has enough energy to escape the a-Si:H by overcoming the work function Ψ then it will be ejected according to equation (2.1) where E_{kin} is the kinetic energy of the electron and E_{vb} the binding energy of the valence band state with respect to E_f (Fermi energy).

$$E_{kin} = h\omega - \Psi - E_{vb} \tag{2.1}$$

This process results in a recreation of the density of states at a higher energy of $h\omega - \Psi$. Measurement of the kinetic energy of ejected electrons allows the valence band density of states to be measured after the subtraction of background noise. To observe the conduction band density of states the opposite procedure is employed. A-Si:H is exposed to an electron beam of known energy E, and a spectrum of photon energies is measured as electrons fall to valence states according to equation (2.2). E_{cb} is the binding energy of the conduction band state relative to E_f. One of the problems with XPS as a technique is that it is not sensitive to smaller electronic orbitals and so states related to hydrogen electrons are not visible. UV photoemission (UPS) is a more appropriate technique if this is required.

$$E_{kin} = E + \Psi - E_{cb} \tag{2.2}$$

The density of states for intrinsic c-Si and a-Si:H measured using XPS is shown in Figure 2.2. The position of the peaks in both spectra shows that the tetrahedral bonding nature of silicon is largely intact in the a-Si:H. The smoothing in the a-Si:H spectra is evidence of bond length and angle distortion, but it does not dominate implying that bonding disorder is a fraction of bond strength. The conduction band in a-Si:H is broadened significantly compared to c-Si, which relates to the energy distribution of silicon outer shell electrons. These are the electrons involved in bonding providing more evidence of disorder relative to c-Si.

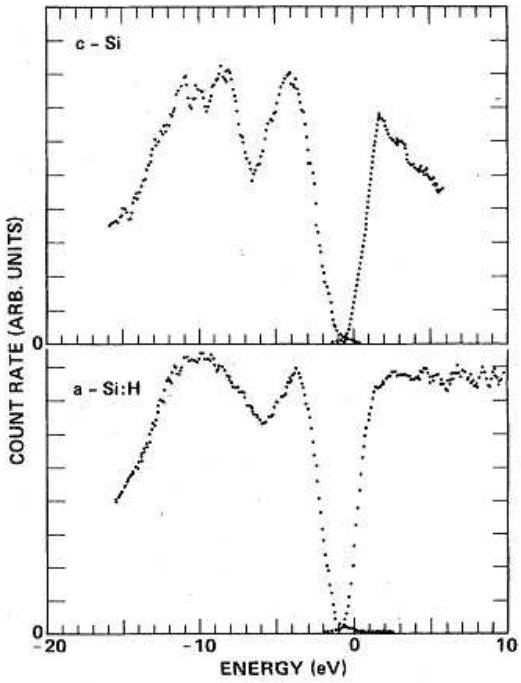

FIGURE 2.2: The valence and conduction band density of states for intrinsic c-Si (upper) and a-Si:H (lower) determined by XPS and inverse XPS, reproduced from [10]. Note the general good agreement between the 2 spectra indicating that the majority of silicon bonding in a-Si:H is similar to the tetrahedral arrangement of c-Si, the a-Si:H density of states appears as a smoothed version of the c-Si density of states

Unfortunately XPS does not possess the resolution required to investigate the density of states at each gap edge, and so a more sensitive technique was developed by Winer and Ley [11]. The technique is known as total yield spectroscopy. Instead of measuring the energy distribution of electrons excited by XPS or UPS, all of the electrons were collected and the energy of the incident light was varied instead from 4.0-6.4eV. The maths involved in the calculation of a valence band state density for a given energy is more involved than for XPS, and is not reproduced here. It will suffice to state that total yield spectroscopy provides a sensitivity enhancement of ≈ 6 decades in the measurement of state densities at energies beneath E_f enabling densities down to 10^{15}cm^{-3} to be determined. Figure 2.3 shows the valence band density of state distribution determined by total yield spectroscopy for intrinsic and p type doped a-Si:H.

The total yield spectra of Figure 2.3 possesses several interesting features. The state distribution does not fall to zero in the gap as it would for c-Si, but again is blurred due to the disorder of the random network. After the energy where a sharp band edge would be present in the c-Si density of states, a region exists where the logarithm of state density varies linearly with energy. This tail of states exists for both the conduction and the valence band, and they have a large influence on the transport properties of a-Si:H. The tails are known as Urbach edges and are described with an energy term (E_u) that refers to their gradient. This is shown in equation (2.3), where N_0 is the density of states

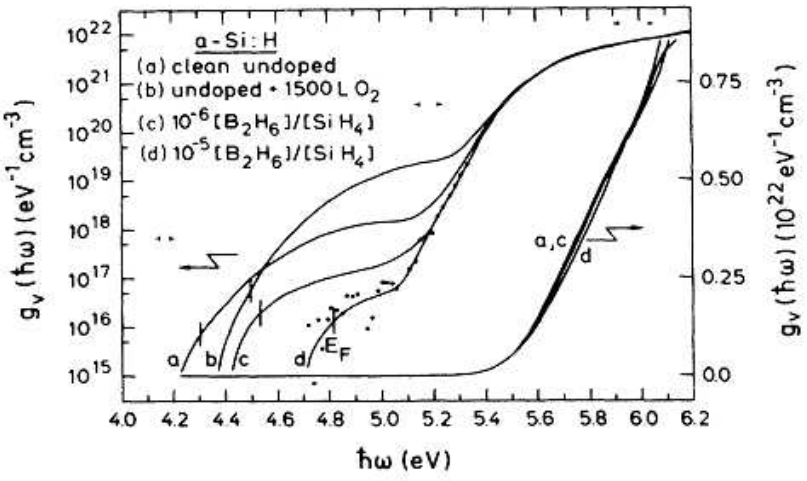

FIGURE 2.3: The valence band density of states determined by total yield spectroscopy (reproduced from [11]) for intrinsic and p type doped a-Si:H, oxygen contaminated intrinsic a-Si:H is also investigated. E_f is marked with vertical bars. Extension of states into the gap can be seen on the linear curves from 5.6eV down, detail of the midgap states is visible on the logarithmic curves indicating a second linear region of state distribution does not exist in the c-Si density of states. The addition of oxygen during a-Si:H deposition increases the midgap state density

at a band edge. Both the conduction and valence band have a value of E_u associated with them, but the conduction band edge cannot be investigated using time resolved spectroscopy as it is depleted of electrons due to the position of E_f. Where band edges occur in the a-Si:H density of states is not straightforward and will be discussed further in section 2.3.1.

$$N(E) = N_0 \exp^{\frac{E_u}{kT}} \tag{2.3}$$

At energies further from the band edge and towards E_f the state distribution decays to a minimum, even high quality a-Si:H will possess a midgap defect density of $\approx 10^{15}$cm^{-3}. It also can be seen that the addition of an oxygen flow to a-Si:H deposition has resulted in the Urbach edge being obscured and an increase in the midgap state density of several decades before E_f is reached. The presence of band tails also explains the observations of Chittick et al. [9], when a-Si:H was found to absorb a small amount of light up to 1500nm. The onset of strong absorption is near 700nm, above this wavelength the band tail states are the dominant factor.

2.3.1 Localisation in amorphous networks

Atoms can have a greater potential associated with them in an amorphous network than a crystalline lattice because of their physical position in the material. An atom that is more isolated from its neighbors due to greater than usual bond lengths and angles will

have a greater potential associated with it and the atom is said to be localised. The greater the potential associated with an atom, the more localised it is and a greater amount of energy is required for carriers to diffuse away from it. Figure 2.4 shows the addition of a random potential V_0 to a crystalline potential with an energy band of width B.

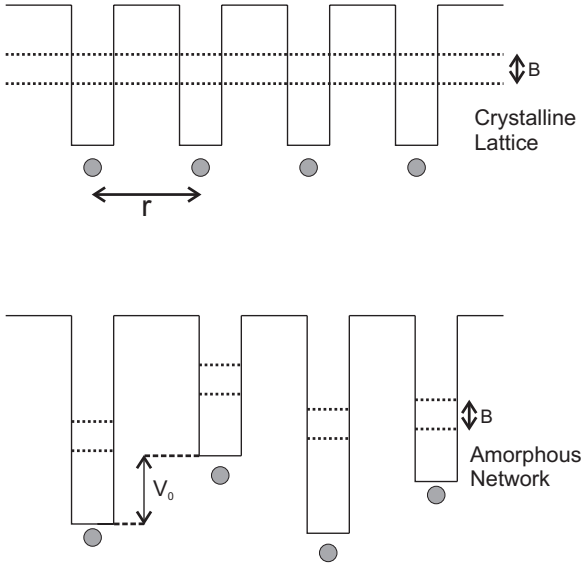

FIGURE 2.4: The potential random disorder (V_0) associated with a random network compared to a crystalline lattice, and the band width B

The requirements for complete localisation in a-Si:H are not met, but a large proportion of sites are localised to a certain extent. Because c-Si is periodic there is no localisation, all atoms in the lattice have the same potential associated with them, and all energy bands line up precisely. In a-Si:H the valence and conduction bands of a localised atom will be shifted with regards to the c-Si potential in proportion to the degree of localisation. Summing this effect over a large a-Si:H random network results in the a-Si:H density of states resembling a smeared c-Si density of states. The disorder potential means that there are now allowable energy levels in what would be the forbidden band gap of c-Si and these are known as localised states, also known as band tail states.

Once an electron or hole falls to a localised state, diffusing away from it requires an input of energy. Typically this is provided by heat in the form of lattice phonons and the carrier will tunnel to another localised state or an extended state. Carriers in extended states will travel to other extended states until they are scattered back to a localised state and the process repeats itself. The only states that will conduct at near 0K are the extended states, carriers in localised states will not be able to diffuse away. Due to the localised states being energetically favourable it is hard to observe conductivity at temperatures beneath 200K.

2.3.2 Localisation and the mobility edge

Localised band tail states that exist beneath E_c and above E_v are particularly important due to their effects on carrier transport. The trapping and release of carriers once they have fallen from an extended to a localised state is a thermally activated process with an activation energy related to the trap depth. The trapping process means that the effective carrier mobility (also called the drift mobility) is lower than the free carrier mobility in the extended states. The energy that separates the conducting region of states from the localised states in both the valence and conduction band is known as the mobility edge, and the difference between the mobility edges is the mobility gap. Due to the localised states being energetically favourable it is impossible to separate their effects on carrier transport at any temperature and so determination of the mobility edge position is not straightforward.

The average free carrier mobility μ_0 is related to the average drift carrier mobility μ_d by equation (2.4) where τ_{free} and τ_{trap} are the times spent in the conducting states and localised states respectively.

$$\mu_d = \mu_0 \left(\frac{\tau_{free}}{\tau_{free} + \tau_{trap}} \right) \tag{2.4}$$

Drift mobility studies are typically performed using the time of flight measurement technique proposed by Spear [12]. A sample of the material under test is sandwiched between two electrodes in a parallel plate arrangement, one of which is transparent or as thin as to be semi transparent. A pulse of short wavelength light is used to generate a charge packet close to the front contact, and the current across the sample is recorded as a function of time using a fixed voltage bias. Figure 2.5 shows the experimental setup. The use of short wavelength light means carriers will be generated close to the surface, and the use of a thick enough sample with an appropriate bias voltage allows investigation of either electrons or holes.

As a charge q moves a distance x across the sample it induces a charge on the electrode of Q, the equation for which is given in (2.5) where d is the sample thickness. If equation (2.5) is differentiated with respect to t then an expression for current is obtained which can be manipulated to include a velocity term v which relates to drift mobility μ_d. Equation (2.6) shows this form where E is the electric field strength across the sample.

$$Q = \frac{qx}{d} \tag{2.5}$$

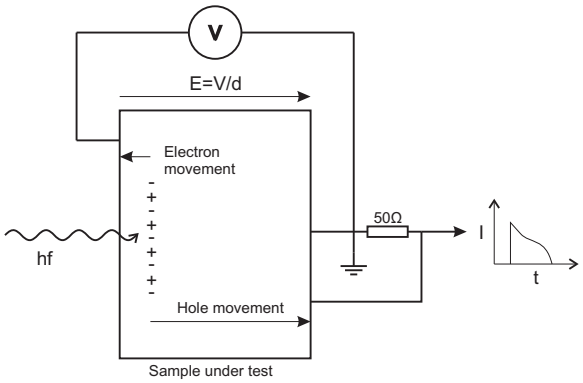

FIGURE 2.5: The experimental setup to determine carrier mobility in amorphous materials reproduced from [12]. Carriers are generated near the front surface of a sample under test using light of energy hf. A voltage bias (V) creates an electric field (E/d) across the sample that separates the carriers and the resulting current as a function of time is recorded

$$\begin{aligned} I &= \frac{dQ}{dt} \\ &= \frac{q}{d}\frac{dx}{dt} \\ &= \frac{qv}{d} \\ &= \frac{qE\mu_d}{d} \end{aligned} \tag{2.6}$$

A better form of equation (2.6) can be determined by considering the time taken for all generated carriers to cross the sample. The equation is given in (2.7) where τ_t is the total transit time. This form is more useful than equation (2.6) as it is not necessary to know the total generated charge q, however it is assumed that E is uniform across the sample.

$$\tau_t = \frac{d}{E\mu_d} \tag{2.7}$$

Experimentally determined values for μ_d at room temperature range from 0.1-10cm^{2}V^{-1}s^{-1} for electrons, and 10^{-2}-10^{-3}cm^{2}V^{-1}s^{-1} for holes [13, 14]. When compared to typical values of electron and hole mobility in c-Si of 1400cm^{2}V^{-1}s^{-1} and 450cm^{2}V^{-1}s^{-1} respectively it is clear that the electronic performance of a-Si:H is substantially degraded due to localisation of energy states and dispersive trapping. A-Si:H solar cells must be designed to overcome this problem.

2.3.3 Absorption of light

Despite the issue of poor carrier drift mobilities in a-Si:H, it is still a promising photovoltaic material. This is because the degradation of electronic properties caused by the localisation of states also affects the optical absorption of the material in such a way that a-Si:H exhibits strong direct gap absorption for wavelengths beneath ≈700-750nm. This is in contrast to c-Si, the absorption characteristic of which is weaker indirect absorption beneath ≈1100nm. The absorption region of a-Si:H exists such that it can efficiently make use of the peak in the AM1.5 solar spectrum centered at ≈500nm (see section 3.8.3).

Optical transitions to and from localised states are allowed inside the mobility gap, and can be observed in transmission measurements at energies above the onset of strong absorption. This weak region of absorption is related to the Urbach edge gradients of the tail states, which are also commonly associated with the disorder of an amorphous network. Measurements of optical absorption can therefore also provide some indication of material quality, although the single value for E_u that is obtained [15] cannot be directly related to either band tail gradient as it is influenced by both.

The absorption of c-Si is known to be related to its indirect bandgap of 1.12eV. Because it is indirect the minimum energy of the conduction band does not occur at the same momentum (k) as the maximum of the valence band. Figure 2.6 shows the offset in k and E for the valence and conduction bands of c-Si. The indirect nature of the c-Si bandgap means that for an electron to be promoted from E_v to E_c, both a photon and a lattice phonon must be involved in the transition. This is a less probable event than a photon being available on its own.

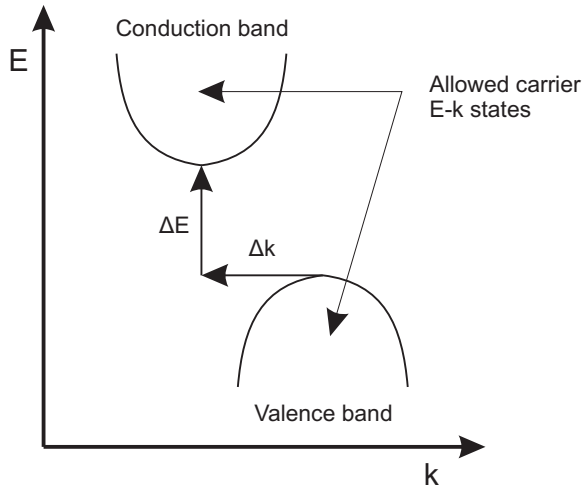

FIGURE 2.6: The E-k relation for an indirect semiconductor showing the shift in energy (ΔE) and momentum (Δk) required to promote an electron from the valence band maximum to the conduction band minimum

Theoretical c-Si possesses a perfect lattice structure with no defects present. In reality it can be grown with a very low concentration of defects and so an approximation to a perfect lattice is still valid. Carriers travelling in such a lattice rarely interact with it as allowable values of k are dictated by the repeating solutions to Schrödinger's equation which is itself a function of the repeating lattice potential. In contrast to this carriers travelling in a-Si:H are scattered due to lattice interactions over distances of several interatomic spacings because of constant variation in the lattice potential. This constant scattering means that k is not required to be conserved in quantum transitions due to the uncertainty present in it. Absorption in a-Si:H is dictated by the density of states and is proportional to the number of states separated by a given value of energy.

Uncertainty in k works for and against a-Si:H. In the same way that a phonon is not required to promote an electron to E_c from E_v, it is also not required for the electron to fall back to its original state and recombine. Carrier lifetimes are low due to this, and if midgap state creation is not suppressed sufficiently during deposition of a-Si:H then the resulting material will be electronically poor or inactive.

The same variation of lattice potential in a-Si:H that causes the deterioration of transport properties is responsible for the enhancement of absorption in an energy range that is well suited to our solar spectrum. In contrast the perfect lattice structure of c-Si provides several decades of improvement in carrier mobility and lifetime, but inhibits absorption due to the indirect nature of its bandgap and the conservation of k in transitions.

The optical gap (E_g) is usually determined by measurements of optical absorption and is similar in magnitude to the mobility gap (E_m) that separates E_v and E_c, but the values are not equal.

2.3.4 Midgap defect states and hydrogen

An a-Si:H network is comprised of a rigid and strained structure of over and under co-ordinated silicon atoms. Hydrogen atoms within the network are less tightly bound, and can diffuse through the material. The incorporation of hydrogen into an a-Si:H network during PECVD is very sensitive to the deposition conditions of the plasma and the substrate temperature used. Atomic hydrogen can also break weak or highly strained Si-Si bonds and in this way can promote a more ordered network. It has also been observed to induce defects in c-Si [16]. This process requires a large concentration of energetic hydrogen atoms at the growing film surface and is one reason why a heated substrate is required to lower the defect concentration of a-Si:H.

Most of the early information on the method of hydrogen bonding in a-Si:H came from IR (Infra Red) spectra such as measured by Lucovsky et al. [17]. Deposition parameters were investigated with regard to the preferred hydrogen bonding mechanism. Low RF power and an undiluted silane flow resulted in a film with predominantly single Si-H

bonds. Samples produced with a substrate temperature above 200C tended to favour hydrogen bonded in SiH and SiH_2 groups, whilst samples prepared at cooler temperatures featured more hydrogen bonded in SiH_2 and SiH_3 groups. The optimum substrate temperature for the highest ratio of SiH:SiH_{2+} bonds was found to be 300C.

It was apparent that the defect density of intrinsic a-Si:H was related somehow to its hydrogen content. Biegelsen et al. [18] studied the relationship between defect generation and hydrogen content of a-Si:H films by annealing them at temperatures of up to 600C for 10 minutes. Defect density was measured by ESR (Electron Spin Resonance), as well as luminous efficiency and hydrogen evolution of the samples. (Electron Spin Resonance detects atoms that have one or more unpaired electrons). Samples tended to evolve hydrogen at a peak that occurred between 300-400C which was linked to an increasing defect density, and decreasing luminous efficiency.

Samples deposited at high power and a low silane:argon ratio tended to evolve (release) hydrogen at a lower temperature than films deposited at a low power from pure silane. The link between increasing spin density and decreasing luminous efficiency would suggest that evolution of hydrogen was creating dangling bonds that in turn corresponded to midgap defect states. Band to band recombination by non-radiative transitions would then have increased which would account for the quenching of the luminescence.

Below 300C the opposite effects were observed, and defect density decreased. As hydrogen evolution was observed for temperatures of less than 150C it was concluded that the reduction in defects was due to passivation by mobile hydrogen atoms. This result agrees with the optimum substrate temperature of Lucovsky et al. [17].

Knights and Lujan [19] found that a-Si:H films prepared at high argon dilutions and RF power, tended to form columnar micro structures. A minimum defect density was observed at 230C for pure silane deposition and low RF (Radio Frequency) power. Increasing the RF power or argon dilution resulted in a greater defect density. An explanation for the evolution of hydrogen at lower temperatures for a-Si:H prepared using high RF power and argon dilution as observed by Biegelsen et al. [18], would appear to be related to the bonding manner of hydrogen in an a-Si:H film that has a columnar micro structure.

Columnar growth occurs when atoms introduced to a growing layer have a low mobility or a high sticking co-efficient and shadow an area such that further atoms that land in the vicinity of the first are likely to bond to it rather than than forming a continuous layer as seen in figure 2.7. This type of growth is referred to as PVD (Physical Vapor Deposition) whilst continuous layer growth is known as CVD (Chemical Vapor Deposition).

A-Si:H deposited by PECVD can be deposited in the PVD or CVD regime. When highly reactive species are formed in a plasma, film growth tends toward PVD and the deposition rate is high. When less reactive species are present the deposition rate is

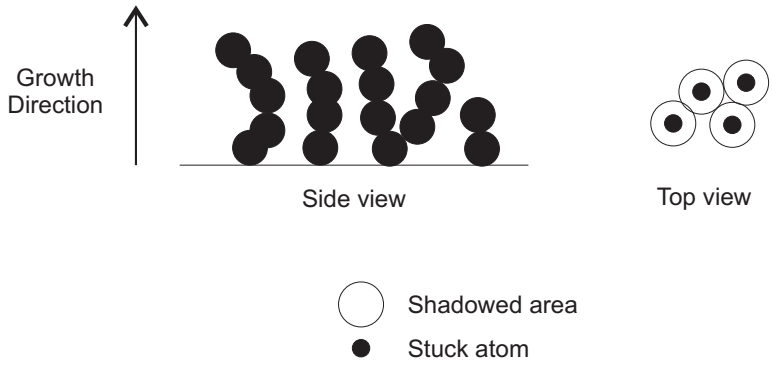

FIGURE 2.7: Atoms forming a low density columnar layer of a-Si:H by PVD growth due to shadowing effects

lowered but the growth method tends toward CVD and the resulting layer will more dense and less subject to oxidation due to reduced surface area. Dilution of silane with inert gas, increased pressure, and higher RF power all shift the growth method toward PVD. Fritzsche et al. [20] observed that a-Si:H film density does decrease with increasing hydrogen content as would be expected, and that films that are composed of 10-15% of hydrogen have densities of a factor ≈0.95-0.9 less than c-Si. (2.33 gcm^{-3})

2.3.5 The transition to μc-Si

When silane is diluted with a sufficient concentration of hydrogen during PECVD, a transition from the growth of a-Si:H to μc-Si will occur. The transition is a function of the silane:hydrogen dilution ratio and RF power [21]. The resulting mixed phase material is termed μc-Si and tends to exhibit a conductivity several orders of magnitude greater than a-Si:H, a reduced bandgap, improved doping efficiency, and a shift towards indirect absorption as it takes on a greater proportion of the properties of c-Si. Tandem cells consisting of a thin a-Si:H top cell and a thicker μc-Si bottom cell are known as micromorph cells (see section 2.8.3).

The range in material properties that can be produced using hydrogen dilution of a-Si:H growth is substantial and a huge area of research in its own right. Hydrogen dilution and the variation of other deposition parameters results in the promotion of a network consisting of small crystalline grains surrounded by regions of a-Si:H. This growth is attributed to the scouring of non ideal Si-Si bonds by hydrogen until only the strongest remain. These grains can be on the nano to the micro scale and provide a way to trade off the beneficial properties of c-Si and a-Si:H against each other.

As growth conditions are adjusted to provide a greater fraction of c-Si the density of states becomes less blurred, band tail width decreases with E_g, and optical absorption worsens. This potential variation in material properties allows the design of complicated multiple junction cells, with each individual cell tailored such that its thickness,

absorption, and conductivity are balanced to make more efficient use of the AM1.5 solar spectrum than a single junction cell.

Several definitions are used (sometimes interchangeably) in literature to refer to a mixed phase material comprised of a-Si:H and a c-Si fraction. μc-Si and nc-Si (nano crystalline Silicon) refer to the average size of the c-Si grains suspended in a-Si:H, whilst pc-Si (proto crystalline Silicon) refers to material produced using deposition conditions just before the transition from a-Si:H to a material with a dominant c-Si fraction. The transition from one phase to the other is dependent on multiple factors including the reactor used to deposit it, which partly explains the lack of strict categorisation.

2.3.6 The theoretical density of states

The theory and experimental measurements presented in this section can be combined in order to build a theoretical model of the a-Si:H density of states. This is of use when considering what effects the alteration of deposition parameters or the introduction of new atoms into the amorphous network might have on the resulting material properties. Figure 2.8 shows a theoretical representation of the density of states for intrinsic a-Si:H with reference to the c-Si density of states.

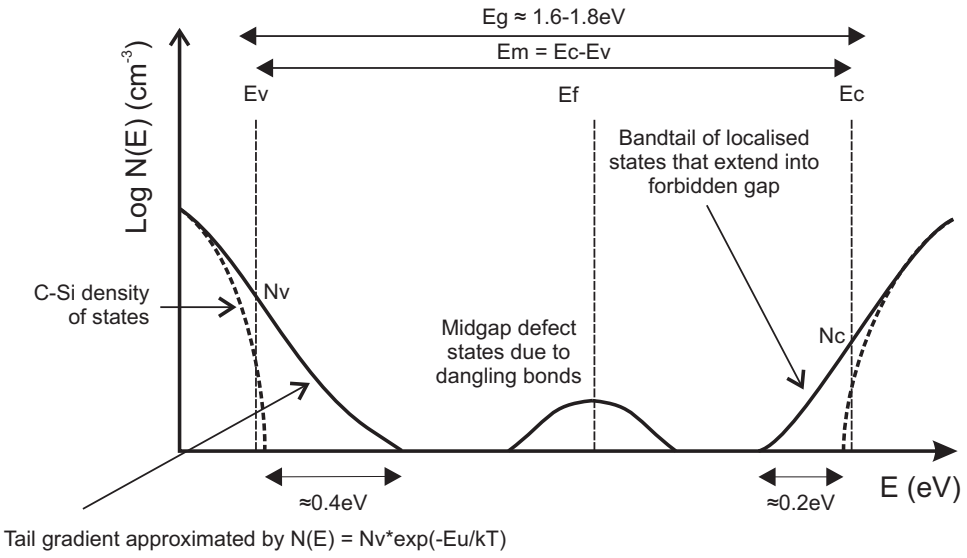

FIGURE 2.8: The amorphous density of states showing the band tail states extending into the forbidden gap, the extended and localised states separated by the mobility gap $E_m = E_c - E_v$, the decreasing exponential density of states in the gap described by E_u, and the midgap states that are related to unpassivated dangling bonds in the amorphous network

The localised and extended states are separated by the mobility edges E_c and E_v, with mobility gap being similar in magnitude to E_g. The localised states have a variation in lattice potential associated with them due to bonding disorder that places them in the energy gap that would be forbidden in the c-Si density of states. The width of the tail

states play an important role in the electronic and optical properties of a-Si:H and are measured using Urbach energies that describe the exponential reduction of the tail state density after the mobility edge.

There is always a midgap density of states in a-Si:H which is related to unpassivated bonds in the amorphous network. In well hydrogenated material the midgap state density is suppressed to a value of $\approx 10^{15}\text{cm}^{-3}$. The density rises several decades for poorly passivated a-Si:H and encourages non-radiative recombination of carriers which degrades electronic performance.

2.4 Conductivity paths

Conduction paths in a-Si:H are very closely related to the density of states distribution. Above the mobility edge carriers are free to move in extended states until they are scattered to a lower energy state. Carriers trapped in localised states can be excited to the extended states for a period of time or may travel further in the localised states by tunneling to another state in close proximity. Tunneling between localised states is known as "hopping", hopping near E_f is possible depending on the density of states distribution at that point. These three methods of conduction were observed by Le Comber and Spear [22] in 1970. Figure 2.9 relates the types of conduction to the appropriate energy levels in the density of states.

In well passivated a-Si:H conduction takes place predominantly at the band edges. This means that the location of the mobility edge and the position of E_f relevant to it are of prime importance. Conduction is thermally activated as a function of a distribution of trap release times and energies. At 0K only extended states could contribute to conduction, but as it is only possible to bring E_f to within 0.2-3eV of E_c at most (see section 2.5) conduction at 0K cannot occur. At less than 200K conduction becomes impossible to measure. This means that the contribution of the extended states to total conduction can never be separated from the influence of the localised states beneath them. Theories of conduction must account for the effects of both.

2.4.1 Experimental determination of conductivity

The conductivity of a-Si:H is typically measured directly using a DC (Direct Current) voltage and a known volume of material. Figure 2.10 shows an experimental set up for measuring the conductivity of a-Si:H. A thin film of a-Si:H typically on the order of 1μm thick is deposited onto an insulating substrate such as a glass slide. Aluminum contacts with a known separation and length are then evaporated onto the film. Because the conductivity of a-Si:H is temperature activated, samples are often mounted such that

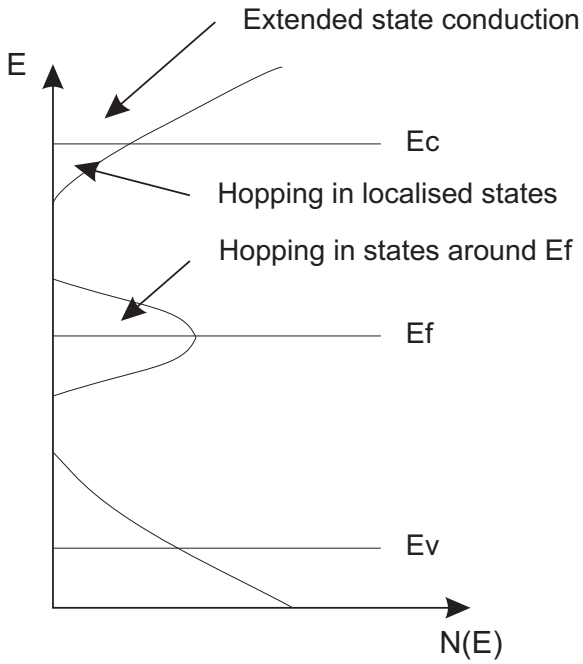

FIGURE 2.9: Conduction paths in a-Si:H with relevance to the density of states. Carriers in extended states can travel to other extended states with a minimum of disruption, or can be scattered to a localised state with a greater potential associated with it. An input of energy is required for the carrier to diffuse away from the site and be promoted back to an extended state or tunnel to another localised state. A small conductivity also exists near E_f due to the midgap state density and hopping carriers.

their temperature can be varied. Conductivity measurements are usually performed under vacuum to prevent heated films forming a surface oxide.

A DC bias is applied to the electrodes and the current passing through them is measured. The current can be converted to conductivity as the volume of material between the electrodes is known. Equation (2.8) shows the relationship between measured current and layer conductivity where V is the applied voltage, I is the measured current, t is the layer thickness, L is the separation between the electrodes and W is the width of the electrodes.

$$\sigma = \frac{I}{V}\frac{L}{Wt} \tag{2.8}$$

Fits to conductivity data are usually expressed as a prefactor and an exponential term that contains an activation energy as shown in equation (2.9) (for a p type sample). E_{tr} is the average energy of the conducting electrons, and σ_0 is the conductivity prefactor. Using equation (2.9), an activation energy of $E_c - E_{tr}$ or $E_{tr} - E_v$ can be determined with σ_0 by an Arrhenius plot of conductivity against $1/T$.

$$\sigma(T) = \sigma_0 \exp^{\frac{-(E_{tr}-E_v)}{kT}} \tag{2.9}$$

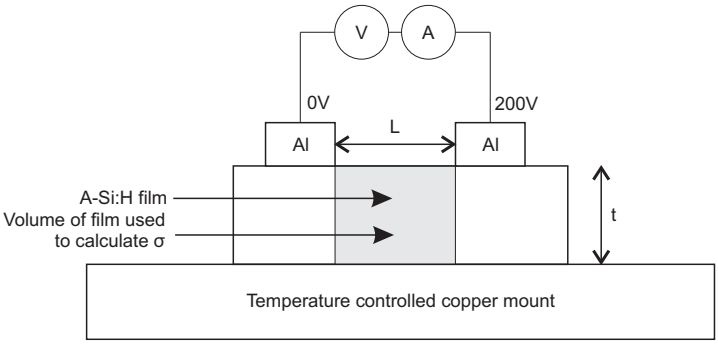

FIGURE 2.10: Experimental setup for the measurement of a-Si:H conductivity using a DC bias and a known volume of material

It is important to remember that heating a-Si:H can induce effects due to the trap related mobility and potentially alterations of the random network. This could cause variation in the parameters determined by conductivity analysis of a-Si:H films prepared using differing growth conditions. In particular E_{tr} and E_f can move as a function of temperature, and mobility gap narrowing has been noticed to occur with increasing temperature by a coefficient of $4.4\text{x}10^{-4}\text{eVK}^{-1}$ [23].

The meaning of σ_0 in equation (2.9) is not immediately obvious. It represents the y-intercept of the expression when plotted in the Arrhenius form of $\ln(\sigma_0)$ against $1/T$. At the y-intercept $1/T$ is undefined and may be interpreted as T being infinitely large. If this is the case then only energy states above E_f will be occupied by electrons and thus σ_0 represents the maximum possible conductivity of the material under test. In this situation the localised states will all be filled with electrons and the only states that would be free to contribute to conduction would be unfilled extended states (if they existed). σ_0 can then be attributed to the conductivity at the mobility edge E_c.

2.4.2 The relationship between conductivity and mobility

Le Comber and Spear [22] discovered three regions of conductivity and electron drift mobility as a function of temperature in 1μm thick intrinsic a-Si:H samples prepared at 200C. For temperatures of 240K or greater the electron μ_d rose from $0.01\text{cm}^2\text{s}^{-1}\text{V}^{-1}$ to $0.1\text{cm}^2\text{s}^{-1}\text{V}^{-1}$ at 300K with a slope that related to an activation energy (E_a) of 0.19eV above 240K and 0.09eV below it. This result led to the suggestion that temperature dependence of μ_d above 240K was a result of electrons being trapped and released into the extended states continuously, and that the localised states extended to 0.19eV below E_c.

The conductivity data also showed a change in gradient at 240K that related to a shift in E_a from 0.62 to 0.51eV. This corresponded to the change in E_a for μ_d of 0.1eV at 240K. Lastly a third region of poor conductivity was visible beneath 200K that levelled off to

$10^{-15}\Omega^{-1}cm^{-1}$. The large decrease in conductivity was attributed to electrons falling from localised states and the main conduction path becoming hopping near E_f.

The change in the drift mobility activation energy was attributed to the mode of conduction. Beneath 240K it is assumed to be phonon assisted hopping between localised states. Above 240K the conduction mechanism becomes the thermally activated release of carriers from localised states, which may interact with the extended states. Subtracting the mobility activation energy from the conductivity activation energy beneath 240K gives 0.51 - 0.09 = 0.42eV. From this it can be concluded that E_f lies 0.42eV beneath the localised states and that conduction occurs by phonon assisted hopping in the localised states with an average trap energy level of 0.09eV above the lowest energy localised state, 0.51eV above E_f. The drift mobility activation energy appears in the activation energy for conductivity in this region as conduction is still thermally activated. Carriers must be thermally promoted to the localised states, and then they must be provided with more thermal energy in order to achieve phonon assisted hopping.

Above 240K the conduction activation energy is 0.62eV which implies that E_c is 0.62eV above E_f, and that the localised states are 0.62 - 0.42 = 0.2eV wide. If it is assumed that this is the mechanism by which conduction is now occurring, carriers can now be directly promoted to E_c and the drift mobility activation energy is no longer considered part of the conductivity activation energy. This theory is given extra credibility as the mobility activation energy for this temperature region is 0.19eV, the same width as the band of localised states. Above 240K conductivity is dominated by extended state transport.

2.5 Doping a-Si:H

Substitutional doping of a-Si:H was first achieved by Spear and LeComber [24] in 1975. Before this discovery it was not sure whether or not substitutional doping was possible due to the method of dopant incorporation into a growing amorphous network. It was argued that atoms would be incorporated in such a manner that all bonds were satisfied. This is in contrast to c-Si where group III or V atoms are constrained to 4 bonds by their position in the lattice. The spare hole or electron from each atom is then readily excited to E_v or E_c at room temperature leaving nearly all donors ionised. Spear and LeComber concluded that if it was possible to observe substitutional doping in a-Si:H then the material would have to have a very low density of mid gap states, and narrow band tails.

Spear and LeComber prepared 0.5μm to 1μm thick layers of a-Si:H from a premade mixture of silane and a small amount of added phosphine or diborane. The reactor used was the same as mentioned in section 2.1. Room temperature conductivity (σ_{RT}) and E_a were then plotted against a range of dopant to silane concentrations expressed as N_{dopant}:N_{silane}

It was discovered that a small addition of phosphine ($N_{phosphine}$:N_{silane} = 6x10^{-6}) was sufficient to cause an conductivity increase of two orders of magnitude. With a $N_{phosphine}$:N_{silane} ratio of 10^{-4}) E_f was brought to 0.2eV of E_c. Near E_c there is a large density of localised states which pins the rise of E_f. Increasing the $N_{phosphine}$:N_{silane} ratio yet further to 10^{-2} brought E_f to 0.15eV of E_c and began to fill the localised states with electrons, conductivity improved by seven orders of magnitude from $10^{-9}\Omega^{-1}cm^{-1}$to $\approx 10^{-2}\Omega^{-1}cm^{-1}$. Intrinsic material was found to possess a slight n type characteristic which was attributed to donor states introduced by oxygen contamination of the gas flow.

A similar effect was observed using diborane as a dopant source. Conductivity increased rapidly by approximately 6 orders of magnitude at $N_{diborane}$:N_{silane} ratios of 10^{-4} to 10^{-2}, and E_f was brought to 0.3eV of E_v. The wider valence band tail prevented E_f from moving as close to E_v as E_c.

The increase in conductivity observed with larger N_{dopant}:N_{silane} ratios suggests that substitutional doping was taking place. As E_f is brought closer to either mobility edge then more carriers become free to move in extended states and the average drift carrier mobility will increase. By equating the known amount of atoms in the gas flow used to deposit the samples with the calculated ratio of dopant states to silicon atom density, Spear and LeComber estimated that only 20% of the available phosphorus atoms were incorporated into the amorphous network such that they contributed to doping. The other 80% were assumed to have their valency requirements satisfied and to be electrically inactive.

2.5.1 The doping mechanism

Substitutional doping was not expected to occur in a-Si:H because any dopant atom could have its valence satisfied as a consequence of being incorporated into an random network. A pentavalent or trivalent dopant atom in a four fold configuration is in a higher energy configuration than its natural state and it is possible that the energy of a plasma could induce such bonding, but then doping of a-Si:H should be influenced by the method of deposition and this is not observed. A mechanism of doping that is possible with a low energy configuration of the impurity atom is required to explain this.

The accepted explanation is that doping in a-Si:H proceeds in the opposite manner to that of c-Si. In c-Si a dopant atom is constrained in its four bond configuration by occupying a lattice site, and electrons or holes are then readily excited from shallow energy states to the bands at room temperature. Street [25] argued that dopants could be incorporated into an a-Si:H network in a similar configuration if they were ionised prior to incorporation. In this way a phosphorus atom would become positively charged and a boron atom would become negatively charged. These configurations are shown

in equation 2.10 and 2.11 where P_x and B_x denote a phosphorus or boron atom with x electrons present in its outermost orbitals. After incorporation in this manner dopant atoms would be free to act as acceptors and donors in a similar manner to their behavior in c-Si.

$$P_5 \rightarrow {P_4}^+ + e \tag{2.10}$$

$$B_3 \rightarrow {B_4}^- + h \tag{2.11}$$

The creation of ionised dopant atoms is controlled by the position of E_f. Both creation mechanisms are supported when E_f is located deep in the gap. As E_f moves towards a band edge the creation of ions is gradually suppressed to provide a self limiting doping density as was observed by Spear and LeComber [24].

2.5.2 Defects and doping

In order to conserve charge there must exist an equal and opposite charge density to that created by ionised dopant atoms. It is found that dangling silicon bonds are the compensating defects. LESR (Light induced Electronic Spin Resonance) measurements made on doped layers in the dark and at low temperature provide weak results that increase drastically with illumination [26]. (LESR resonances indicate the presence of unpaired electrons in chemical or atomic species under illumination). The resonance observed can be attributed to silicon dangling bonds and a roughly equal density of band tail electrons or holes released from defects. This can be explained in terms of electrically neutral dangling bonds releasing an electron or hole to a band tail under illumination and creating charged dangling bond deep defects as shown in figure 2.11.

Doped samples exhibit a larger density of defects ($\approx 10^{18} cm^{-3}$) compared to undoped samples ($\approx 10^{16} cm^{-3}$). Due to the large concentration of defects generated as a result of substitutional doping in a-Si:H, the minority carrier recombination rate increases due to non-radiative recombination through the enhanced density of midgap defect states [26].

2.6 Cell development

A-Si:H cells have been in development now for over 3 decades. From the original pn junction structure they have evolved to pin based designs in order to combat poor drift mobility and provide effective generated carrier collection over the intrinsic region. This is achieved using the built in electric field of the pn junction. Tandem and triple junction cells (which are created by stacking two or more pin junctions in series) have

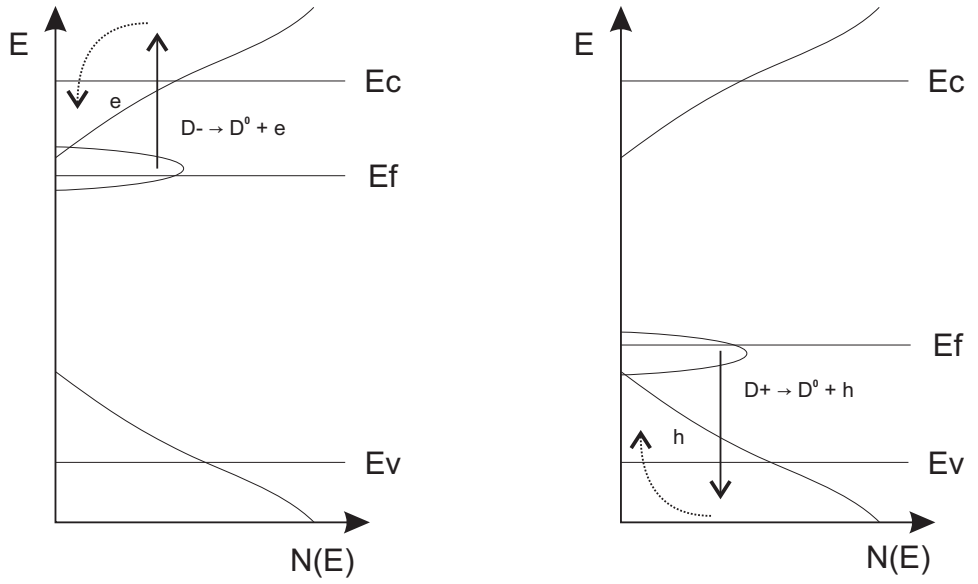

FIGURE 2.11: The creation of neutral dangling bond defects due to doping in n-type (left) and p-type (right) a-Si:H

been fabricated using a variety of materials allowing more efficient use of the AM1.5 solar test spectrum with varying results. A correctly designed multiple junction cell will possess a forward voltage that is the sum of all junctions in series, but current flow is limited to the pin junction that provides the smallest current and so careful matching is required.

The remainder of this chapter will provide an outline of how progress in the field of a-Si:H photovoltaics has resulted in the materials and cell designs under investigation today. It is assumed the reader has knowledge of the terms that describe an IV characteristic under illumination, but if not the topic is discussed in section 3.8.1. Discussion of cell orientations (superstrate and substrate) can be found in section 3.6.

2.6.1 The Staebler-Wronski effect

In 1977 Staebler and Wronski [27] discovered that the photocurrent of an a-Si:H cell would slowly decrease with exposure to light soaking. The original photo current of a cell was found to be restorable with an anneal at 150C or sometimes a large reverse bias. This effect was termed the Staebler-Wronski effect, and it was attributed to breaking Si-Si or Si-H bonds in the random amorphous network when exposed to light. This increases the midgap defect density and hence recombination current.

The Staebler-Wronski effect is accepted as a limitation of a-Si:H technology. Sometimes cells can lose as much as 10% of their initial efficiency after light soaking, and this is referred to as a stablised efficiency. Whilst it is a very real issue for a-Si:H technology it is a substantial problem that decades of research has not yet entirely eliminated and

as such it was felt that investigation into the effect would be beyond the scope of the project in terms of available time. Efficiencies quoted for cells created as part of the work detailed in this report are not stabilised.

2.7 Developments in the 1970s

2.7.1 The first a-Si:H pn junction and solar cell

The first a-Si:H device was a demonstration of a pn junction by Spear et al. [28] in 1976. Rectification had previously been observed using a Schottky diode formed by the interface between an a-Si:H layer and a metal contact [29] but this was the first diode to be created using only doped a-Si:H layers. It was found that the forward current was exponentially related to the forward voltage and that current under reverse bias was related to the temperature of the sample by an activation energy of 0.56eV. This suggests that the average energy state that electrons will fall to before recombining is 0.56eV beneath E_c. Fitting the diode IV characteristic to the ideal diode equation (3.5) resulted in an ideality factor of 2, this indicates that forward current flow in the device was recombination limited.

The first a-Si:H solar cell was made by Carlson and Wronski [30] in 1976. It consisted of a-Si:H on ITO coated glass in a pin superstrate configuration with an aluminium rear contact. A-Si:H was deposited from a silane glow discharge using diborane and phosphine as dopants. The p layer was ≈10nm thick and the n layer several times that, with a 1μm intrinsic layer in between. Under AM1 test conditions the cell was 2% efficient with FF = 0.4, I_{sc} = 10.5mA, and V_{oc} = 790mV. I_{sc} rose to 14mA under heating to 125C demonstrating trapping of carriers in localised states. Quantum efficiency measurements showed maximum absorption at 0.5μm. For forward voltages of less than 0.5V the diode ideality factor was ≈2, indicating that current was limited by recombination in a similar manner to the earlier results of Spear [28].

2.7.2 Increasing efficiency in pin a-Si:H cells

The efficiency of pin cells did not increase drastically in the years following Carlson and Wronski's initial cell. In 1981 Uchida et al. [31] achieved 4.3% efficiency using a metal substrate structure and a 1cm^2 single junction pin test cell. In the same year Kuwano et al. [32] produced a cell similar in structure with an efficiency of 4% and an area of 1cm^2. The relationship between increasing p layer thickness, increased V_{oc}, and reduced I_{sc} was also commented upon by Kuwano. Efficiency loss was analysed as a result of increasing the area of a planar cell structure, through the concept of the increasing series resistance of a front electrode in a substrate cell configuration.

The first a-Si:H tandem cell was created by Hamakawa et al. [33] in 1979. The best cell obtained used only one pin junction and was 4.5% efficient, but up to 5 cells in series were demonstrated to still be photoactive with a V_{oc} of more than 2V. The short circuit current in a tandem cell is limited to the lowest current supplied by any individual pin cell, and careful design of the individual cell thicknesses is required in order to balance the current generated by each. In general the thickness of each cell must exponentially increase towards the rear of the device as more long wavelength light is collected according to the absorption co-efficient ($\alpha(\lambda)$) of the a-Si:H material used.

Nakamura et al. [34] created a tandem cell with the second cell absorbing layer being an alloy of a-Si:H and a-Ge:H (Hydrogenated amorphous Germanium). Combining amorphous silicon and germanium allows narrowing of the mobility gap towards a-Ge:H (1.4eV). The aim was to enhance absorption of long wavelength light that would not not possible with a-Si:H due to the inability to sustain an electric field across an absorbing layer of sufficient thickness. Similar problems were encountered to the first tandem cell [33]. Current matching with differing materials becomes a many dimensional problem where multiple absorption spectra must be considered alongside layer thicknesses and transport properties. The tandem cell structure resulted in an efficiency of 3.2% and a FF of 0.6. I_{sc} was lacking which is attributable to un-optimised current matching and defects in the a-SiGe:H (Hydrogenated amorphous Silicon Germanium) layer, but enhanced absorption of long wavelength light at 600nm was detected compared to single junction a-Si:H cells.

2.7.3 Schottky barrier cells

Carlson [35] achieved a 5.5% efficient Schottky barrier cell in 1977, using a stainless steel substrate with 5nm of n type a-Si:H and 1μm of intrinsic material as the absorbing layer. Various metal layers were used to create the barrier, along with a palladium contact and a 45nm zinc oxide anti reflection layer. The use of a Schottky barrier can improve V_{oc} due to the work function of the metal, and cells made by this method with a platinum barrier exhibited values of V_{oc} up to 865mV. For the same cell J_{sc} was 7.8mAcm^{-2} and FF was 0.58. Voltages of up to 865mV and currents of up to 12mAcm^{-2} were obtained for other samples. The illumination used was similar to the AM1 spectrum and 65Wm^{-2} in intensity.

The area of the barrier cells that were made was only 0.02cm^2. Upscaling a measured current density to assume a 1cm^2 in this manner is a legitimate measurement of efficiency, but by only selecting regions of high quality material it is possible to remove the effect of poorer quality material surrounding it from the overall result. As such this result is more of an indication of potential for larger scale devices than a true efficiency result. Haruki et al. [36] attempted to improve the efficiency of a 100cm^2 module to that of a 1.2cm^2 cell in 1982. As cell area is scaled up, inhomogeneities in the absorbing

layer become increasingly important along with design features such as an efficient front contact scheme. These are not issues for a small area cell.

It is interesting to note that when the light used to test the cell was blue filtered, the FF increased to 0.7. The short wavelength light generates carriers close to the surface of the material and collection efficiency is improved if the device is illuminated such that holes are generated close to the p layer. Hole drift mobility is lower than electron drift mobility in a-Si:H due to the wider valence band tail states, by generating carriers close to the p layer less holes will recombine than if they had to traverse more of the intrinsic layer. Trapped carriers increase the cell's internal series resistance, whilst a large defect density decreases conductivity due to carrier loss by non radiative recombination. If the pin junction was illuminated from the opposite side using the same spectrum and irradiance FF would have decreased.

Madan et al. [37] reported a similar result in 1980 of a 6.3% efficient cell using a Schottky barrier and a substrate configuration on molybdenum. Cells with an area of 0.04cm^2 were tested and as such the validity of the efficiency is again questionable. A silicon fluoride/hydrogen mix was used as a precursor instead of silane but the cell was deposited by glow discharge in the same manner. The midgap state density was measured as 10^{16}cm^{-3} for a-Si:H deposited in this manner which was the lowest known density at that time. It is now considered readily achievable using a silane/hydrogen plasma.

Research into Schottky cells did not continue much beyond the late 1970s. Whilst straightforward and cheap to fabricate, advancements in heterojunction pin cell design overtook barrier technology.

2.7.4 Heterojunction cell design

Schottky barrier cells had an advantage over pin cells in the 1970s with regards to obtaining the most efficient devices as they were only required to have one doped region of a-Si:H at the rear of the cell. In a pin cell the short wavelength response would be dominated by the doped layer at the front of the cell with its large defect density and high recombination rate.

To improve the collection of short wavelength light in pin cells Tawada et al. [38] introduced a p type a-SiC:H (Hydrogenated amorphous Silicon Carbide) window layer to the front of a pin superstrate cell to make a heterojunction device. The superstrate pin structure was always expected to exhibit superior device performance due to the short hole diffusion length in a-Si:H, and the absorption of the p layer was the limiting factor for the design. Anderson and Spear [39] showed that the optical gap of a-Si:H increased with the carbon content of the layer and as such acts as a window that transmits photons that would normally be absorbed in the doped layer to the intrinsic region. Figure 2.12

shows the band diagram of a pin device with an a-SiC:H window layer and an aluminium back contact.

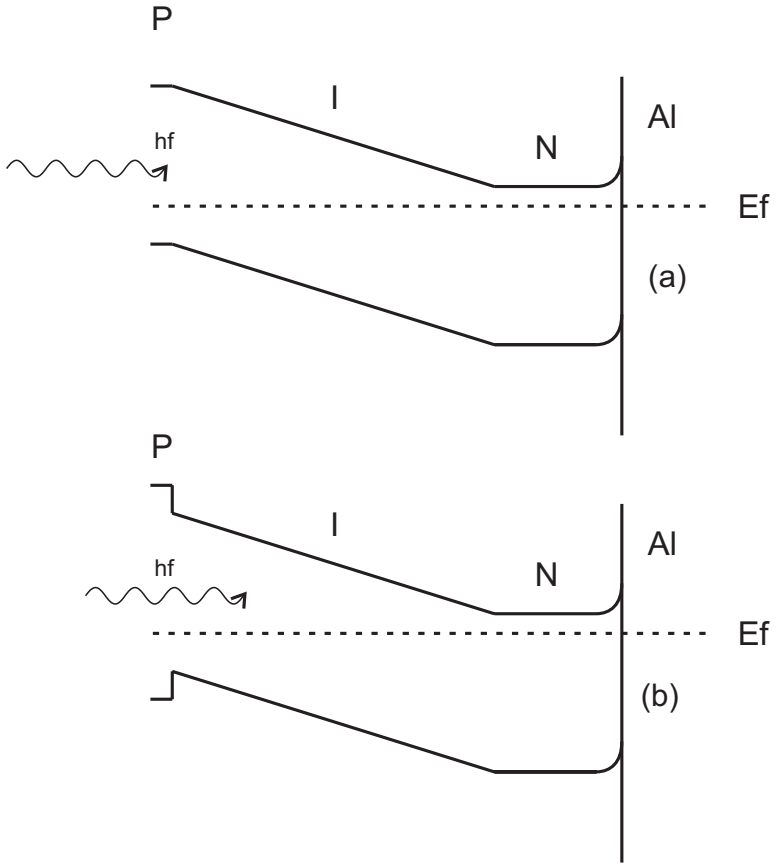

FIGURE 2.12: The band diagram of a conventional pin cell (a), and with a wide band gap SiC window layer (b) with emphasis on the enhanced transmission of short wavelength light to the intrinsic region due to the increased value of E_g

Conductivity measurements were taken using the a-SiC:H window layers. The undoped conductivity was $10^{-10}\Omega^{-1}cm^{-1}$, rising to $10^{-4}\Omega^{-1}cm^{-1}$for 5% diborane doped material and $10^{-2}\Omega^{-1}cm^{-1}$for 0.1% phosphine doped material. The activation energy of the conductivity was 1.08eV for undoped material, 0.4eV for p type, and 0.2eV for n type.

A $0.033cm^2$ cell fabricated with an a-SiC:H window layer had the characteristics of V_{oc} = 0.887V, J_{sc} = 12.33, FF = 0.653 and was 7.14% efficient. The improved carrier collection is shown in the enhanced FF and V_{oc} has also benefitted from the increased built in potential of the heterojunction. The internal quantum efficiency of the device was measured over the 400-700nm wavelength range and compared to a standard pin superstrate cell with no carbon present in the p layer. Figure 2.13 shows the enhancement in quantum efficiency that a wide band gap window layer provided. The results obtained by comparing the performance of cells with and without a wide bandgap window layer can be seen in section 4.6.

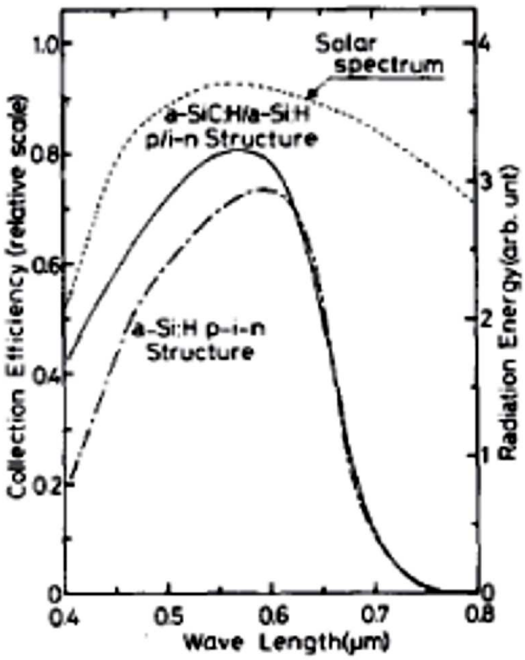

FIGURE 2.13: Comparison of the collection efficiency of an a-SiC:H/a-Si:H heterojunction cell and an a-Si:H homojunction cell. Reproduced from [38]

2.8 Developments in the 1980s and 1990s

2.8.1 Breaking the 10% efficiency barrier

The first published result to break the 10% efficiency barrier was Catalano et al. [40] in 1982. An efficiency of 10.1% was obtained for a single pin junction, with a device area of 1cm^2. In 1984 Yamazaki et al. [41] improved on this result for a single junction superstrate cell by minimising the defect density in the intrinsic layer via reduction of the oxygen and boron concentration in the intrinsic layer. Silane was stored in stainless steel cylinders instead of iron, and the glass/TCO (Transparent Conducting Oxide) substrates were baked in an oven prior to deposition to minimize oxygen contamination. Cells of 1.05cm^2 were produced and an efficiency of 10.5% was measured with a J_{sc} of 19mAcm^{-2} and a FF of 0.65. The exceptional current is an indication of the high quality of material, and the optimum thickness of the intrinsic layer was found to be 700nm. The improvent in efficiency to over 10% was encouraging evidence that a-Si:H technology could perhaps compete with more established materials on a cost per Watt basis.

2.8.2 Improvements in tandem and single junction cells

Guha et al. [42] published data in 1986 on tandem cells made using fluorinated a-Si:H and a-SiGe:H to enhance the long wavelength response. The p type layers were deposited

such that they were composed of μc-Si:H (See section 2.3.5). By altering the deposition region from a-Si:H to μc-Si:H the conductivity of a layer is significantly increased, E_f can be brought closer to E_v or E_c, and absorption of light decreases. This results in improvements for V_{oc}, J_{sc}, and FF. Table 2.1 shows the improvement in material quality as a-Si:H moves to μc-Si at the expense of optical absorption efficiency.

The tandem cell was 13% efficient, with $V_{oc} = 2.58$, $J_{sc} = 7\text{mAcm}^{-2}$, and FF=0.72. A single cell was 10.7% efficient. At the time of publication the design achieved the highest efficiency for a single and a tandem cell. All cells produced were 1cm^2, and so the figures quoted are a good indication of the design's potential.

	a-Si:H	μc-Si
σ_d ($\Omega^{-1}\text{cm}^{-1}$)	10^{-4}-10^{-3}	1-20
E_a (eV)	0.3-0.4	0.02-0.05
E_g (eV)	1.5-1.6	1.9-2
α (cm^{-1}) at 550nm	10^5	$3\text{x}10^4$

TABLE 2.1: Parameters of fluorinated p type a-Si:H compared to fluorinated p type μc-Si reproduced from [42]

In 1988 Yang et al. [43] improved on the tandem design of Guha by using a triple cell configuration with an a-SiGe:H bottom cell that was capable of absorbing 10% of light at 900nm. The cell parameters were $V_{oc} = 2.55$, $J_{sc} = 7.66\text{mAcm}^{-2}$, FF = 0.7, and the cell was 13.7% efficient. At the same time Fukuda et al. [44] obtained an efficiency of 12% for a single pin junction by improving the qualities of an a-SiC:H p type window layer, lowering the oxygen concentration in the intrinsic region, and grading the doping leading into a μc-Si n layer. Specifically the improvements in p and intrinsic layer quality led to an increase in the FF to 0.77, whilst V_{oc} and J_{sc} were 0.87V and 17.9mAcm^{-2}. Although very efficient, this cell was complicated to produce and involved two different deposition techniques. It does show that a-Si:H based technologies can obtain a similar FF to c-Si based cells if care is taken to optimise them.

Kazama et al. [45] improved the performance of a heterojunction pin cell by using a "δ doped" a-SiC:H p layer. The p layer was comprised of thin layers of boron and a-SiC:H sandwiched together in an alternating structure. The reasoning for the design is that the resulting p layer will possess enhanced photoconductivity and a greater than usual boron concentration which would improve V_{oc}. An improved photoconductivity an order of magnitude greater than that of a normal a-SiC:H p layer was measured, but the dark conductivity also increased. The structure improved V_{oc} to 0.93V for a single junction cell, using 2 boron layers surrounded by 2nm undoped a-SiC:H layers. The best cell produced was 11.5% efficient. In 1991 Higuchi et al. [46] refined the technique further by changing the boron dopant source and deposition technique to PECVD. The best cell produced with the refinements in place was a 12.3% efficient single pin junction.

It is noticeable that from the late 1980s onwards publications became less focused on device efficiency as large improvements became more and more unlikely due to a-Si:H technology drawing closer to its fundamental limits. Instead device stability and improvements in areas such as FF became more prominent as researchers started trying to apply the now relatively mature technology to real world devices and larger areas. A lot of effort was spent on bringing the designs of the early 1980s up to their potential, in particular varying E_g and absorption of tandem cell layers to take advantage of more of the solar spectrum and solve the current matching problems associated with such designs.

In 1992 Yang and Guha [47] achieved a stabilised efficiency of 11.16% with a double junction a-Si:H/a-SiGe:H tandem cell. The germanium concentration in the lower cell was varied with distance to grade E_g. Grading the lower cell in this way had previously been shown to result in a more efficient tandem cell [48].

2.8.3 Micromorph cells

The first change in direction in a-Si:H cell design for a decade occurred in 1993, with the introduction of the micromorph cell. Results had recently been published suggesting that intrinsic μc-Si was was more stable under high irradiances and heating than a-Si:H, slightly n type, and that E_g was comparable with a-SiGe:H at $\approx$ 1.4eV [21, 49]. The material exhibited properties in between those of a-Si:H and c-Si, but it was the stability of the material under prolonged illumination that convinced researchers it was a promising photovoltaic material. Prior to this μc-Si had been incorporated into cells to improve doping efficiency and the series resistance of p and n type layers.

Fluckiger et al. [50] were first to publish results of a single junction pin cell based on the material. A compensated μc-Si layer was developed by micro doping with 10ppm of diborane. This had the effect of decreasing conductivity to $3\text{x}10^{-8}\Omega^{-1}\text{cm}^{-1}$from $2\text{x}10^{-3}\Omega^{-1}\text{cm}^{-1}$and increasing the activation energy from 80meV to 517meV, compensating the initial n type character of the material. The photoconductivity of the compensated layers was found to increase slightly with light soaking at 590nm, whereas conventional a-Si:H layers showed a drop of $5\text{x}10^{-2}\Omega^{-1}\text{cm}^{-1}$after a week.

The p layer doping efficiency was investigated in terms of thickness, and it was found that layers between 20-30nm thick possessed a conductivity of $1\text{-}10\Omega^{-1}\text{cm}^{-1}$and E_a of less than 0.02eV. This increase in conductivity and doping efficiency is a indicator of μc-Si material compared to a-Si:H. Even films of 15nm or less had conductivities of $\approx 10^{-2}\Omega^{-1}\text{cm}^{-1}$which is several decades greater than that of p type a-Si:H ($\approx 10^{-5}\Omega^{-1}\text{cm}^{-1}$).

The best result for a pin superstrate cell made entirely using μc-Si was V_{oc} = 440mV, J_{sc} = 16.8mAcm^{-2}, and FF = 0.51. The device was 3.8% efficient. Absorption of light at 800nm was demonstrated, which would be impossible with an a-Si:H device. V_{oc} was

low, and it was suggested that a thin a-Si:H p type buffer layer could be used to increase it. Research into micromorph cells began to quickly gather interest in the same way that research into a-Si:H cells did a decade before, primarily due to their increased stability under light soaking.

2.8.4 Improvements in micromorph cells

Fischer et al. [51] improved upon the initial micromorph cell in several ways. To use a μc-Si pin cell most effectively it was inserted as the bottom cell of a tandem a-Si:H/μc-Si structure. In this way V_{oc} was boosted by the a-Si:H front cell, a-SiGe:H and its high defect density was replaced with μc-Si that could also absorb long wavelength light, and the bottom cell could be made thicker due to the superior conductivity of μc-Si. Stability under light soaking was expected to improve as the majority of the device was μc-Si.

The problem of having to compensate for the n type character of intrinsic μc-Si was solved by the use of a gas purifier to suppress oxygen in the precursor feed to the plasma. This allowed the μc-Si intrinsic layer to be extended to a thickness of 3.6μm. A boron compensated layer was limited to roughly 2μm in thickness.

The highest stabilised efficiency obtained for a single junction μc-Si cell was 7.7%. As expected J_{sc} was high (over 25mAcm^{-2}) and the cell absorbed light up to 1000nm in wavelength. When incorporated into a tandem cell current matching was obtained with a 0.3μm a-Si:H cell at about 13mAcm^{-2}. The stabilised tandem cell efficiency was 10%.

Torres et al. [52] and Keppner et al. [53] both attempted to increase the deposition rate of μc-Si by increasing the plasma excitation frequency and by depositing μc-Si in the presence of argon respectively. The high hydrogen dilution required to form a μc-Si layer reduces the deposition rate of μc-Si, sometimes to less than than 0.1nms^{-1}. Torres et al. [52] reported deposition rates of up to 0.43nms^{-1} with a plasma excitation frequency of 130MHz and a single junction efficiency of 4.9%.

Keppner et al. [53] deposited material at up to 1nms^{-1} and were also able to vary the average μc-Si grain size by varying the argon dilution. (A similar enhancement in a-Si:H deposition rate by depositing in the presence of inert gases had been noted [54], but the defect density of the grown material increased with the atomic weight of the inert gas used). The single junction efficiency was 3.15% and so it appears increasing the deposition rate of μc-Si may be detrimental to a cell's performance, but unfortunately perhaps necessary for a realistic deposition time of a several μm thick absorbing layer.

2.9 Development from 2000 to the present

Present day cells based on a-Si:H technology have not changed significantly since the introduction of the micromorph cell in 1993. Existing designs are still being refined, commonly with a view to commercial production. A-SiGe:H has been largely replaced as the bottom cell in tandem structures by μc-Si, although it is sometimes used as the middle cell in a triple stack configuration. A-SiC:H is still in use as a window layer for a-Si:H cells which are typically used as a thin top cell in a multiple junction configuration.

Vetterl et al. [55] reported a tandem a-Si:H/μc-Si cell that was 12% efficient with a 2μm absorbing μc-Si layer. It was found that the best μc-Si for solar applications was grown by carefully monitoring the silane/hydrogen dilution ratio to keep it close to the transition from a-Si:H. The issue of stability was not mentioned and so this is most likely an unstabilised figure. In 2002 Meier et al. [56] improved the light trapping of a micromorph design by changing the TCO to zinc oxide (a wide bandgap TCO). This design had an unstabilised efficiency of 12.3% with a 2μm thick absorbing μc-Si bottom cell.

The current best reported efficiency for an a-Si:H based cell is 14.6% (13% stabilised) by Yang et al. [57] in 1997. The cell was composed of an a-Si:H/a-SiGe:H/a-SiGe:H structure in an nip configuration on a stainless steel substrate and there is debate over whether or not μc-Si or nc-Si is a better material than a-SiGe:H for inclusion in such a design. In 2005 Yang et al. [58] replaced the lower cell with nc-Si and reported a 14.6% (12.6% stabilised) cell. They concluded that nc-Si was a potential replacement for a-SiGe:H but noted concerns about the ability to deposit it using a commercial process. Schropp et al. [59] reported a 10.9% efficient a-Si:H/a-SiGe:H/nc-Si stack structure using a silver/ZnO back contact in 2008. The deposition procedure was hot wire CVD rather than PECVD, but it is reported here because the techniques are relatively similar, and the use of stainless steel foil for a substrate also qualifies them as flexible cells.

Typically a micromorph tandem cell structure is limited by the current that the thin top a-Si:H cell can supply. If the thickness of the top cell is increased the cell stability under light soaking will be negatively affected, defeating the point of the micromorph concept. The most significant advance in recent years for multiple junction cell design was to place a conductive layer between the top and bottom cell of a micromorph stack that possesses a refractive index less than the a-Si:H top cell. Using a similar top contact such as SiO or ZnO, a waveguide is formed around the top cell increasing the optical path length experienced by light travelling into it. If the waveguiding layers are also textured then an even bigger increase in optical path length can be achieved as light is reflected and scattered. Figure 2.14 shows how the waveguiding effect occurs.

This approach was tested by Buehlmann et al. [60] who fabricated a micromorph cell with an n type 95nm thick SiO intermediate conducting layer between the top and bottom

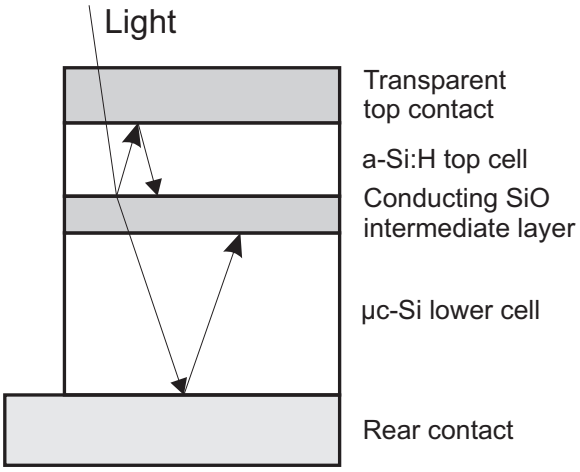

FIGURE 2.14: Use of a conducting SiO intermediate layer to improve optical path length in the top a-Si:H cell of a micromorph stack as reported by Buehlmann et al. [60]. If the refractive index of the top contact and the intermediate layer are less than the a-Si:H layer they surround, then waveguiding action will occur increasing the optical path length and top cell current generation. The top contact thickness may also be tuned as an anti reflective coating

cell. This was not the first attempt at such a device but it was the first to be produced in situ without breaking vacuum, other approaches used a ZnO intermediate layer which required multiple deposition techniques. The cell was 12.2% efficient (unstabilised), representing a relative performance increase of 8% over a cell without the reflecting layer.

2.10 Flexible substrates

The majority of a-Si:H cell production has focused on non flexible substrates. The best performing early cells used a pin superstrate configuration which required the use of a transparent substrate. The majority of flexible substrates are non transparent and therefore only viable in a substrate configuration. As substrates and deposition technology have improved over time and new photovoltaic grade materials have been discovered, use of flexible substrates poses less of a challenge then in previous decades. There is still much less published material available relating to flexible substrates than for rigid substrates, but momentum is beginning to gather.

Okaniwa et al. [61] [62] deposited single junction a-Si:H cells onto polyimide substrates in 1982 and 1983. Stainless steel was sputtered onto the polyimide substrates and single junction cells were grown in a pin substrate configuration. A best efficiency of 6.36% for a 0.09cm^2 area cell was reported. Lower efficiencies were obtained than when using a stainless steel substrate which was attributed to the increased surface roughness of the sputtered stainless steel on polyimide. The cells remained stable for 150 days and could be folded repeatedly without the efficiency deteriorating. For the time this was a

good result, especially considering the non-optimal layer order. Identical cells based on a stainless steel substrate were 7% efficient.

Since that attempt at cell fabrication using a flexible substrate, research in the area was comparatively low for many years as interest in new materials, multiple junction structures, and the race for greater efficiencies superseded it. Only in the last 10 years as efficiency figures have reached the point of diminishing returns with existing cell designs, has significant attention returned to reducing the cost per Watt of cells by cost reduction rather then improvements in efficiency. Flexible substrates allow a reduction in cost when compared to TCO coated glass, coupled with the possibility of roll to roll deposition which could also lower production costs. Use of a lightweight and flexible substrate also allows a reduction in transport costs and permits architectural applications where the use of rigid substrates would not be possible.

Japan was a pioneer in developing flexible a-Si:H technology to module sized areas. Yoshida et al. [63] [64] [65] began research in 1992 and in 2000 achieved a stabilised conversion efficiency of 9% using a tandem a-Si:H/a-SiGe:H module 40x80cm^2 in area. A stabilised 11% efficient 1cm^2 triple junction a-Si:H/a-SiGe:H/a-SiGe:H cell was also fabricated, both designs used a polyimide substrate. Also in 2000 Yoshida et al. [63] fabricated a 1cm^2 triple junction a-Si:H/a-SiGe:H/a-SiGe:H cell on polyimide as part of an effort to scale production of flexible substrate cells to 60x40cm^2 areas using a roll to roll process. The cells were 9-10% efficient when stabilised.

Research continued in the rest of the world during this period, and in particular Yang et al. [57] still hold the world record for a 13% efficient (stabilised) triple junction a-Si:H/a-SiGe:H/a-SiGe:H cell on stainless steel foil. Use of stainless steel foil is not ideal as a flexible substrate bcause it is still expensive compared to polymers and more vulnerable to bending and tearing. The advantage of using it is that it can withstand the temperatures where the best photovoltaic amorphous material is known to be grown.

In recent years there have been two approaches to resolving the issue of using high processing temperatures with lower melting point polymer substrates. The first was to optimise material quality at lower substrate temperatures and deposit directly onto polymers, and the second was to apply a lift-off procedure known as the Helianthos process.

The Helianthos process involves the deposition of a cell in reverse order onto aluminium foil coated with TCO. The TCO on the aluminium foil will eventually become the top contact of the cell. Once deposition is complete a rear contact is applied and the stack is bonded to a flexible polymer substrate. The aluminium foil is then etched away, the advantage of the process being that the foil can withstand the processing conditions that the polymer film could not. Figure 2.15 shows the steps of the procedure.

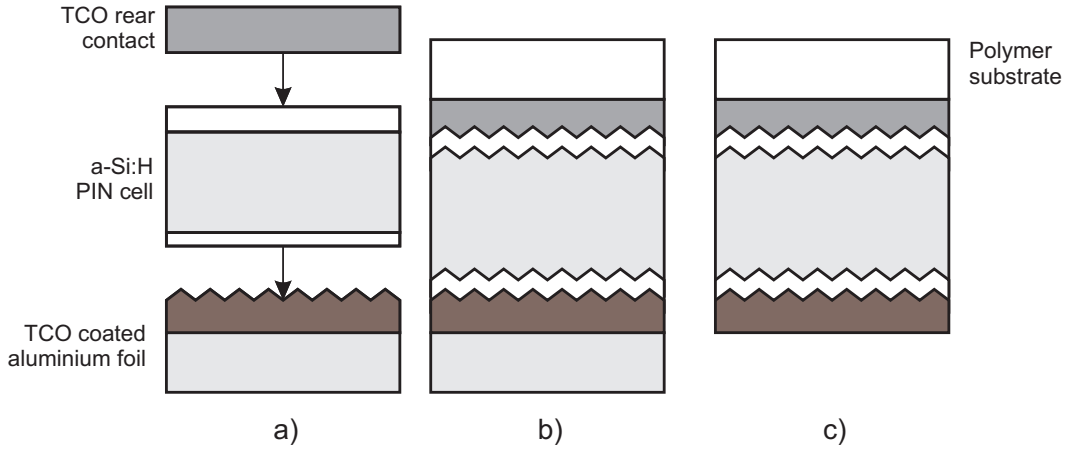

FIGURE 2.15: Construction of a polymer substrate flexible nip substrate cell by the Helianthos process. a) A pin substrate cell is deposited onto a previously prepared TCO/aluminium foil substrate followed by a TCO rear contact. b) A Polymer substrate is laminated onto the rear of the cell. c) The original aluminium substrate is chemically etched away to create the cell

Using the Helianthos process Liu et al. [66] deposited single junction pin cells with an initial efficiency of 7.69%. Van den Donker et al. [67] achieved an initial 60cm^2 module efficiency of 9.4% using a micromorph structure, and Li et al. [68] reported a 7.4% efficient tandem 25cm^2 minimodule using a tandem a-Si:H/nc-Si structure produced by hotwire CVD. These results were all published in 2007-2008.

Several research groups have been bypassing the requirements for this process by opting to deposit directly onto the final substrate at low temperature and tailoring the growth conditions to compensate for it. Brinza et al. [69] used a substrate temperature of 100C and grew single junction a-Si:H cells on stainless steel substrates with a view towards moving the process to a low temperature polymer substrate in the future. The degradation in the properties of a-Si:H grown at this temperature was countered by careful control of the hydrogen dilution, and the best cell was 5.5% efficient. Filonovich et al. [70] grew single junction a-Si:H nip substrate cells at 150C directly onto PEN (PolyEthylene Naphthalate) also resulting in a 5.5% best efficiency. Söderström et al. [71] also used PEN substrates upon which were deposited silver/ZnO textured back reflectors. A single junction a-Si:H cell was grown on top using μc-Si doped layers. An n type nc-SiC wide band gap buffer layer was found to improve series resistance. An initial efficiency of 8.8% was demonstrated using an absorbing intrinsic thickness of 270nm. The cell structure was optimised further [72] by converting it to a micromorph cell and including an intermediate ZnO reflecting layer in the same manner as Buehlmann et al. [60], immediate and stabilised efficiencies of 11.2% and 9.8% were reported. These results were all published in 2008-2009.

2.11 Summary of a-Si:H development

Figure 2.16 shows the improvements made in cell efficiency over the last 3 decades separated by cell design. The efficiencies are from all cells discussed in previous sections, and where possible stabilised efficiencies are used.

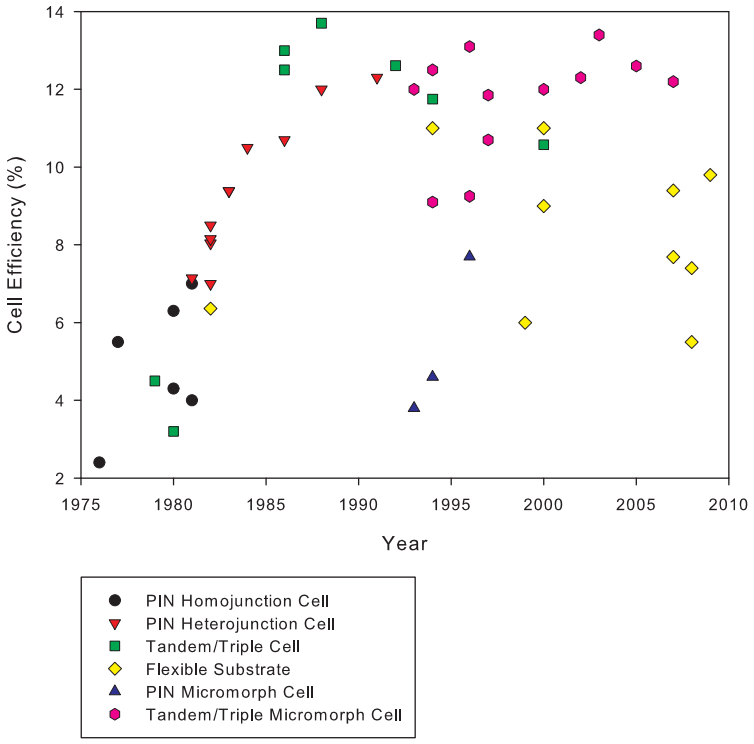

FIGURE 2.16: Published figures of cell efficiency with respect to design from 1976 to 2009. Stabilised efficiencies are preferred if provided by authors, more recent publications are likely to contain both an immediate and stabilised figure of efficiency

Two main trends are visible in the data. The first is the development of the single junction homojunction cell into the single junction heterojunction cell from 1976 to the mid 1990s, the best reported efficiencies were ≈12%. This figure should be probably be reduced by roughly 2% to account for stabilisation. The second trend of research starts in the early 1990s and continues to the present day fuelled by the discovery of μc-Si. Initially single junction μc-Si cells were grown and then combined with an a-Si:H top cell to form the micromorph tandem design which was found to be more stable under light soaking than fully amorphous tandem cells.

Research into multiple junction cells is scattered, mainly due to the variety in cell design. For a cell to be included in the tandem/triple cell category it must be fully amorphous. Tandem cells tend to possess better efficiencies than single junction cells but suffer from design complications relating to current matching of the individual junctions. The most efficient cell is currently a 13% a-Si:H/a-SiGe:H/a-SiGe:H triple junction structure

[57], and replacement of the lower cell with nc-Si has been trialled [58]. The stabilised efficiency was found to be slightly lower (12.6%) but with more work it is probable that the cell will be optimised further and the resistance of nc-Si to degredation will improve its efficiency beyond that of the all amorphous cell. A move to more than 3 junctions to improve efficiency seems unlikely as it will rapidly bring diminishing returns. Instead it is predicted that advancements in efficiency will be obtained by improvements in light harvesting, specifically through improved texturing and intermediate reflecting layers. This will increase the optical thickness of current limiting single junctions whilst retaining the stability of thin cells.

There has been comparatively little published research into moving cell fabrication to flexible substrates, but this trend is changing slowly as efforts are made to lower the cost per Watt of thin film technology by reducing production costs. Current research is divided between a transfer process from aluminium foil to a polymer substrate and lowering the substrate temperature so polymer substrates can be directly exposed to deposition without compromising material quality. From work published so far, it would appear that the area of low temperature cells derived from a-Si:H and deposited onto flexible substrates is a important area for current research.

Chapter 3

Fabrication and analysis

3.1 Plasma enhanced deposition of a-Si:H

A-Si:H films and solar cells produced for this report were deposited with an inductive PECVD reactor designed by Plasma Quest Ltd. Precursors are introduced into the reactor through a front or rear manually operated valve and are then disassociated by an RF plasma. This plasma is generated inductively using a circular antenna sited around a quartz tube. A substrate is clamped to an electrically heated copper mount and atoms, ions, and disassociated molecules form part of a growing thin film of a-Si:H at the substrate's surface. System pressure is maintained by a Seiko-Seiki turbo pump which is backed by a BOC Edwards drystar pump. Unreacted gas molecules and reactive species generated by the plasma are removed from the reactor, and processed by a CLEANSORB scrubber to remove pyrophoric, toxic, and hazardous gases before the flow is exhausted from the system completely. The system pressure during deposition was typically 10^{-2}mbar to 10^{-1}mbar with this pumping arrangement. Figure 3.1 shows the flow of gas through the reactor, the generated plasma, and the pumping scheme.

The gases used in the production of a-Si:H layers and devices were silane, diborane, phosphine, hydrogen, and methane. Silane is the source of the precursors for a-Si:H formation while diborane and phosphine act as dopant sources. Hydrogen is used to ensure effective defect passivation, and can also control film quality to an extent by scouring weaker bonds and promoting stable growth. If enough hydrogen is present then the growing a-Si:H film can become μc-Si or nc-Si. A plasma of methane and silane results in the deposition of SiC which is used as a wide band gap window layer.

All gases are supplied undiluted with the exception of the dopant gases which are a 1% mix in hydrogen. This is a safety measure due to their toxicity. Due to the toxic nature of the dopants and because silane spontaneously combusts in contact with air in concentrations greater than 4%; a 2.5slm (standard liters per minute) flow of nitrogen is

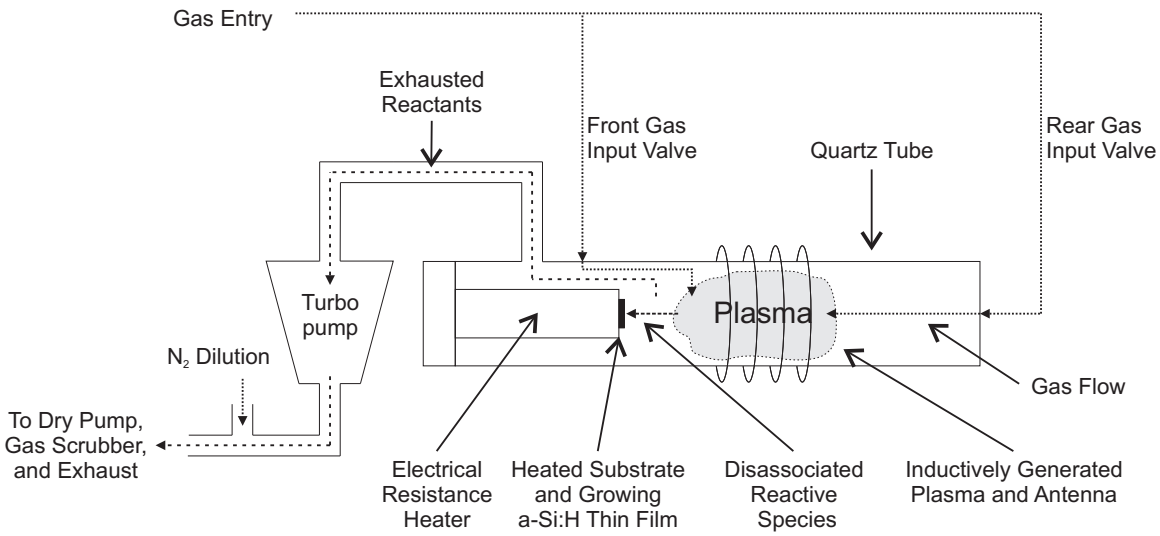

FIGURE 3.1: A system diagram showing the PECVD reaction chamber and gas flows. Gases are introduced by either or both of the front and rear reactor valves, and disassociated by an inductive plasma. Atoms, ion, and reactive species then form a growing thin film through deposition onto a heated substrate

introduced after the turbopump to dilute these gases to safe concentrations before they are scrubbed and exhausted from the system.

The deposition of a-Si:H takes place by incorporation of SiH_n precursors into a growing film [73]. These precursors are created by the disassociation of silane as shown in equations (3.1), (3.2), and (3.3) [74]. The value of energy listed for every reaction is required to decompose a silane molecule.

$$SiH_4 \leftrightharpoons SiH_2 + H_2 \qquad (2.2eV) \tag{3.1}$$

$$SiH_4 \leftrightharpoons SiH_3 + H \qquad (4.0eV) \tag{3.2}$$

$$SiH_4 \leftrightharpoons Si + 2H_2 \qquad (4.2eV) \tag{3.3}$$

An optimised plasma deposition will favour the creation of precursors over recombination back into silane or larger molecules comprised of silane. Factors that affect the reaction direction include the gas pressure in the reactor, the gas flow rate, and the RF power. Pressure determines the mean free path of a molecule in the chamber and whether reactions are favored at the film surface or not. Raising gas flow rates will cause the pressure to increase. High RF power raises the kinetic energy of all particles in the chamber, particularly electrons due to their low mass.

Higher system pressure is useful for maintaining a high deposition rate, but the use of a high system pressure and a corresponding large RF power will result in the formation of macroscopic polysilane particles or agglomerates within the reactor which complicate the deposition process. The polysilane particles appear as dust around the reactor and they can be incorporated into a growing film which is undesirable.

A more significant problem is that when dust is present it can swirl around the reactor when it is pumped down from atmospheric pressure after inserting a new substrate. This can cause dust to settle on the surface intended for deposition and initial growth at these points will be prevented. This causes pin holes which will lead to shunts when a contact is deposited to complete the cell. Figure 3.2 illustrates this problem. The density of pin holes in a film caused in this way can be minimized by carefully pumping down the reactor from atmospheric pressure at a slow rate if dust is present from previous use.

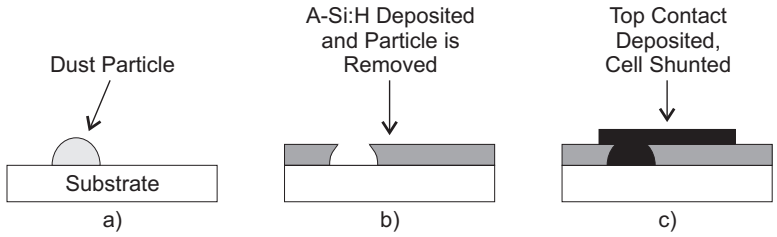

FIGURE 3.2: Cell shunt caused by a pin hole in a deposited a-Si:H film. Dust is moved to the surface of a substrate intended for deposition due to pumping down of the reactor (a). A-Si:H is deposited but the dust particle masks an area of the substrate. During substrate removal from the reactor the dust particle is dislodged by handling of the sample (b). A top contact is deposited to complete the cell but also contacts the substrate though the pin hole left by the dust particle causing a shunt (c)

High RF power, fast gas flow rates (increased system pressure), and increased substrate temperature all have the effect of providing extra energy to reactions which encourages the incorporation of higher order precursors into growing a-Si:H layers, promoting a cross linked SiH_n structure instead of singly bonded hydrogen atoms. An a-Si:H film structure with a majority of single and strongly bonded hydrogen atoms more closely resembles c-Si and will have a correspondingly lower defect density [73]. A careful balance of these 3 parameters is required to obtain optimum a-Si:H material depending on the required deposition rate. The substrate temperature is particularly important as it influences the distribution of Si-H bond strength, optimum temperatures of 200-300C result in a-Si:H that is more stable due to a stronger average Si-H bond strength [17].

3.2 RF source

The RF source was a manually tunable 40MHz Comdel RF amplifier which could supply 1kW of power to a 50Ω inductive antenna located around the quartz tube reactor. The RF power could only be set to a multiple of 10W, which hampered fine adjustment of RF

power as a process parameter. This was unfortunate as a-Si:H deposition only requires a relatively small RF power input. Ideally the RF source would have been less powerful but more tuneable.

Figure 3.3 shows how an inductive antenna is used to create a plasma remotely from a substrate; whilst the same substrate is directly in contact with the larger field strength of the capacitative reactor and will be subject to ion bombardment in the plasma sheath near the grounded electrode. The RF power employed when depositing a-Si:H using an inductive plasma is usually greater than the power required for an equivalent capacitative plasma due to the proximity of the plasma to the growing film and the reduced gas volume between the electrodes.

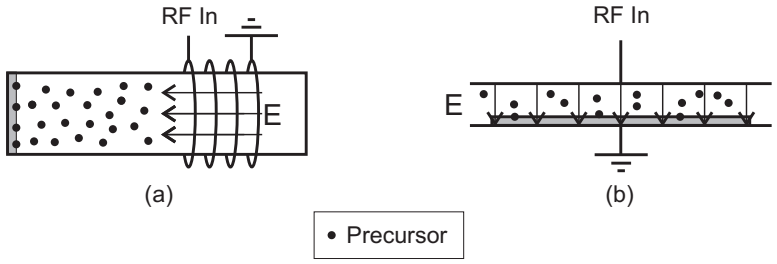

FIGURE 3.3: Generation of a remote inductive plasma (a), and a direct capacitative plasma (b). Note how use of a remote inductively coupled plasma reduces the plasma density at the substrate whilst allowing reactive species to diffuse to it. By contrast the dense capacitative plasma is in direct contact with the growing film. E represents the applied electric field

Inductive plasmas have the potential to produce high quality a-Si:H at lower temperatures than would be optimal for capacitative growth. A-Si:H grown using a capacitively generated plasma will be subject to bombardment by high energy ions and particles which can cause defects, use of a higher substrate temperature serves to anneal these defects during growth. By generating a plasma remotely from a growing film and allowing disassociated precursors and atoms to arrive at the surface in the presence of a reduced plasma concentration and field strength, it should be possible to reduce the defect density caused by bombardment. This means a lower substrate temperature can be used to grow a-Si:H for a given defect density when compared to capacitative PECVD. A major disadvantage of inductive coupling is that uniform growth is harder to maintain over large areas whereas it is straightforward using capacitative PECVD as a result of the electrode geometry.

3.2.1 Inductive plasma generation

The first reactor that produced a-Si:H with a low enough defect concentration to be of use electronically was inductive [9], but since then use of a remote plasma to deposit a-Si:H is not nearly as heavily documented as direct plasmas. However some results have been published. Wang and Lucovsky [21] used an inductive remote plasma in 1990 to

deposit μc-Si micro-doped with boron to compensate it and produce intrinsic PV grade material. Excited helium was used to disassociate silane. A feature of this deposition method was that it was possible to keep the final hydrogen content of a film lower than with a direct plasma for a given substrate temperature. Films that would normally required a substrate temperature of 200-250C were deposited at substrate temperatures as low as 150C.

Johnson et al. [75] found that using a remote plasma substrate temperatures of up to 400C could produce layers with ≈10% bonded hydrogen, which is very similar to a-Si:H produced around 250C using a more conventional capacitative reactor. The films grown with a remote plasma exhibited greater stability, which was attributed to a more stable bonding structure (a narrower distribution of Si-H bond energies) of hydrogen promoted by the higher temperature and the location of the growing film away from the direct effects of the plasma.

Stevens and Johnson [76] found that the temperatures of 400C and 250C for remote plasma and glow discharge growth corresponded with the maximum intrinsic stress (measured at the substrate temperature directly after growth) of a-Si:H layers. This was attributed to growth conditions that provided a large concentration of "invasive" hydrogen that would penetrate a growing layer and hydrogenate deeper Si bonds rather than only hydrogen at the surface of a film contributing to growth. The conclusion of intrinsic layer stress being related to the a-Si:H micro structure was supported by a further increase in intrinsic stress after the transition of a-Si:H to μc-Si with increasing hydrogen flow.

3.2.2 RF frequency

The most common RF frequency used in PECVD is 13.56MHz. The reasons for this choice were existing standards, and the wide availability of RF technology operating at that frequency. Because of these reasons 13.56MHz was not chosen as an optimised frequency for PECVD deposition and there is substantial evidence that higher excitation frequencies are better suited to a-Si:H deposition. Use of a high frequency RF source has been shown to increase deposition rates and grain size when depositing a-Si:H and μc-Si [77, 49, 78]. Increased μc-Si deposition rates are desirable in order to make devices thicker than several μm commercially viable.

Howling et al. [79] compared the effect of varying the generation frequency of a 5W capacitative plasma from 13.56MHz to 70MHz on the deposition of a-Si:H. It was found that the deposition rate increased from 0.33nms^{-1} at 13.56MHz to 1nms^{-1} at 70MHz. The films produced all had defect densities of less than 1-2x10^{16}cm^{-3} and Urbach energies of less than 60meV. When the RF power was increased at 13.56MHz to obtain a 1nms^{-1} deposition rate the defect density increased. It is assumed that deposition of a-Si:H by

inductive PECVD would benefit from increased RF frequency in the same manner via improved disassociation of silane molecules.

3.3 Substrate heater

In order to deposit optimum quality a-Si:H, a heated substrate is required. This was provided by a nichrome wire resistance heater sandwiched between copper plates and sprung loaded against the copper substrate mount. The heater was sited behind a sealed flange so that air could be pumped out and a vacuum maintained to prevent oxidisation of the nichrome wire and copper plates. Connections to the heating element were passed through the flange and brought to the heater element using solid copper wire. This sealed unit was mounted on rails such that it could slide out of the PECVD reactor to allow for sample exchange. Figure 3.4 shows the sprung loaded heater and how it inserts into the reactor. A water jacket surrounds the heater to remove heat from the sides, and the front and rear flanges that support the quartz reactor tube are also water cooled.

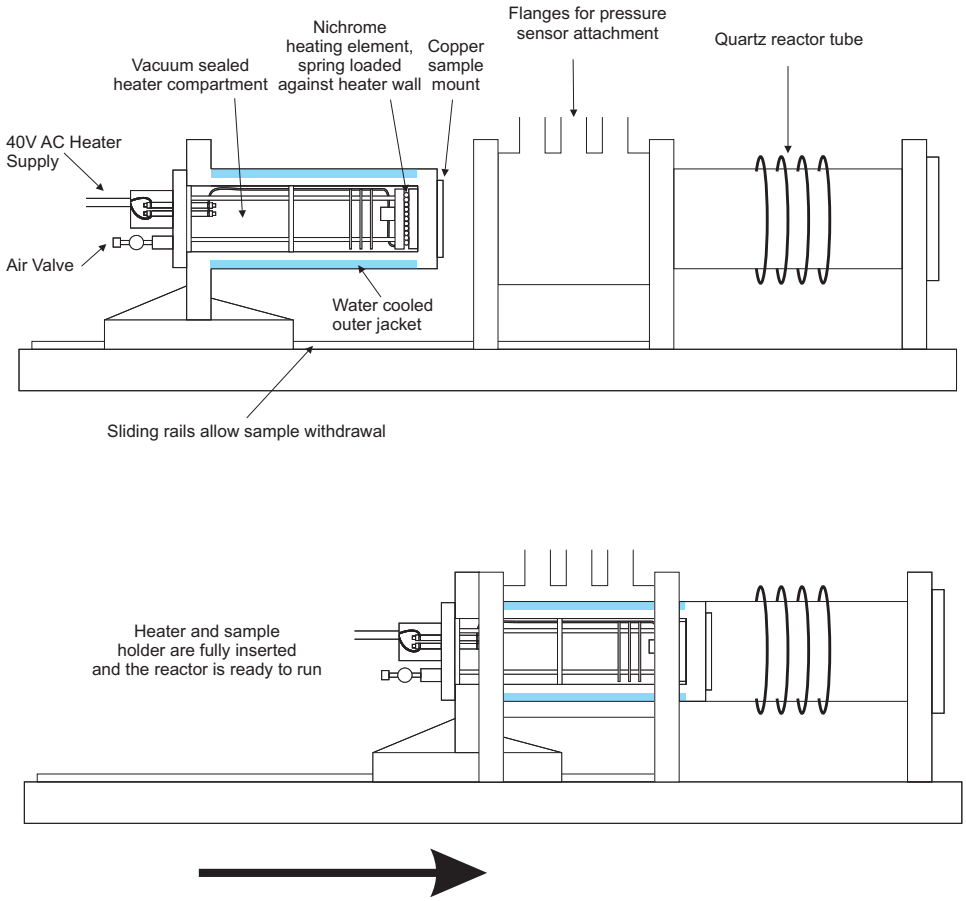

FIGURE 3.4: Detail of the electrical substrate heater including insertion into the reactor, internal wiring, water cooling, and the vacuum seals that prevent heater oxidisation

Substrate temperature was controlled by a Eurotherm 91e PID controller, the feedback sensor for which is a K-type thermocouple inserted into the copper substrate mount.

The PID controller is used in conjunction with a solid state relay and a 6:1 step down transformer to switch a 40V AC signal to the resistance element as needed to maintain a preset substrate temperature. The maximum heater current draw was 33.5A measured using a clamp meter, making the total RMS power supplied to the element slightly under 1KW.

Over the course of the project, the heating element had to be repaired multiple times due to the nichrome wire melting, usually at the ceramic junction box where it was joined to the copper feed. It is suspected that this was due to localised heating effects. Nichrome wire has a melting point of 1400C, but its dissipation would be poor due to the vacuum and the ceramic beads that isolated it.

3.4 Gas flow and delivery

As previously mentioned (see section 3.1) 5 gases were available for use during deposition. Silane was the source of the silicon based precursors that enabled deposition. The diborane mix was the source of boron atoms which acted as a p type dopant and also hydrogen, likewise the phosphine mix supplied phosphorus atoms (which acted as an n type dopant) and also hydrogen. Pure hydrogen was connected to the system to enable high dilutions of silane. Finally methane was used in tandem with silane to deposit silicon carbide which is a wide bandgap semiconductor that can be doped p and n type, and therefore is suitable for fabricating window layers.

Silane is pyrophoric above a 4% concentration in oxygen and diborane and phosphine are toxic above a level of a few ppm in air, so precautions had to be taken in order to ensure user safety during PECVD operation. Gases were supplied from pressurised cylinders located in sealed and exhausted cabinets, and gas delivery to the PECVD reactor was controlled by pneumatic valves on every delivery line. These pneumatic valves were switched from a gas control unit which in turn was allowed to operate by a PCS (Plant Control System). The PCS monitored the pressure of nitrogen used for the dilution of exhausted gases, and the pressure of an air line required to operate the pneumatic valves. It also received a signal from a toxic gas monitoring system with multiple hydride and hydrogen gas detectors located around the PECVD reactor, the drypump, the exhaust system, and the gas cylinders. If a gas leak, or a lack of air or nitrogen pressure was detected the PCS would automatically shut all pneumatic valves whilst sounding an alarm. Both the PCS and the gas control unit were activated via keyswitches, the keys for which were located away from the PECVD reactor.

Figure 3.5 is a schematic of the gas delivery system to the PECVD reactor including monitoring systems and control signals. The gas control unit outputted 8 24V DC control signals that activated pneumatic valves. The request gas signal from the gas control unit activated a pneumatic valve on every gas line that was sited directly after cylinder

regulation. The process gas signal activated a valve on every gas line simultaneously that was situated before a MFC (Mass Flow Controller). MFCs are adjustable valves that controlled the individual flow rate of gases to an accuracy of 0.1sccm, the flow rates were set using an MKS controller located by the gas control unit. The use of MFCs allowed individual gas flow rates to be accurately set as deposition process parameters. Lastly each gas line had an individually selected valve located after its MFC which allowed varying combinations of gas flow to the reactor to be selected as required for a deposition process. The bypass valves allowed the removal of MFCs from the gas delivery path in order to fully evacuate the lines after a deposition had finished and the system was to be shut down.

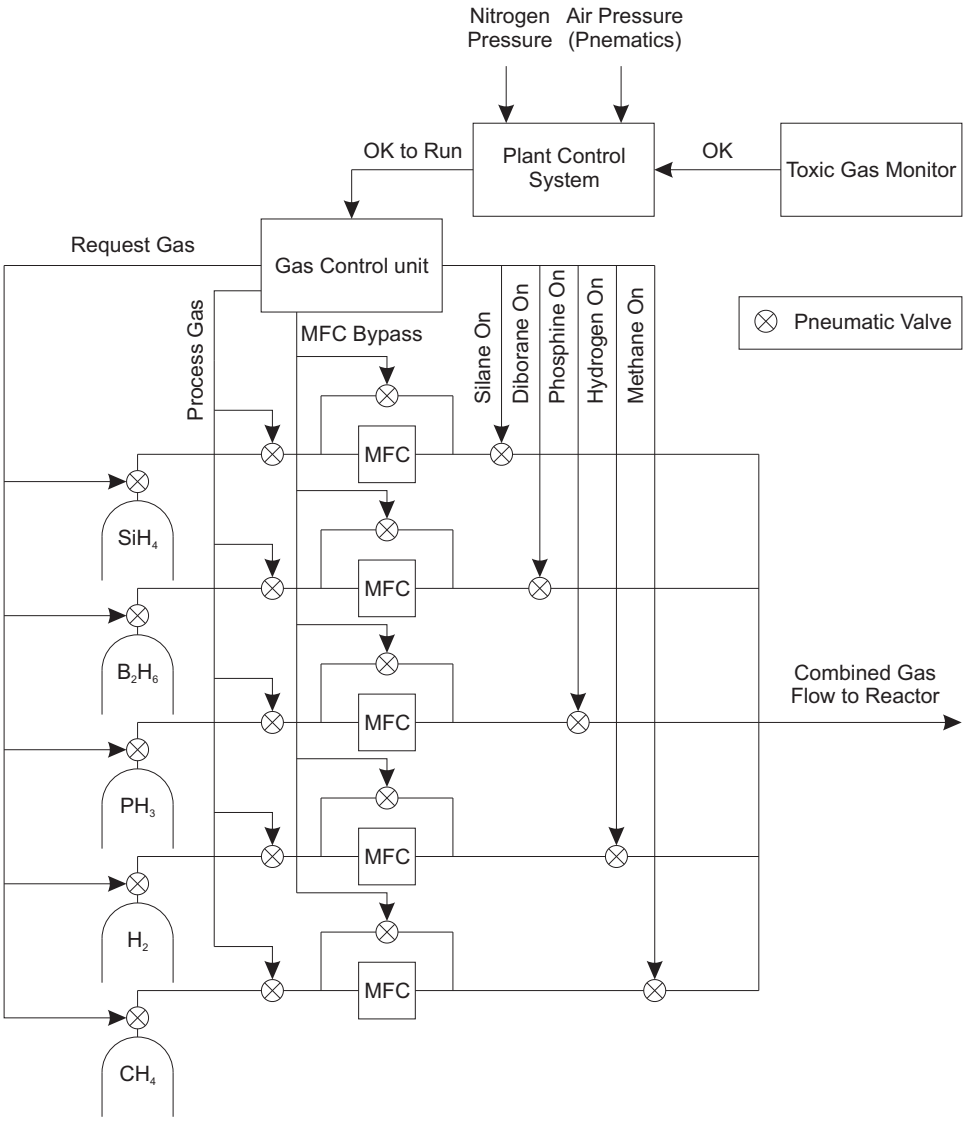

FIGURE 3.5: A schematic of gas delivery from pressurised cylinders to the PECVD reactor, where individual gas flow rate is limited by MFCs. Gas flows are controlled by pneumatically activated valves which are switched by a gas control unit. The gas control unit is given permission to operate by a PCS which monitors toxic gas levels, air pressure for the pneumatic valves, and nitrogen pressure for the dilution of exhausted gases

The PECVD reactor was equipped with several sensors to monitor pressure during deposition and pumping. The reactor itself had a Pirani gauge, a Barocel pressure transducer, and a cold cathode Penning gauge attached. A second Pirani gauge was mounted on the backing line for the turbopump. The Pirani gauges and the Barocel were manufactured by BOC Edwards and the cold cathode gauge was made by MKS instruments as was the active multiple gauge controller.

A Pirani gauge measures pressure by monitoring the resistance of a wire which depends on the wire's temperature. Gas molecules colliding with the wire lower its temperature and so pressure can be deduced. Pirani gauges are suitable for operation from atmospheric pressure to 10^{-4}mbar. A Barocel gauge capacitively measures the displacement of a membrane in order to measure pressure. It is used over an operating range similar to a Pirani gauge, except that it will work close to atmosphere pressure. In the pressure range of 10^{-2}mbar to 1mbar it is considered more accurate than the Pirani reading and all system pressure readings quoted in this report are taken from the Barocel gauge. A Penning gauge works by measuring the disruption of an ion beam by gas molecules and is used to measure high vacuums of 10^{-6}mbar to 10^{-4}mbar. It was primarily used to calculate very low base pressures obtained using the turbopump that the Pirani and Barocel gauges could not.

3.5 Contact deposition

After a-Si:H deposition a final contact is required to complete a cell and these contacts were deposited by thermal evaporation of aluminium. The evaporation chamber was also equipped with an e-beam (electron beam) source to deposit metals with higher melting points such as chromium, molybdenum, tungsten, and tantalum. The chamber was evacuated with a rotary oil pump and then pumped further using a cryopump that enabled pressures of 10^{-7}mbar to be reached prior to deposition. After contact evaporation, cells were annealed in an oven for 30 minutes at 150C to reduce series resistance and reduce any Schottkey barriers present between the aluminium contact and the a-Si:H.

The thermal evaporation vessel was a 0.5mm thick tungsten boat, and this was heated by a 230V AC mains variac stepped down to 6V AC. 80V AC supplied from the variac was sufficient to evaporate aluminium. Thermal evaporation of material was preferred over e-beam where possible because thermal evaporation takes seconds to deposit a relatively thick layer, however accurate control of the layer thickness is not possible. Thermally evaporated aluminium contacts of varying thickness were compared to 200nm thick contacts deposited using e-beam evaporation and no effects were observed.

The e-beam source filament was powered by a 4500V DC power source, which could supply a maximum current of 600mA. When supplying this maximum current the voltage

source dropped under load to 3000V DC but this was sufficient to evaporate tungsten which has a melting point of 3422C. For high melting point metal depositions the crucibles used to hold material were either molybdenum or tungsten. The deposition rate for metals evaporated by e-beam was dependent on the beam current, but typically 0.2nms^{-1} to 0.4nms^{-1} was observed. The deposition rate was calculated with a quartz crystal thickness monitor, and the total deposited layer thickness was measurable to 0.1nm.

Some cell orientations required transparent contacts to be deposited after cell fabrication, and this was achieved by RF reactive sputtering of an indium tin target in the presence of oxygen. This resulted in ITO deposition which is a wide bandgap n type semiconductor with good conductivity due to oxygen atoms acting as electron donors to the conduction band at room temperature. The sputterer used to deposit ITO was designed by Plasma Quest Ltd and specific details are proprietary.

3.6 Cell production

There are 2 configurations that planar amorphous silicon cells can be grown in. The first is termed superstrate and the cell is illuminated through the substrate it is deposited on which is usually TCO coated glass. The second is known as substrate configuration and occurs when a cell is deposited onto an opaque substrate and must be illuminated through a deposited transparent top contact. Figure 3.6 shows both device configurations.

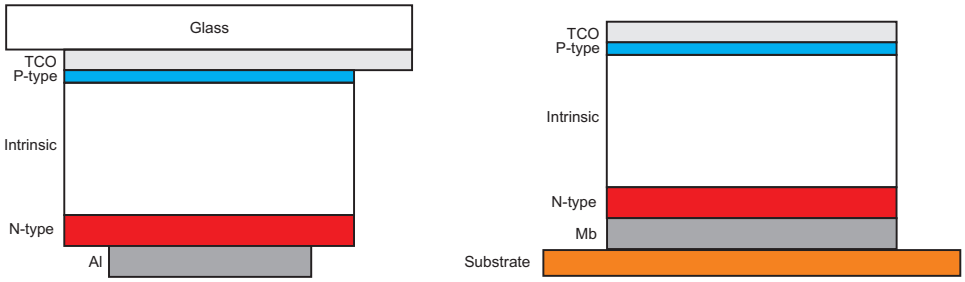

FIGURE 3.6: The superstrate cell configuration (left) and the substrate cell configuration (right)

A-Si:H cells must be grown with an intrinsic region as opposed to a pn junction to compensate for low carrier drift mobilities. The electric field across the intrinsic region is required to achieve effective separation of generated carriers and a rectifying junction.

Both configurations are usually illuminated through a TCO/p layer interface. This improves device performance by generating most carriers close to this interface, lowering hole recombination probability. Due to the low hole mobility of a-Si:H, efficient collection is a priority for ensuring good cell performance. The n layer is adjacent to a reflecting metallic back contact which is also typically n type improving cell series resistance. If a

conducting substrate such as stainless steel is used in substrate configuration the n layer can be grown directly on it. In other cases such as deposition onto flexible or organic substrates a layer of molybdenum or a similar metal is usually evaporated or sputtered onto the substrate prior to a-Si:H deposition. Glass pre-coated with TCO that has been optimised to improve the electrical and optical properties of a-Si:H cells in a superstrate configuration is the most commonly employed substrate, as a thin p layer can be grown on it without the problem of cells shunting due to TCO surface roughness.

Pin and nip cells were grown in a superstrate configuration on tin oxide coated soda lime glass during the project, and nip cells were also grown in the substrate configuration. Regardless of cell orientation all substrates were suitably cleaned before a-Si:H deposition, typically with IPA (IsoPropAnol) followed by a nitrogen clean to remove dust. The substrate was then mounted on the heater head and an area of it was masked with a glass slide to allow contacting of the TCO after a-Si:H deposition. The reactor was then vacuum pumped to base pressure and when the required substrate temperature and base pressure were achieved, the larger pump valve to the turbopump was closed and a smaller process valve opened. This increased gas residence time and system pressure to prevent a slow deposition rate. All gas lines were also evacuated to base pressure before any gas cylinders were opened to minimize process contamination. Before deposition all gas lines were pre-flowed for at least 5 minutes as another measure against process contamination.

Gas flow was established for the first layer to be deposited and given ten minutes to allow thorough mixing before plasma turn on. After a plasma was struck and deposition had commenced, gases were switched on or off as required to deposit layers in sequence and if necessary a plasma break was employed between layer deposition to minimize cross layer dopant contamination. In particular a plasma break and gas flush is very important when depositing nip substrate cells after n layer deposition. If this is not observed then intrinsic layer contamination will ensue and the cell will be reduced to a pn junction as opposed to pin which will heavily degrade performance.

When a deposition was completed, the sample was removed from the PECVD reactor and aluminium or ITO contacts were deposited by either e-beam evaporation, thermal evaporation, or RF sputtering using an aluminium shadow mask. Cells were given a contact anneal for thirty minutes at 150C to improve series resistance and to reduce Schottky barriers at the back contact/a-Si:H interface. Carrier mobilities in a-Si:H are low when no field is present, so there was no need to isolate individual cells as only a-Si:H located between a deposited contact and the substrate would contribute to light collection. Therefore the active cell area can be defined by the deposited contact, with edge effects being negligible. Using this method each deposition yielded multiple cells for characterisation with a minimum of post deposition processing.

A problem with this method of defining individual cells is that there is a parasitic resistance associated with each cell due to the TCO located between it and the aluminium contact located on the TCO. This resistance increases with the distance of the cell from the contact on the TCO. Figure 3.7 shows a top down and cross section view of multiple cells grown on one substrate, and the parasitic resistance associated with each cell (R_{TCO}).

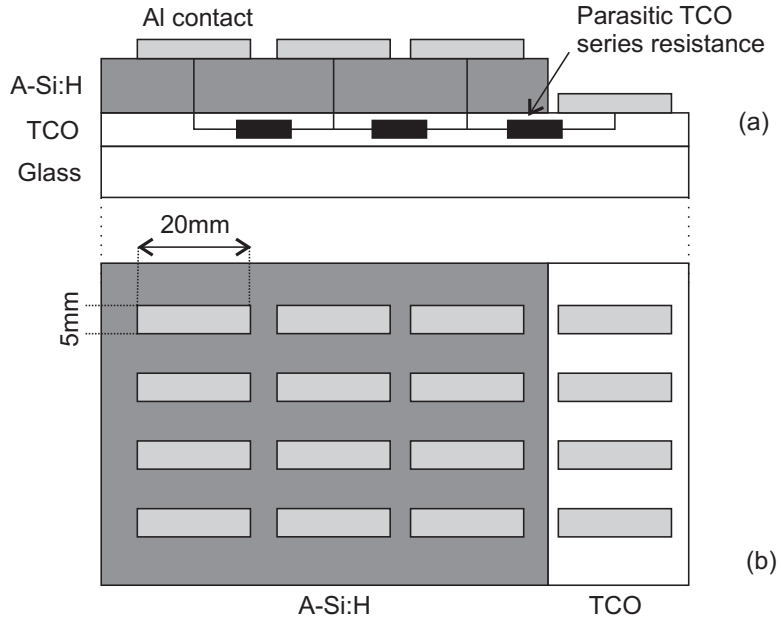

FIGURE 3.7: The production of multiple a-Si:H cells on one substrate as seen in cross section (a), from the top down (b) and the parasitic TCO resistance associated with each cell

If R_{TCO} between a cell and a contact is known then a measured IV characteristic can be corrected using equation (3.4). Typical measured values of R_{TCO} are 10-20Ω where distance is measured from the center of a cell to the center of the contact it is brought out to via the TCO.

$$V_{\text{corrected}} = V_{\text{uncorrected}} + R_{\text{TCO}} I \tag{3.4}$$

3.7 Analysis methods

When analysing samples of a material such as a-Si:H and especially when research is intended for an application such as PV, it is important to consider both optical and electronic properties. Either of these areas on their own will yield important information, but by combining them it is possible to build up a more complete picture of device operation. Analysis of a-Si:H in this thesis takes two forms. The first is work on complete cells for which IV characteristics are measured in darkness and under illumination where appropriate so that diode model parameters can be extracted. Perhaps the most important measurement that can be taken from a cell IV characteristic is a figure of efficiency, but restricting device characterisation to such a simple measurement would not give any significant insights into its operation.

The second set of techniques focus on measurements performed using thin homogeneous layers of a-Si:H. Electronic measurements of conductivity performed at different temperatures can provide a figure for the activation energy of conduction (which relates to verification of doping efficiency), and a conductivity prefactor. This type of measurement is very useful with regards to verifying the doping efficiency of a deposition process, testing intrinsic a-Si:H to make sure it has not been contaminated with dopants during deposition, and examining a-Si:H for the presence of crystalline material. To compliment the conductivity measurements spectroscopic ellipsometry was performed to determine complex refractive index and E_g amongst other model parameters.

3.8 Measurement of cell IV characteristics

3.8.1 The ideal solar cell model

The equivalent circuit of an ideal solar cell is shown in Figure 3.8 and is comprised of an ideal diode in parallel with a photo-generated current source. The current source flows in the opposite direction to the diode forward current. The model also includes the parasitic shunt and series resistances R_{shunt} and R_s. R_{shunt} represents current loss by recombination inside the diode and would be infinitely large in an ideal device. R_s is the internal series resistance and is heavily influenced by the resistivity and thickness of a-Si:H layers in a device and the interfaces between them. R_s is a parameter that is related to 3D current paths in a cell (especially when under illumination) and as such is sometimes referred to as the lumped series resistance. In an ideal cell it would be 0.

The expression for the flow of current in an ideal diode (I_D) is given in equation (3.5) where I_s is the reverse saturation current, V the applied voltage, and k is Boltzmann's constant. T and q have their usual meanings.

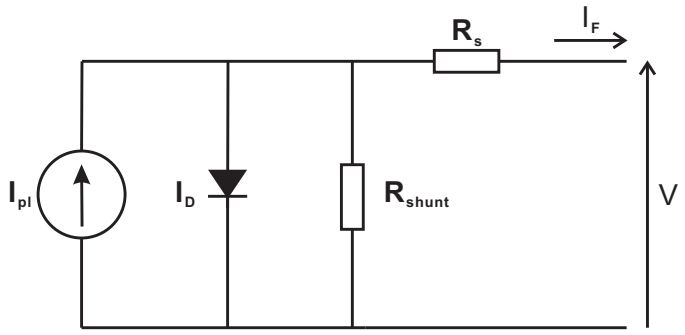

FIGURE 3.8: The ideal diode model with photo current I_{pl}, and non-ideal resistive elements R_s and R_{shunt}

To model an ideal solar cell the photo-generated current I_{pl} is placed in parallel with this expression and flows in the opposite direction. This results in equation (3.6). If the current and voltage losses due to the non-ideal parasitic resistances R_{shunt}, R_s, and a diode ideality factor υ are included, the equation becomes (3.7). The diode ideality factor (υ) is introduced to model recombination in a device. If the only current present is the ideal diffusion current then $\upsilon = 1$, and if a recombination current dominates then $\upsilon = 2$.

$$I_D = I_s(\exp^{\frac{qV}{kT}} - 1) \tag{3.5}$$

$$\begin{aligned} I_F &= I_{pl} - I_D \\ &= I_{pl} - I_s(\exp^{\frac{qV}{\upsilon kT}} - 1) \end{aligned} \tag{3.6}$$

$$I_F = I_{pl} - I_s(\exp^{\frac{q(V+(I_F R_s))}{\upsilon kT}} - 1) - \frac{V + (I_F R_s))}{R_{shunt}} \tag{3.7}$$

By setting I_F to zero in equation (3.6), an expression for V_{oc} is obtained which is given in equation (3.8). V_{oc} is the forward voltage bias where $I_D = I_{pl}$ and there is no current flow. V_{oc} is a logarithmic function of I_s and I_{pl}. I_{sc} (short circuit current) is the current flow at zero voltage bias, which is given by $-(I_s + I_{pl})$, I_s is typically $\approx$ 4 orders of magnitude lower than I_{pl} and often ignored when analysing illuminated IV.

$$V_{oc} = \frac{kT}{q} \ln(\frac{I_{pl}}{I_s}) \tag{3.8}$$

As an extension to the single diode model it is possible to fit an expression to an IV characteristic that is comprised of 2 exponential current sources with differing but fixed ideality factors. In c-Si diodes this approach is used to account for radiative band to band

recombination ($\upsilon = 1$) at the same time as recombination in the space charge region ($\upsilon = 2$). This model is also applicable to amorphous silicon due to the midgap defect density that exists at any point in a cell that facilitates recombination. A-Si:H cells are more leaky than c-Si cells, which is seen in reduced values of R_{shunt}. Sometimes the quality factor of the first diode expression is allowed to vary. The equation for current flow using the double diode model is shown in (3.9), whilst the equivalent circuit model consists of the ideal model shown in Figure 3.8 with the current source I_D replaced by 2 sources in parallel. An expression for the circuit with I_D replaced by 2 current sources is given in equation (3.9) where J_{01} and J_{02} (Acm^{-2}) are the prefactors for the exponential current sources. J_{01} represents the forward current, and J_{02} the current lost through recombination.

$$\begin{aligned} I_F &= I_{pl} - J_{01}(\exp^{\frac{q(V+(I_F R_s))}{kT}} - 1) \\ &- J_{02}(\exp^{\frac{q(V+(I_F R_s))}{2kT}} - 1) - \frac{V + (I_F R_s))}{R_{shunt}} \end{aligned} \tag{3.9}$$

3.8.2 The IV characteristic

An IV characteristic is measured by performing a voltage sweep from a small reverse to forward bias whilst measuring current flow at each bias point. Typical sweep values are ±1V of bias. An illuminated IV characteristic provides a figure for cell efficiency if the irradiance of the illumination source is known. I_{sc} and V_{oc} can also be determined directly from the vertical and horizontal intercepts of the sweep.

IV characteristics measured under illuminated and dark conditions are both useful for the purposes of parameter extraction. In particular a method exists whereby R_s can be determined by comparing the 2 curves [80]. Dark IV characteristics were only measured for the cells reported on in chapter 7 due to a lack of equipment that was capable of measuring the low reverse saturation currents beforehand. For this reason analysis in this thesis primarily focuses on fitting parameters to IV characteristics measured under illumination.

Figure 3.9 shows a typical illuminated IV characteristic using real measured data. The corresponding power function is shown alongside it and this is created by multiplying every voltage bias point of the IV characteristic by the current measured at that bias. The power function is inverted about the horizontal axis to make the graph easier to read but usually power would be negative as the cell is generating energy, not consuming it. Important labelled features of the graphs include V_{oc}, I_{sc}, the shifting of the IV characteristic by I_{pl}, and the maximum power point. The maximum power point co-ordinates are (V_{mp}, I_{mp}) and they are the located at the peak of the power function.

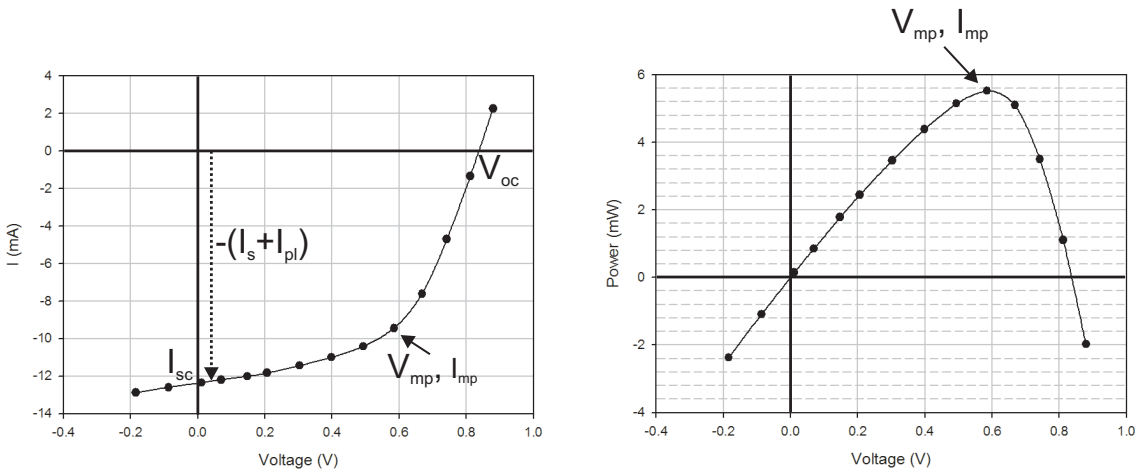

FIGURE 3.9: A solar cell IV characteristic under illumination and its corresponding power function. Important points to note are V_{oc}, I_{sc}, the photo-generated current I_{pl}, and the coordinates of the maximum power output point V_{mp} and I_{mp}

The FF (Fill Factor) is the ratio of the power a cell would supply if it was ideal ($P = V_{oc}I_{sc}$), compared to the real maximum power output. ($P = V_{mp}I_{mp}$) The equation for the FF is given by equation (3.10). The FF defines the "squareness" of the IV characteristic and an IV characteristic with a high FF will have a pronounced knee in its power curve toward V_{oc}. A FF of 0.7 for an a-Si:H cell would be considered very good, whilst 0.8 is normal for a well designed and fabricated c-Si cell. The FF depends on the efficiency of generated carrier collection for a given forward voltage. This makes it strongly affected by R_s which represents the ability of a cell to collect generated carriers at higher forward voltages near V_{oc} when the built in field is strongly reduced. At bias voltages closer to 0 R_{shunt} dominates but will have a less pronounced effect in a well designed cell.

$$FF = \frac{V_{mp}I_{mp}}{V_{oc}I_{sc}} \tag{3.10}$$

Cell efficiency (η) is related to the FF by (3.11), where A_c is the area of the cell in m^2 and E is the test irradiance measured in Wm^{-2}. Fabricated cells typically have an area of $1cm^2$, and the standard test irradiance is $1000Wm^{-2}$ (see section 3.8.3), so that the maximum output power of a $1cm^2$ cell in mW tested with the AM1.5 spectrum is also its efficiency.

$$\eta = 100 \times \left(\frac{P_{\text{out}}}{P_{\text{in}}}\right) = 100 \times \left(\frac{V_{oc}I_{sc}FF}{A_cE}\right) \tag{3.11}$$

3.8.3 Standard cell test conditions and the direct AM1.5 spectra

The standard test spectrum for photovoltaic cells is the direct global AM1.5 (Air Mass 1.5) spectrum. This is defined from 200nm to 5000nm in units of $Wm^{-2}nm^{-1}$ for a 37° sun facing tilted surface. The total irradiance of the direct AM1.5 spectrum is normalised to $1000Wm^{-2}$, the power contribution of any part of the spectrum can be obtained by integrating between the relevant wavelengths. Figure 3.10 shows the spectrum from 200nm to 2500nm published by NREL[1] (National Renewable Energy Laboratory). It can be seen that the peak of the spectrum is located between 500-600nm which is ideally placed for absorption by a-Si:H.

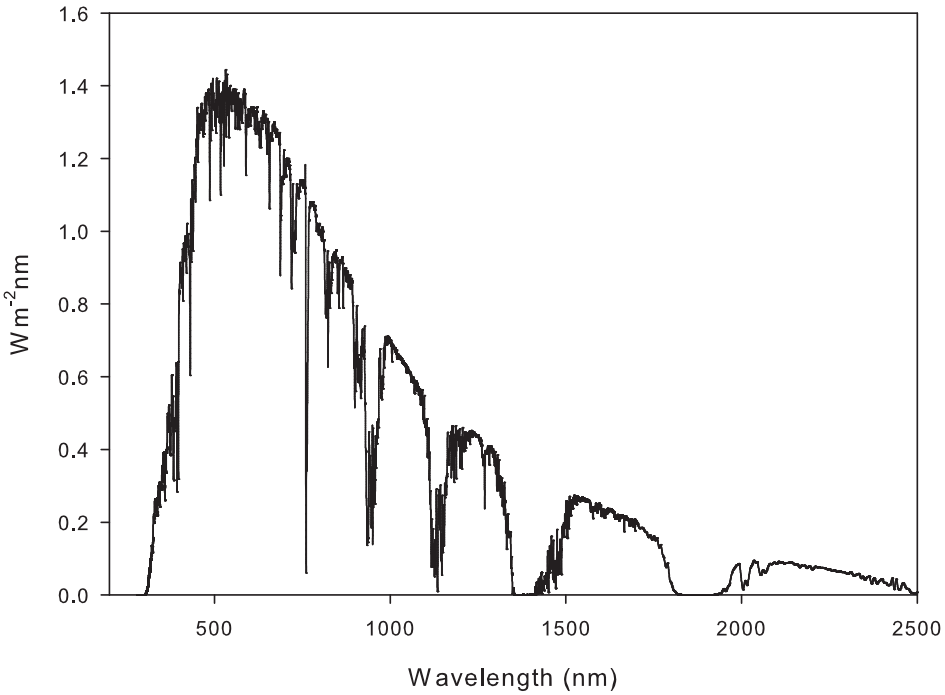

FIGURE 3.10: The direct AM1.5 standard test spectrum. Note the peak at 500-600nm which is very well suited to being strongly absorbed by a-Si:H

3.8.4 IV measurement and illumination sources

IV characteristics and any other measurement that required illumination of a sample were made with 2 different sets of equipment during this project. Every measurement made during chapter 4 and 5 was carried out using an initial experimental set up which was later upgraded for measurements made in chapter 7.

Initial IV characteristic measurements were made with a mercury lamp which provided an irradiance of $540Wm^2$. This was measured using a c-Si Sensol reference cell calibrated

[1] `http://rredc.nrel.gov/solar/spectra/am1.5/`

to the direct global AM1.5 spectrum [81]. All photocurrents measured using this light source were therefore scaled up by a factor of 1/0.54 in order to correspond with the standard test conditions of 1000Wm^{-2} and care was taken to use the same area of illumination for every measurement to minimize errors from non-constant irradiance.

IV characteristics were recording by biasing devices with a Keithley 228A source meter and the current was recorded at each bias point. Each bias point had to be selected and data recorded by hand, which made characterising multiple cells a slow process. The data measured for pin cells using this technique agreed well with published parameters for single junction a-Si:H cells, and so the lamp was deemed suitable for use. Unfortunately the 228A source meter was not sensitive enough to measure the reverse saturation currents of cells with reliable accuracy and so results in chapter 4 focus on illuminated IV characteristics.

To overcome some of the shortcomings of this measurement system, a new light source was required and it was decided to use a lamp with a large luminaire to distribute a more intense irradiance over a larger area. The bulb chosen was a Osram metal halide model with a 250W power rating and its luminaire enclosure (which is also a reflector) measured 30cm^2. By calibrating the irradiance with the same Sensol cell reference cell as the previous test light source it was found that 1000Wm^{-2} was delivered at a perpendicular distance of 90mm underneath the end of the bulb. A frame was constructed to keep the light source at this level reliably and the point marked for future sample placement reference. Due to the increased irradiance of this source compared to the mercury bulb it was found necessary to air cool samples in order to prevent a rise in temperature which might affect measured photo-currents.

Figure 3.11 shows the irradiance of the lamp as measured with the Sensol calibration cell as a function of the area underneath the luminaire. By placing cells or a-Si:H films under test in the area of illumination that provided 1000Wm^{-2}, current scaling was no longer required.

To complement the new light source a more modern Keithley source meter was acquired. The model 2400 source meter[2] is capable of current measurements to a level of 10pA and is also equipped with a GPIB interface and an RS232 serial connection for remote control. This enabled control software to be written in Labview for the purpose of automating IV characteristic measurement. Labview is software that allows the interfacing of a PC with external equipment for the purposes of data aquisition and analysis through custom user written graphical interfaces. By automating IV measurement many data points can be quickly collected allowing the measurement of multiple cells in a relatively small time. Several seconds were required to measure a 20 data point IV characteristic using this method which reduced noise in IV characteristic data due to changes in ambient

[2] `http://www.keithley.com/products/currentvoltage/voltagecurrentsourcing/?mn=2400`

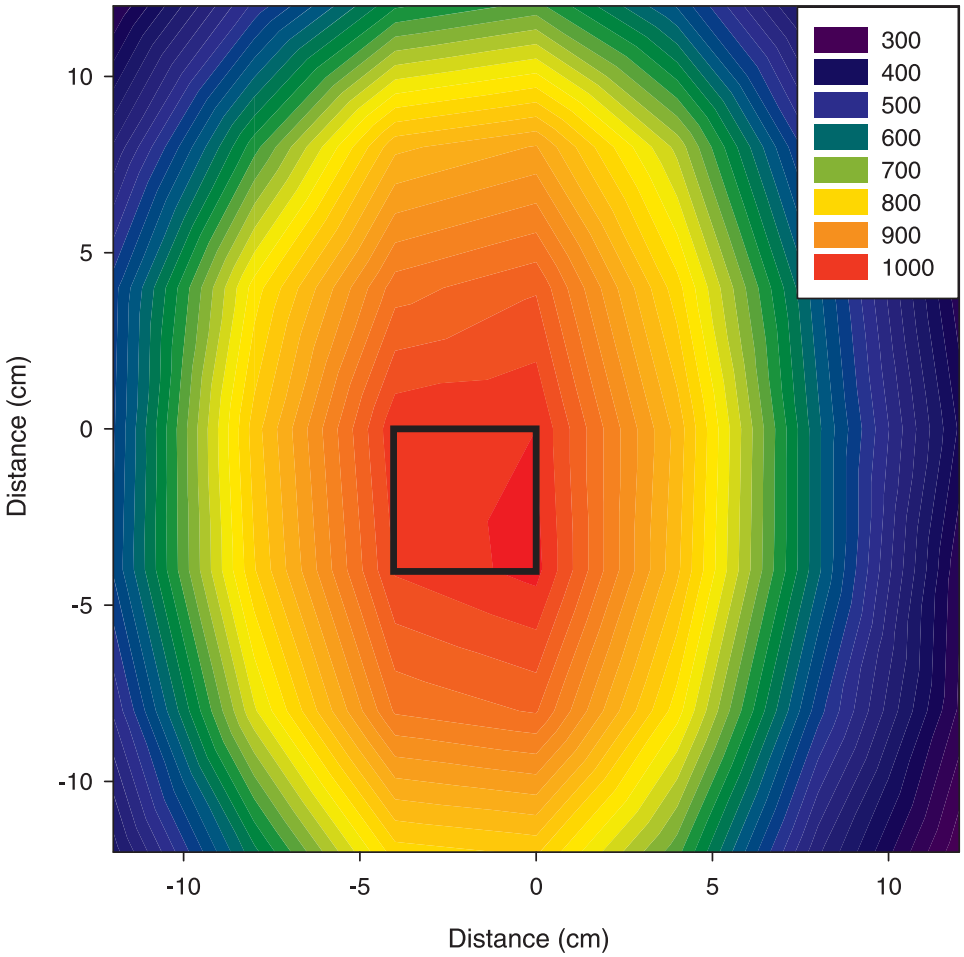

FIGURE 3.11: The irradiance (W/m^2) of a 250W Osram metal halide bulb enclosed in a $30cm^2$ reflective luminaire as a function of distance. A square area of $16cm^2$ near the tip of the bulb (indicated by the black square) provides a near constant irradiance of $1000Wm^{-2}$ calibrated using a Sensol reference cell [81]

temperature and irradiance. The model 2400 source meter is capable of accurately measuring the low reverse saturation currents required for dark IV characterisation.

Both sets of test equipment measured photo-currents using lamps that produce a white spectrum, however they cannot truly reproduce the continuous AM1.5 test spectrum although their irradiance was calibrated to it. Even with non-ideal spectra the light sources are still useful for observing trends in grown material and cell performance although absolute performance would differ under a true AM1.5 standard test spectrum.

3.8.5 IV characteristic parameter extraction

Initial analysis of an IV characteristic can be readily interpreted. Determination of a cell's efficiency, FF, V_{oc}, and I_{sc} can be as simple as identifying them on a graph. This can even be done visually if a quick result is desired. For more complex analysis data fitting is required. By fitting equations to measured data points, usually via a least

squares regression method information can be extracted that relates to the parasitic resistances, recombination current, and ideality factors present in a cell.

Several models have been discussed already in section 3.8.1. The most simplistic is the single current source diode model with parasitic resistances and a varying ideality factor modelled with equation (3.6). A more detailed model in common use is the double diode equation, which includes a current source that models current loss due to recombination in parallel with a conventional diode current source. These current sources are usually modelled with fixed ideality factors of 1 and 2 to simulate diffusion and recombination currents respectively, and the parasitic resistances R_s and R_{shunt} are shared between them. Sometimes the ideality factor of the diffusion current source is allowed to vary.

To fit these models to measured data a program called IVFIT[3] developed by Burgers et al. [82] of the ECN (Energy research Center of the Netherlands) was employed. The program is released under a free software license and use of it for research is encouraged by the author. It can fit data using any of the discussed models.

The IV data shown in Figure 3.9 was fitted using each model in turn, and the residuals between the actual and fitted current values are shown as a function of voltage in Figure 3.12. No constraints were imposed upon any of the fitting parameters. The fitting residuals are all less than $2\text{x}10^{-4}$A for every voltage bias point, indicating that a close fit to the data was achieved by each model as all data points are at least one order of magnitude greater. It would not be possible to discern the difference between the fitted data sets and the original with the eye if plotted.

All 3 models show a very similar fit to the data from reverse bias to 0.4V, which is to be expected as that is the region where current varies with voltage in the most linear fashion. From 0.4V to 0.6V the single diode model performs better than both double diode models, but after 0.6V its performance worsens as the strongly exponential forward diffusion current becomes dominant. The double diode models manage to fit the data very well in this region (0.6V to 0.9V) with low residuals. The use of any model would appear to be a suitable choice if the only goal was accurate IV data fitting.

To better establish which model is most suitable for use it is necessary to compare the fitting parameters generated by each. Table 3.1 contains the fitting parameters extracted by each model. Where a parameter is not used by a model, it is marked n/a.

All values of R_s and R_{shunt} are in close agreement, with the single diode model estimating a slightly lower R_s and higher R_{shunt}. The double diode models both also extract similar values for the recombination current prefactor J_{02}, and this is due to the constant ideality factor of 2 associated with it in both cases. The single diode ideality factor and the double diode model ideality factor that is allowed to vary are unusual in that they are outside the theoretical range of 1 to 2. This means that a physical interpretation of their

[3] `http://www.ecn.nl/en/zon/products-services/i-v-curve-fitting-program-ivfit/`

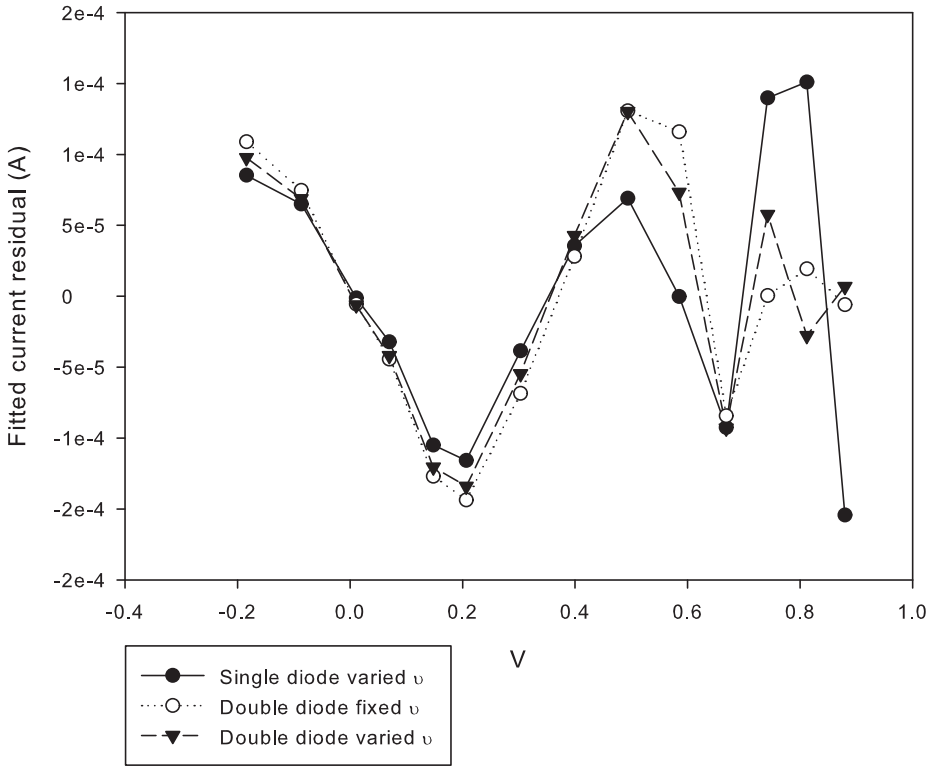

FIGURE 3.12: Residuals resulting from fitting data to the IV characteristic of Figure 3.9 using a single diode model with a varying ideality factor, a double diode model with fixed ideality factors of 1 and 2, and a double diode model in which the first ideality factor is allowed to vary

Model	Single diode fixed n	Double diode fixed n	Double diode varying n
J_{01} (A)	$0.35\text{x}10^{-07}$	$0.68\text{x}10^{-17}$	$0.10\text{x}10^{-27}$
J_{02} (A)	n/a	$0.73\text{x}10^{-09}$	$0.58\text{x}10^{-09}$
υ_1	2.60	1	0.55
υ_2	n/a	2	2
R_s (Ω)	11.39	14.23	15.10
R_{shunt} (Ω)	302.92	287.19	290.15

TABLE 3.1: Extracted parameters for 3 different diode models fitted to the IV characteristic shown in Figure 3.12

meaning is not possible. J_{01} is also much lower than expected for the variable ideality factor double diode model due to the choice of υ.

There were no significant differences in the values for the extracted resistances between the models, so it was decided to make the double diode model with fixed ideality factors the method by which IV characteristics would be parameterised. A single diode model cannot adequately describe the behavior of a-Si:H cells because of the substantial recombination current contribution. This is why the single fitted υ is greater than 2.

By using fixed ideality factors in the double diode model, values of J_{01} and J_{02} obtained from different IV characteristics can be directly compared. A direct comparison would not be possible if υ_2 was also allowed to vary. Any difference in J_{01} and J_{02} between samples should be directly attributable to differences in cell design and fabrication.

3.9 Conductivity analysis

Fabricating and analysing complete and functional solar cells is the end goal of this project, but by growing a whole cell at once a series of factors is compounded which leaves the designer with little idea as to where a problem during fabrication exists if a cell performs poorly or is even dead when measured. The approach of measuring the properties of individual homogeneous thin films provides a method by which problems during cell fabrication can be isolated to a particular cell feature, for example a lack of dopant during an n type layer deposition.

The symptoms of this problem could be interpreted from an IV characteristic (specifically reduced V_{oc} and increased R_s), but there would be no way of knowing which of the two doped layers were at fault. Being able to measure the electronic suitability of thin films for incorporation into a complete cell speeds up the design process by reducing reliance on long depositions. It is possible to perform a series of single layer 15 minute depositions to investigate the doping efficiency resulting from a particular phosphine to silane ratio for example, and then incorporate that knowledge into a full 45 minute cell deposition. Conductivity analysis can also verify if undoped a-Si:H is intrinsic, or whether it was contaminated during deposition. The basic theory behind conductivity measurements was discussed in section 2.4.1, but it shall be expanded on here with details of the experimental setup used to measure it.

The conductivity of an intrinsic semiconductor is given in equation (3.12) where n is the electron concentration, p the hole concentration, and μ the average carrier drift velocity. For an extrinsic semiconductor the equation is usually simplified to one term as n $\gg$ p or p $\gg$ n.

$$\sigma = q(\mu_{\mathrm{p}} p + \mu_{\mathrm{n}} n) \tag{3.12}$$

μ_{p} and μ_{n} are controlled by the density of states distribution, which is itself a function of material quality and so can be regarded as constant. n and p are the parameters that determine conductivity and they are calculated from equations (3.13) and (3.14) respectively, where $F(E)$ is the electron probability distribution, and $1-F(E)$ is therefore the hole probability distribution. $Z(E)$ is the density of states distribution in a-Si:H (see Figure 2.8).

$$n = \int_{E_c}^{\infty} F(E)Z(E) \tag{3.13}$$

$$p = \int_{0}^{E_v} (1 - F(E))Z(E) \tag{3.14}$$

Electrons are Fermions and so the electron probability distribution over the valance and conduction band is described by the Fermi-Dirac distribution given in equation (3.15), centered around the Fermi energy E_f. The position of E_f is fixed by the values of n and p at thermal equilibrium. Introducing dopant atoms will change n and p and therefore shift the position of E_f towards E_c or E_v.

$$F(E) = \frac{1}{1 + \exp\frac{(E-E_f)}{kT}} \tag{3.15}$$

E_f is the energy at which $F(E) = 1 - F(E) = 0.5$ and as such is the center of the electron and hole probability distribution. The only other parameter which influences the distribution is the temperature (T). Figure 3.13 shows examples of $F(E)$ using 3 different temperatures. At 0K the system has no energy and all of the electrons are in their ground state. Every state beneath E_f is filled by an electron and every state above it is occupied by a hole. As the temperature increases electrons are promoted from lower to higher energy levels and every state above E_f has a finite probability of being occupied by an electron. As temperature increases the probability distribution broadens.

A linear increase in temperature has the effect of exponentially increasing the electron density above a certain energy level, and the hole density below it. In c-Si this level would be either E_v or E_c as no states exist between them. A-Si:H does not behave in quite the same way as localised states extend into the gap past E_v and below E_c. These states are filled as are the extended states past them, and their effects on net conductivity are accounted for in a-Si:H by decreased values of μ_{p} and μ_{n}.

When $F(E)$ is multiplied by the theoretical expression for $Z(E)$ in c-Si, it is found that the sum of electrons and holes that contribute to conduction is still proportional to temperature, and hence conductivity is proportional to temperature also. The relationship

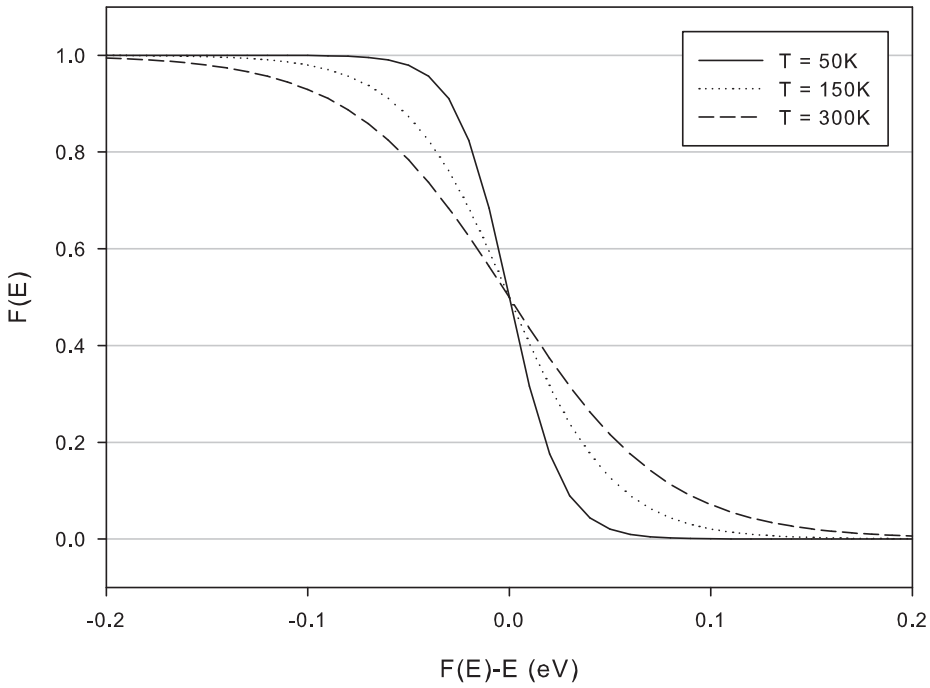

FIGURE 3.13: The electron probability distribution function $F(E)$ shown a temperature of 50K, 150K, and 300K. As the temperature increases electrons and holes are distributed across a wider band of states centered around E_f

between conductivity and temperature in c-Si is given by equation (3.16), where E_a is the conduction activation energy ($E_c - E_f$ or $E_f - E_v$) and σ_0 is the conductivity prefactor that is derated with decreasing temperature. Due to the well defined band edges in c-Si, only one exponential term and activation energy are required to describe conductivity.

$$\sigma = \sigma_0 \exp^{\frac{-E_a}{kT}} \tag{3.16}$$

To improve the model of conduction for use with a-Si:H, a second exponential term is added to make equation (3.17). The second term describes the average conductivity path in the localised states relative to E_f, whilst as before the first term describes the onset of conduction once carriers have reached the extended states at E_c or E_v. The contribution to conductivity from carriers in the localised states is expected to be much less than carriers in the extended states due to trap release times and heavy scattering. A term to describe hopping conduction at E_f is not included in equation (3.17) as it would be many orders of magnitude smaller than the existing terms, especially at moderate to high temperatures.

$$\sigma = \sigma_0 \exp^{\frac{-E_{a0}}{kT}} + \sigma_1 \exp^{\frac{-E_{a1}}{kT}} \tag{3.17}$$

Figure 3.14 shows the conductivity models for c-Si and a-Si:H with reference to the differing density of states and the activation energies of the different conduction paths in each material. The energy of the average conduction path in the localised states E_{loc} will be found under E_c or over E_v. The density of states extends approximately 0.2eV into the gap for n type a-Si:H and 0.4eV for p type, $E_c - E_{loc}$ and $E_{loc} - E_v$ would be expected to fall within these values.

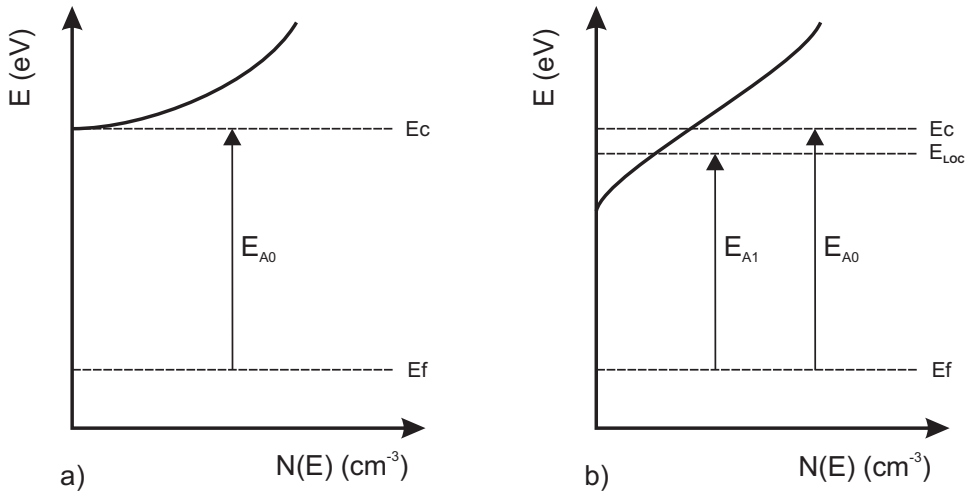

FIGURE 3.14: Conduction activation energies in c-Si (a), and a-Si:H (b). The conductivity of A-Si:H can be modelled with an extra conduction path to account for the contribution of the localised gap states beneath E_c. The average conduction path energy in the localised states is termed E_{loc} yielding a second conduction activation energy of $E_{loc} - E_f$

3.9.1 Experimental Setup

No equipment for the purposes of measuring conductivity existed at the start of this project, so everything had to be constructed from scratch. A stainless steel chamber was selected to house the sample under test so measurements could be carried out in a vacuum and total darkness. A 160mm flange and stainless steel door was welded to it for access to change samples. An aluminium sample mount was machined to dimensions of 120x100x20mm and placed inside the chamber on a ceramic support to isolate it thermally from the chamber. Two 10mm diameter holes were bored 80mm into the rear of the block so that a pair of 230V 150W cartridge heaters (supplied by Fastheat UK) could be placed inside it to provide a heating source. A 3mm diameter, 40mm deep hole was also created centrally at the rear of the block so a thermocouple could be placed inside it to monitor the block and sample temperature. Figure 3.15 shows a top down plan of the aluminium sample mount design. Samples were placed centrally on the block and electrically contacted by spring loaded flat ended probes, heat sink compound was used to thermally bond samples to the substrate mount and ensure that the thermocouple measured temperature was as accurate as possible with regards to the sample under test.

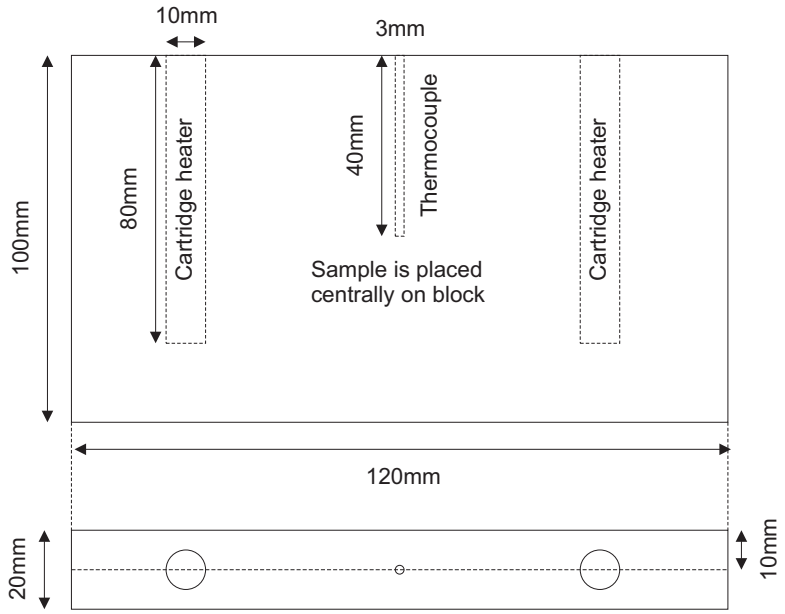

FIGURE 3.15: Detail of the aluminium sample mount for conductivity measurements, note the ability to insert two cartridge heaters and a central thermocouple to control sample temperature

The 230V AC supply to the cartridge heaters was switched by a Eurotherm 2216e PID temperature controller which used the type-K thermocouple inserted into the center of the aluminium block as its feedback sensor. This arrangement enabled the temperature of the sample mount to be controlled to within ±0.5C of a preset value. This scheme was very similar to the one used to control the temperature of the PECVD substrate mount (see section 3.3). The cartridge heaters had to be replaced several times due to burning out, the reason for this most likely being excessive heat build up in the heaters as a result of heat conduction to the aluminium block being limited by the vacuum present in the chamber. The holes that the cartridges were seated in were machined and finished to a close tolerance, but there seems no other explanation for the failures. If the heating element was redesigned, a better choice may have been a Thermocoax wire[4] brazed to the underside of the aluminium block. This approach would also require a step down transformer to be inserted between the 2216e and the Thermocoax heating element.

A Keithley model 6487 picoammeter[5] was selected to measure the resistivity of samples placed in the chamber. It has a low current measurement limit of 10fA, and is capable of supplying a bias voltage of up to ±500V making it ideal for high resistance low current measurements. The model 6487 supports a remote GPIB and RS232 interface (as does the model 2400 source meter, see section 3.8.4) which allowed automation of conductivity measurements. Custom software was developed in Labview to allow automated setup of the thermo-controller and pico-ammeter, along with automated measurements of current when sample temperature had reached a predefined and stable value. Another advantage

[4] `http://www.thermocoax.com/pd_heating_elements.htm`
[5] `http://www.keithley.com/products/locurrhiresist/?mn=6487`

of this process is straightforward correlation of current and temperature measurements. Figure 3.16 shows the interaction between the various components of the experimental setup for the measurement of sample conductivity.

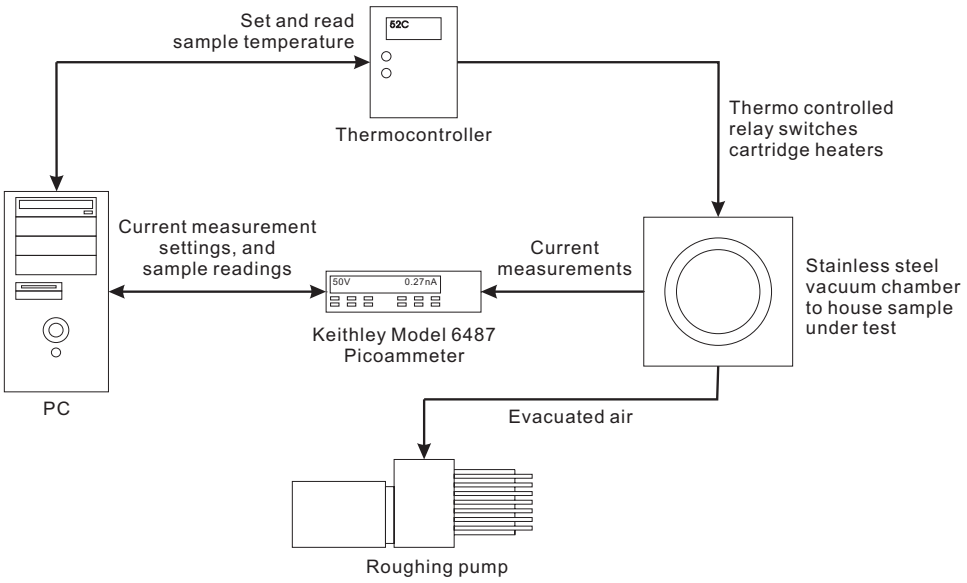

FIGURE 3.16: The full experimental setup for performing dark conductivity measurements on a-Si:H samples, data flow and interactions between individual system components

3.9.2 Sample preparation and experimental technique

To convert a measured current to a conductivity it is necessary to know several details about the sample under test. Conductivity is related to current by (3.18), where V and I are the voltage bias and measured current. The volume of material contributing to conduction is determined by the width (W), length (L), and thickness (t) of a cuboid located between the conducting contacts used to probe the sample. These contacts are deposited onto the a-Si:H film by thermal or electron beam evaporation (see section 3.5). As a non conducting substrate was required, glass slides cleaned with IPA followed with a nitrogen dusting were used.

$$\sigma = \left(\frac{I}{V}\right)\left(\frac{L}{W}\right)\left(\frac{1}{t}\right) \tag{3.18}$$

A prepared a-Si:H film with evaporated conducting contacts is shown in Figure 3.17 where the use of a mask during contact deposition has defined L as 2mm, and W (20mm) is the width of the glass slide substrate. To measure the thickness of the deposited a-Si:H film (t), a second glass substrate was mounted alongside the initial sample for a-Si:H deposition. Correction fluid was used to mask a straight line length ways across the center line of this second substrate, which was removed after a-Si:H deposition by immersion in a solvent and an ultrasonic bath. This method leaves a well defined step

profile which was measured at intervals of 5mm along the length of the slide using a mechanical Talystep stylus profiler, t is interpreted as the median measured thickness.

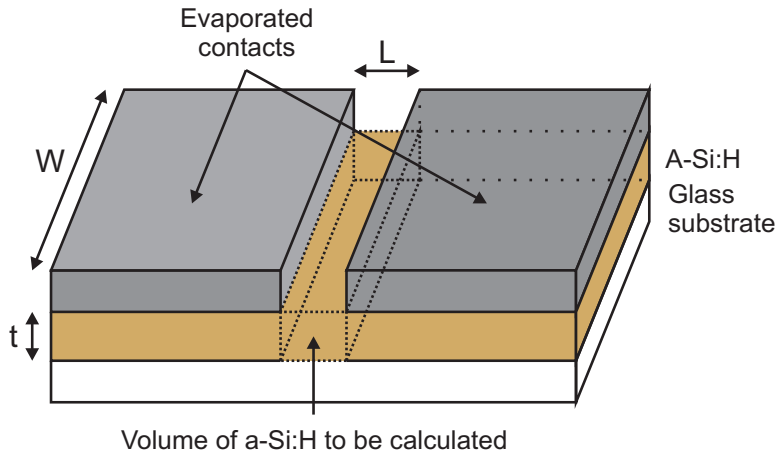

FIGURE 3.17: The volume of a-Si:H that contributes to conduction between two deposited contacts. The dimensions W, L, and t are required to be known along with the bias voltage and the corresponding measured current, before a value of conductivity can be calculated

Aluminium was used as an evaporation source to deposit contacts. To avoid the problem of hydrogen release and aluminium diffusion into the a-Si:H underneath it during heating of the sample, sample heating was limited to 150C. Research into the diffusion of aluminium into a-Si:H has been a popular topic in the last decade because it results in a polycrystalline material with a p-type characteristic [83, 84, 85, 86, 87]. The low temperature preparation of a thin film with a large crystalline silicon fraction via the annealing of an a-Si:H/aluminium stack structure is of interest to many fields, including research into thin film solar cells. Papers published indicate that a temperature of 200C is the minimum required to observe diffusion between layers and so lends strength to the assumption that 150C is not high enough to cause the deterioration of samples during analysis.

It was found that when samples were heated to 150C in vacuum, the measured current would peak and slowly stabilise to a final value over the course of approximately half an hour. This conductivity decrease was attributed to the release of water vapour from samples. Another explanation could be that the microstructure of measured samples was changing due to heating. The theory of water vapour release is given credibility over this because ≈100C was the temperature at which the measured current began to decay.

Taking into account these 2 factors, the temperature range for current measurements was defined as 150C and below, with the temperature first being raised to its maximum value and only allowed to vary after the measured current had stabilised. Initially samples were allowed to naturally cool to a lower temperature limit with data being logged every 3 seconds. This approach was felt to lack accuracy especially at lower temperatures due to non-uniform cooling of the sample and its aluminium mount. Measured currents would

be lower than expected for a given temperature indicating that the sample under test was cooling faster than the measured temperature at the center of its mount. Allowing a natural cool down could also take several hours making multiple samples very slow to analyse.

To improve on the natural cool down method a series of temperature steps was employed. The sample was heated to 150C and once the measured temperature and current had both stabilised data was logged for 5 minutes. The temperature set point would then be dropped by a pre-determined amount and the process repeated until an end temperature set point was reached. This system had the advantage of ensuring that the sample and its mount were always in thermal equilibrium before data logging commenced for each temperature set point. Measuring current for 5 minutes at temperature set points of 150C to 100C in intervals of 10C took just over an hour. This was because the thermo controller could accurately control the temperature descents with almost no overshoot. In addition to this, because the final temperature set point was 100C another sample could be loaded as soon as the previous experiment was complete. Use of this method meant that multiple samples could be analysed relatively quickly.

A voltage bias of 10V was found to result in linear Ohmic behavior and would drive currents in the order of nA to μA over the volume of a-Si:H discussed depending on sample doping. Increasing the voltage bias to 50V was found to induce heating effects in an a-Si:H sample under test, resulting in an increasing runaway measured current.

3.9.3 Interpreting conductivity data

Figure 3.18 shows conductivity data collected at temperatures of 150C to 100C in 10C intervals as previously described. The sample under test was intrinsic a-Si:H with a thickness of 230nm. The form of the data appears to fit the predicted exponential relationship between current and temperature reasonably well.

If it is assumed that the observed conductivity can be modelled with a single exponential term as shown in equation (3.16), taking the natural logarithm of this expression results in equation (3.19). This equation is now in the form of $y = mx + c$ where $c = \ln(\sigma_0)$ and $m = -\frac{E_a}{k}$ if x is taken as $\frac{1}{T}$. A linear polynomial fit to the data can therefore be used to directly determine E_a and σ_0. Once this is achieved, the conductivity at room temperature can be extrapolated by evaluating the expression with T set to 300K.

$$\begin{aligned} \sigma &= \sigma_0 \exp^{\frac{-E_a}{kT}} \\ \ln\sigma &= \ln\sigma_0 + \ln\exp^{\frac{-E_a}{kT}} \\ \ln\sigma &= \ln\sigma_0 - \frac{E_a}{k}\left(\frac{1}{T}\right) \end{aligned} \tag{3.19}$$

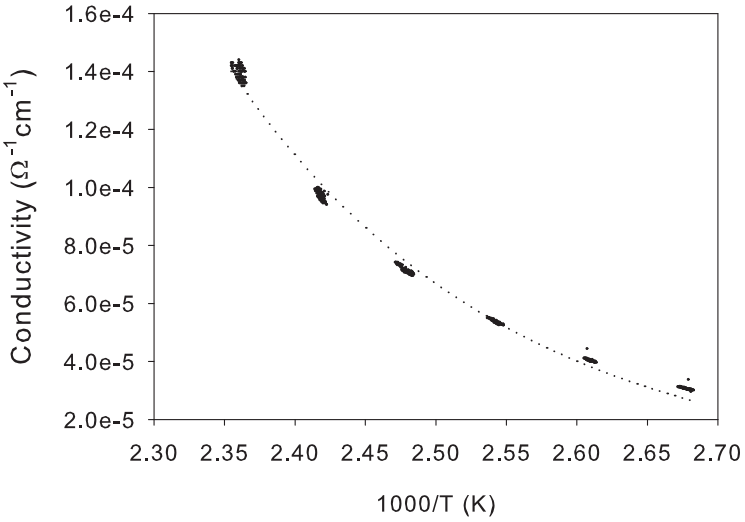

FIGURE 3.18: Conductivity measured as a function of temperature for a 230nm thick layer of intrinsic a-Si:H. The dashed line is a negative exponential least squares fit to the data and is shown as a guide to the eye

Figure 3.19 shows the relationship between the natural logarithm transform of conductivity and temperature. As expected a linear polynomial least squares fit fitted to the data using Matlab appears to be reasonably accurate. The linear fit results in values of σ_0=8.86Ω^{-1}cm^{-1}and E_a=-0.41eV. The fit also corresponds to a room temperature conductivity of 1.34x10$^{-6}\Omega^{-1}$cm^{-1}.

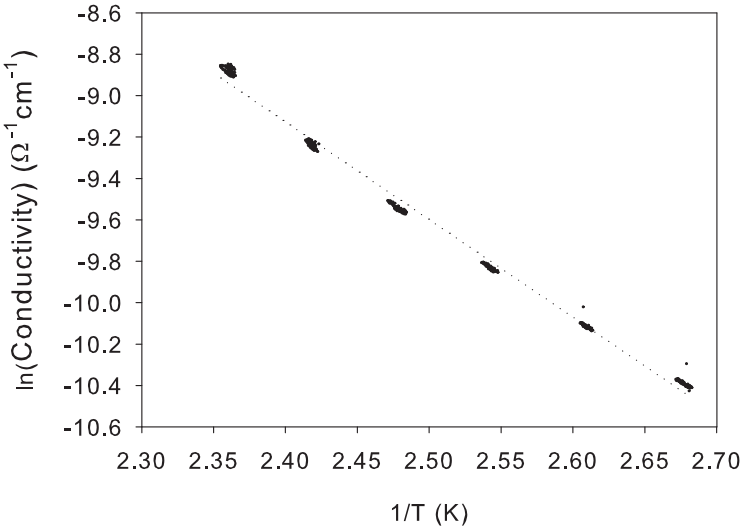

FIGURE 3.19: A natural logarithm transformation of conductivity measured as a function of temperature for a 230nm thick layer of intrinsic a-Si:H. The dotted line is a linear polynomial least squares fit to the data as described in equation (3.19)

The parameters extracted from the single linear fit to the data are not quite as would be expected for intrinsic a-Si:H. In particular E_a is lower than expected. Le Comber and Spear [22] reported activation energies of 0.5-0.6eV for conduction in intrinsic a-Si:H. The value of conductivity is also several decades greater than their reported value. This could be a consequence of a reduced conduction activation energy or perhaps due to changes in the micro structure of a-Si:H under test due to differing deposition conditions. The deposition conditions used to produce this measured sample are known to produce intrinsic material as they were used to fabricate cells that exhibited above average conversion efficiencies.

Measurement error is an unlikely cause of inaccurate fitted data as an advantage of logging data at single temperature points for periods of time is that the measurement drift is clearly visible in the data afterwards. Repeated sampling at each temperature set point provides robustness against measurement outliers because all points are equally weighted for the purpose of data fitting. Specifically a single linear polynomial fit underestimates conductivity at the first and last temperature point, whilst the other points are underestimated. It appears that the data could be better approximated by two linear polynomial fits instead of one.

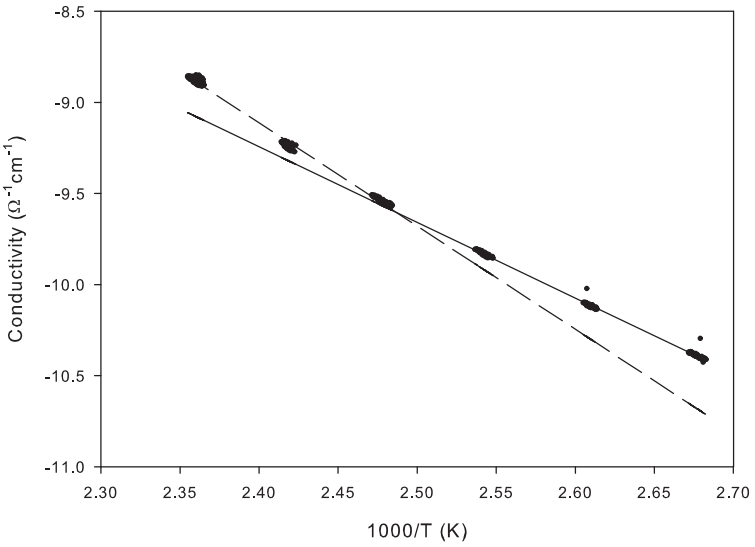

FIGURE 3.20: An improved fit to the conductivity data compared to Figure 3.19 is achieved by using 2 linear polynomial fits (the broken and the solid line) instead of 1 to describe different regions of observed conductivity. These regions relate to conduction in the localised and extended states

Figure 3.20 shows the same data as seen in Figure 3.19, but with 2 linear polynomial fits to it made instead of 1. One fit was made to conductivity measurements taken at a temperature of less than 125C, and the second fit was made to data measured above it. The combination of the 2 fits describes the data more accurately than the single fit and indicates that there are two differing conduction paths as expected for a-Si:H. The conductivity prefactor obtained from the higher temperature fit was $88.39\Omega^{-1}\text{cm}^{-1}$as

opposed to $2.02\Omega^{-1}cm^{-1}$from the lower temperature fit. This demonstrates the large conductivity increase obtained from promoting carriers from localised to extended states.

Analysis of the fits revealed that E_a increases from 0.36eV to 0.49eV. This is exactly the type of behavior that Le Comber and Spear [22] observed, but their published change in E_a was from 0.51eV to 0.62eV. The difference between these values of energy is very similar (0.13eV, 0.11eV) indicating that the average conduction path in the localised states relative to E_f is very close in both samples. The change in activation energy occurred at 240K for Le Comber and Spear [22], whilst the change in the presented data is seen at 400K. This difference is attributable to differing micro-structures of the two samples caused by different deposition conditions, this will have caused disparities between the density of state distributions.

An issue with describing conductivity as a combination of 2 linear polynomial fits is that the corresponding equations can not simply be summed to create one equation that can describe conductivity over the temperature range of interest. Using 2 linear polynomial fits to describe 2 different paths of conduction is inaccurate from a descriptive point of view as at any temperature there will be some contribution to conduction from both paths. To extract a model valid over the entire temperature range of interest using terms for conduction a sum of exponential terms is required to be fitted to the original conductivity data without a logarithm transformation. This least squares fit is achieved by using the constrained least squares solver from the TomLab optimisation environment[6] with Matlab. The starting values of E_a and σ_0 are taken as the solutions from the double linear fit.

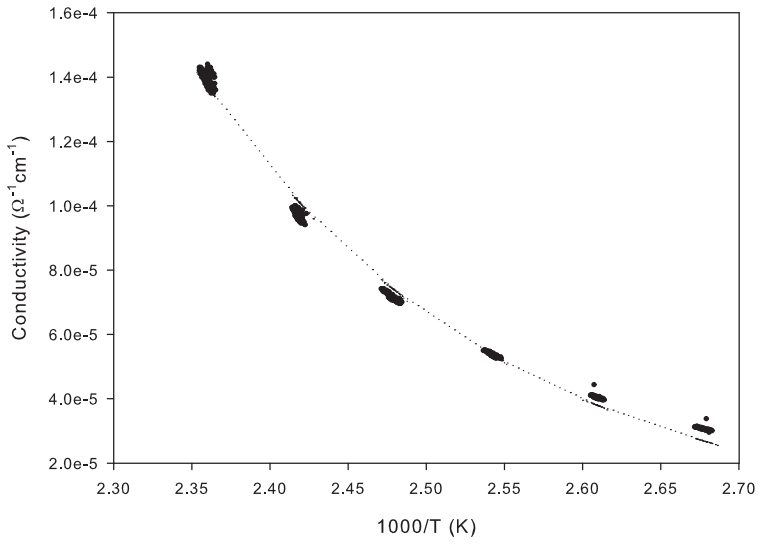

FIGURE 3.21: A double exponential term least squares fit (dashed line) is made to the conductivity data incorporating two activation energy terms and 2 conductivity prefactors

[6] `http://tomopt.com/tomlab/`

Figure 3.21 shows this double term exponential fit along with the original conductivity data. The extracted values of E_a moved from 0.36eV to 0.49eV to 0.38eV and 0.51eV. The conductivity prefactors do not change appreciably. The fit to the data is poorest at lower temperatures. This could be improved by adding a contribution to the conductivity to account for hopping at E_f, but it is not considered here as it does not impart information about the band structure of a-Si:H.

It has been shown that the conductivity of intrinsic a-Si:H samples can be accurately modelled with a two term exponential equation. This can be approximated by 2 linear polynomial fits applied to the conductivity data after it has been transformed using the natural logarithm. This technique can be used to extrapolate a value of dark conductivity at room temperature and to compare the relationship between E_f and E_c or E_v. Heavily doped samples can sometimes be approximated well by a single linear fit as E_f is so close to a band edge that conduction in the extended states dominates from medium to high temperatures.

3.10 Determination of optical properties

So far the analysis methods discussed in this chapter have all used data obtained by electronic measurement. (Optionally stimulated by light in the case of IV characteristic measurement.) As the intended application of the a-Si:H discussed in this report is PV, optical characterisation of samples is also important. In particular the determination of E_g and E_u is desirable as these terms describe the strong and weak regions of absorption present in an amorphous material that relate to its density of states.

It is possible to determine these parameters from a transmission spectrum by means of an optical model for an absorbing thin film on an infinitely thick substrate. This task is complicated by the presence of fringes in the transmission spectrum created by coherent interference of light in the thin film. There has been significant work on the process to overcome this [88, 89, 90], but it was found that it was almost impossible to eliminate the effect of the fringes entirely from the series of absorption coefficients that was determined. Transmission measurements are still of use for roughly identifying the onset of weak and strong absorption, but differences in sample thickness and the presence of interference fringes make analysis using them problematic.

To overcome the limitations of transmission measurement, ellipsometry was chosen as an alternative technique. The ellipsometer used was a JA Woollam variable angle M-2000D model which was equipped with a deuterium and a tungsten halide broadband light source. This allowed spectroscopic measurements from 200-1600nm to be taken at high speed using CCD array detection, and made the system ideal for characterising the optical properties of a-Si:H. Measurements could be taken at multiple angles for a

single sample, from a grazing angle of incidence to 45°. Measurements at multiple angles provide assurance that an optical model is robust if it can account for all of them.

This section will discuss the theory that links transmission and ellipsometry measurements, and introduce the Cody-Lorentz oscillator which was used to model absorption in amorphous films.

3.10.1 The interaction of light with materials

Light can be considered as an electromagnetic wave travelling in a medium, the speed of light (c) assumes that the medium is a vacuum. In order to perform ellipsometry it is necessary to measure the polarisation state of light which is related to the behavior of its electric field with respect to space and time. The electric field is always orthogonal to the direction that the light is travelling in, so the behavior of the electric field can be described by two components that are perpendicular to each other. These components are often represented in the x and y axis, whilst light travels in the z axis. The relationship between the x and y axis perpendicular components of light in terms of phase and amplitude describes the polarisation state of light. Linear polarisation is a result of the components being in phase, whilst circular polarisation requires out of phase components of equal amplitude. Elliptical polarisation is observed when the components possess a phase shift that is not a multiple of $\pi/2$ and non-equal amplitudes. This is the most common polarisation state of light and also the state that ellipsometry depends on to function. Unpolarised light has a completely random phase difference and amplitude. Figure 3.22 shows the 3 possible polarisation states.

A description of how light propagates in a medium is also required and this is described by the complex refractive index. The complex refractive index is comprised of a real and imaginary term and is given in equation (3.20). n is the real refractive index which is a constant of proportionality between the phase velocity of light in a vacuum, and the phase velocity of light in the medium under examination (v). This relationship is given in equation (3.21). k is the extinction coefficient that describes the attenuation of light in a medium, it is related to the absorption coefficient ($\alpha(\lambda)$) by equation (3.22). $\alpha(\lambda)$ is used in Beer's law (see equation (3.23)) to describe the reduction in intensity of light in a medium as a function of distance (d). Beer's law would allow direct determination of $\alpha(\lambda)$ from a transmission spectrum of a thin film if it were not for the presence of interference fringes. When interference fringes are present, only the maxima are valid points where $\alpha(\lambda)$ and therefore $k(\lambda)$ can be directly determined.

$$\hat{\mathrm{n}} = n + ik \tag{3.20}$$

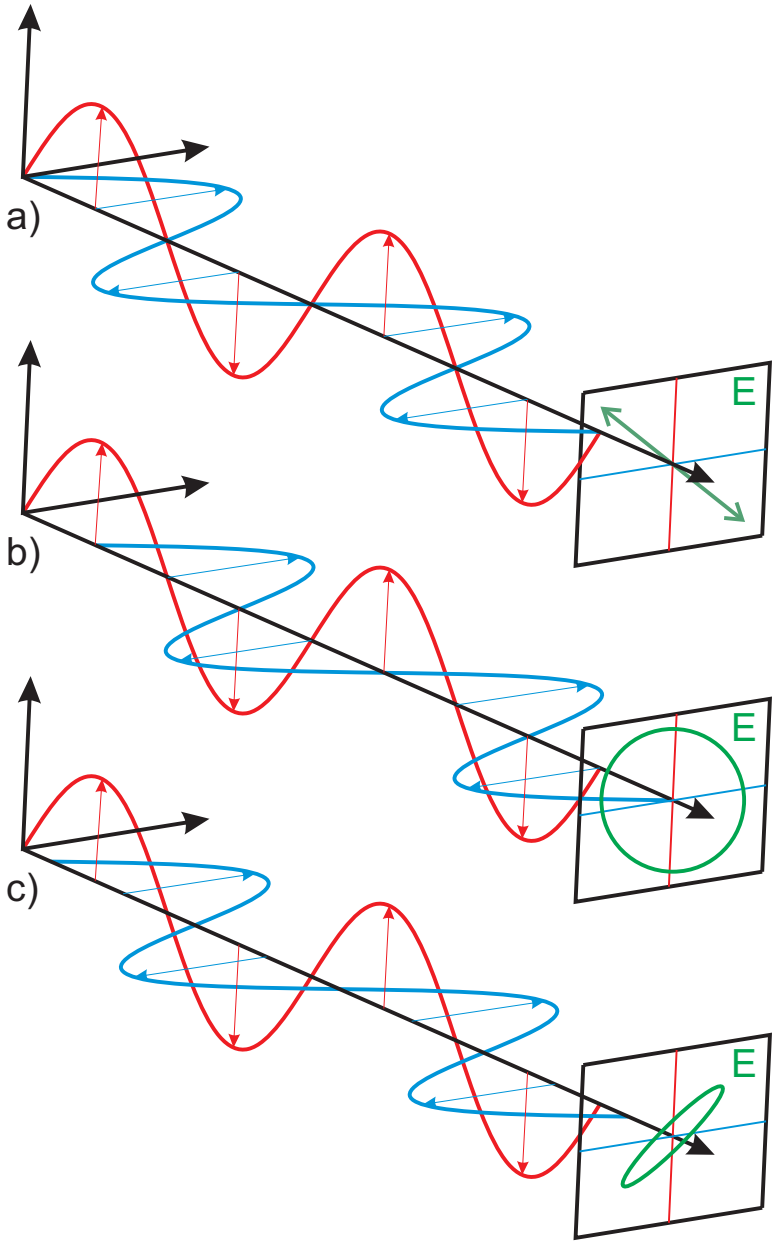

FIGURE 3.22: The 3 possible polarisation states of light travelling in the z axis, with an electric field described by orthogonal components in the x and y axis

$$v = \frac{c}{n} \tag{3.21}$$

$$\alpha(\lambda) = \frac{4\pi k(\lambda)}{\lambda} \tag{3.22}$$

$$I(d) = I_0 \exp^{-\alpha d} \tag{3.23}$$

3.10.2 The behavior of light in thin films

The propagation of light through an absorbing medium is illustrated in Figure 3.23. A light wave travels through air (n=1, k=0) and encounters an absorbing film (n=3.5, k >0). The absorbing film has a positive value of k and as such the amplitude of the light wave is attenuated exponentially as a function of the distance it travels in the thin film according to equation (3.23). The phase velocity of the wave also decreases due to the increase in the real part of the complex refractive index. Upon leaving the film the light wave encounters a transparent glass substrate (n=1.5, k=0) and reverts to a phase velocity close to its original, whilst the amplitude remains constant again.

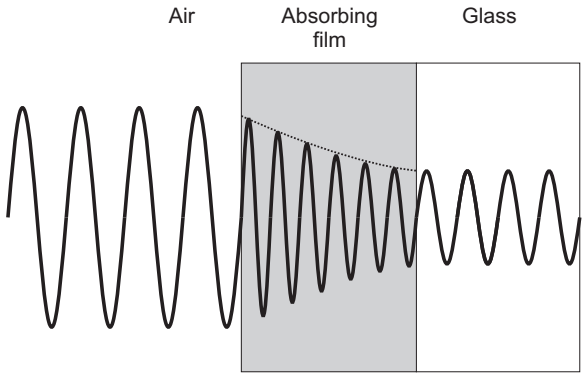

FIGURE 3.23: The effects of the complex refractive index on the amplitude and phase velocity of a light wave travelling in air (n=1, k=0) that encounters an absorbing thin film (n =3.5, k >0) and then a glass (n=1.5, k=0). Note the exponential absorption in the thin film due to the non zero value of k and the change in phase velocity due to variation in n

The behavior of light at an interface is more complicated than described in Figure 3.23. When light encounters an interface between 2 mediums of different real refractive index n_1 and n_2, some of the light will be reflected at the same angle of incidence (θ_i) and some will be refracted into the new medium at a changed angle (θ_r). The angles are measured relative to a vector normal to the medium interface. This behavior is Snell's law and it is given in equation (3.24).

$$n_1 \sin(\theta_i) = n_2 \sin(\theta_r) \tag{3.24}$$

A visual representation of Snell's law is shown in Figure 3.24. The amplitude of the s and p (perpendicular and parallel) polarised electric field components of the reflected and refracted light can be evaluated using the Fresnel equations listed in equations (3.26)-(3.28). If the incoming light wave is at normal incidence to the medium interface then the equations simplify as the sinusoid terms can be directly evaluated.

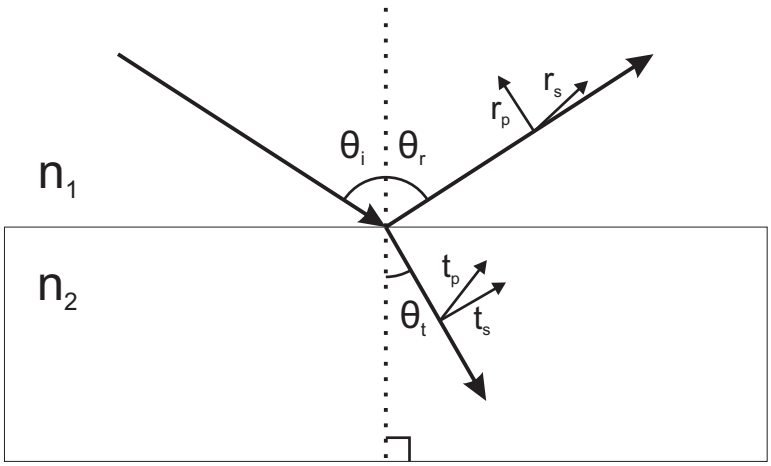

FIGURE 3.24: An incident ray of light is both reflected and refracted at an interface (Snell's law, equation (3.24)) between mediums of real refractive index n_1 and n_2. It is possible to consider each ray in terms of its s and p (perpendicular and parallel) polarised electric field components and evaluate them in terms of Snell's law individually (see equations (3.26)-(3.28))

$$r_s = \left(\frac{E_r}{E_i}\right)_s = \frac{n_i \cos(\theta_i) - n_t \cos(\theta_t)}{n_i \cos(\theta_i) + n_t \cos(\theta_t)} \tag{3.25}$$

$$r_p = \left(\frac{E_r}{E_i}\right)_p = \frac{n_t \cos(\theta_t) - n_i \cos(\theta_i)}{n_t \cos(\theta_t) + n_i \cos(\theta_i)} \tag{3.26}$$

$$t_s = \left(\frac{E_t}{E_i}\right)_s = \frac{2n_i \cos(\theta_i)}{n_i \cos(\theta_i) + n_t \cos(\theta_t)} \tag{3.27}$$

$$t_p = \left(\frac{E_t}{E_i}\right)_p = \frac{2n_i \cos(\theta_i)}{n_i \cos(\theta_t) + n_t \cos(\theta_i)} \tag{3.28}$$

With knowledge of of how light behaves at medium interfaces and the rate of its absorption in a medium with $k > 0$, it is possible to build a picture of its behavior when encountering single or multiple thin films. Light entering a thin film reflects and refracts at every boundary causing a coherent wavefront to exit the thin film in both directions, each successive bounce of the light reduces the electric field amplitude. Light entering the substrate does not return to it coherently because the substrate is infinitely thick in comparison to the thin film, it is assumed to be lost.

Figure 3.25 shows the coherent reflection of light from a thin film on a substrate and lists the amplitude and phase difference of the first 3 waves. t_{xy} and r_{xy} are the relative amplitudes of the light waves that are transmitted and reflected after encountering an interface between mediums of refractive index n_x and n_y. The phase difference resulting from a light wave travelling once through the thin film at an angle of θ to the normal is given in equation (3.29), where d is the thickness of the thin film, t is the optical path length travelled, and n is the refractive index of the film.

$$\beta = 2\pi \left(\frac{t}{\lambda}\right) n \tag{3.29}$$

where

$$t = \frac{d}{\cos(\theta)} \tag{3.30}$$

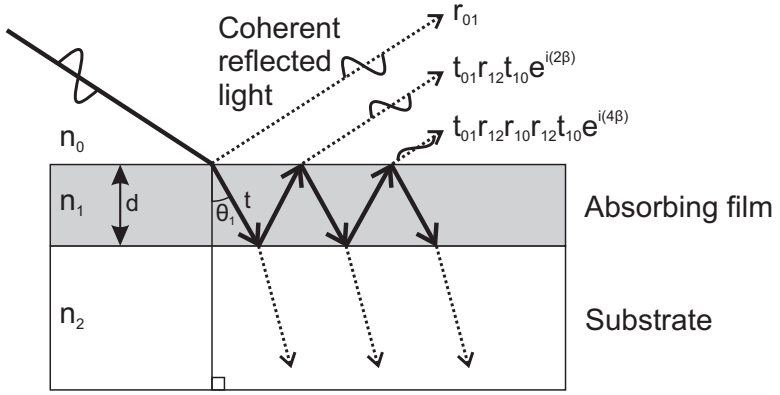

FIGURE 3.25: The coherent exit of light waves from a thin film. The amplitude of the electric wave is attenuated by loss at each successive medium interface. The amplitude and phase difference (β, see equation (3.29) is given for the first 3 waves to exit the thin film

The amplitude and phase change of successive light waves reflecting from the thin film can be expressed as a geometric series which can be summed to infinity. The sum is given in equation (3.31). The result indicates that interference between the reflected light waves is a sum of the singly reflected wave with no phase change and a second component with a reduced amplitude that experiences a phase change of 2β. If the thin film is absorbing ($k > 0$) then an extra factor of $\exp^{-2\alpha t}$ is introduced to further reduce the amplitude of successive waves that exit the thin film. Equation (3.31) will sum to a limit as the evaluation of $r_{10}r_{12}\exp^{i(2\beta)}$ will result in a magnitude of less than unity.

$$\begin{aligned} r_{01} + \sum_{j=0}^{j=\infty} ar^j &= r_{01} + \frac{a}{1-r} \\ &= r_{01} + \frac{t_{01}r_{12}t_{10}\exp^{i(2\beta)}}{1 - r_{10}r_{12}\exp^{i(2\beta)}} \end{aligned} \tag{3.31}$$

Ellipsometry works on the basis of sensing the relative change in the phase and magnitude of the s and p electric field components. A light beam of known polarisation (usually linear) is directed onto a target and the polarisation state of the reflected light is measured. The relative change in amplitude is known as Ψ, and the relative phase change as Δ. Equations (3.32) and (3.34) show how these parameters are determined. If only the relative change in amplitude was detected the technique would be equivalent

to a measurement of reflection, the addition of relative phase change determination adds sensitivity to very small film thicknesses.

$$\tan(\Psi) = \frac{|R_p|}{|R_s|} = \frac{\left(\frac{E_r(p)}{E_i(p)}\right)}{\left(\frac{E_r(s)}{E_i(s)}\right)} \tag{3.32}$$

$$\begin{aligned} \Delta &= \Delta_{pp} - \Delta ss \\ \Delta_{pp} &= \Delta_r(p) - \Delta_i(p) \\ \Delta_{ss} &= \Delta_r(s) - \Delta_i(s) \end{aligned} \tag{3.33}$$

3.10.3 Interpreting data provided by ellipsometry

Figure 3.26 shows Ψ and Δ measured at a single angle of 70°, the sample was an intrinsic a-Si:H film deposited onto a glass substrate. The region of strong absorption can be seen beneath 700nm and both Ψ and Δ respond to it. The wavelengths where Δ completes a 2π phase shift and moves from 270° to -90° are related to the thickness of the a-Si:H film, and the same periodic behavior is also seen in Ψ. The ratio of the peaks to the troughs seen in the transparent long wavelength region of Ψ relate to the difference between the refractive index of the glass substrate and the refractive index of the a-Si:H film.

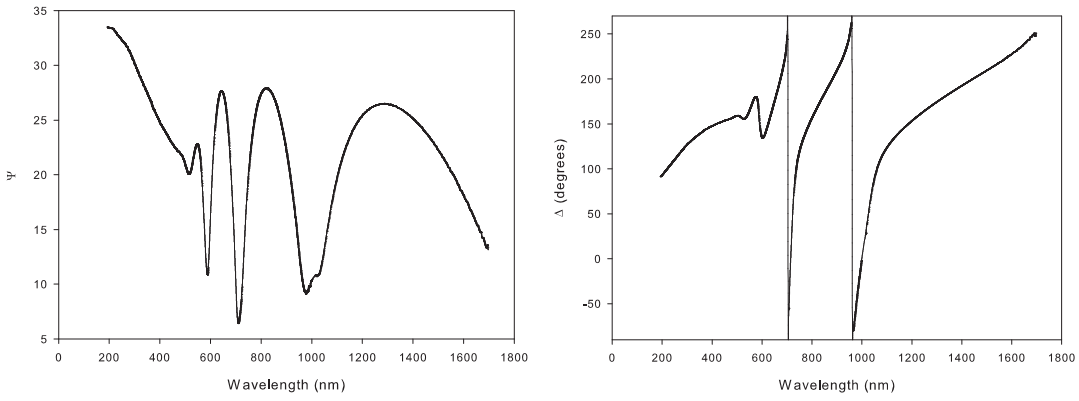

(a) Ψ (b) Δ

FIGURE 3.26: Ψ and Δ of an intrinsic a-Si:H thin film on a glass substrate measured from 200-1600nm at 65°

In order to make use of Ψ and Δ, they must be related to the complex refractive index of the materials that comprise the sample under test. This is achieved by constructing a model of the sample under test and calculating the theoretical values for Ψ and Δ that correspond to it. The theoretical values are then compared to the measured data

and the model is adjusted in order to minimize the MSE (Mean Square Error) between them. When a small enough value of MSE is achieved and the model parameters make physical sense, a sample can be characterised with confidence. Typically a value for MSE of less than 20 is acceptable, less than 10 is considered very good, and less than 5 indicates an excellent match between the model and the measured data.

Models consist of a stack of thin films on a substrate. Each film has it's own complex refractive index defined as a function of wavelength and a thickness associated with it. Films may also have other non-ideal properties associated with them such as refractive index grading, an effective medium mix with a second material, or in the case of the uppermost thin film an average value of surface roughness. The a-Si:H sample was modelled as a 3 layer stack consisting of a Corning glass substrate, a thin film with unknown complex refractive index and thickness (the a-Si:H), and a top layer of native oxide with unknown thickness. The glass substrate is modelled with a Cauchy series to define n, and an exponential absorption edge in the UV beneath which k is positive. The native oxide layer uses predefined constants for its complex refractive index [91].

The phase shifts observed in Δ and the shape of the curves in Ψ allow close approximations of thickness to be found for the a-Si:H and native oxide layer. The a-Si:H layer is assumed to be transparent at wavelengths where $E < E_g$ and n can be modelled using a Cauchy series in this region. Thicknesses obtained by this method are not perfect as the phase shifts in Δ and Ψ are related to n as well as layer thickness (see equation (3.29)), and a Cauchy series is an approximation of the true form of n.

Using this method the native oxide and a-Si:H thicknesses are found to be 3.47nm and 309nm respectively. Values of Ψ and Δ obtained using this model are shown in Figure 3.27 alongside the original measured data. The breakdown of the model for photon energies where $E > E_g$ can clearly be seen.

With the close approximations of layer thickness so far obtained, it is possible to enhance the model to account for absorption in the a-Si:H film. n and k are defined by individual smooth spline characteristics that are Kramers-Kronig consistent. Points on the splines are allowed to vary at fixed energy intervals. A 2D parameter space in n and k is searched for a solution that minimizes the MSE, and then this is parameterised with one or more oscillator models to give the splines physical meaning.

The chosen model for absorption in amorphous semiconductors was the Cody-Lorentz oscillator [92], which is similar to the more conventional TauC-Lorentz oscillator but behaves differently in a small absorption onset region above E_g. Both of these models differ from standard Lorentz oscillators by modelling Urbach absorption near and beneath E_g. Figure 3.28 shows how the model defines absorption in terms of the imaginary dielectric constant ϵ_2 where E_0, A,and B_R are the center energy, amplitude, and broadening of the Lorentz oscillator, E_p is a transition energy from the band edge to Lorentzian absorption, E_t is a transition energy from the band edge to Urbach absorption, and E_u

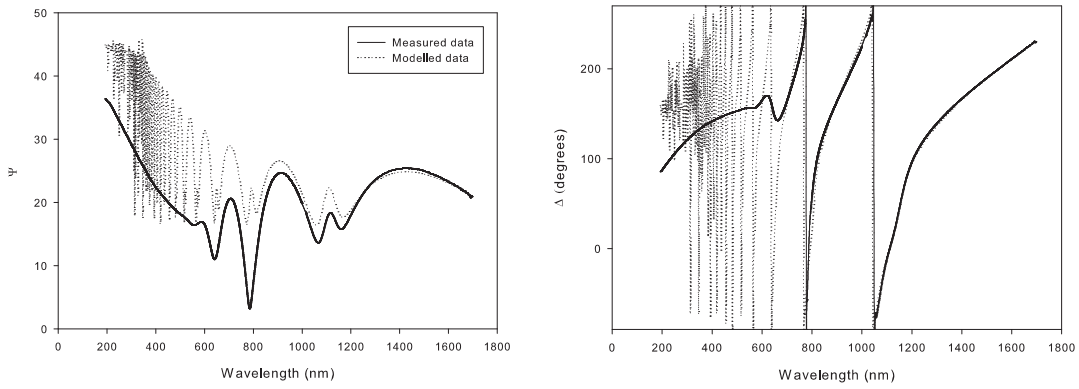

(a) Ψ (b) Δ

FIGURE 3.27: Ψ and Δ obtained by modelling the a-Si:H thin film as a transparent material with n defined by a Cauchy series. The thickness of the a-Si:H and native oxide layer can be determined by this method by matching Ψ and Δ in the long wavelength region below E_g. The model is not valid for photon energies close to or above E_g due to absorption in the a-Si:H film

describes the gradient of the Urbach absorption region. ϵ_2 is the imaginary part of the dielectric constant which is related to the complex refractive index by equation (3.34).

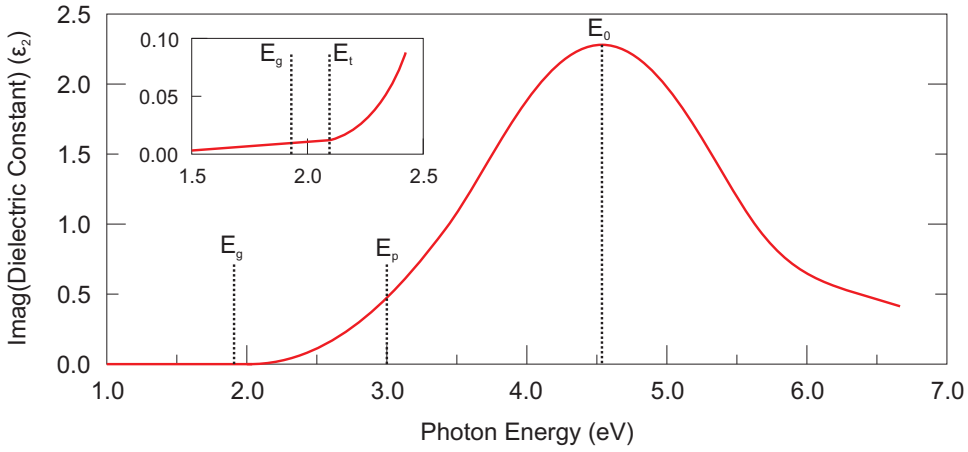

FIGURE 3.28: Energy parameter definitions for the Cody-Lorentz oscillator

$$\begin{aligned} \epsilon &= \epsilon_1 + i\epsilon_2 \\ &= (n + ik)^2 \end{aligned} \tag{3.34}$$

where

$$\epsilon_1 = n^2 - k^2$$
$$\epsilon_2 = 2nk$$

The regions of absorption described by the Cody-Lorentz oscillator are given in equation (3.35). The transition energies E_p and E_t define the proportionality of absorption relative to E_g.

$$\epsilon_2 \propto \begin{cases} \frac{(E-E_g)^2}{E^2} & \text{where } (E > E_g + E_p) \\ (E - E_g)^2 & \text{where } (E_g + E_p > E > E_g + E_t) \\ \exp(\frac{E}{E_u}) & \text{where } (E_g + E_t > E) \end{cases} \tag{3.35}$$

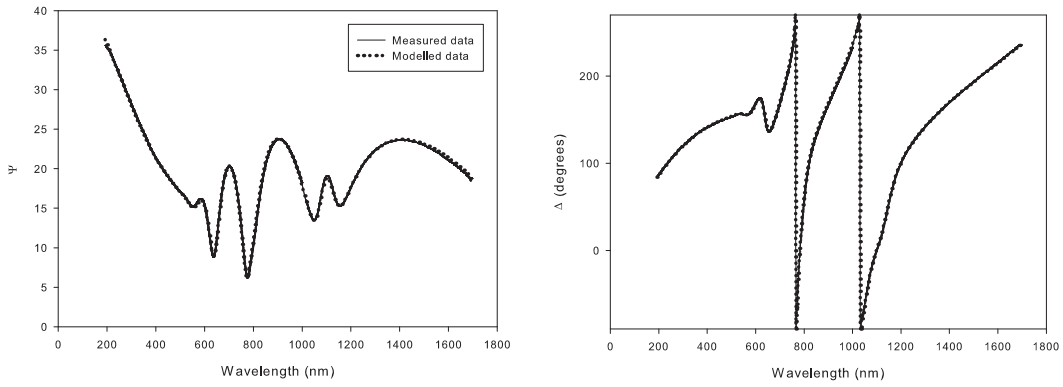

(a) Ψ (b) Δ

FIGURE 3.29: Modelled values of Ψ and Δ fitted to measured data using a single Cody-Lorentz oscillator to describe absorption. Thicknesses were previously calculated using a Cauchy series approximation at longer wavelengths (see Figure 3.27). The agreement between the data and model is excellent with a MSE of 7.80 over the entire spectral range

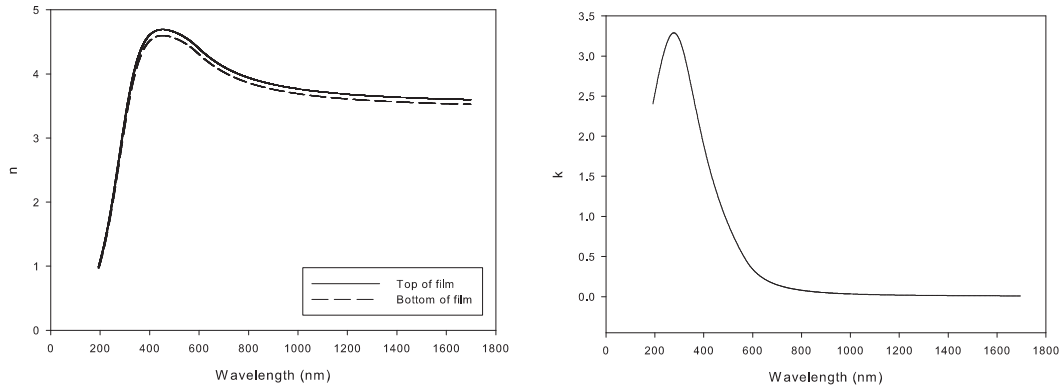

(a) n (b) k

FIGURE 3.30: n and k as determined directly from a Cody-Lorentz oscillator used to model absorption in an a-Si:H film. The parameters are Kramers-Kronig consistent and n is graded from the bottom to the top of the a-Si:H film with a variation of 2%

Figure 3.29 shows the fit between modelled and measured values of Ψ and Δ using a single Cody-Lorentz oscillator to describe absorption in the a-Si:H layer. Approximate layer thicknesses were previously determined using a Cauchy series to model the long wavelength transparent region (see Figure 3.27). The MSE calculated over the entire spectrum was 7.80 which indicates that a fit was obtained to a high degree of accuracy. To improve the fit beyond a single oscillator, refractive index grading was employed which allowed n to vary in 5 linear steps from the bottom to the top of the a-Si:H layer and n was found to vary by 2%. Grading predominantly improves fitting in the longer wavelength region where k is low and n has the most impact. Backside reflections from the glass substrate were also included in modelling and account for a relatively minor increase in fit accuracy.

n and k can be directly obtained from the Cody-Lorentz oscillator parameters of A=67.9, B_r=2.81, E_0=3.95eV, E_g=1.62eV, E_p=0.68eV, E_t=0.54eV, and E_u=0.28eV. They are shown in Figure 3.30.

The variation of k with wavelength matches with what is expected, the onset of strong absorption occurs near 700nm, peaking at ≈300nm. The Urbach region accounts for a very small amount of absorption to ≈900nm. If required $\alpha(\lambda)$ could be calculated from k using equation (3.22) which in turn could be used to calculate a transmission spectrum for any given thickness of the a-Si:H sample using equation (3.23). The absorption of a series of samples could be compared using either of these methods although $\alpha(\lambda)$ is arguably the most useful form.

Spectroscopic ellipsometry is a very powerful technique for non-destructive characterisation of thin films, and especially for those intended for PV based use. It is most useful when performed alongside complementary techniques that can determine the transport properties of thin films.

Chapter 4

Initial pin and nip cell fabrication on TCO coated glass

At the commencement of practical work the only characterisation available was illuminated IV and photo-conductivity measurement. As the PECVD reactor had only recently been restored to an operational capacity and tested it was decided that the first phase of work would focus on depositing complete cells if it was possible to create them, the intention behind this being to fabricate the most efficient pin and nip cells possible using any substrate temperature. By attempting this experience was gained with the operation of the reactor whilst establishing the boundaries of what was achievable in order to prepare for more sophisticated lower temperature experiments in the future. Extra characterisation equipment was designed and assembled during this project phase to prepare for this.

4.1 The photoconductivity of intrinsic a-Si:H

Before the deposition of doped a-Si:H and complete cells was attempted, the photoconductivity of undoped intrinsic a-Si:H was investigated to assert that PV grade a-Si:H could be deposited. Photoconductivity is an important measurement for material intended for PV applications as it quantifies a response to light and demonstrates semiconducting action. Films of intrinsic a-Si:H were grown by varying silane flow rate, substrate temperature, and the RF power delivered to the plasma. The substrates used were standard soda lime glass coated with tin oxide that was laser scribed to form isolated 1cm wide strips of conducting oxide. The width of the laser scribed grooves was measured with an optical microscope and found to be 0.2mm.

A-Si:H was deposited for 15 minutes using a matrix of conditions at two RF power settings to assess achievable deposition rates and photo-conductivities. Layer thickness

was measured with a Talystep stylus profiler by covering an area of the substrate during deposition and using the resulting step profile. The deposition rate ranged from 0.2nms^{-1} to 0.3nms^{-1} which is in the expected range for PECVD, but arguably lower than expected when using a 40MHz RF source (see section 3.2.2). This is probably because use of a turbo pump lowers the process pressure by 1-2 decades and reduces the arrival and reaction rate of neutral species at the growing film surface.

Figure 4.1 shows how the laser scribed TCO creates a volume of a-Si:H that can be used to calculate photoconductivity in the same manner as described in section 2.4.1. The calculated photoconductivity contains error due to the approximation of the volume of a-Si:H that contributes to current flow and because the resistance of samples was measured using a multimeter accurate to only ≈0.1MΩ. The errors in these measurements are small in relation to their absolute values however and so the variation in the calculated values of photoconductivity can be considered real.

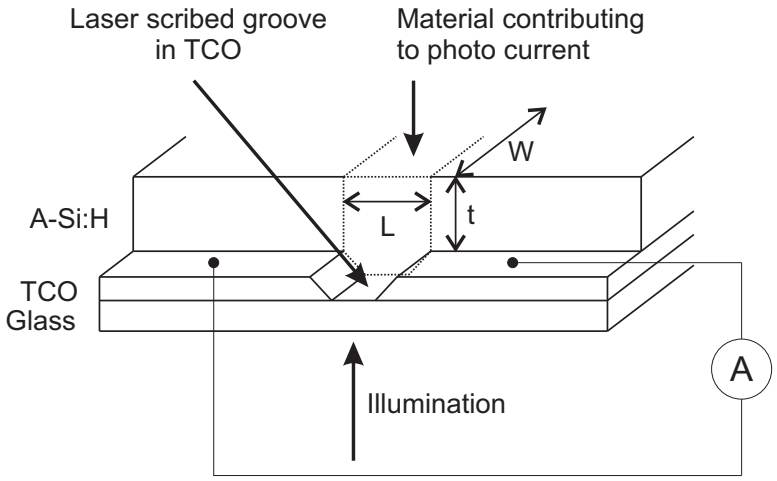

FIGURE 4.1: Measurement of intrinsic a-Si:H photoconductivity using laser scribed TCO

Figure 4.2(a) shows measured photoconductivity as a function of silane flow and substrate temperature. The pressure was 1.2x10^{-1}mbar with a silane flow of 35sccm ranging to 4.8x10^{-2}mbar with a flow of 15sccm. The RF amplifier could not be tuned to deliver 30W to a silane flow of less than 15sccm. Deposition with 30W of power favours a low silane flow rate and a temperature of 220C although higher substrate temperatures would be expected to also produce good results.

Increasing the RF power to 40W results in an increase in the maximum photoconductivity to 7.5x10$^{-5}\Omega^{-1}$cm^{-1}using a higher silane flow of 25sccm (see figure 4.2(b)), but increases the photoconductivity for all silane flow rates at 200C. This could be explained by the increased RF power improving the surface mobility and penetration of hydrogen atoms resulting in a smaller defect density and an increased photo current. The improvement can be attributed to more effective film passivation as deposition rates did not significantly change with the increased RF power and so it is reasonable to expect that the microstructure of films deposited using 30W and 40W remains similar.

The dark conductivity of samples could not be measured due to a lack of equipment capable of a sensitive enough current measurement, but if it is assumed to be $\approx 10^{-7}$-$10^{-8}\Omega^{-1}cm^{-1}$based on published literature [24] then the ratio of dark to light conductivity is two to three decades, which is the same as the best reported ratio by Chittick et al. [9] at the discovery of a-Si:H. This measurement indicates photovoltaic grade material was deposited.

The results suggest that a further increase of photoconductivity could be obtained by increasing substrate temperature to 250C, especially in combination with use of a lower RF power. It is also possible to use a gas feed of hydrogen and silane for intrinisic a-Si:H deposition, which should improve danglng bond passivation at lower substrate temperatures, increase process pressure, and allow lower silane flows to couple more effectively with the RF antenna. Deposition rate would suffer due to film erosion by hydrogen, but system pressure would increase which could have an overall positive influence. There should exist a trade-off between the hydrogen flow and pressure for optimum material quality and fast deposition.

The ability to compensate for lower substrate temperatures with increasing RF power indicates that device grade a-Si:H could be fabricated at 200C or lower, which is a promising result for future work with flexible substrates. Increasing RF power widens the process window with regards to silane flow and substrate temperature, presumably until the point of polysilane formation or plasma damage to the growing film.

4.2 Initial pin cell development

It was decided that work on cells should initially focus on the empirical aspects of depositing whole devices rather than the analysis of individual layers. This was due to an lack of equipment that was sensitive enough to measure the small dark current that flows in a-Si:H. Even if conditions for the deposition of ideal individual layers are known issues such as the interface between doped and intrinsic layers, doping gradients, and possible contamination of intrinsic material by undesired dopant must be taken account of when depositing complete cells. These problems can be mostly mitigated by the appropriate use of plasma breaks and gas flushes during deposition. Measurement of individual layer properties is desirable as it can provide assurance that of material quality but cell performance can be poor even with ideal individual layers if the interactions between them has not been considered.

The properties of a-Si:H have been studied in depth since the 1970s, and are well documented. Cells were deposited in an attempt to reproduce past performance in the fields of pin homojunction and heterojunction cells. This provided experience with a-Si:H

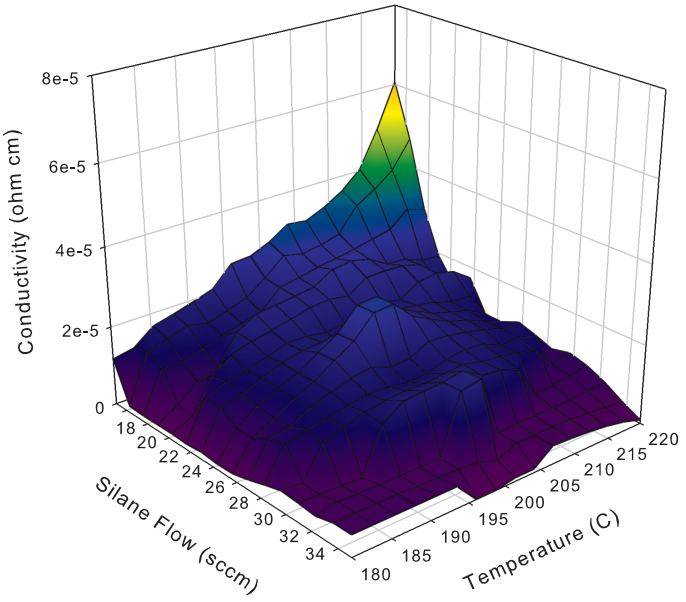

(a) Photoconductivity of intrinsic a-Si:H grown with 30W of RF power

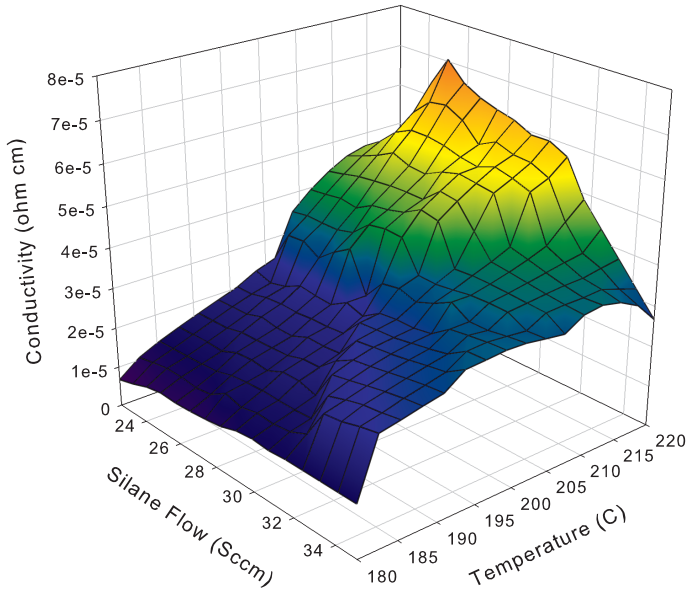

(b) Photoconductivity of intrinsic a-Si:H grown with 40W of RF power

FIGURE 4.2: Photoconductivity of intrinsic a-Si:H as a function of silane flow and substrate temperature with 30W and 40W of RF power. A higher photoconductivity is evidence of increased carrier mobility or concentration assuming that the Fermi level remains static between samples. Use of the higher RF power allows a greater variation in silane flow rate and substrate temperature whilst maintaining good photoconductivity

deposition that it was hoped would enable the transfer of low temperature a-Si:H deposition onto flexible substrates. A target of 8-10% efficient heterojunction pin superstrate cells to be deposited onto TCO covered glass was set.

4.2.1 Sample naming scheme

Cells are referred to as a combination of 3 numbers and a letter. The 3 numbers represent the date when the cell was created and the letter is used to distinguish between cells if more than one was made in a day. E.g. cell 6-7-7-b was the second cell made on the sixth of July, 2007.

4.2.2 The first pin cell

The first pin cell (5-4-7-a) was deposited at a substrate temperature of 220C and an RF power of 40W using the front valve of the PECVD reactor. The silane flow was 20sccm, with 10sccm of 1% diborane mixture during p layer deposition and 10sccm of 1% phosphine mixture during the n layer deposition. The deposition times for the layers were 1 minute for the p layer, followed by a 5 minute flush period, a 30 minute intrinsic layer deposition, and a 5 minute n layer deposition. The system pressure during intrinsic layer deposition was $8x10^{-2}$mbar. The deposition times were estimated from the $0.25nms^{-1}$ deposition rate determined from previous work, in order to create a device with dimensions of approximately 10nm/500nm/100nm for its pin structure. These dimensions are typical of a well performing pin cell [44]. An IV characteristic was measured before and after a 30 minute 150C anneal.

The extracted pre and post anneal double diode parameters of the cell are shown in table 4.1. The IV characteristics incorporate an allowance for a 20Ω series resistance due to TCO. This was approximated by using a multimeter to measure the resistance from the center of a cell contact to the center of its corresponding TCO contact. The extracted values of series resistance are of a similar magnitude which helps to validate this adjustment.

5-4-7-a	Pre Anneal	Post Anneal
V_{oc} (V)	0.76	0.72
I_{sc} (mA)	10.6	14.0
R_s (Ω)	42.8	15.4
R_{shunt} (Ω)	103	146
J_{02} (A)	$2.47x10^{-9}$	$8.28x10^{-9}$
FF	0.33	0.46
η (%)	2.68	4.60

TABLE 4.1: Double diode fitting parameters for cell 5-4-7-a before and after a 30 minute 150C anneal. The corresponding IV characteristics are shown in Figure 4.2.2

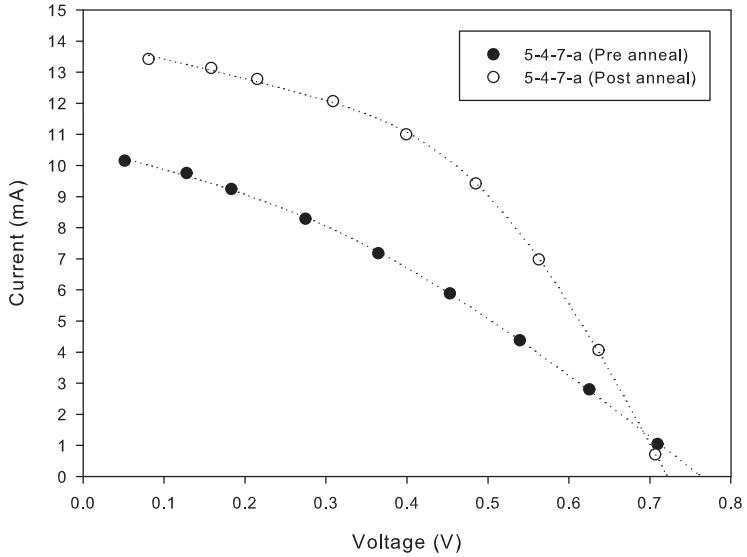

FIGURE 4.3: Pre and post anneal IV characteristics of the first deposited cell (5-4-7-a) using a substrate temperature of 220C and 40W of RF power. The dotted lines correspond to the fitted double diode parameters for each IV characteristic after a 20Ω correction for R_{TCO}

The cell was functional in its pre-anneal state, but post anneal nearly every double diode parameter had noticeably improved. The most effective change was the reduction in R_s and corresponding rise in I_{sc}. R_{shunt} rose slightly and the recombination current J_{02} dropped in tandem as would be expected. The slight drop in V_{oc} is offset by the rise in FF. Because cell performance increased so sharply it was likely that one or more of the interfaces between the cell contacts and the a-Si:H was non-Ohmic and that the anneal either reduced the contact series resistance or redistributed hydrogen and passivated defects.

An efficiency of 4.60% for cell 5-4-7-a in its non-optimised post anneal state was an encouraging first result, and demonstrated that the PECVD reactor was suitable for the fabrication of a-Si:H based PV cells.

4.2.3 Possible reactor contamination

Immediate follow-up work to investigate changes in deposition parameters resulted in a greater than expected number of electrically dead cells. Cells that were active suffered from decreased V_{oc} and I_{sc} when compared to cell 5-4-7-a. This deterioration in performance was attributed to reactor contamination as it had not been cleaned since the beginning of the project and silicon had steadily built up on the reactor walls and would fall off during the plasma generation resulting in intrinsic layer contamination and poor device performance.

The reactor was cleaned using a plasma and a carbon fluoride/oxygen mix of 92:8% for several hours until no a-Si:H deposits were visible on the reactor walls. A reactor clean was perfomed from this point onwards every time it was suspected that reactor contamination was affecting cell performance. It was also noticed that a cleaned reactor could take some time to "bed in" and that there was a time period for deposition in which best device performance could be obtained that occured after cleaning.

After cleaning the reactor was dismantled to fix a leak that had developed which was isolated to a faulty O ring seal. The seal was replaced and an extraneous target holder that allowed the reactor to be modified from PECVD to sputtering was removed as it was providing a large increase in surface area for polysilane dust to be deposited onto. The reactor and heater mount were then conditioned with a silane/hydrogen plasma at 200C for 30 minutes before being returned to use.

4.3 Optimising the p layer thickness

P layer thickness and doping concentration is of primary importance when trying to fabricate efficient a-Si:H cells. If the p layer is too thick I_{sc} will suffer as a result of short wavelength generated carriers recombining, due to the large defect density observed in doped a-Si:H and the inability to tunnel across the layer. If the p layer is too thin V_{oc} will decrease and in the extreme case of a unformed or extremely thin p layer rectifying diode behaviour will not be observed. A p layer that is too thin may also not be able to sustain an electric field over the intrinsic region of the device in which case collection of generated carriers will be impacted, R_{shunt} and I_{sc} will worsen, and J_{02} should increase. The p layer deposition time was varied to determine the optimum p layer thickness. 20sccm of hydrogen was added to each deposition from start to finish to ensure that intrinsic layer growth was not depleted of hydrogen.

Cells were created with p layers deposited for 40 seconds (2-5-7-a), 50 seconds (3-5-7-a), and 60 seconds (3-5-7-b). The substrate temperature was 220C, and the RF power was 40W. The intrinsic and n layer were deposited for 30 and 5 minutes respectively, and there was a 5 minute plasma break between the p and intrinsic layer to minimize diborane contamination. The cells were annealed at 150C for 30 minutes after contact deposition. Figure 4.4 shows the IV characteristics of the cells whilst table 4.2 lists the fitted double diode parameters for each cell.

Increasing the p layer deposition time has a positive effect on all cell parameters at 40, 50, and 60 seconds of growth time. This data shows that a p layer deposited for 60 seconds could still be too thin, as the fitted diode parameters do not worsen compared to the other cells. J_{02} for cell 2-5-7-a does not appear to make sense and this is attributed to the cell having an almost linear IV characteristic that is difficult to resolve as a combination of two diodes, hence the strange result. The performance of cell 3-5-7-b

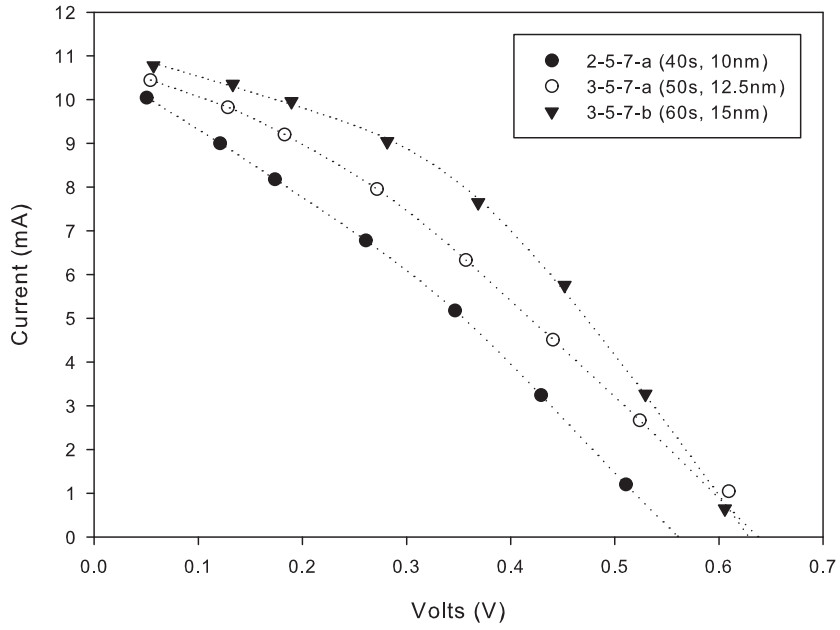

FIGURE 4.4: The effect of reducing the p layer deposition time from 60 seconds (3-5-7-b) to 50 seconds (3-5-7-a) and 40 seconds (2-5-7-a) using a substrate temperature of 220C and 40W of RF power. Assuming a deposition rate of 0.25nm^{-1} these times correspond to thicknesses of 15nm, 12.5nm, and 10nm respectively. The dotted lines correspond to the fitted double diode parameters for each IV characteristic after a 20Ω correction for R_{TCO}, the greatest voltage bias point for cell 3-5-7-a was removed from fitting due to the influence of a Schottkey barrier

Cell	2-5-7-a	3-5-7-a	3-5-7-b
P layer deposition time (s)	40	50	60
Estimated thickness (nm)	10	12.5	15
V_{oc} (V)	0.56	0.63	0.62
I_{sc} (mA)	10.7	10.8	11.2
R_s (Ω)	36.0	38.8	26.7
R_{shunt} (Ω)	34	87	118
J_{02} (A)	7.18x10^{-15}	5.43x10^{-9}	3.17x10^{-9}
FF	0.30	0.33	0.40
η (%)	1.81	2.27	2.85

TABLE 4.2: Double diode fitting parameters for cells 2-5-7-a, and 3-5-7-a, and 3-5-7-b

is unexpected as it was created using a very similar fabrication process to cell 5-4-7-a which was twice as efficient post anneal. The change is probably due to altered post clean growth conditions inside the PECVD reactor, and the deposition rate could also have decreased due to increased hydrogen etching during film growth.

The p layer deposition time was increased further to 90 seconds (9-5-7-a) and 120 seconds (10-5-7-a) in order to further investigate the region where the optimum thickness was suspected to be found. The IV characteristics of these cells are shown in Figure 4.5 and the double diode fitting parameters are listed in table 4.3. The original cell that was deposited before the PECVD reactor was cleaned (cell 5-4-7-a, see section 4.2.2) is included as a comparison.

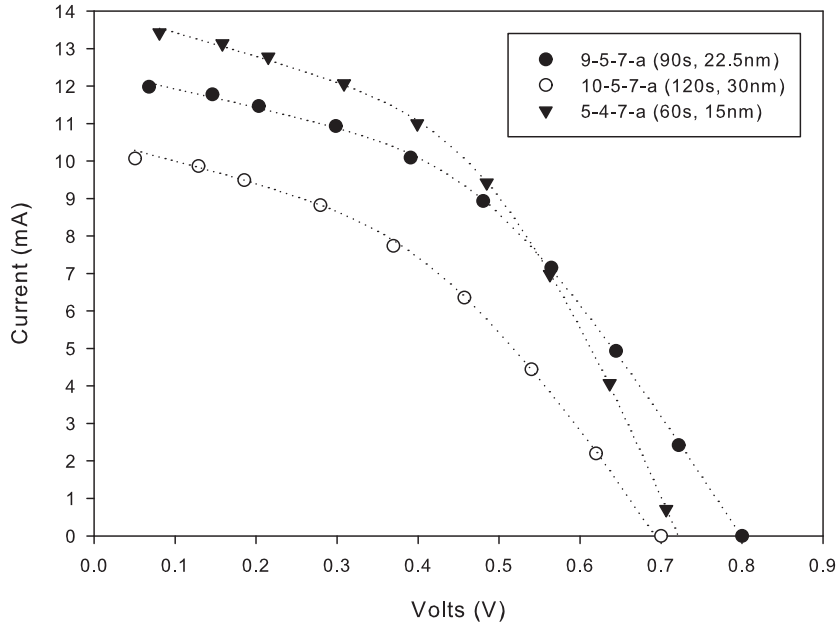

FIGURE 4.5: The effect of increasing the p layer deposition time from 90 seconds (9-5-7-b) to 120 seconds (10-5-7-a), using a substrate temperature of 220C and 40W of RF power. Assuming a deposition rate of $0.25nm^{-1}$ these times correspond to thicknesses of 22.5nm, and 30nm respectively. The dotted lines correspond to the fitted double diode parameters for each IV characteristic after a 20Ω correction for R_{TCO}, the greatest voltage bias point for cell 10-5-7-a was removed from fitting due to the influence of a Schottkey barrier

Cell 9-5-7-a is a significant improvement over the cells with thinner p layers. It is comparable to cell 5-4-7-a, especially in terms of FF and efficiency, although I_{sc} has been reduced slightly at 12.4mA to 14mA which is probably related to a change in p layer thickness. The trade off between the cells is that the gain in R_s is balanced by a gain in V_{oc}. As p layer thickness increases V_{oc} would be expected to reach a limit near 0.8V whilst R_s would also continue to rise. Cell 10-5-7-a shows the problems associated with a p layer that is too thick. I_{sc} is down from 11.73mA to 9.81mA, V_{oc} has decreased

Cell	9-5-7-a	10-5-7-a	5-4-7-a
P layer deposition time (s)	90	120	60
Estimated thickness (nm)	22.5	30	15
V_{oc} (V)	0.79	0.77	0.72
I_{sc} (mA)	12.4	10.4	14.0
R_s (Ω)	26.8	46.1	15.4
R_{shunt} (Ω)	179	132	146
J_{02} (A)	8.41×10^{-10}	2.11×10^{-11}	8.28×10^{-9}
FF	0.43	0.35	0.46
η (%)	4.30	2.87	4.60

TABLE 4.3: Double diode fitting parameters for cells 9-5-7-a, and 10-5-7-a

slightly which is related to the loss of current, and all cell resistances and FF have worsened.

Figure 4.6 shows how the fitted double diode parameters respond to increasing p layer deposition time. The best deposition time can be seen clearly near 90 seconds, represented by an improvement in all aspects of the cell.

4.4 Optimising the doping efficiency of the p layer

The most important part of an a-Si:H cell is the p layer, the thickness and doping of which is critical to device performance. Previous experiments (see section 4.3) had shown that the thickness of the p layer could be optimised and so the next logical step was to ensure that the doping efficiency of the layer was maximised, as if it was found not to be then the layer could potentially be further thinned.

4.5 Changing the gas input valve

Previous cell yields were not found to be consistent, deposition processes would typically yield up to 50% non-active or performance degraded cells per substrate. A cause of this could have been the method by which gases were introduced to the reactor via the front gas valve, between the plasma and the exit to the pump. This could have contributing to an unreliable process because there was no way of knowing how effectively gas molecules introduced to the reactor were disassociated by the plasma, or if they were directly pumped before they could generate neutral species that could contribute to growth. In particular it was noticed that processes could be improved by the constant addition of extra hydrogen, which is a light and easily pumped gas. Processes without this addition could well have been starved for hydrogen, resulting in a higher density of midgap states in deposited a-Si:H.

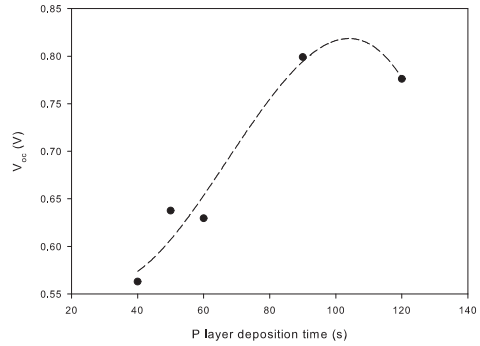

(a) V_{oc} as a function of p layer deposition time

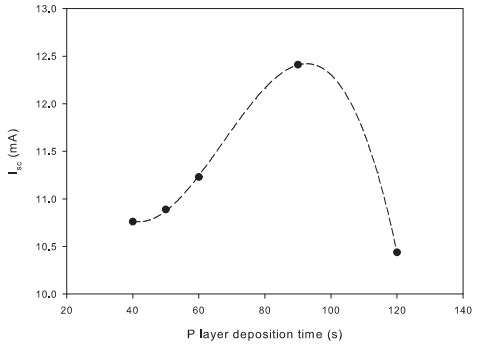

(b) I_{sc} as a function of p layer deposition time

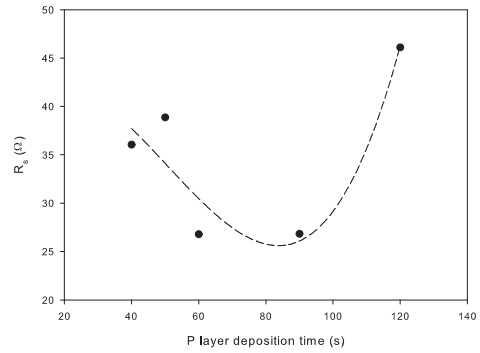

(c) R_s as a function of p layer deposition time

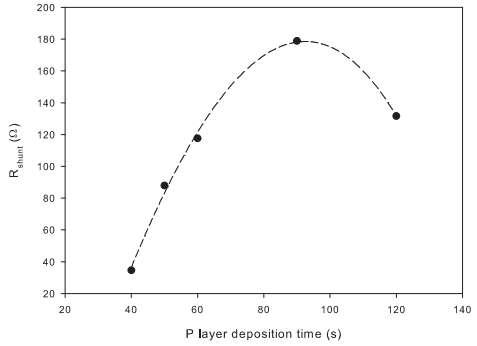

(d) R_{shunt} as a function of p layer deposition time

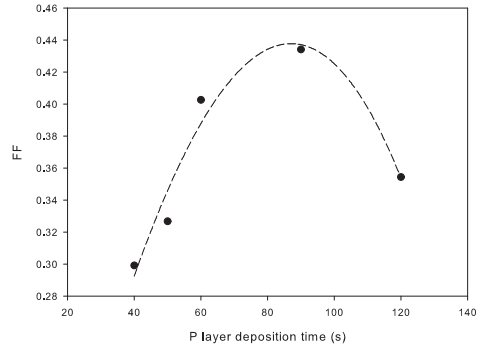

(e) FF as a function of p layer deposition time

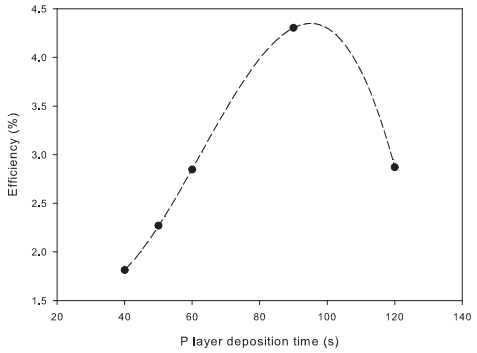

(f) Efficiency as a function of p layer deposition time

FIGURE 4.6: Double diode determined cell parameters plotted as a function of p layer deposition time. Cells were all grown using a substrate temperature of 220C and 40W of RF power. The dashed lines are cubic polynomial best fit curves included as a guide to the eye, an improvement in every parameter can be observed near 90 seconds corresponding roughly to a 22.5nm thick p layer

Dead or degraded cells often exhibited a low V_{oc} which is usually due to a too thin or inadequately doped p layer. To improve gas disassociation and the interaction of reactive species with the growing film, a decision was made to use the rear gas valve rather than the front such that gases introduced to the reactor encountered the plasma first, and then subsequently the heated substrate and the pump valve. In this way it was expected that a more reliable rate of disassociation and more consistent deposition processes would be achieved.

Details of this change and the resulting difference in gas flow can be seen in Figure 3.1, (see section 3.1).

4.5.1 Use of the rear gas input valve

Samples were prepared to investigate what differences using the rear input valve would make to cell performance. It was expected that cell yield would increase on a per substrate basis and that repeated processes would become more consistent due to increased gas disassociation. The process used a 60 second p layer deposition with 10sccm of 1% diborane mixture, a 30 minute intrinsic layer deposition with 20sccm of silane and hydrogen, and a 5 minute n layer deposition using 10sccm of 1% phosphine mixture. The substrate temperature was 220C, and 40W of RF power was supplied to the plasma. The cell was 29-5-7-a, and the deposition precedure was identical to that of cell 3-5-7-b with the exception that the rear gas entry valve was used instead of the front. The IV characteristics of both cells are shown in Figure 4.7. A 60 second p layer deposition time is not the optimum that was observed in Figure 4.6, but by shortening it, any change in doping efficiency due to the change of gas input valves should be observable.

The IV characteristic of cell 29-5-7-a is not the improvement that was expected. I_{sc} has reduced with V_{oc}, and there is a pronounced current barrier at 0.12mA. This current barrier is due to a Schottky diode formed because of a non-Ohmic interface between a conducting contact and an inadequately doped a-Si:H layer. As transport through the p layer is predominantly attributed to quantum tunneling due to its thinness, the interface that is likely to be responsible is between the n layer and the aluminium contact. The Schottky diode will be reverse biased with respect to the cell when it is operating under forward bias, so the Schottky diode prevents the transport of electrons to the aluminium contact because they are the majority carrier in the n type material. The barrier will break down with enough forward bias and this behavior was observed after roughly half a volt ($\approx$ 1.2V of forward bias). The Schottky diode is very likely to be a result of inadequate n layer doping.

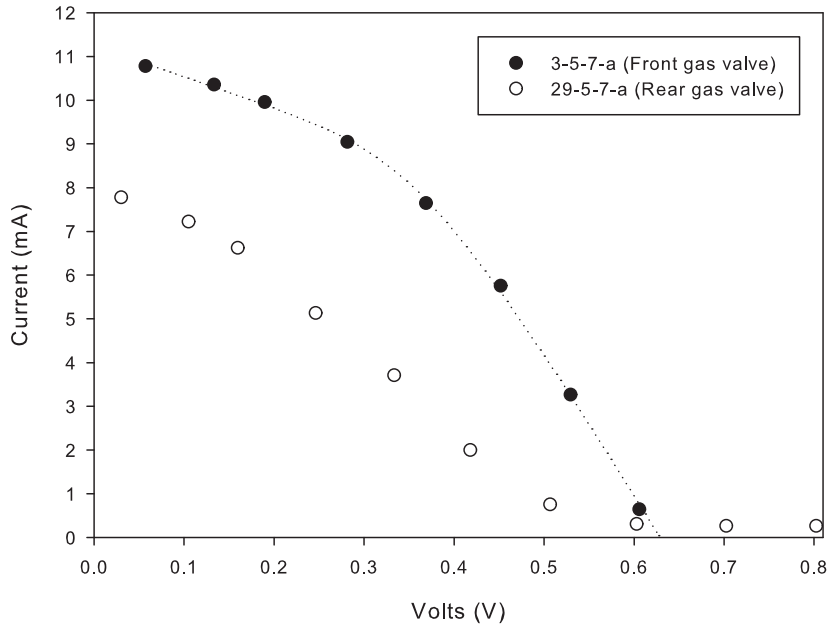

FIGURE 4.7: The effect of changing gas input valve on cells produced with a substrate temperature of 220C and 40W of RF power, the dotted line represents the double diode fit to the IV characteristic of cell 3-5-7-a. The IV characteristic of cell 29-5-7-a is not fitted as a pronounced Schottkey barrier is seen to be present

4.5.2 Increasing the substrate temperature

Previous results have shown that the dopant:silane ratio used during p and n layer deposition for cell 29-5-7-a was sufficient to create functional cells. To try and recover the doping efficiency the substrate temperature was raised to 250C and the deposition of cell 29-5-7-a was repeated to observe the effect. Figure 4.8 shows the IV characteristics of this cell (29-5-7-b) and of the original cell (29-5-7-a) produced using a substrate temperature of 220C.

The higher substrate temperature recovers the diode curve well. Shunt and series resistances are still poor and V_{oc} is low at just above 0.7V, but the IV characteristic knee is much more pronounced than for cell 29-5-7-a. The beginning of a small Schottky barrier was seen near 0.8V for cell 29-5-7-b, but as its effect is located in the first quadrant of the IV curve it is ignored. This is evidence that doping efficiency could be improved further to obtain higher values of V_{oc}.

A 10sccm flow of 1% diborane mixture during p layer deposition provided effective doping when using the front gas entry valve, but it is reasonable to suspect that it might have to be altered to account for the changed gas dynamics when using the rear valve. This result indicates that there is enough dopant available when using a 10sccm flow of 1% diborane mixture and 1% phosphine mixture to produce working cells, but that the move to using the rear gas valve has either lowered the amount of dopant incorporated

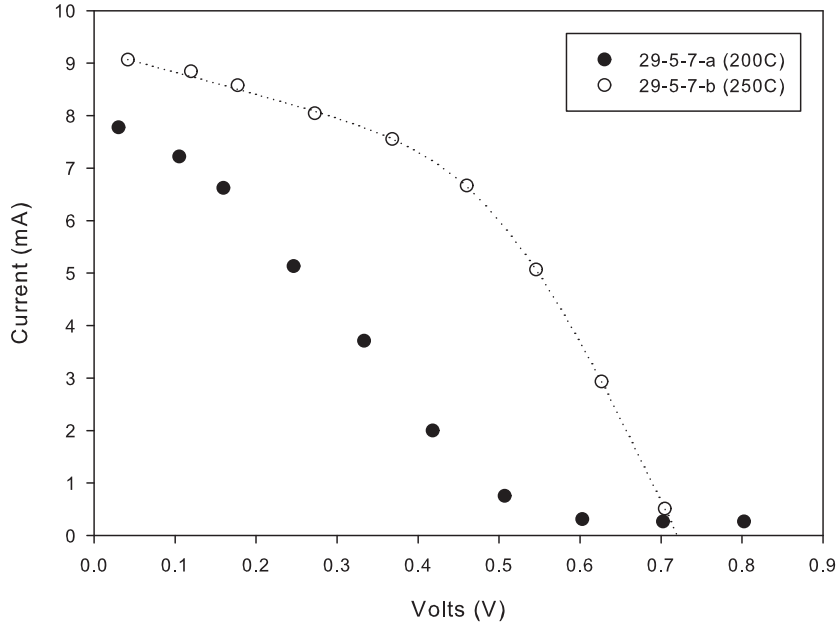

FIGURE 4.8: The effect of increasing substrate temperature from 220C (29-5-7-a) to 250C (29-5-7-b) using the rear gas entry valve and 40W of RF power, the dotted line represents the double diode fit to the IV characteristic of cell 29-5-7-b. Use of the higher substrate temperature recovers the IV characteristic well

into the growing film or that dopant atoms tended to be incorporated as inactive atoms with their valency requirements satisfied. The improved IV characteristic observed as a result of the higher substrate temperature could be due to either of these issues or a combination of both. The move of the gas entry point from close to the substrate to much farther away will also have reduced the process pressure at the growing film surface. The system pressure did change from $9.7\text{x}10^{-2}$mbar to $8.3\text{x}10^{-2}$mbar during the p layer deposition as measured by a barocel gauge when using the front and rear gas entry valve respectively. The gas flow was the same in both cases. Restoring the system pressure to its prior value via an increased gas flow rate could improve doping efficiency and possibly deposition rate.

4.5.3 Increasing the diborane flow

Increasing the substrate temperature was beneficial to doping efficiency and overall performance, but V_{oc} was lower than the previous best cell deposited using the front gas valve. In an attempt to improve V_{oc} back to 0.8V, the 1% diborane mixture flow during p layer deposition was increased to 60sccm from 20sccm to triple the ratio of dopant:silane flow. The p layer was deposited for 40 seconds (in case doping efficiency did improve), the intrinsic layer for 20 minutes using 20sccm of hydrogen, and the n layer for 5 minutes with 10sccm of 1% phosphine mixture. A 20sccm flow rate of silane was used during the

entire process. The p layer deposition time was reduced from the previous best result of 90 seconds to account for the higher system pressure (due to increased diborane flow) and to compensate for the expected increase in gas disassociation from using the rear valve. The substrate temperature was kept at 220C to be compatible with previous results, and the RF power was 40W. The system pressure during p layer deposition was $1.3\text{x}10^{-1}$mbar, approximately twice what it was using the lower diborane flow.

The IV characteristic of the cell (31-5-7-a) is shown in Figure 4.9. The IV characteristic of the previous best cell deposited using the front gas valve during the p layer thickness variation series of experiments (9-5-7-a) is included as a comparison. The extracted cell parameters are listed in table 4.4.

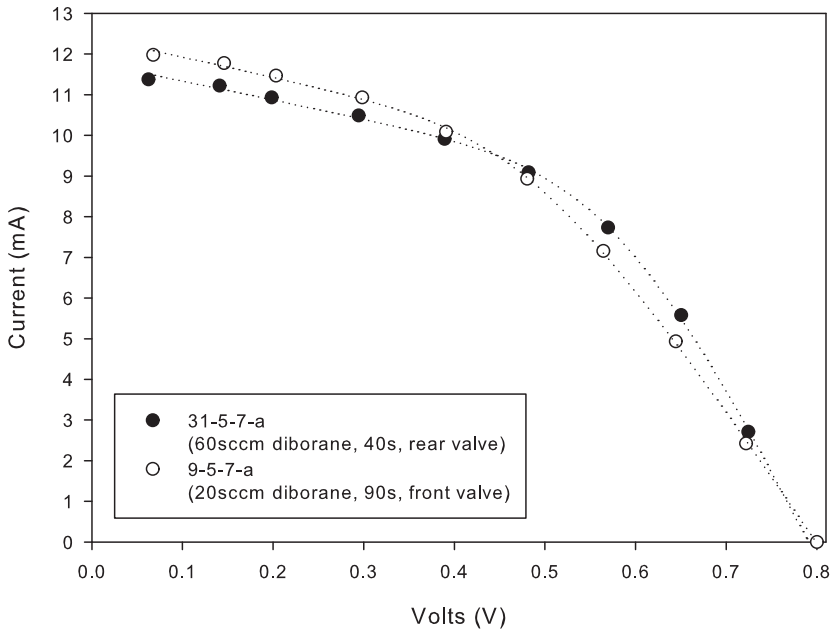

FIGURE 4.9: The effect of changing the 1% diborane mixture flow, p layer deposition time, and gas entry valve using a substrate temperature of 220C and 40W of RF power. Cell 9-5-7-a was grown using 20sccm of 1% diborane mixture, a 40 second p layer deposition time, and the front gas entry valve. Cell 31-5-7-a was grown using 60sccm of 1% diborane mixture, a 90 second p layer deposition time, and the rear gas entry valve. The dotted lines are double diode IV characteristic fits corresponding to the parameters listed in table 4.4

Cell	31-5-7-a	9-5-7-a
V_{oc} (V)	0.79	0.80
I_{sc} (mA)	11.8	12.4
R_s (Ω)	23.2	30.2
R_{shunt} (Ω)	217.5	205.4
J_{02} (A)	$1.20\text{x}10^{-9}$	$8.41\text{x}10^{-10}$
FF	0.48	0.43
η (%)	4.52	4.30

TABLE 4.4: Double diode fitting parameters for cells 9-5-7-a and 31-5-7-a

Raising the diborane flow rate succeeded in restoring V_{oc} to 0.8V. The higher diborane flow rate has also improved R_s, presumably by creating a thinner p layer that still contains a comparable amount of active dopant to cell 9-5-7-a. I_{sc} is down slightly at 12.4mA to 11.8mA but this could be attributed to a lower pressure during intrinsic layer deposition and therefore a reduced deposition rate. A longer deposition or a higher silane flow rate would probably restore it. Despite the current loss the cell created with the rear gas valve exhibits a better FF and efficiency which is mainly attributable to improvement in R_s. This result highlights the importance of p layer thickness control and doping to a well performing cell.

The yield of functional cells on the substrate of cell 31-5-7-a was 80%, which was an improvement on previous substrates that were deposited onto using the front gas valve where typically ≈50% of cells would be lost due to badly formed or incomplete p layers.

4.6 Incorporating a silicon carbide window

After changing the gas entry point and restoring V_{oc} to 0.8V by increasing diborane flow and p layer doping efficiency, it was decided to incorporate methane into the gas flow during p layer deposition in an attempt to produce a heterojunction cell with a wide mobility gap window layer (see section 2.7.4). If successful this should increase I_{sc} due to more light being admitted to the intrinsic region of the cell, which would also improve V_{oc}. V_{oc} should also be boosted by the increased V_{bi} (built in voltage) of the heterojunction cell structure.

The method of cell deposition was the same as for cell 31-5-7-a (see section 4.5.3) with the exception of the p layer conditions. The p layer was deposited for 60 seconds instead of the previous 40 with 60sccm of 1% diborane mixture and 20sccm of silane. 20sccm of methane was added to the p layer gas flow of cell 4-6-7-a, and 40sccm of methane was added to the p layer gas flow of cell 5-6-7-a. The p layer deposition time was increased to compensate for a potential loss of doping efficiency which could cause dead cells. The substrate temperature and RF power were kept constant at 220C and 40W. A further cell (5-6-7-b) was produced using a substrate temperature of 250C but was otherwise identical to cell 4-6-7-a.

Figure 4.10 shows the IV characteristics of cell 4-6-7-a (40sccm methane) and cell 5-6-7-a (20 sccm methane). The 20sccm flow of methane added during p layer deposition resulted in the beneficial effect of increased I_{sc}, with 12.68mA measured as compared to 10.65mA for cell 31-5-7-a. V_{oc} did not change from 0.8V which was unusual as a slight increase was expected in line with I_{sc}, but the increase in current shows that the p layer optical gap has widened and that this has improved the short wavelength response of the device. The increase to 40sccm of methane has worsened the p layer doping efficiency and a Schottky barrier can be seen near V_{oc} in the IV characteristic. A methane flow

rate of 10sccm was also tested but all devices produced were either dead or showed extremely poor performance.

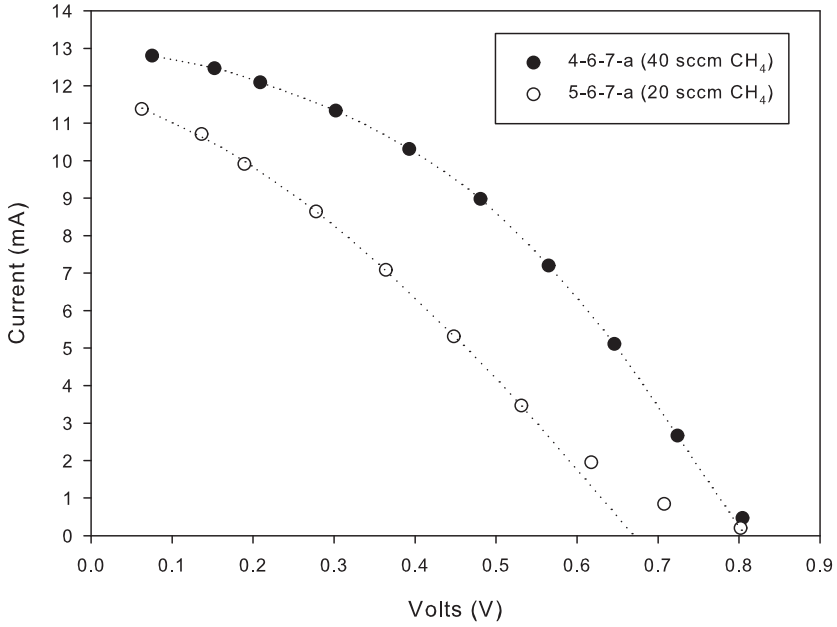

FIGURE 4.10: The effect of varying methane flow from 20sccm to 40sccm during a 60 second p layer deposition, using a substrate temperature of 220C and 40W of RF power. The dotted lines correspond to the fitted double diode parameters for each IV characteristic (see table 4.5) after a 20Ω correction for R_{TCO}, and some data points were removed from fitting due to a Schottkey barrier effect near V_{oc}

Figure 4.11 shows the IV characteristics of cell 4-6-7-a (220C, 40sccm methane) and cell 5-6-7-b (250C, 20sccm methane). Increasing the substrate temperature to 250C had a positive effect on cell performance. V_{oc} has improved from 0.8V to 0.82V which indicates that either the mobility gap of the p window layer has widened further or p layer doping efficiency has increased. As I_{sc} went up to 12.68mA from 12.91mA, the former is more plausible. A small Schottkey barrier can still be seen in both characteristics which is likely to be related to the n layer doping efficiency as a substrate temperature of 250C has already been shown to be able to recover Schottky barriers relating to poor p layer doping (see section 4.5.2).

4.6.1 Double diode fitting parameters

Table 4.5 lists the double diode fitting parameters for cells 4-6-7-a, 5-6-7-a, and 5-6-7-b. The data points for cell 5-6-7-a that correspond to the Schottky barrier ($V > 0.5$) were not included in the fit as they would result in inaccurate values for V_{oc}, FF, and η. For the same reason the IV data point closest to V_{oc} for cells 4-6-7-a and 5-6-7-b was also not included in the data fitting as the small barrier effect would have slightly inflated V_{oc}.

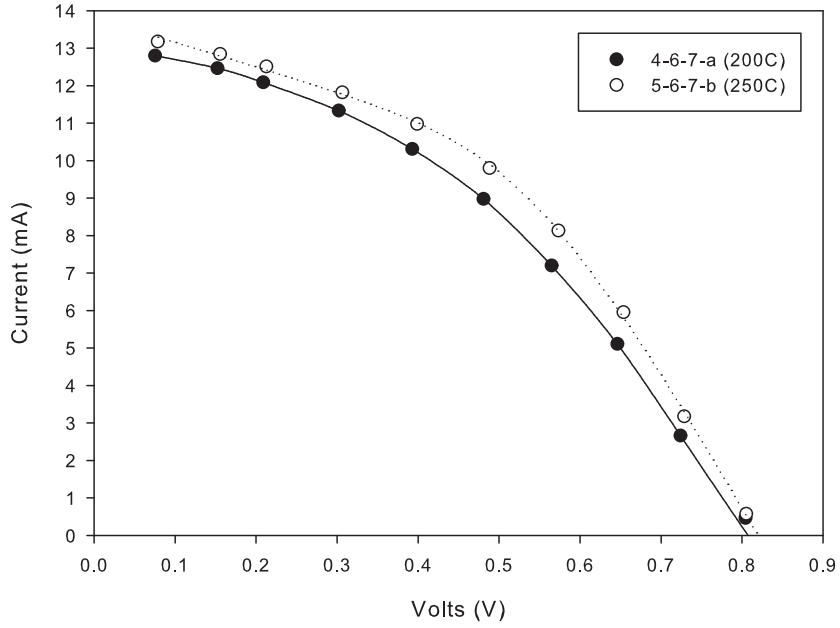

FIGURE 4.11: The effect of incorporating 20sccm of methane into a 60 second p layer deposition whilst varying the substrate temperature from 220C to 250C and using 40W of RF power. The dotted lines correspond to the fitted double diode parameters for each IV characteristic (see table 4.5) after a 20Ω correction for R_{TCO}, and some data points were removed from fitting due to a Schottkey barrier effect near V_{oc}

Cell	4-6-7-a	5-6-7-a	5-6-7-b
V_{oc} (V)	0.81	0.68	0.82
I_{sc} (mA)	13.4	12.0	13.8
R_s (Ω)	25.2	36.3	26.7
R_{shunt} (Ω)	122	87.6	153
J_{02} (A)	$1.38\text{x}10^{-9}$	$1.57\text{x}10^{-8}$	$6.69\text{x}10^{-10}$
FF	0.40	0.31	0.43
η (%)	4.38	2.57	4.86

TABLE 4.5: Double diode fitting parameters for cells 4-6-7-a, 5-6-7-a and 5-6-7-b

Cell 5-6-7-b is 4.86% efficient which is an improvement on the previous best efficiency of cell 5-4-7-a (4.60%). Whilst I_{sc} and FF are very similar between cells, the addition of methane to the p layer deposition to form a wide mobility gap silicon carbide window has increased V_{oc} by 0.12V due to the enhanced V_{bi} of the heterojunction cell structure. A 1:1 ratio of silane to methane was found to be the optimum flow for p layer deposition, whilst a 1:2 ratio affected V_{oc} and R_s negatively, and a 2:1 ratio resulted in dead cells.

A higher substrate temperature of 250C was found to improve cell performance again (see section 4.5.2), most noticeably through an improvement in R_{shunt} and a corresponding drop in J_{02} of half a decade. This result suggests that a-Si:H deposition at 250C results in electronically superior material to 220C. This is probably related to the predominant bonding configuration of hydrogen or the midgap defect density which could

be investigated using IR transmission or ESR measurements.

4.7 Removal of the turbo pump

It was decided that before further experiments were to be attempted, the turbo pump should be removed from the PECVD system and that the dry pump alone would be sufficient for further work. There were several reasons for this:

- It was required to dilute the pump output flow with nitrogen that was inserted after the turbo pump to keep any silane present under its flammability limit in air. The 2.5slm of nitrogen that was required raised the backing pressure of the turbo pump such that there was a combined gas flow limit of ≈100sccm that could be supplied to the reactor before the system pressure began to approach the turbo pump backing pressure. This problem resulted in a limit on the total flow of gas into the reactor, in order to maintain an acceptable differential acrosss the turbo pump. Having similar pressures at both the input and the output of the turbo pump would reduce pumping efficiency and could have potentially cause the problem of back streaming nitrogen into the PECVD reactor due to the low pressure differential. With the turbo pump removed, nitrogen could be directly inserted into the dry pump that backed it. The system pressure was then no longer restricted as the nitrogen purge was isolated from the PECVD reactor, and so a higher silane flow rate was possible.
- A dry pump cannot reach as low a base pressure as a turbo pump, and therefore the system pressure for any given input gas flow rose approximately 1 decade (mbar). The average system pressure rose from $\approx 10^{-2}$mbar when using the turbo pump to $\approx 10^{-1}$mbar with only the dry pump. This improved deposition rates and is considered a more suitable pressure for a-Si:H deposition.
- As work with a-Si:H is essentially a dirty process due to the density of midgap defect states that exists in even good quality material, the low base pressure provided by the turbo pump had no measurable effect on the quality of a-Si:H deposited.

Figure 4.12 shows the relationship between system pressure and the input gas flow using hydrogen with no plasma. The dry pump provides a more linear relationship between the two variables above 20sccm and at least a decade increase in system pressure for any input gas flow. System pressure would increase if an identical flow of a heavier gas such as silane was used, but the difference would be marginal in relative terms.

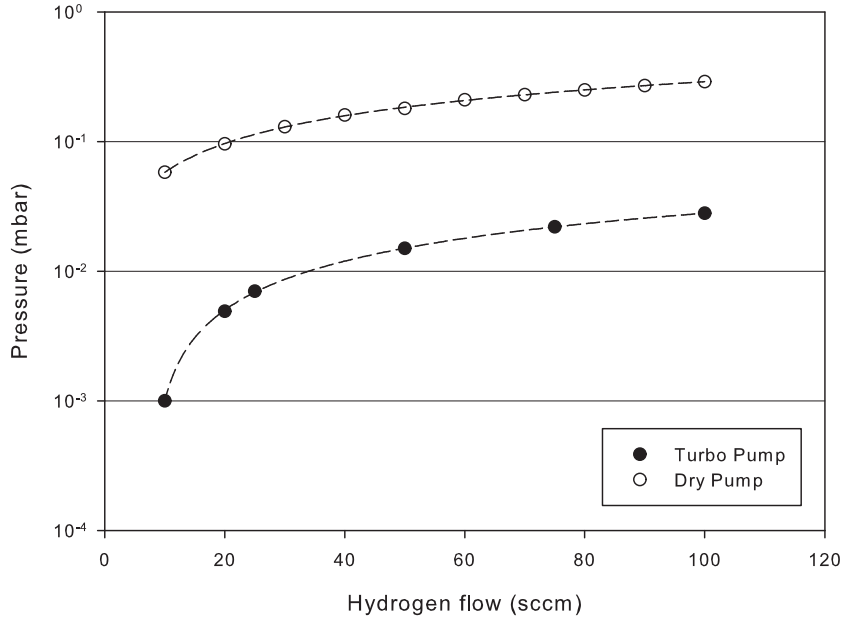

FIGURE 4.12: System pressure as a function of hydrogen flow rate with and without a turbo pump attached. The dashed lines are fits to the data to guide the eye

4.7.1 The effect of higher system pressure on cell production

To investigate the difference that removing the turbo pump had made to the process developed so far, cell 4-6-7-a (see section 4.6) was reproduced using identical deposition parameters after the pump removal to create cell 11-6-7-a. The IV characteristics of both cells are shown in figure 4.13. The system pressure during intrinsic layer deposition was 7.7x10^{-2}mbar with the turbo pump present compared to 2.1x10^{-1}mbar after it was removed.

The system alterations seem to have worsened cell performance at first impression as I_{sc} has reduced with V_{oc}. When the IC characteristics are inspected further it is seen that the cell produced using a higher pressure exhibits a more pronounced knee in its IV characteristic because FF and R_{s} have improved.

It was noticed that dust was present post deposition on the edges of the substrate used with the higher pressure. This was an indication that material was arriving faster than it could be incorporated into the growing film, or that the higher pressure was promoting the formation of polysilane species. If the dust was related to the arrival rate of desirable species then use of a higher substrate temperature could perhaps have helped to avoid this, but it would also have been confirmation that the deposition rate had increased. Thicker than expected doped layers due to this were probably responsible for the reduced I_{sc}.

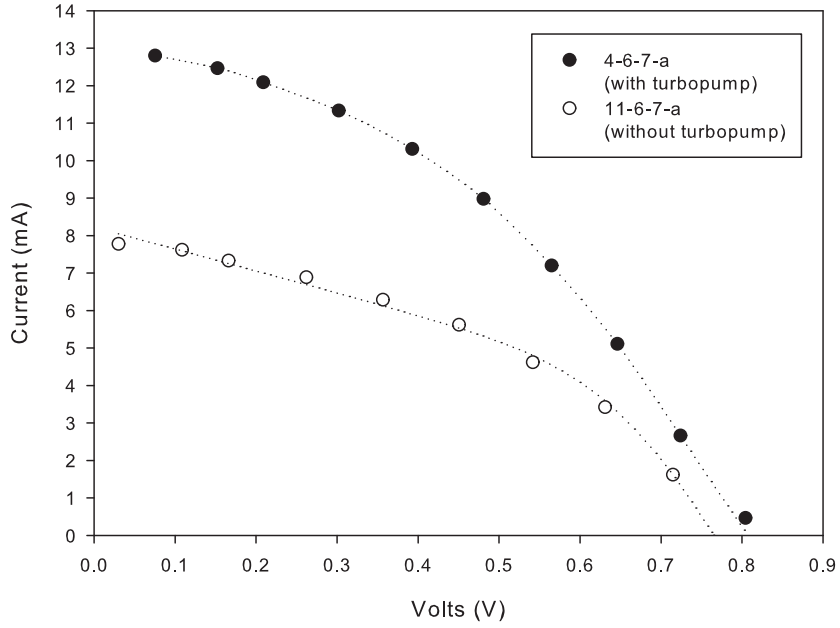

FIGURE 4.13: The effect of increased system pressure on a previously grown cell utilising an a-SiC:H wide bandgap p layer, a substrate temperature of 220C, and an RF power of 40W. The dotted lines correspond to the fitted double diode parameters for each IV characteristic (see table 4.6) after a 20Ω correction for R_{TCO}

To test this hypothesis the deposition process was altered to parameters that would better suit the higher system pressure. The p layer was deposited for 30 seconds with 20sccm of silane, 60sccm of 1% diborane mixture, and 20sccm of methane. The gas flow in the subsequent layers were adjusted to be close to this flow rate. The intrinsic layer was deposited for 20 minutes with 40sccm of hydrogen and 40sccm of silane, and the n layer was deposited for 2.5 minutes (150 seconds) using 50sccm of silane and 25sccm of 1% phosphine mixture. The RF power was kept constant at 40W but the substrate temperature was raised to 250C as it was expected to improve performance based on previous results. As so many deposition parameters changed at once after the turbo pump removal it was a reasonable time to also change the standard deposition temperature. The cell was 18-6-7-b and its IV characteristic is shown in Figure 4.14. Double diode fitting parameters are listed along with those for cells 4-6-7-a and 11-6-7-a (see Figure 4.13) in table 4.6.

By removing the turbo pump which raised system pressure by approximately a decade, deposition rates increased meaning that the deposition times for doped layers could be cut. The higher pressure seems to have solved the problem of Schottky barriers as it can be seen from Figure 4.14 that cell 18-6-7-b is a well behaved diode. The IV characteristic is much stiffer than previous results which infers that R_s and R_{shunt} have improved as a result of the higher pressure and deposition rate.

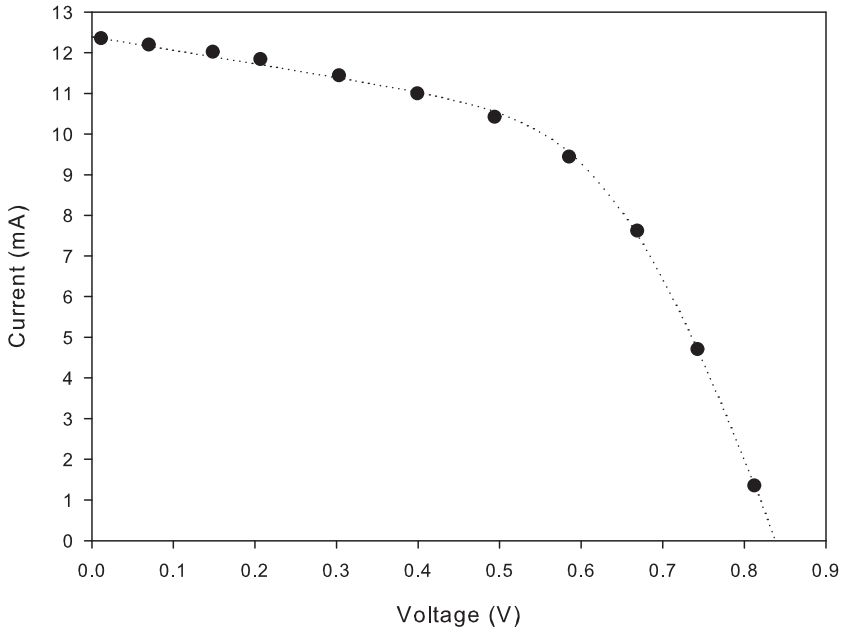

FIGURE 4.14: The effect of increased system pressure on a cell (18-6-7-b) with adjusted deposition times to compensate for the increased system pressure due to removal of the turbopump, a substrate temperature of 250C, and an RF power of 40W. The dotted line corresponds to the fitted double diode parameters (see table 4.6) after a 20Ω correction for R_{TCO}

4.7.2 Double diode fitting parameters

In order to quantify improvements over previous results, double diode fitting parameters were determined for cells 11-6-7-a and 18-6-7-b. Data for cell 4-6-7-a is reproduced from table 4.5.

Cell	4-6-7-a	11-6-7-a	18-6-7-b
V_{oc} (V)	0.81	0.78	0.83
I_{sc} (mA)	13.4	8.5	12.4
R_s (Ω)	25.2	17.6	14.26
R_{shunt} (Ω)	122	137	287
J_{02} (A)	$1.38\text{x}10^{-9}$	$1.26\text{x}10^{-9}$	$7.30\text{x}10^{-10}$
FF	0.40	0.40	0.54
η (%)	4.38	2.57	5.59

TABLE 4.6: Double diode fitting parameters for cells 4-6-7-a, 11-6-7-a and 18-6-7-b

Cell 18-6-7-b has benefited from the adjusted deposition times, and is 5.59% efficient compared to the previous best efficiency of 4.86% (cell 5-6-7-b, see section 4.6). Improvements are seen in all double diode parameters but the most significant is the increase in R_{shunt}, which more than doubled from 137Ω to 287Ω between cells 11-6-7-a and 18-6-7-b. This change is mirrored in the decrease of J_{02} which indicates a reduced recombination current related to a-Si:H of superior electronic quality due to the changes to system

pressure and substrate temperature. The reduction in doped layer thickness will also have contributed to the change in J_{02}, and evidence for the reduction in layer thickness is seen in the decrease of R_s.

These improvements in cell efficiency were a significant result considering that they were a result of a relatively ad-hoc approach to optimisation. It is also interesting to note that any improvement that was gained by using the turbo pump to provide a cleaner process via a lower base pressure was outweighed by the quality of a-Si:H that was produced after it was removed and the process pressure increased. Perhaps the best aspects of both approaches could have been combined if higher flow rates of silane had been possible.

4.8 Optimising the n layer thickness

So far most attention has been paid to verifying and optimising the performance of intrinsic material and p layer effect on cell performance by photoconductivity and IV measurements respectively. The n layer has been neglected in favour of this work because it has a less significant effect on cell performance. As long as an n layer is sufficiently doped to support an electric field across the intrinsic region, cell performance will be reasonable if all other regions are accounted for. However photo-generated electrons must still cross the n layer to reach an external circuit and contribute to current flow, therefore the n layer should ideally be as thin as possible to minimize recombination whilst still containing enough active dopant to generate V_{bi}. With this in mind the n layer deposition time was altered from 150 seconds (cell 18-6-7-b, see section 4.7.1) to 120 seconds (cell 20-6-7-b), and 90 seconds (cell 19-6-7-a). The IV characteristics of these cells are shown in Figure 4.15.

The advantage of an optimised n layer thickness can be clearly seen in Figure 4.15. The 150 second deposition resulted in a n layer that was too thick and I_{sc} suffered because of excessive recombination. The cell with a 90 second n layer has a Schottky barrier due to inadequate doping at the aluminium/a-Si:H contact interface, current loss due to the barrier can be seen. The lack of doping can be explained by the method in which the n layer is produced. The phosphine gas MFC is opened after the intrinsic layer deposition has finished, but a certain amount of time is then required for the phosphine partial pressure to achieve equilibrium with the other gas partial pressures in the reactor. If the n layer deposition is stopped before this equilibrium is achieved then doping efficiency will suffer. Cell 20-6-7-b strikes a balance between reaching a doping level that can create an Ohmic contact with the aluminium back contact and sustain a field across the device, with minimal majority carrier recombination in the n layer.

The double diode fitting parameters for cells 18-6-7-b, 20-6-7-b, and 19-6-7-a are given in table 4.7. Cell 20-6-7-b was 7.35% efficient and was the best performing cell to date.

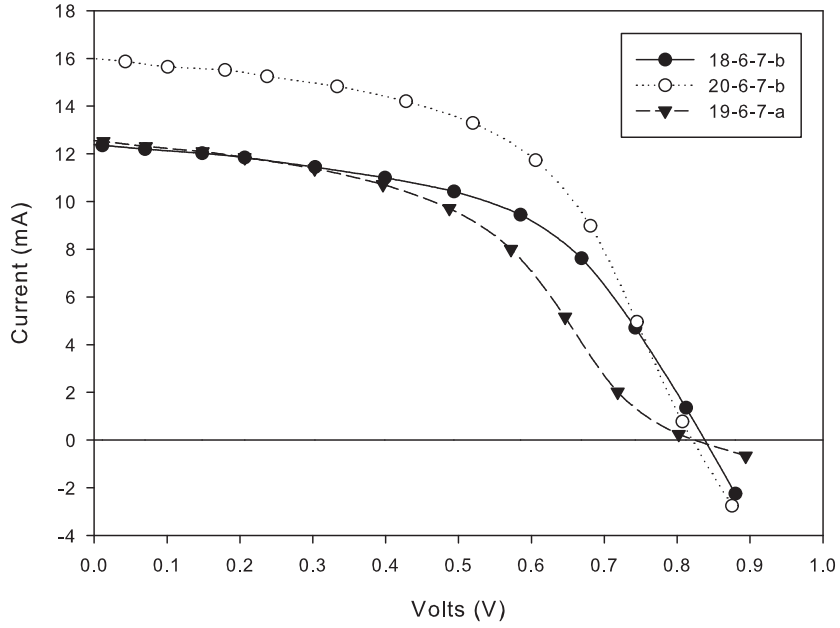

FIGURE 4.15: The effect of changing the n layer deposition time from 150 seconds (18-6-7-b), to 120 seconds (20-6-7-b) and 90 seconds (19-6-7-a) using a substrate temperature of 250C and 40W of RF power, approximate n layer thicknesses are noted. Note the Schottky barrier produced with the shortest n layer deposition time and that V_{oc} increases with n layer deposition time. The dotted lines correspond to the fitted double diode parameters (see table 4.7) after a 20Ω correction for R_{TCO}. The last two data points for cell 19-6-7-b were not included in fitting due to the presence of a Schottkey barrier

The rise in efficiency is linked to the increase in I_{sc} given that the FF was almost the same for every cell. The longest n layer deposition time did marginally increase V_{oc} but at the cost of a greater recombination current and associated drop in I_{sc}.

Cell	18-6-7-b	20-6-7-b	19-6-7-a
V_{oc} (V)	0.83	0.82	0.76
I_{sc} (mA)	12.4	16.0	12.5
R_s (Ω)	14.26	14.12	15.53
R_{shunt} (Ω)	287	239	255
J_{02} (A)	7.30×10^{-10}	1.01×10^{-10}	3.49×10^{-9}
FF	0.54	0.55	0.51
η (%)	5.59	7.35	4.82

TABLE 4.7: Double diode fitting parameters for cells 18-6-7-b, 20-6-7-b and 19-6-7-a

4.8.1 Removing the Schottky barrier

To test the theory of a minimum n layer deposition time being required to ensure that an Ohmic contact was achieved, cell 19-6-7-a was re-fabricated. This time a 5 minute plasma break and gas flush was inserted between the intrinsic and n layer in order to

allow all gas partial pressures in the PECVD reactor time to stabilise before deposition re-commenced. This cell was 20-6-7-a and its IV characteristic is shown with cell 19-6-7-a (no plasma break and gas flush) in Figure 4.16.

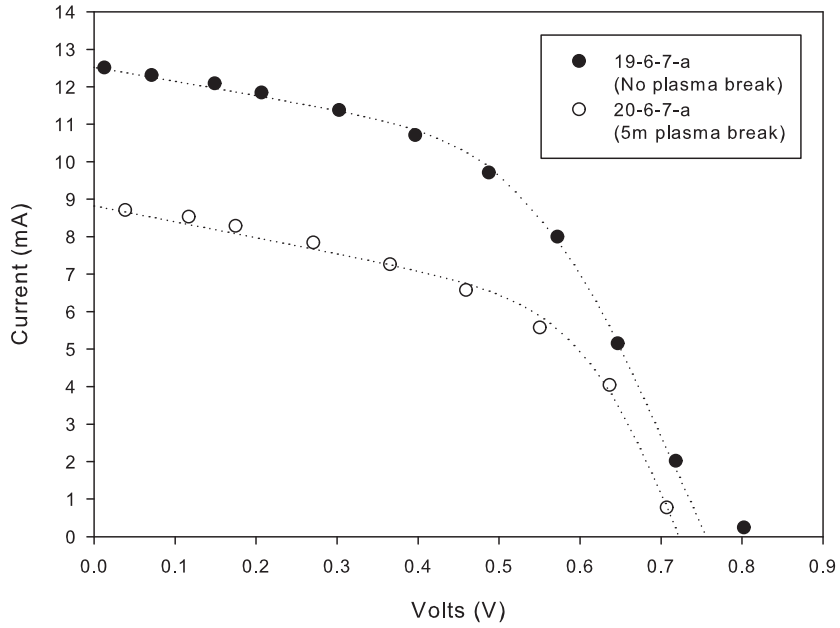

FIGURE 4.16: Removing a Schottky diode (19-6-7-a) by inserting a plasma break before a 90 second n layer deposition (20-6-7-a). The dotted lines correspond to the fitted double diode parameters after a 20Ω correction for R_{TCO}

Allowing the phosphine partial pressure to reach equilibrium did remove the Schottky barrier, but it also degraded I_{sc} and consequently V_{oc}. The reason for loss of current is not apparent, especially as the FF and parasitic resistances do not vary appreciably between the curves. It seems apparent that the decrease in I_{sc} should be linked to a change in the interface between the intrinsic and n layer, or the properties of the n layer alone. An increase in defect density due to a worsened interface as a result of the plasma break should alter R_{shunt} however, and this is not seen.

The decrease in I_{sc} is similar in magnitude to that seen in Figure 4.15, when the n layer thickness is increased by ≈10nm. The change in IV characteristic is similar to what was observed when the plasma break was included in deposition, and so it is reasonable to conclude that the effective n layer thickness has increased due to allowing the phosphine partial pressure to stabilise. This should be accounted for in future deposition processes that include gas flushes.

4.9 Changing the cell substrate

All cells reported on so far in this report were deposited onto standard 2mm TCO covered soda lime glass. No technical details were available for the glass and as such it was decided to replace it with a commercially available glass substrate. The replacement chosen was 1mm thick Asahi type-U tin oxide coated glass and the transmission spectra is shown in Figure 4.17 with the transmission spectra of the previous substrate.

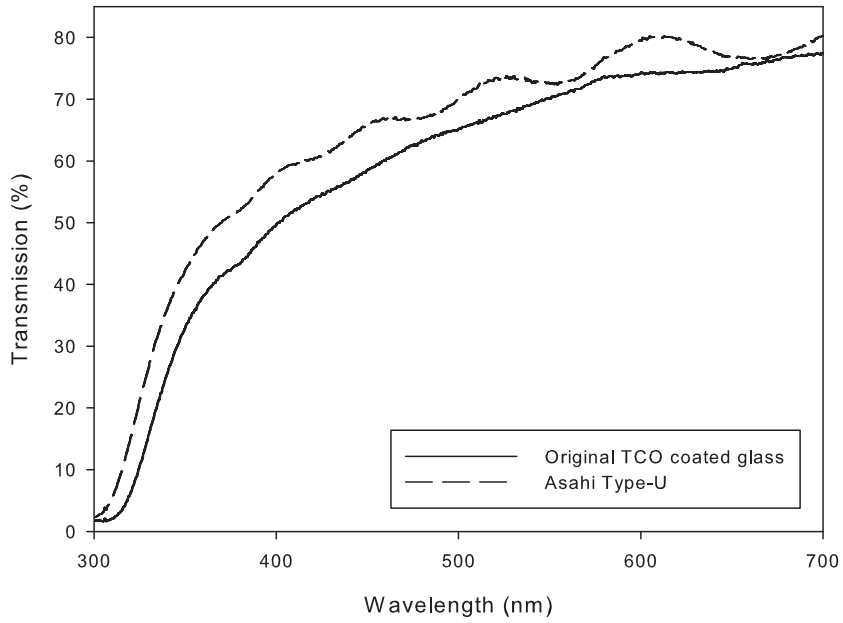

FIGURE 4.17: Transmission from 200-700nm of TCO coated Asahi type-U glass and standard TCO coated soda lime glass

The Asahi glass is 6-8% more transmissive across the region of the spectrum that corresponds to the absorption region of a-Si:H. Interference ripples are visible in the transmission spectra for the Asahi U-type glass which means that the TCO layer on it is thicker than on the original substrates. The sheet resistance of the samples was similar, 9.2Ω/□ for the Asahi U-type compared to 8.1Ω/□ for the original TCO (measured using a Jandel 4 point probe).

The deposition procedure of cell 18-6-7-b (see section 4.7.1) was repeated using the new substrate to produce cell 25-6-7-a. The IV characteristics for both cells are shown in Figure 4.18, and the double diode fitting parameters for both cells are listed in table 4.8. The parasitic resistance associated with the TCO of cell 25-6-7-a was reduced to R_{TCO} =5Ω due to the drop in resistivity of the TCO compared to the original substrate.

The enhancement of available photocurrent due to the change in substrate transmission is reflected by the 2.7mA increase in I_{sc}. Fitting parameters relating to recombination are relatively unchanged but the drop in R_s is significant, especially considering that

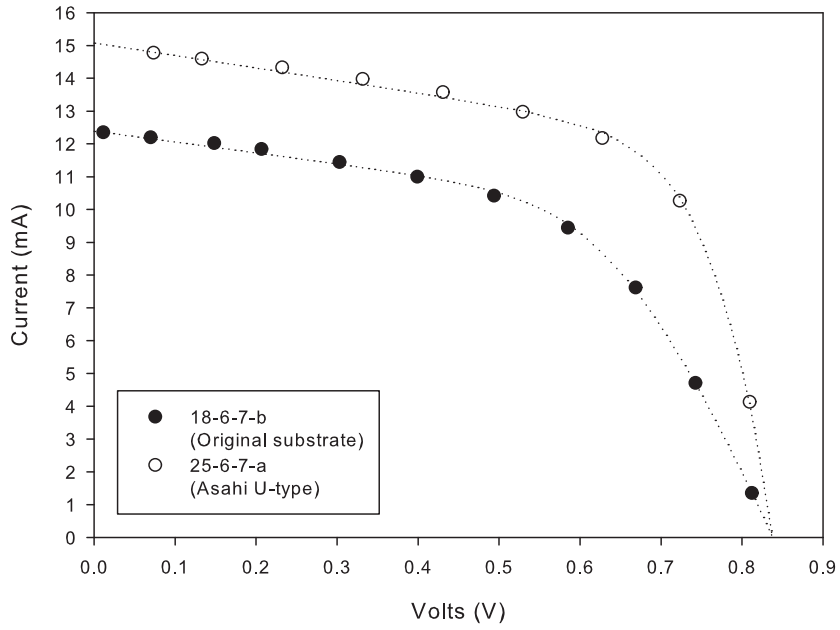

FIGURE 4.18: The effect of changing substrate to TCO coated Asahi type-U glass (25-6-7-a) from standard TCO coated soda lime glass (18-6-7-b). Use of the Asahi U-type improves I_{sc} and the collection of light forward voltages close to V_{oc}. The dotted lines correspond to the fitted double diode parameters after a 20Ω R_{TCO} correction for cell 18-6-7-b, and a 5Ω R_{TCO} correction for cell 25-6-7-a

Cell	18-6-7-b	25-6-7-a
V_{oc} (V)	0.84	0.84
I_{sc} (mA)	12.4	15.1
R_s (Ω)	14.26	2.36
R_{shunt} (Ω)	287	261
J_{02} (A)	$7.3\text{x}10^{-10}$	$9.43\text{x}10^{-10}$
FF	0.53	0.62
η (%)	5.59	7.89

TABLE 4.8: Double diode fitting parameters for cells 18-6-7-b, and 25-6-7-a

the R_{TCO} adjustment to the cell IV characteristic was lowered from 20Ω to 5Ω. The reduction of R_s is seen in the characteristic as a much more pronounced knee in the curve towards V_{oc} which is quantified by the rise in FF.

The physical explanation of R_s is the ability of a cell to provide a forward current (I_F) given a forward bias (V_F). As V_F increases, the voltage that defines the average electric field over the intrinsic cell region reduces by $V_{bi} - V_F$ and carrier velocities decrease to the point where the photo generated drift current is balanced equally by I_F in the opposite direction. A cell with low R_s is able to supply a greater forward current for a given forward bias and in the case of cell 25-6-7-a it is the enhancement in transmission of light that allows this to be possible. In particular short wavelength light generates carriers close to the interface of the p layer and intrinsic region where decreased carrier

velocities do not enhance recombination as significantly as if carriers were generated further into the intrinsic region.

It is also likely that the ability of the Asahi U-type glass to scatter light (haze) is optimised for a-Si:H cells whereas the previous substrates TCO coating was not. This would also enhance the absorption of photons closer to the p and intrinsic region interface producing the effect of lowering R_s as described above.

4.10 Decreasing R_{TCO} through cell layout

To decrease R_{TCO} associated with cells and IV characteristic measurement further, cell orientation was rotated by 90 degrees in order to arrange the longest edge of the cell top contact in parallel with the bottom contact. This should allow a potential fourfold reduction (20/5) in the TCO resistance as measured from the p layer to a contact located on the TCO. This change is possible as the TCO coating on the Asahi U-type glass was not laser scribed like previous substrates. The downside to the change is that only 3 cells have the lowest TCO resistance associated with them per the maximum substrate area that can be fitted onto the PECVD heater head instead of six previously. Figure 4.19 shows the reduced resistance layout compared to the previous arrangement of cells.

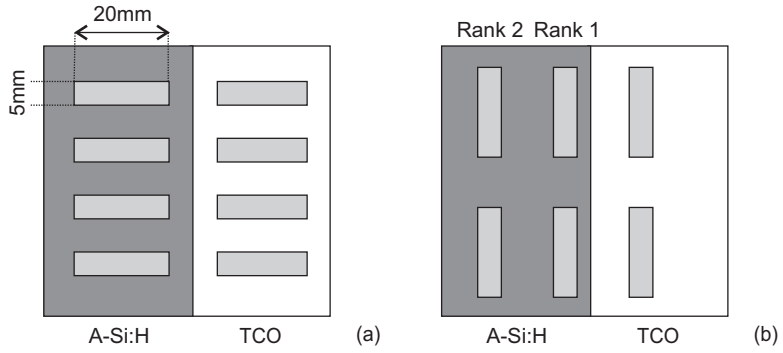

FIGURE 4.19: The new cell layout arrangement (b). Cells were rotated 90 degrees from the original layout (a) to reduce R_{TCO}, which corrections had to be made for when analysing IV characteristics

The process of cell 25-6-7-a (see section 4.18) was repeated using the new layout to create cell 26-6-7-a, and the IV characteristics of a first and second row device are shown compared to the original in Figure 4.20. The extracted double diode parameters are listed in table 4.9. An adjustment to the IV characteristics for R_{TCO} resistance is not performed in order to assess the effect on R_s by changing the cell rotation.

The expected decrease in R_s was not seen in either of the front 2 rows of cells on the rotated cell layout. The performance of the first row cell in fact worsened dramatically whilst the second row cell was very similar to the original in terms of V_{oc} and I_{sc}, R_s was expected to be high due to the far location of the cell.

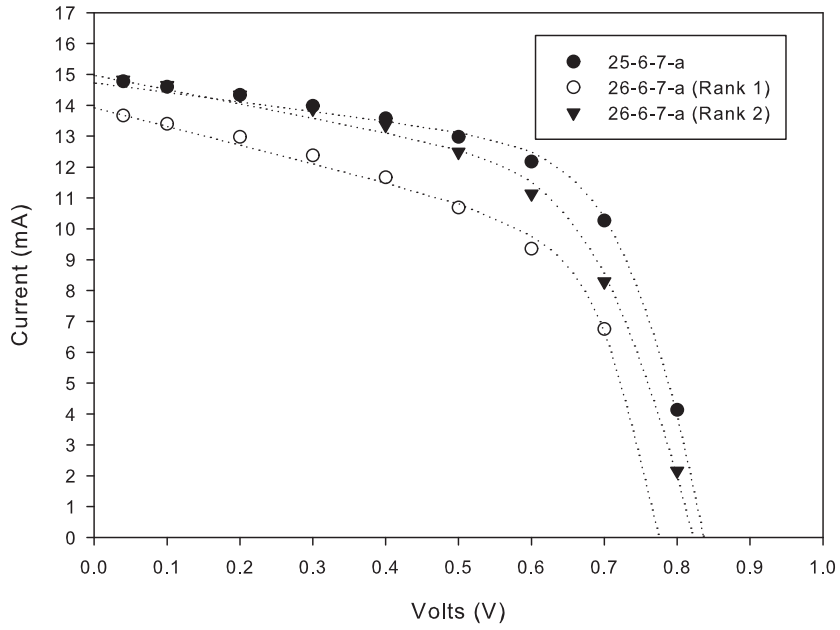

FIGURE 4.20: Cell IV characteristics before (25-6-7-a) and after (26-6-7-a) layout rotation with no adjustment for TCO resistance. The dotted lines correspond to the fitted double diode parameters with no correction for R_{TCO}

Cell	25-6-7-a	26-6-7-a (Row 1)	26-6-7-a (Row 2)
V_{oc} (V)	0.84	0.78	0.83
I_{sc} (mA)	15.1	13.9	15.0
R_s (Ω)	2.36	3.61	9.01
R_{shunt} (Ω)	261	161	217
J_{02} (A)	$9.43\text{x}10^{-10}$	$2.29\text{x}10^{-9}$	$1.11\text{x}10^{-9}$
FF	0.62	0.54	0.55
η (%)	7.89	5.85	6.85

TABLE 4.9: Double diode fitting parameters for cells 25-6-7-a, and 26-6-7-a. Data from multiple rows of sample 26-6-7 is presented (see Figure 4.19 as a guide to how the cell layout changed)

The poor performance of the front row rotated cell can be explained by considering that it was located too close to the edge of the deposited a-Si:H. The TCO was masked by a microscope slide during deposition meaning that the TCO immediately next to it was shadowed which resulting in a reduced deposition rate close to the masked area. This would create a thinner diode in parallel with a reduced area cell of the expected thickness if a cell was located too close to the a-Si:H edge. Thinner doped layers would have worsened V_{oc} whilst the missing intrinsic a-Si:H reduces available photo current as was observed. Figure 4.21 illustrates this situation. Cells are orientated such that their longest edge is in parallel with the a-Si:H edge after being rotated, therefore the effect is magnified comparison to the original orientation.

This problem was resolved by ensuring that sufficient distance between cells and the

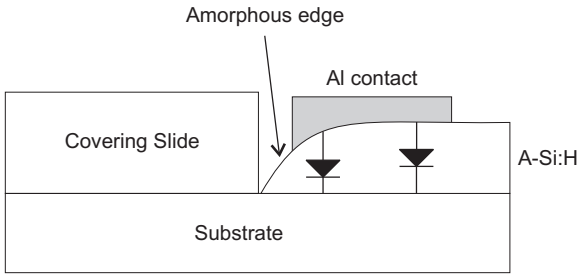

FIGURE 4.21: A cell located too close to the edge of a-Si:H deposition resulting in a partial area that is thinner than expected which worsens performance due to thinner doped layers and less light absorption

amorphous film edge was maintained. A gap of several mm was sufficient to avoid degradation of cell characteristics and was utilised in the production of all further cells. It was found that once this minimum distance was observed that a decrease in R_{TCO} for a given process was possible, but the improvement was not as significant as expected and often R_{TCO} was comparable to the original layout.

4.11 The fabrication of a μc-Si n layer

An attempt was made to fabricate a μc-Si n type emitter and apply it to the cell structure developed so far. The increased conductivity of μc-Si should decrease recombination in the layer, decrease R_s, and allow E_f to be bought closer to E_c due to a reduction in the density of localised gap states. This movement of E_f could increase V_{oc}, but the optical gap should also narrow as a result of the transition from a-Si:H to μc-Si which would imply the opposite effect.

The deposition process for this cell (11-7-7-b) was unchanged from that of cell 25-6-7-a (see section 4.18) with the exception of the n layer. To encourage μc-Si growth a combined flow of 3sccm silane, 1.5sccm 1% phosphine mixture, and 95.5sccm hydrogen was used. As the phosphine was pre-mixed with 99% hydrogen, a 3:97 flow rate ratio of silane to hydrogen was created. The surplus hydrogen scours weak bonds at the surface of the growing a-Si:H film promoting crystalline growth. This effect drastically slows the deposition rate of a-Si:H and to account for this the n layer deposition time was set to 10 minutes instead of the usual 2. The cell IV characteristic is shown in Figure 4.22 and the corresponding extracted double diode parameters are listed in table 4.10 along with the parameters of cell 25-6-7-a for comparision (the previous best cell, see section 4.18). The R_{TCO} correction employed was 5Ω.

Whilst the overall performance of cell 11-7-7-b is a slight improvement on that of cell 25-6-7-a, the double diode parameters are similar and the improvement in efficiency is relatively minor. The small rise in V_{oc}, R_s and R_{shunt} suggests that the n layer thickness may have slightly increased whilst the density of gap states has been reduced.

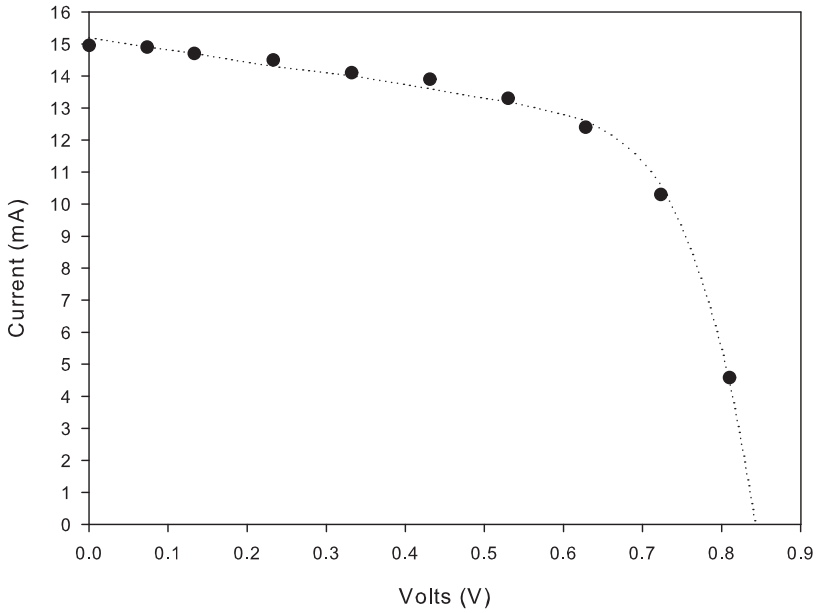

FIGURE 4.22: The IV characteristic of cell 11-7-7-b, the dotted line corresponds to the fitted double diode parameters after a 5Ω R_{TCO} correction

Cell	25-6-7-a	11-7-7-b
V_{oc} (V)	0.84	0.845
I_{sc} (mA)	15.1	15.2
R_s (Ω)	2.36	2.81
R_{shunt} (Ω)	261	276
J_{02} (A)	9.43×10^{-10}	8.69×10^{-10}
FF	0.62	0.62
η (%)	7.89	8.05

TABLE 4.10: Double diode fitting parameters for cells 25-6-7-a, and 11-7-7-b

The difference in I_{sc} cannot be relied upon as the error between the measured current data points and the double diode equation reaches a maximum of 3% near the knee of the curve and is similar to the difference in I_{sc} at $V = 0$. However the effect of this error on the calculated device efficiency is not significant.

Increasing the hydrogen:silane flow ratio made a small positive difference to cell performance, but no strong evidence of a transition to a μc-Si n layer is seen in the IV characteristic, and the process was found not to be reliable when repeated.

4.12 Inverting the cell structure to nip

As a final piece of work at 250C with complete cells, cell structure was inverted to nip from pin. This is a non-ideal configuration due to most carriers being generated close to the front of the cell by short wavelength light that a-Si:H responds well to. This leaves

holes to travel almost the entire cell including the now thickened p layer rear contact whilst electrons have a relatively short distance to traverse before they can contribute to an external current. The interface between the p layer and the aluminium contact will also lower V_{oc} due to band bending with the n type aluminium. The performance differences between pin and nip cells are of interest as any cell created on an opaque flexible substrate would have to be of the latter configuration.

The gas flows for all process stages were unaltered from cell 25-6-7-a (see section 4.18), only the layer deposition order was reversed to create the nip cells. Methane was initially used during the n layer deposition to investigate if n type a-SiC:H could be produced but it was found that it worsened cell performance. Contamination of the intrinsic layer with phosphine still present in the PECVD reactor after n layer deposition was initially a problem, but a 5 minute plasma break and gas flush was found to successfully remove any remaining phosphine before intrinsic deposition.

The best cells were created with a 1 minute n layer deposition and a 2 minute p layer deposition using 40W of RF power and a substrate temperature of 250C. Cells were prepared with a 20 minute intrinsic layer deposition (23-8-7-a) and a 15 minute (23-8-7-b) intrinsic layer deposition. The IV characteristics are shown in figure 4.23, and the extracted cell parameters are listed in table 4.11.

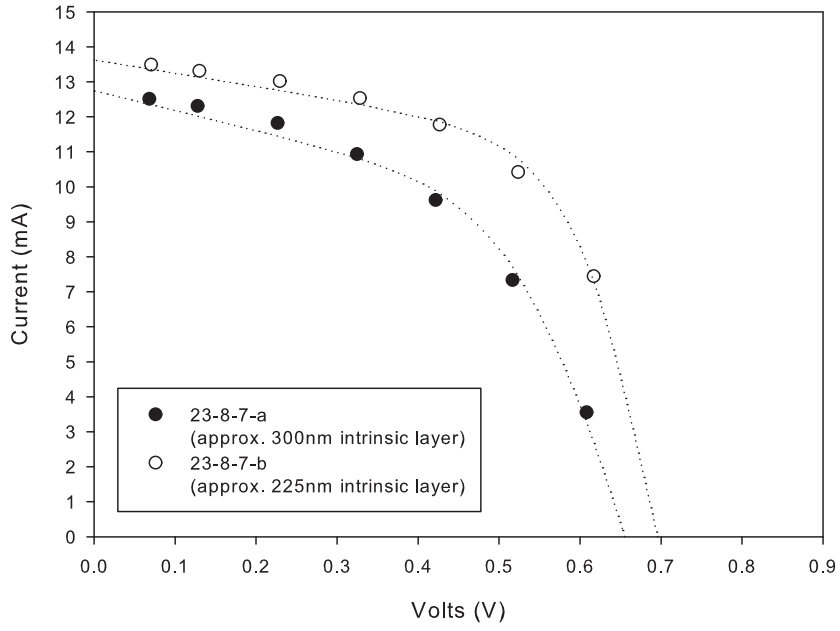

FIGURE 4.23: The effect of thinning the intrinsic layer of an inverted nip cell structure on glass with a substrate temperature of 250C and 40W of RF power, the dotted lines correspond to the fitted double diode parameters after a 5Ω R_{TCO} correction. Note how the thinner cell exhibits an improved FF and efficiency due to enhanced collection of optically generated carriers

Cell	23-8-7-a	23-8-7-b
V_{oc} (V)	0.66	0.69
I_{sc} (mA)	12.5	13.4
R_s (Ω)	9	1.36
R_{shunt} (Ω)	213	264
J_{02} (A)	2.80x10^{-8}	1.46x10^{-8}
FF	0.52	0.61
η (%)	4.31	5.77

TABLE 4.11: Double diode fitting parameters for cells 23-8-7-a and 23-8-7-b

The total photo-current collected at $V = 0$ is greater for the thinner cell, which implies that even without an applied bias more many generated carriers are recombining in the thicker cell. The increase in I_{sc} is also the cause of the improvement in Voc.

The dominant effect on the IV characteristic of cell 23-8-7-a is seen when a forward bias is applied, the electric field strength over the intrinsic region decreases as the bias is applied and the collected photo-current drops at the same time that the opposite diffusion current begins to rise. This is the cause of the high R_s observed in cell 23-8-7-a. By thinning the intrinsic layer of cell 23-8-7-b photo-generated carriers can still be collected effectively with a forward bias and near V_{oc}, the high value of the FF reflects this. Cell 23-8-7-b is 5.77% efficient which is significant considering the lack of optimisation.

4.13 Chapter summary

The work reported in this chapter can be concluded by stating that the PECVD reactor was found to be suitable for the deposition of PV grade a-Si:H as demonstrated by the photo-conductivities that were measured, and the functional cells that were fabricated. From the values of V_{oc} that were observed it can be concluded that the doping levels of n and p type a-Si:H were found to be consistent with previously reported literature [24] along with I_{sc} and η.

The values for efficiency obtained cannot be totally verified as compliant to the AM1.5 test standard, but again they agree with previously reported values for single junction pin homojunction a-Si:H cells. In defence of this it is most useful to consider cell efficiency measurements relative to each other when analysing the effect of varying a process parameter. The best measured efficiency was 8.05% for a pin structure cell and 5.77% for an nip structure cell which is a respectable result for 3 months of work and a solid foundation for future work with more exotic substrates.

Chapter 5

Optical and electrical properties of amorphous films grown at 200C

The properties of individual homogeneous layers prepared by PECVD are of interest as they can provide an insight into how cells can be optimised step by step. By maximising the electrical and optical performance of each cell component individually, the parameter space for complete cell optimisation is reduced and a reliable starting point is obtained. Homogeneous thin film analysis also allows a variation in process parameters to be closely linked with any resulting changes in measured layer properties.

The most efficient cells were grown using a substrate temperature of 250C in chapter 4, and so it was decided to study films of a-Si:H deposited at the lower temperature of 200C. Whilst this is not considered a low substrate temperature from the point of view of current research (Hishikawa et al. [93] deposited PV grade a-Si:H at substrate temperatures of less than 100C in 1991), it was felt that trying to obtain functional cells at appreciably lower temperatures whilst migrating the process to flexible substrates would not be possible in the limited time available for practical work. 200C is generally regarded as below the optimum substrate temperature for a-Si:H cell fabrication and it is hoped that the techniques employed in this chapter will be used again in the future to characterise a-Si:H deposited at more challenging substrate temperatures.

Before any a-Si:H was deposited, the gas delivery inside the PECVD reactor was altered. Previously the gas entry point into the reactor was a valve at the front or rear of the quartz tube. (See Figure 3.1 for more detail). A gas distribution ring was attached to the front gas delivery point and sited such that feed gases were inserted directly into the plasma in front of the mounted substrate from multiple angles. It was expected that this would provide a more even distribution of neutral species for film growth than a single point of entry.

5.1 Characterisation of intrinsic a-Si:H films

Intrinsic films of a-Si:H were grown at differing substrate temperatures, RF powers, and silane flow rates in order to gain insight into how these growth conditions affected the optical and electronic properties of the material. Films were produced at 200C and 250C using 50W and 80W of RF power. 3 silane flow rates (25, 50, 75 sccm) were employed at 200C and no extra hydrogen dilution was used for any of the depositions. The substrates were standard microscope slides that were cleaned with IPA and dusted with a nitrogen flow before use. Figure 5.1 shows how 2 slides were positioned on the heater head per run.

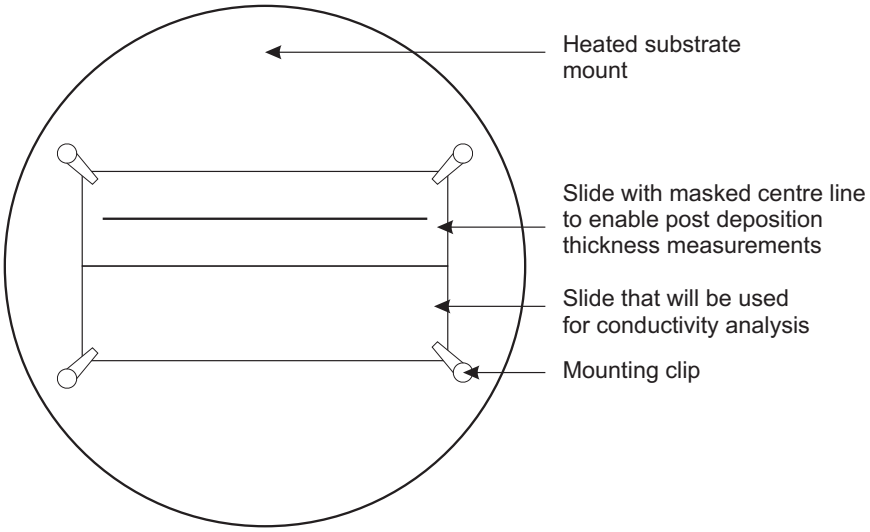

FIGURE 5.1: The arrangement of 2 substrate microscope slides on the PECVD heater head. Use of multiple slides allows for optical and electrical characterisation of samples without re-use

Films were characterised using conductivity measurements as a function of temperature, and ellipsometry in parallel with a transmission spectrum taken at the center point of each sample. Layer thickness was measured every 5mm along the center line of the glass slide from the left hand edge using a Talystep stylus profiler to evaluate uniformity of deposition. The thickness reported from this technique is the median as a mean average would be affected by outliers. More in depth details of these techniques can be found in chapter 3.

Conductivity measurements were performed from 150-100C in 10C cool down steps, with data collected at every step point for 5 minutes to provide redundancy against error. As also mentioned in chapter 3 a region of increased conductivity was observed above 125C for every sample. Conductivity analysis is therefore separated into a region above and below this temperature for each sample. Ellipsometry is performed primarily to obtain a figure for E_g, but also provides information on sample thickness which can be correlated with the measurements obtained with the Talystep. The model used in ellipsometry consisted of an absorbing thin film with a thin native oxide on a transparent

glass substrate. Light absorption in the thin film was described using a single Cody-Lorentz oscillator which was chosen for its ability to describe sub band gap absorption with an Urbach energy term.

7 intrinsic films were grown using the conditions shown in table 5.1. The results of the conductivity analysis are listed in table 5.2, and the parameters of the Cody-Lorentz oscillator user to describe absorption in the a-Si:H film are listed in table 5.3.

Sample	Ts (C)	RF Power (W)	Silane Flow (sccm)
4-12-7-a	200	50	25
4-12-7-b	200	50	50
4-12-7-c	200	50	75
11-12-7-a	200	80	50
11-12-7-b	250	80	50
11-12-7-c	250	50	50
11-12-7-d	200	80	25

TABLE 5.1: Growth conditions for a series of intrinsic a-Si:H samples

Samples 4-12-7-c and 11-12-7-a were not characterised as deposition of a-Si:H did not occur. An loose powder was found to be distributed over the substrates when the PECVD reactor was unloaded indicating that growth of a-Si:H did not even reach the stage of nucleation. The lack of deposition can be explained by a depletion of neutral species present in the plasma as growth conditions promoted the formation of polysilane chains (the dust) instead.

Dust formation was only a problem at the lower substrate temperature of 200C in combination with either a high silane flow rate or RF power. This suggests that the possible process window narrows with respect to these conditions as the substrate temperature is decreased. Previous work showed that a decrease in the photo-conductivity of an a-Si:H film deposited at a reduced substrate temperature could be reversed by employing a larger RF power (see section 4.1), the formation of polysilanes here indicates that there are limits to this restoration process.

The model used to fit ellipsometry data consisted of an a-Si:H layer on a glass substrate and covered with a native oxide. Absorption was described with a single Cody-Lorentz oscillator which contains terms for E_u and E_g amongst others. Backside reflections from the bottom of the glass substrate were accounted for as depolarisation data indicated that this was an issue at wavelengths above the optical gap of a-Si:H. It was found that allowing the refractive index of the a-Si:H to vary linearly in 5 equally spaced steps improved fitting accuracy at longer wavelengths and the % of variation from the lowest to highest index is listed as the inhomogenity of a film.

	100-125C			125-150C			
Sample	σ_{RT} (Ω^{-1}cm^{-1})	σ_0 (Ω^{-1}cm^{-1})	E_{a1} (eV)	σ_{RT} (Ω^{-1}cm^{-1})	σ_0 (Ω^{-1}cm^{-1})	E_{a2} (eV)	ΔE_a (eV)
4-12-7-a	2.01x10^{-6}	2.05	-0.358	5.58x10^{-7}	8.84	-0.489	0.131
4-12-7-b	1.05x10^{-5}	1.74	-0.311	4.44x10^{-6}	26.7	-0.404	0.093
11-12-7-b	1.40x10^{-5}	0.55	-0.273	7.38x10^{-6}	5.87	-0.357	0.084
11-12-7-c	5.26x10^{-6}	4.75	-0.355	2.67x10^{-6}	33.77	-0.423	0.068
11-12-7-d	2.12x10^{-6}	1.04	-0.339	9.40x10^{-7}	11.36	-0.422	0.083

TABLE 5.2: Results from conductivity analysis of the intrinsic a-Si:H films prepared using the growth conditions listed in table 5.1. Dividing the analysis into two separate regions of temperature allows an approximation of the gap state width ($\Delta E_a = E_{a2} - E_{a1}$), and the determination of the contribution of each current path to the conductivity at room temperature

Sample	E_g (eV)	E_u (eV)	Tox (nm)	Thickness (nm)	Inhomogeneity (%)	MSE
4-12-7-a	1.75	0.071	9.59	248.87	0.83	11.46
4-12-7-b	1.77	0.083	7.52	194.80	1.29	4.13
11-12-7-b	1.66	0.071	8.90	383.69	2.45	8.17
11-12-7-c	1.71	0.075	7.22	258.83	2.80	7.22
11-12-7-d	1.83	0.058	11.0	394.67	-0.56	16.19

TABLE 5.3: Optical parameters as determined by ellipsometry for the a-Si:H films listed in table 5.1. Tox is the thickness of the native oxide present on the a-Si:H film

5.1.1 Interpretation of results

Although the limited sample size makes trends in measured properties with respect to growth conditions difficult to identify with confidence, there appears to be a correlation between E_g and the substrate temperature. Generally a higher substrate temperature results in a decreased value for E_g and better electronic properties.

This effect has been observed previously [94, 95, 96] and has been attributed to a shift in hydrogen content with increasing substrate temperature [15]. Published results agree with measured values of $E_g \approx 1.75eV$ for a substrate temperature of 200C, decreasing towards $E_g \approx 1.7eV$ as the substrate temperature is increased to 250C. An optical gap of 1.7eV enables strong absorption of wavelengths under 730nm. By contrast a-Si:H with an optical gap of 1.75eV (typical of the films deposited at 200C) will strongly absorb wavelengths under 709nm.

E_{a2} for all the films is sufficiently large ($> 0.35eV$) to suggest that they are intrinsic with a slight n type characteristic which is typical of a-Si:H. The difference between the activation energies (ΔE_a) is important as it provides an estimate of how far the localised states extend into the forbidden gap, which in turn affects carrier mobility via an average trap depth and therefore cell performance. This measurement is an approximation of E_u and is a parameter that can be obtained through optical and electrical analysis.

The values of E_u obtained by both types of analysis are close in terms of magnitude, but differ on a per sample basis. This is to be expected due to the differences in technique and the volume of material that contributes to each measurement, but the similarity of the values obtained lends credence to the choice of the Cody-Lorentz oscillator to model absorption. It is also important to remember that whilst the optical gap of a film may be similar in magnitude to the mobility gap, the two terms are not directly equivalent and activation energies obtained by electrical analysis will be influenced more by the mobility gap and vice versa for optical measurements. Figure 5.2 shows the absorption coefficient as a function of wavelength for all the films, where the effect of E_u can be seen as sub gap absorption beyond the values for E_g listed in table 5.3.

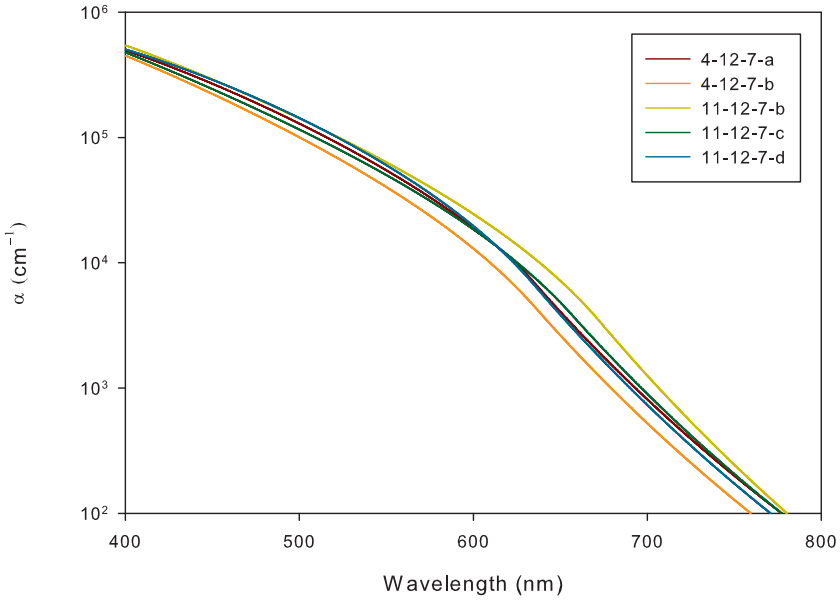

FIGURE 5.2: $\alpha(\lambda)$ measured using ellipsometry for the intrinsic amorphous films listed in table 5.1. Note the sub optical gap absorption that is a result of localised states extending into the forbidden gap, a feature common to amorphous materials which is modelled by an Urbach energy term (E_u)

The most conductive film is 11-12-7-c. This is unsurprising as it was produced using conditions similar to the intrinsic layer of the most efficient cell previously reported on. (See chapter 4, section 4.11). σ_0 is greater than all other samples in either region of conductivity and σ_{RT} is approximately 2 decades less than an estimated typical intrinsic photo-conductivity (see Figure 4.2). The importance of each conduction path can be assessed by comparing the ratio between both values of σ_{RT} , and it is observed that for film 11-12-7-c each region makes an approximately equal contribution at room temperature.

The value for ΔE_a was the smallest of all the films, suggesting a thinner band of localised states which would also agree with a shift to a more ordered microstructure where mono hydride bonding is favoured. This agrees with the high measured value for conductivity.

In tandem with the narrowing of the optical gap, this shift in micro structure illustrates why higher substrate temperatures are preferred when depositing a-Si:H by PECVD to the point where hydrogen can no longer be incorporated effectively into a growing film. Increasing the RF power to 80W whilst maintaining the substrate temperature and silane flow rate (11-12-7-b) resulted in the lowest optical gap that was measured (1.685eV), correspondingly the absorption coefficient is the largest over all wavelengths (see Figure 5.2), however the conductivity was the worst observed of any film.

Lowering the substrate temperature to 200C worsens the conductivity of all films, whilst the absorption coefficient is found to be similar to the higher temperature film 11-12-7-c over 400-800nm. The one exception is film 4-12-7-b (50W, 50sccm) for which σ_0 reduces only slightly when compared to 11-12-7-c over both regions of conduction, whilst the absorption coefficient worsens significantly from 400-800nm. This film has the largest optical gap of all samples (1.765 eV), and the optical performance can be contrasted with film 11-12-7-b (lowest optical gap, greatest absorption).

The two best performing films deposited at 200C are 4-12-7-a and 11-12-7-d, both grown using a 25 sccm silane flow rate with 50W and 80W of RF power respectively. Measured conductivity is similar in each region of temperature, but a significant difference is that $\Delta E_a = 0.131$eV for film 4-12-7-a, and $\Delta E_a = 0.083$eV for film 11-12-7-d. This would imply that the width of localised states almost doubles, but it also pushes E_{a2} to 0.489eV for film 4-12-7-a which makes it the most intrinsic film produced. The performance of these lower temperature films again illustrates the compromises that can be made between substrate temperature, RF power, and silane flow rate in order to maximise desirable properties.

Film thickness measured with a Talystep at 10mm intervals along the glass slide substrate is shown in Figure 5.3. Note the good agreement between the thicknesses measured at 35mm (slide centre) and the thickness determined by ellipsometry listed in table 5.3, data for ellipsometry was measured centrally for each sample.

Several trends are evident in the thickness data. Firstly RF power appears to be important when considering deposition rate. Films 11-12-7-b and 11-12-7-d were grown with 80W of RF power, all other films used 50W. The deposition rate for these samples exceeds that of all others quite significantly. An increase in the silane flow rate at a constant RF power does not have the same effect, and can even worsen the deposition rate (see 4-12-7-b). This can be explained by RF power being the rate limiting factor for the disassociation of silane into neutral species that can contribute to a growing film.

Secondly there is a decrease in thickness towards the right edge of the substrate that is observed with almost every film. This is because the right side of the substrate is located closest to the pump valve and so the plasma is depleted more of species on that side of the reactor. Film 4-12-7-a seems to avoid this effect, possibly due to its relatively low rate of deposition and silane flow rate. Between this and its acceptable optical and

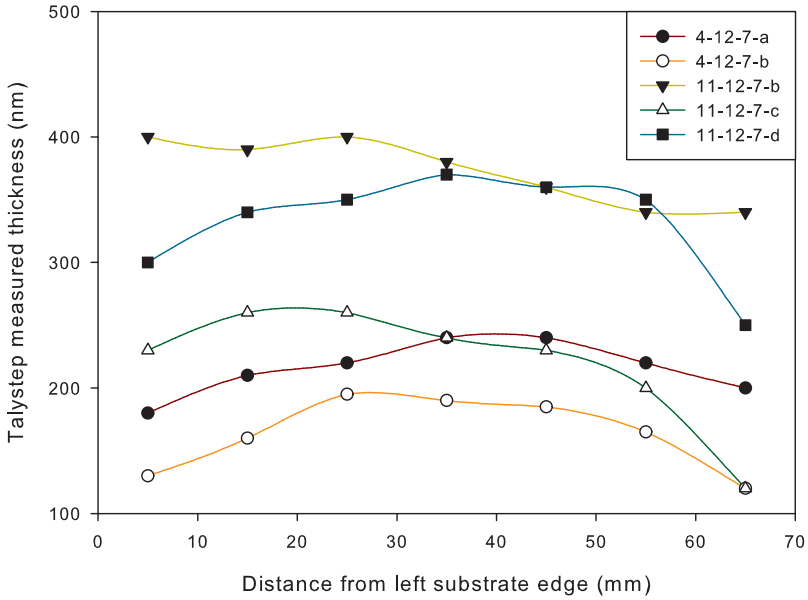

FIGURE 5.3: Thickness measured as a function of distance across the substrate for the intrinsic a-Si:H films prepared using the growth conditions listed in table 5.1. Measured thickness can be considered accurate to ±10nm if less than 300nm, and ±20nm if greater. The substrate was mounted on the PECVD head using the arrangement shown in Figure 5.1

electronic properties it appears a good choice for cell fabrication whilst attempting to keep the active thickness variation as low as possible over multiple cells.

5.2 Characterisation of doped a-Si:H films

The work with intrinsic samples was extended to include a series of films prepared using a range of doping ratios. It was already known that effective doping at 250C was possible due to the fabrication of well functioning cells (see chapter 4), but the shift in bulk Fermi level and other material properties were never quantified. Rather optimal dopant flows were discovered through a process of trial and error.

Growth conditions previously used for sample 4-12-7-a (200C, 50W RF power) were modified to incorporate a flow of 1% diborane mixture or 1% phosphine mixture. Table 5.4 lists all the films that were created along with the corresponding doping ratio. A 1% diborane mixture flow of more than 60 sccm produced dust in the reactor due to the process pressure.

The doping ratio is given by equation (5.1), the factor of 100 is included because dopant gases were diluted to 1% in hydrogen.

Sample	Silane Flow (sccm)	1% Phosphine Mixture Flow (sccm)	1% Diborane Mixture Flow (sccm)	Doping ratio
16-1-8-a	25	0	5	0.002
16-2-8-b	25	0	15	0.006
21-1-8-a	25	0	30	0.012
21-1-8-b	25	0	45	0.018
21-1-8-c	25	0	60	0.024
29-1-8-b	25	5	0	0.002
31-1-8-a	25	10	0	0.004
29-1-8-b	25	20	0	0.008
31-1-8-b	25	40	0	0.016

TABLE 5.4: Growth conditions for a series of doped a-Si:H samples produced at 200C with 50W of RF power

$$\text{Ratio} = \frac{\text{Flow}_{(\text{Dopant})}}{100 \times \text{Flow}_{(\text{Silane})}} \tag{5.1}$$

The films were characterised using ellipsometry and dark conductivity measurements from 100C to 150C. Dark conductivity analysis was split into two regions of temperature as before. This is not so necessary for analysis of films where effective doping has taken place because the shift of the bulk Fermi energy should marginalise the localised states contribution to conductivity when compared to the extended states at the temperatures of interest. If this is the case then the values for σ_{RT} , σ_0 and especially E_a should agree with each other across both temperature regions. (The data can be interpreted with one straight line as opposed to two). Where a difference in these measurements is observed, a film is likely to be still near intrinsic. Table 5.5 lists the results of the dark conductivity analysis.

	100-125C			125-150C			
Sample	σ_{RT} (Ω^{-1}cm^{-1})	σ_0 (Ω^{-1}cm^{-1})	E_{a1} (eV)	σ_{RT} (Ω^{-1}cm^{-1})	σ_0 (Ω^{-1}cm^{-1})	E_{a2} (eV)	ΔE_a (eV)
16-1-8-a	$2.60\text{x}10^{-7}$	188	-0.480	$1.60\text{x}10^{-7}$	580	-0.510	0.03
16-1-8-b	$8.40\text{x}10^{-7}$	586	-0.474	$7.30\text{x}10^{-7}$	808	-0.492	0.02
21-1-8-a	$3.23\text{x}10^{-5}$	478	-0.428	$2.91\text{x}10^{-5}$	667	-0.438	0.01
21-1-8-b	$5.41\text{x}10^{-5}$	401	-0.401	$4.99\text{x}10^{-5}$	527	-0.418	0.017
21-1-8-c	$6.89\text{x}10^{-5}$	386	-0.402	$6.60\text{x}10^{-5}$	447	-0.407	0.005
29-1-8-b	$1.54\text{x}10^{-4}$	50.1	-0.329	$1.28\text{x}10^{-4}$	90.1	-0.349	0.02
31-1-8-a	$2.02\text{x}10^{-4}$	25.8	-0.304	$1.52\text{x}10^{-4}$	62.7	-0.334	0.03
29-1-8-c	$3.23\text{x}10^{-4}$	57.7	-0.313	$2.91\text{x}10^{-4}$	82.4	-0.324	0.011
31-1-8-b	$2.08\text{x}10^{-4}$	62	-0.326	$1.73\text{x}10^{-4}$	109	-0.346	0.02

TABLE 5.5: Results from conductivity analysis of the doped a-Si:H films prepared using the growth conditions listed in table 5.4

As expected the values of ΔE_a are low and there is little variation between the analysis regions for any film. Especially for the heavily doped films, ΔE_a could be considered an

indication of the error involved in the determination of E_a.

Doping appears to have been successful due to the direct shift in σ_{RT} of 2 decades for diborane doped films, and 3 decades for phosphine. E_F also moves significantly which is considered to be a direct indication of substitutional doping. Phosphine is the more effective dopant, a much smaller doping ratio than diborane is required to significantly alter dark conductivity. An interesting point of note is that while σ_{RT} is a decade larger for n type films compared to p type, this relationship is reversed for σ_0 indicating a greater potential conductivity with increasing temperature for p type a-Si:H. This is perhaps due to the band tail of states found above E_v being wider than the band beneath E_c.

Figure 5.4 shows the change in σ_{RT} and E_a as a function of the doping ratio for both n and p type films. The correlation between the 2 measurements is immediately obvious, although the interpretation of E_a as $E_c - E_f$ or $E_f - E_v$ is sometimes less so. For a highly conductive n or p type film the choice is clear, but for example the value of σ_{RT} obtained for the two lowest doping ratios of diborane does not indicate well doped a-Si:H. In this case it is likely that E_f still lies closer to E_c than E_v. (The small amount of p type doping has possibly compensated the naturally slightly n type state of the a-Si:H). The significant shift in σ_{RT} for the next doping ratio step in the series implies that E_a should be then considered as relative to E_v. Bringing E_f to 0.4eV from E_v and 0.3eV from E_c is typical of measurements that have been previously reported for a-Si:H [24, 97].

The optimum doping ratio is determined by the smallest value of E_a located after the peak of the sharp rise in conductivity. Increasing the doping ratio beyond this point is not beneficial. This can be observed in Figure 5.4 when the phosphine doping ratio is raised to 0.016, E_a and σ_{RT} are reduced from their previous optimum values. The most effective doping is observed at a 1% diborane mixture flow of 60sccm and a 1% phosphine mixture flow slightly greater then 20sccm. These flow rates are extremely similar to those determined by trial and error whilst working with a substrate temperature of 250C (see sections 4.5.3 and 4.8), which implies that there is no significant change in the amount of active dopant incorporated into the growing a-Si:H film between these temperatures.

5.2.1 The optical gap and band structure

The investigation of optical properties using ellipsometry showed that E_g and E_u are both influenced by the addition of dopant to a-Si:H. Figure 5.5 shows the change in both properties as a function of the doping ratio. E_g reduces as dopant is added whilst E_u increases, both as an approximately linear correlation with the doping ratio. The variation of E_g with doping has been identified previously [98, 99, 100, 101], and the variation of E_g in p type films corresponds closely with measurements performed by

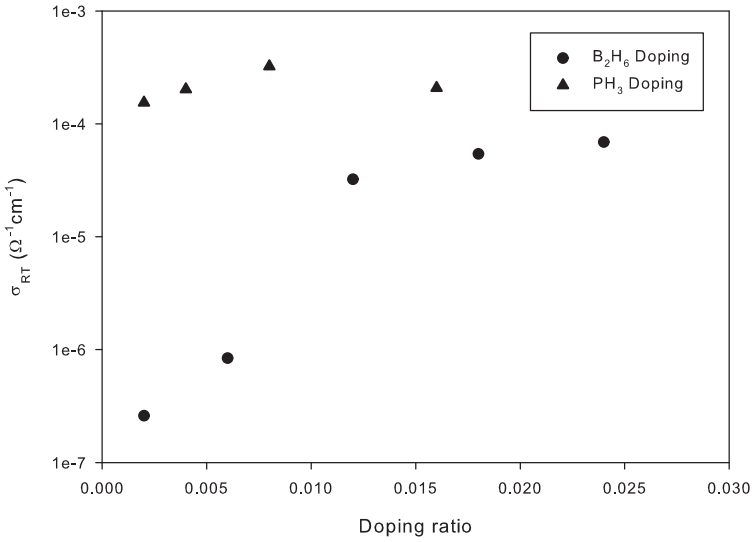

(a) Conductivity

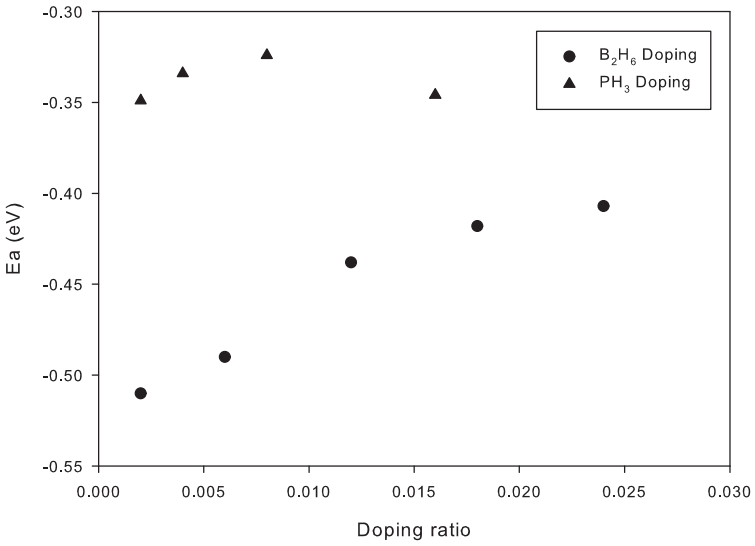

(b) Activation energy

FIGURE 5.4: σ_{RT} and E_a measured for doped a-Si:H films prepared using the doping ratios listed in table 5.4. Note how only a small addition of phosphine can dramatically increase conductivity, whilst a significantly larger addition of diborane is require to achieve the same effect. Even with an effective doping ratio the diborane doped p type films still exhibit a σ_{RT} of one decade less than a phosphine doped n type film

Hadjadj et al. [102]. However to the authors knowledge this is the first time E_g has been determined by use of a Cody-Lorentz oscillator to model amorphous absorption as opposed to extrapolation using a TauC plot. Table 5.6 lists the optical parameters determined by ellipsometry and the model used was the same as for intrinsic a-Si:H, see section 5.1.

Sample	E_g (eV)	E_u (eV)	Tox (nm)	Thickness (nm)	Inhomogeneity (%)	MSE
16-1-8-a	1.80	0.143	10.19	217.71	1.76	9.63
16-1-8-b	1.75	0.132	7.67	249.82	1.56	7.12
21-1-8-a	1.54	0.202	8.27	238.82	2.39	6.13
21-1-8-b	1.45	0.231	8.28	231.70	2.23	6.69
21-1-8-c	1.48	0.249	7.92	226.86	1.59	5.66
29-1-8-b	1.77	0.087	8.27	236.02	1.78	12.20
31-1-8-a	1.74	0.114	8.40	209.45	1.58	9.88
29-1-8-c	1.71	0.140	8.19	202.66	3.21	8.02
31-1-8-b	1.59	0.281	7.62	182.98	1.49	5.76

TABLE 5.6: Optical parameters determined by ellipsometry for the doped a-Si:H films listed in table 5.4

E_g was found to decrease from 1.78eV to 1.48eV with increasing diborane doping, and from 1.75eV to 1.58eV with phosphine doping. The reduction was roughly linear with respect to the doping ratio, with the narrowing due to phosphine doping possessing a shallower gradient than diborane. Narrowing due to diborane slows after a doping ratio of 0.0180. σ_{RT} , E_a, and E_u do not change significantly beyond this point which suggests that it is close to the effective limit for diborane doping if all other growth conditions were unchanged.

Attributing the changes in E_g and E_u to increasing disorder in the amorphous network as a result of introduced dopant is plausible. Due to the ability of phosphorus and boron atoms to bond with 4 or 3 neighbouring atoms, the a-Si:H network is likely to be distorted from its conventional configuration of silicon and hydrogen bonding where the dominant bonding configuration is sp^3. Changes in E_g for intrinsic a-Si:H are attributed to the hydrogen content of a film and this may also be relevant to doped samples, but the variation in the E_g of intrinsic a-Si:H films is not as extreme as is seen in doped films. An explanation for the extra narrowing observed in doped samples is that new bonding configurations are made possible by the addition of dopant atoms which can contribute states deeper into the gap than is observed in intrinsic a-Si:H. These states widen both band tails and bring E_c and E_v closer together by increased distortion of the amorphous network.

Evidence for increased distortion and with it a narrowing of E_g and E_m is provided by E_u, which is related to the extension of band tails into the mobility gap. Figure 5.9(c) shows that E_u varies linearly with E_g, indicating that the disorder introduced into the amorphous structure widens band tails which in turn narrows the optical gap.

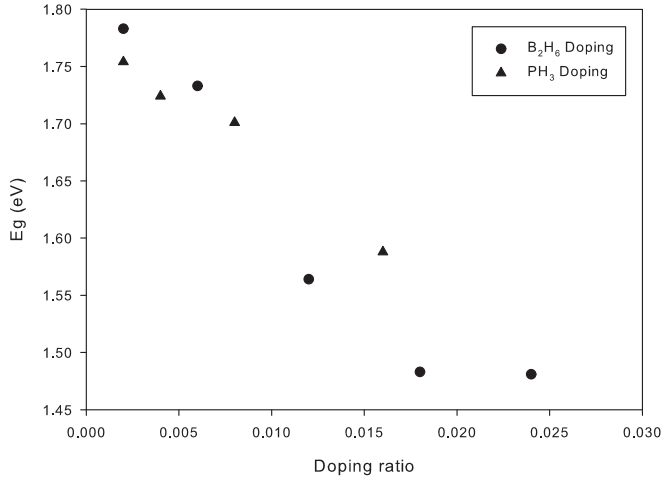

(a) E_g as a function of doping ratio

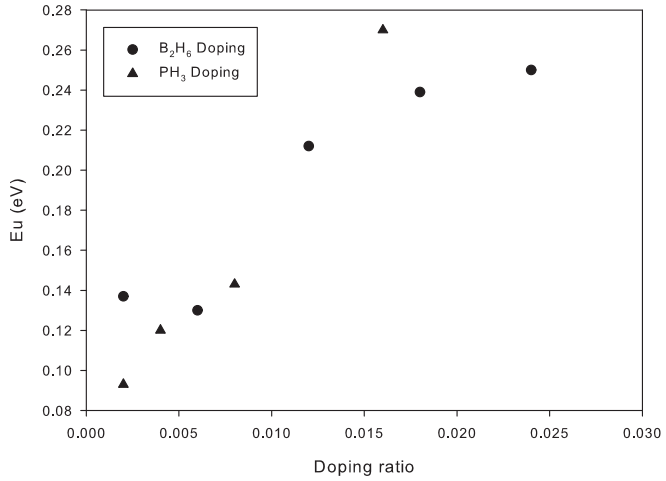

(b) E_u as a function of doping ratio

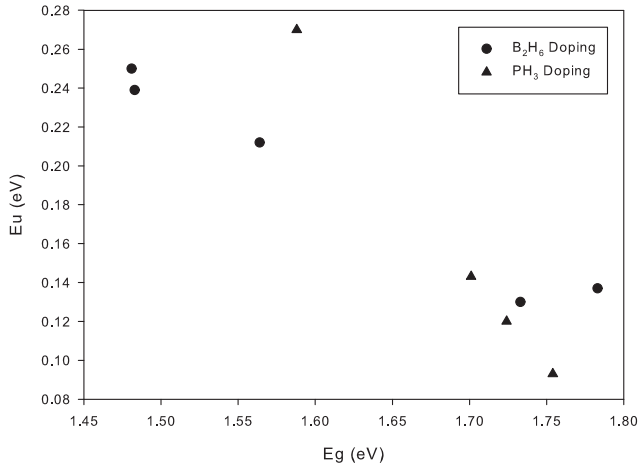

(c) E_u as a function of E_g

FIGURE 5.5: E_g and E_u as determined by ellipsometry for the films listed in table 5.4. There is a strong linear correlation between both measurements and the doping ratio

With knowledge of the variation in E_g and E_a as a function of the doping ratio, a model of how doping alters the band structure of a-Si:H can be built. Figure 5.6 indicates the shift of E_f as a function of the doping ratio. Equal narrowing of E_c and E_v is assumed. This assumption has been shown to be inaccurate; E_v narrows more than E_c but the difference is small at 53meV per decade of doping ratio for E_v compared to -39meV for E_c [102], so for the purposes of a visual representation the shift may be assumed to be equal.

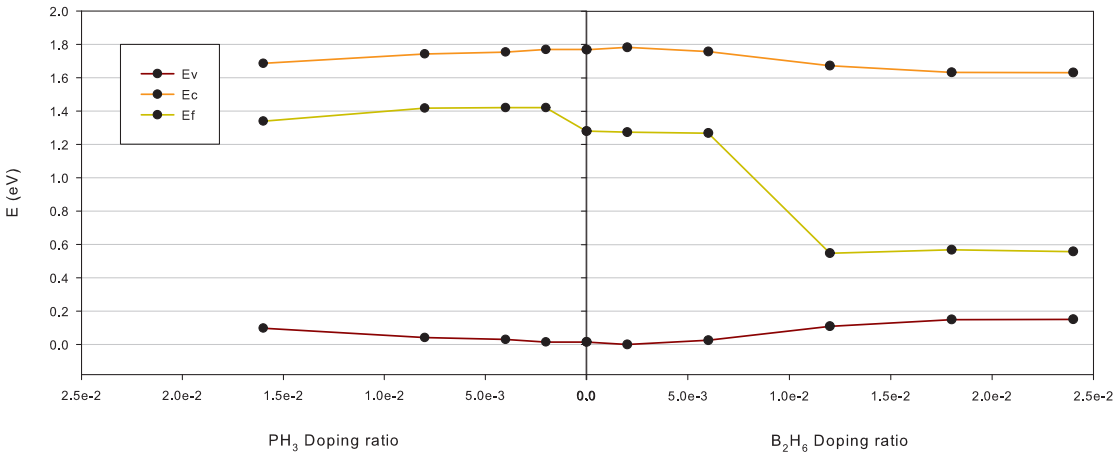

FIGURE 5.6: The shift in E_f and narrowing of E_g as a function of the doping ratio. E_c and E_g are assumed to narrow equally

The implications of a narrowing E_g when a-Si:H is doped are substantial when considering cell design. It is already widely accepted that careful control of doped layer thickness is essential to good cell performance due to the small minority carrier lifetime present in these regions as a result of dopant atoms that introduce mid gap states which act as deep traps [103]. A low minority lifetime means that the thickness of doped layers must be reduced as much as possible in order to minimize absorption of light in them, any carriers generated in doped a-Si:H will quickly recombine without contributing current flow to an external load. Gap narrowing is undesirable as it results in improved absorption of photons with energy $E > E_g$, increasing values of E_u create the same effect for photons with energy $E < E_g$.

Figure 5.7 shows the absorption coefficient as a function of wavelength for all n and p type layers produced, the absorption coefficient of a typical intrinsic film (4-12-7-a, table 5.1) produced at 200C is also shown as a reference. The increase in absorption of the doped films is substantial over a large portion of the wavelength range, especially for the p type films.

Well doped layers are required for cells to operate well in the first instance, but the trade off between electrical and optical properties must be observed. Doping beyond

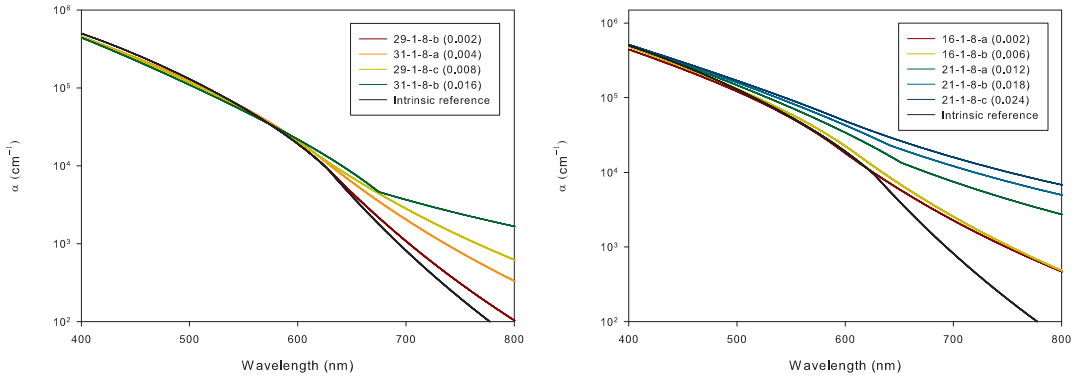

(a) n type a-Si:H (b) p type a-Si:H

FIGURE 5.7: The absorption coefficient from 400-800nm as determined by ellipsometry for the doped a-Si:H films listed in table 5.4 (The doping ratio is listed for each film). Note how larger doping ratios increase absorption of light across the spectrum through the narrowing of E_g and increase in E_u

the point of most effectiveness will reduce cell performance. The ability of the initial doped window layer in a cell to pass short wavelength light is particularly important with regards to obtaining high FF and low R_s

5.3 Characterisation of p type a-SiC:H films

Following on from the previous work which showed how doped a-Si:H is undesirable as a window layer, films of p type a-SiC:H were grown in order to investigate the effects of varying the silane to methane flow rate ratio. It is already been shown that a-SiC:H suitable for PV applications can be grown at 250C (see section 4.6).

The ratio of methane:silane flow was varied from 0.8 to 1.6, these choices match the two ratios chosen for previous work with complete cells at 250C. All the samples produced for analysis along with their growth conditions are listed in table 5.7.

Sample	Silane Flow (sccm)	Methane Flow (sccm)	Ratio
17-4-8-c	25	20	0.8
17-4-8-a	25	25	1
17-4-8-b	25	30	1.2
21-4-8-a	25	35	1.4
21-4-8-b	25	40	1.6

TABLE 5.7: Growth conditions for a series of doped a-SiC:H samples produced at 200C using 50W of RF power. 60 sccm of 1% diborane mixture was added to all depositions

Samples were characterised by measurements of dark conductivity and ellipsometry, and again conductivity analysis was split into two regions of temperature. As the films

are doped this approach should not be necessary but it is performed for the sake of continuous analysis. If conduction occurs via a similar path in each region the results obtained will not vary appreciably between temperature regions. Table 5.8 lists the parameters obtained via conductivity analysis.

	100-125C			125-150C			
Sample	σ_{RT} (Ω^{-1}cm^{-1})	σ_0 (Ω^{-1}cm^{-1})	E_{a1} (eV)	σ_{RT} (Ω^{-1}cm^{-1})	σ_0 (Ω^{-1}cm^{-1})	E_{a2} (eV)	ΔE_a (eV)
17-4-8-c	3.03x10^{-7}	15	-0.458	1.92x10^{-7}	59.3	-0.506	0.048
17-4-8-a	3.61x10^{-7}	8.2	-0.438	2.33x10^{-7}	31.6	-0.485	0.047
17-4-8-b	5.06x10^{-7}	8.6	-0.431	2.71x10^{-7}	55.9	-0.496	0.065
21-4-8-a	9.59x10^{-8}	269	-0.622	2.88x10^{-9}	9362	-0.746	0.124
21-4-8-b	1.32x10^{-9}	49963	-0.809	9.49x10^{-10}	132654	-0.843	0.034

TABLE 5.8: Results from conductivity analysis of the doped a-Si:H films prepared using the growth conditions listed in table 5.7

Increasing the methane flow has a pronounced effect on all conductivity parameters. σ_{RT} slowly increases and then rapidly drops 2 decades as it is increased. The best values obtained for σ_{RT} in doped a-Si:C films are still 1-2 decades beneath those obtained with intrinsic a-Si:H grown at 200C. At a methane:silane ratio of less than 1.2 films exhibit p type behaviour, with $E_a \approx 0.49$eV. This is a larger activation energy than was observed for p type a-Si:H films (≈ 0.4eV), probably caused by widening of the valance band tail and the subsequent pinning of E_f as a result of increased disorder in the amorphous network [104].

With a methane:silane ratio greater than 1.2, E_a rapidly increases to 0.8eV indicating that a-SiC:H growth has shifted towards being weakly p type and close to intrinsic in nature. This is perhaps due to a shift from the majority sp^3 bonding found in low or zero carbon a-Si:H films to a mixture of sp^2 and sp^3 bonding as the carbon content of the films increases. A shift in bonding such as this could cause boron to be incorporated in predominantly electrically inactive configurations which would result in the weakly p type films that were measured. A network of silicon and carbon atoms also becomes distorted due do the disparity in Si-Si and Si-C bond length, meaning that the fourfold sp^3 bonding configuration a boron atom requires to donate a hole would be expected to become rarer with increasing carbon content.

The dramatic increase in σ_0 with a ratio greater than 1 appears perhaps to be possibly erroneous data when compared to previous measurements with a-Si:H, however a Meyer-Neldel [105] relationship is seen to exist (a linear correlation between $\ln(\sigma_0)$ and E_a). A Meyer-Neldel relationship has been shown to be a property of amorphous films [106]. A plot of $\ln(\sigma_0)$ against E_a is shown in Figure 5.8.

The linear best fit in Figure 5.8 can be described using equation (5.2) where T_m is the material characteristic temperature, E_σ is the conductivity activation energy (identical to E_a), and σ_{00} is a conductivity constant determined from the y-axis intercept of

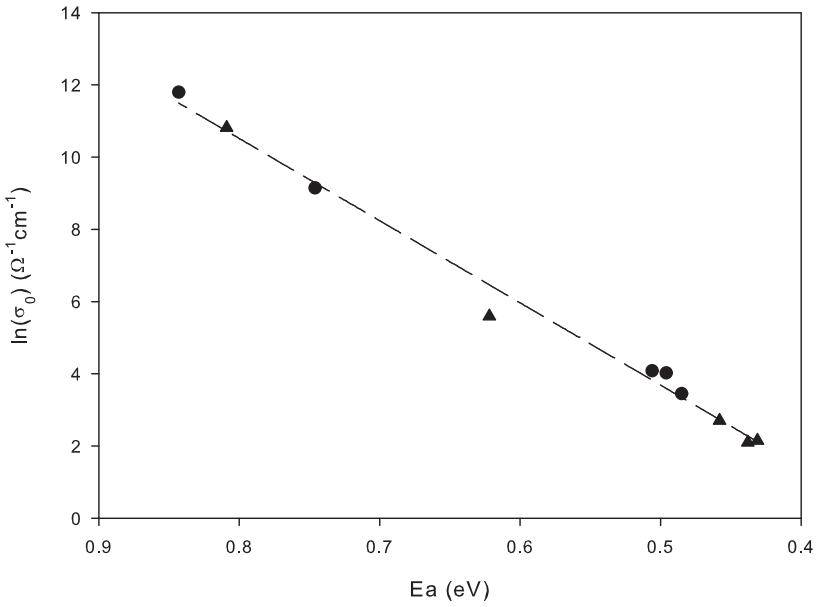

FIGURE 5.8: $\ln \sigma_0$ as a function of E_a for the a-SiC:H films listed in table 5.8, data from the higher temperature region is marked with a circle, and data from the lower temperature region with a triangle. The dashed line is a linear least squares fit. A strong linear correlation exists confirming that the a-SiC:H films follow a Meyer-Neldel relationship

Figure 5.8. Equation (5.2) has a near identical form to equation (3.16) which was used to determine the conductivity prefactor and activation energy from conductivity data as a function of temperature.

$$\ln \sigma_0 = \ln \sigma_{00} + \frac{E_\sigma}{kT_m} \tag{5.2}$$

If equation (3.16) is substituted into equation (5.2), equation (5.3) is obtained, where it is assumed that E_σ is positive, and that $T = T_m$.

$$\begin{aligned} \ln \sigma(T) + \frac{E_\sigma}{kT} &= \ln \sigma_{00} + \frac{E_\sigma}{kT_m} \\ \sigma(T_m) &= \sigma_{00} \end{aligned} \tag{5.3}$$

Equation (5.3) states that every film that follows a Meyer-Neldel relationship will possess the same extrapolated conductivity at the characteristic temperature T_m. σ_{00} and T_m can be determined from the linear fit of Figure 5.8 and are found to be 4.58x10^{-4} Ω^{-1}cm^{-1}and 509K respectively (E_σ =0.044eV).

The existence of the Meyer-Neldel relationship in amorphous semiconductors is a consequence of the energy dependent transport mechanisms relating to localised states and

a density of states that may also vary with temperature since increased temperature reduces the energy required to remove carriers from traps and defects and therefore also increases conductivity [107]. C-Si does not follow the Meyer-Neldel relationship for example as it has sharp and well defined band edges present in the density of states meaning that σ_0 does not vary with changes in E_a or temperature.

The Meyer-Neldel relationship is of definite interest with regard to the behaviour of amorphous semiconductors, and would be worth further research. For the present purposes of this thesis it will suffice to conclude that the data obtained for a-SiC:H films is accurate, despite the unexpected large values of E_a and σ_0 measured for several of the a-SiC:H films grown using larger flows of methane.

5.3.1 The optical gap and band structure

The optical gap of each a-SiC:H film was determined by ellipsometry in a similar fashion to previous work with a-Si:H. A thin native oxide was not included in the model as it was not found to improve the accuracy of data fitting, instead the surface roughness of the a-SiC:H films was allowed to vary which is accounted for as a combination of air and a-SiC:H using effective medium theory. Grading the refractive index of the a-SiC:H films with 5 linear regions increased fitting accuracy, particularly in the longer wavelength region. Table 5.9 lists the optical constants obtained and Figure 5.10 shows the absorption coefficient of each film from 400-800nm. E_g, E_u, and film thickness are shown as a function of the silane:methane flow ratio in Figure 5.9.

Sample	E_g (eV)	E_u (eV)	Roughness (nm)	Thickness (nm)	Inhomogeneity (%)	MSE
17-4-8-c	2.037	0.321	7.43	578.66	-0.52	15.13
17-4-8-a	2.269	0.313	6.04	525.69	-4.21	12.49
17-4-8-b	2.219	0.259	7.8	494.96	-0.56	8.45
21-4-8-a	2.062	0.225	9.81	437.81	-0.09	8.74
21-4-8-b	2.04	0.157	9.71	448.58	-1.92	15.19

TABLE 5.9: Optical parameters determined by ellipsometry for the a-SiC:H films listed in table 5.7. Note how the inhomogeneity of the refractive index grading is negative as opposed to all the a-Si:H films which all had positive values. This implies that the refractive index at the top of the a-SiC:H films is lower than than the bottom, the opposite was found to be true for a-Si:H films

Every film shows an widening of E_g due to the incorporation of carbon into the amorphous network, the trend peaks near a unity silane:methane flow ratio where E_g was found to be ≈2.3eV. The deposition rate roughly doubled when compared to conventional a-Si:H deposition as a result of the increased supply of reactants and the increase in system pressure ($5.1\text{x}10^{-1}$mbar compared to $2.3\text{x}10^{-1}$mbar). E_u decreases with an increasing flow of methane, indicating that the amorphous network becomes less distorted.

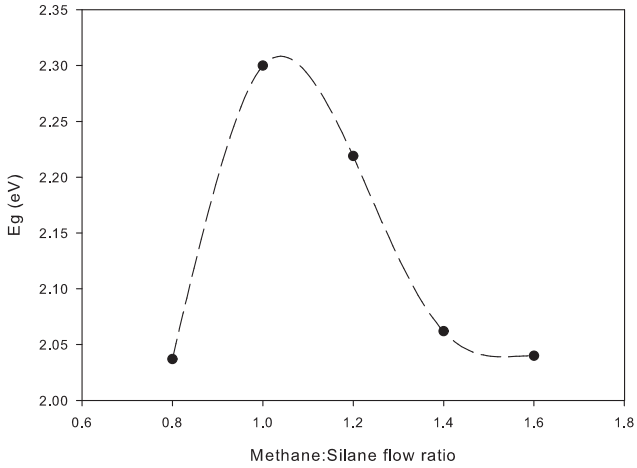

(a) E_g as a function of silane:methane ratio

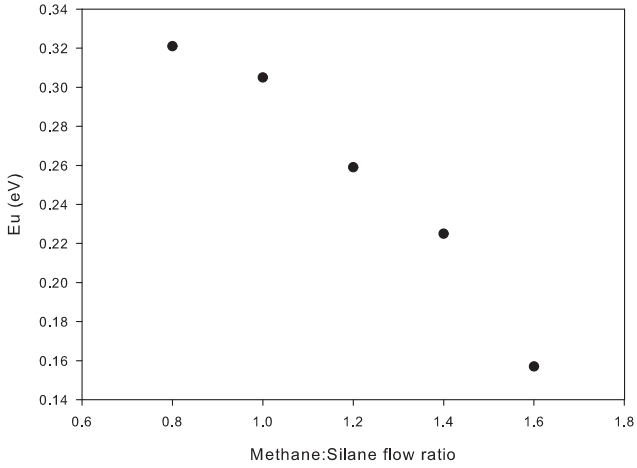

(b) E_u as a function of silane:methane ratio

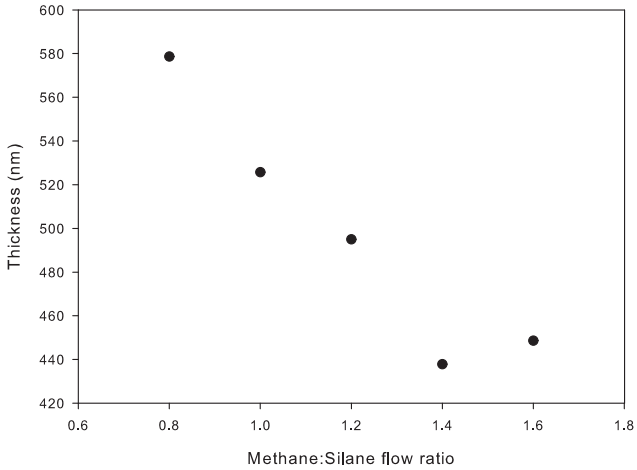

(c) Film thickness as a function of silane:methane ratio

FIGURE 5.9: E_g, E_u, and film thickness as determined by ellipsometry for the films listed in table 5.7. The dashed line fit is included in the plot of E_g as a guide to the eye

This coincides with the large increase in E_a that was previously noted, and lends support to the theory that boron is incorporated into the amorphous network in electrically inactive configurations that help to relieve lattice stress.

The deposition rate falls off as the methane:silane flow ratio is increased beyond 1, which is unexpected due to the continued rise in system pressure with increased flow of precursor gases. The relatively large concentration of carbon present in the plasma may act to suppress the creation of species involved in deposition. The change in deposition rate for p type a-SiC:H as opposed to a-Si:H must be accounted for to prevent the creation of excessively thick window layers during cell deposition.

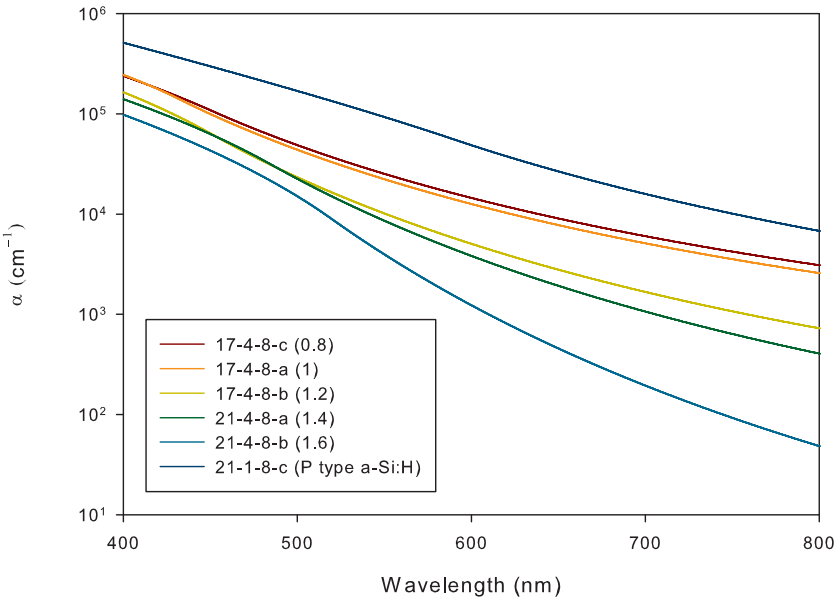

FIGURE 5.10: The absorption coefficient from 400-800nm as determined by ellipsometry for the a-SiC:H films listed in table 5.7 (The methane:silane ratio is listed for each film). The absorption coefficient of a p type a-Si:H film is included as a reference

Relying on E_g as an indication of a films optical absorption can be misleading, especially when using a model such as a Cody-Lorentz oscillator as opposed to a direct TauC plot extrapolation. It can be seen from Figure 5.10 that there is a significant difference in absorption between films 17-4-8-a and 17-4-8-b, despite E_g being similar for both and the largest measured of all samples. Film 21-4-8-b exhibits a large reduction in absorption for all wavelengths when compared to all the other films, but lack of effective doping prevents its use as a cell window layer. It should be noted that even an unoptimised p type a-SiC:H window layer will still easily outperform standard p type a-Si:H optically.

The analysis of a-SiC:H films presented here indicates that a silane:methane flow ratio of 1.2 results in the best compromise of electrical and optical properties suitable for the creation of a p type a-SiC:H window layer. Effective doping is maintained with

E_a=0.496eV, and optical absorption is 0.5-1 decade lower than a comparable p type a-Si:H across the wavelength range of interest.

5.4 Nip superstrate cells fabricated at 200C

Before attempting to fabricate nip substrate cells on a flexible Kapton substrate, nip superstrate cells were deposited onto TCO coated glass at 200C using the optimum film growth conditions identified previously in this chapter. Cell orientation is inverted between the designs but the order of layer deposition is the same. This allows investigation of the interfaces between cell regions which are affected by deposition time and doping, and information about this is relevant to both cell structures regardless of orientation. A comparison to the nip superstrate cells grown at 250C (see section 4.12) could also quantify the performance difference resulting from the change in substrate temperature, although the 250C nip cells were not extensively optimised. An n type a-SiC:H window layer was not used because it was not found to improve performance at either substrate temperature.

Phosphine is a more effective dopant than diborane, and because n type a-Si:H was the first region to be deposited a plasma break and gas flush was required before intrinsic a-Si:H deposition to ensure cross layer contamination was minimized. Silane was allowed to flow during this 10 minute break to keep the substrate surface temperature as constant as possible and to dilute any remaining phosphine. All cells were deposited using 25sccm of silane, 25sccm of 1% phosphine mixture, 60sccm of 1% diborane mixture, and 50W of RF power. These dopant flow ratios were established as optimal by work with individual films in this chapter at 200C (see section 5.2). All IV characteristics presented have been adjusted for 5Ω of TCO series resistance. Table 5.10 lists the layer deposition times for each of the 6 cells, and table 5.11 lists the double diode fitting parameters determined for each cell.

Sample	N layer (mins)	I layer (mins)	P layer (mins)
18-3-8-a	1	20	5
18-3-8-b	1	30	5
19-3-8-a	0.5	20	5
19-3-8-c	1	20	3
20-3-8-a	1	20	2
20-3-8-b	1	10	3

TABLE 5.10: Growth conditions for a series of nip superstrate cells deposited onto TCO coated glass at 200C, using 50W of RF power

Cells 18-3-8-a and 18-3-8-b included a p type layer that was suspected to be too thick, but it was a suitable starting point for optimisation. All substrates included at least several functioning cells, fabrication at 200C was generally less reliable than at 250C in

Cell	18-3-8-a	18-3-8-b	19-3-8-a	19-3-8-c	20-3-8-a	20-3-8-b
$V_{\rm oc}$ (V)	0.66	0.73	0.49	0.74	0.68	0.64
$I_{\rm sc}$ (mA)	13.6	14.1	13.9	12.6	12.3	14.1
R_s (Ω)	13.0	28.1	14.3	19.0	27.7	11.5
R_{shunt} (Ω)	48.6	50.3	66.5	91.9	76.8	147.0
J_{02} (A)	$9.87\text{x}10^{-9}$	$4.57\text{x}10^{-9}$	$5.85\text{x}10^{-7}$	$3.28\text{x}10^{-9}$	$9.66\text{x}10^{-9}$	$1.71\text{x}10^{-8}$
FF	0.31	0.32	0.37	0.40	0.35	0.49
η (%)	2.78	3.33	2.54	3.73	3.00	4.59

TABLE 5.11: Double diode fitting parameters for the cells listed in table 5.10

terms of dead cells per substrate. The thicker intrinsic region of cell 18-3-8-b improved I_{sc} and V_{oc} as expected, with R_s doubling due to the lower built in field. The combined effect was positive with regard to cell efficiency, the cell with the thicker intrinsic layer (18-3-8-b, ≈400nm) was 3.33% efficient as opposed to 2.78% for the thinner (18-3-8-a, ≈270nm). The IV characteristics of both cells are shown in Figure 5.11(a). The increase in V_{oc} from 0.66V to 0.73V seems unusually large considering that doped layer thickness was not adjusted between samples, but non uniform deposition is probably responsible. There could also be a small Schottkey barrier present in cell 18-3-8-b which slightly enhances V_{oc}.

To minimize parasitic resistances and carrier recombination, the doped layer thickness was thinned keeping a constant intrinsic layer thickness of ≈270nm. The n layer deposition time was halved to 0.5 minutes for cell 19-3-8-a, whilst the p layer deposition time was cut to 3 and 2 minutes respectively for cells 19-3-8-c and 20-3-8-a. The reduction in n layer thickness was too great (19-3-8-a), V_{oc} reduced significantly and performance was poor as a result. Reducing p layer deposition to 3 minutes (19-3-8-c) maintained V_{oc} and the improvement in carrier collection is shown by FF increasing to 0.4 from 0.3, and R_{shunt} to 90Ω from ≈50Ω. Cell efficiency rose to 3.73% as a result. Further reduction in the p layer thickness was not beneficial (20-3-8-a), resulting in similar fitting parameters to a cell with the original thicker p region (18-3-8-a) as doping efficiency dropped at the a-Si/Al contact interface. IV characteristics for these 3 cells are shown in Figure 5.11(b).

Performance of these 5 cells was disappointing, efficiency did not exceed 4%. The change that recovered a sharp diode characteristic was to further reduce intrinsic layer deposition time to 10 mins. This created an active thickness of ≈130nm. By thinning the intrinsic layer carrier collection near V_{oc} was still effective, R_{shunt} almost doubled to 143.5Ω whilst maintaining a relatively low value of R_S (11.5Ω), and the cell was 4.59% efficient.

The IV characterisation light source was changed from the mercury lamp used for previous measurements to a metal halide bulb that had stable output over a larger area (see section 3.8.4) for these IV characteristic measurements. The irradiance of the metal halide bulb was matched to the AM1.5 standard of 1000Wm^{-2}, but its output spectrum was not precisely known. If there was one or more spikes of short wavelength light present (common in metal halide lamp spectra), this could have resulted in exaggerated

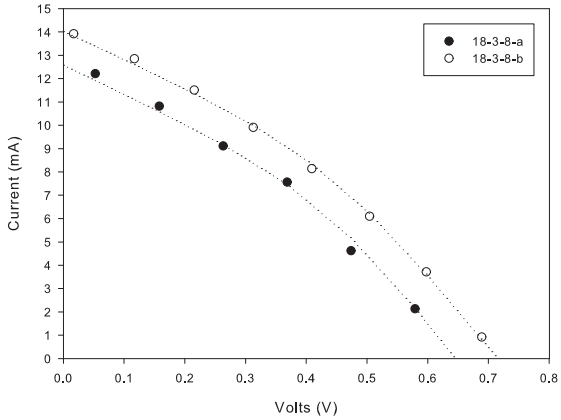

(a) Thickening the intrinsic region from ≈270nm (18-3-8-a), to ≈400nm (18-3-8-b)

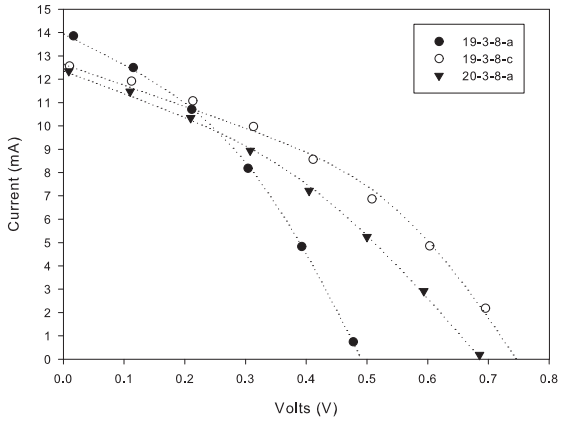

(b) Thinning the n type window layer (19-3-8-a), and the p type rear layer (19-3-8-c and 20-3-8-a)

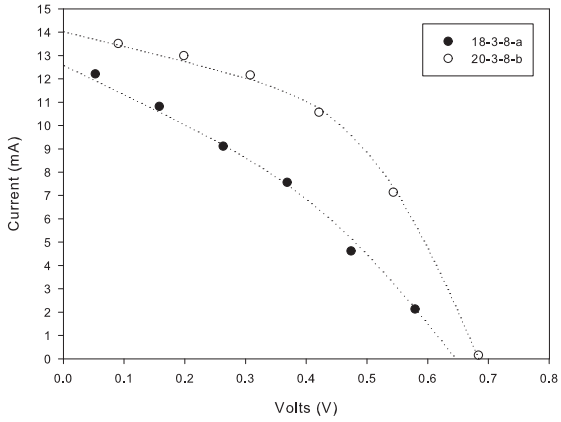

(c) Thinning the intrinsic layer to ≈130nm (20-3-8-b), cell 18-3-8-a is shown as a comparison

FIGURE 5.11: IV characteristics of the cells listed in table 5.10, the associated double diode fitting parameters are listed in table 5.11, and the deposition parameters are listed in table 5.10. The dotted lines correspond to the fitted double diode parameters after a 5Ω R_{TCO} correction

performance measurements of thinner cells due to a surplus of lower wavelength light absorbed near the p and intrinsic layer interface. Thinner nip cells would perform well under these test conditions as generated holes would have less distance to travel to the p region without recombining. To ensure measurements were not affected by this issue thicker nip cells previously deposited at 250C were measured using the new bulb and results were found to be in good agreement with previous measurements.

Figure 5.12 shows the absorption of light in varying thicknesses of intrinsic a-Si:H using the known absorption coefficient (see Figure 5.2, film 4-12-7-a). A 10nm thick p layer was included in the calculation, light absorbed in this layer was assumed to be lost. Absorption in the intrinsic region was calculated with equation (5.4) where d_p, d_i, α_p, and α_i are the thicknesses and absorption coefficients of the p type and intrinsic layers respectively.

$$\alpha(\%) = \exp^{-d_p\alpha_p(\lambda)}\left(1 - \exp^{-d_i\alpha_i(\lambda)}\right) \tag{5.4}$$

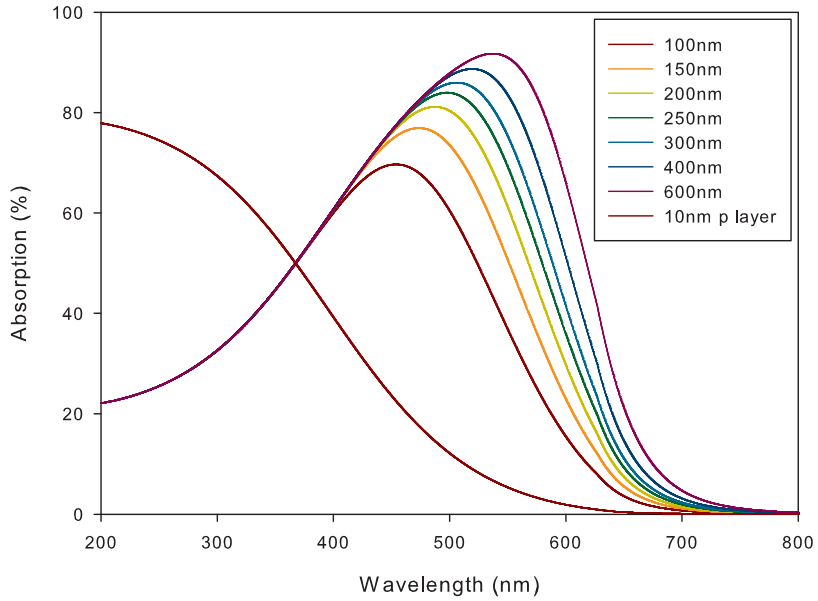

FIGURE 5.12: % absorption of light as a function of frequency for intrinsic a-Si:H regions of varying thickness, a 10nm thick p layer is included in the calculation and light absorped in it is assumed to be lost

Figure 5.12 shows that collection of light does not increase linearly with the width of the intrinsic region due to the exponential nature of absorption. The amount of light lost to even a relatively thin p layer is substantial, at 400nm nearly 40% of light is absorbed before reaching the intrinsic region. The increase in absorption that could be gained by thickening an intrinsic layer of 150nm to 250nm is relatively small compared to what was initially achievable. If carrier diffusion lengths were similar to the thinner intrinsic thickness then it is clear that increasing it for a minimal increase in absorption of light

would be negated by recombination of generated carriers, especially as the forward bias on a cell is increased and the built in field strength declines. This effect is observable in Figure 5.11(c), and highlights the tradeoff between optical and electronic design which must be considered when fabricating solar cells, especially where limits on growth conditions mean that less than optimal material or cell configurations must be accounted for.

5.5 Chapter summary

The work presented in this chapter shows a systematic study of the individual layers that make up an a-Si:H cell deposited at a lower than optimum substrate temperature of 200C. Analysis of optical and electronic properties was presented and the necessity of trading performance in one area for another was observed.

The electronic properties of intrinsic films did not change significantly from deposition at 200C compared to 250C, but narrowing of E_g did occur with increased substrate temperature. Deposition rate was found to be a function of RF power and substrate temperature, although film uniformity suffered at higher RF power. This would perhaps not have been such an issue if the plasma was generated capacitively rather than inductively.

An increase of several decades in the dark conductivity was measured for both p and n type a-Si:H compared to intrinsic material. The bulk Fermi level was brought to 0.3eV from E_c in n type films and 0.4eV from E_v in p type films. The optimum silane:dopant flow ratio using 25 sccm of silane were found to be 1:0.01 for n type films and 1:0.024 for p type. These values were unchanged from the ratios determined by trial and error with complete cells at grown at 250C. Linear narrowing of E_g was found to occur as a function of doping ratio which is undesirable as it increases absorption of light in doped regions, carriers generated in this way will recombine before they can deliver current to an external load. E_u was found to increase linearly with the silane:dopant flow ratio, this is attributed to widening band tails as a result of states added near E_v and E_c through the incorporation of electrically active dopant atoms into the amorphous network.

To alleviate the problem of strong light absorption in p type window layers of a-Si:H, p type a-SiC:H films were created. A maximum value of E_g=2.3eV was determined near a methane:silane flow ratio of 1:1 using a silane flow of 25 sccm. Doping was successful using 60sccm of 1% diborane mixture and a methane:silane flow ratio of less than 1.2, the bulk Fermi level was brought to 0.5eV from E_v. Increasing the methane:silane flow ratio further resulted in a decrease in E_u and E_f being pulled back towards mid gap making films weakly p type. This is explained by the extra carbon atoms promoting the incorporation of diborane into the amorphous network in electrically inactive threefold configurations, helping to relieve lattice stress and reducing disorder which is reflected

in the decrease of E_u. This could be related to a shift from a majority of sp^3 bonded carbon atoms to a a majority of sp^2 bonded carbon atoms. The a-SiC:H films produced were found to follow a Meyer-Neldel relationship with a characteristic temperature of 509K which corresponds to 0.044eV.

Figure 5.13 shows the relationship between E_a and σ_0 for all films reported on in this chapter, separated by type. Each group of films occupy a distinct 2D parameter space with intrinsic material showing the most variation, however it must be considered that intrinsic films were deposited at two different substrate temperatures whilst all other films were not. Generally values of E_a obtained for intrinsic films are small and indicate a slight n type characteristic but the low values of σ_0 do not agree with this and if intrinsic material was truely n type it would have been impossible to fabricate cells with it. It is possible that E_f is fixed near E_c and away from mid gap by the presence of charged defects in the density of states resulting from unpassivated Si bonds.

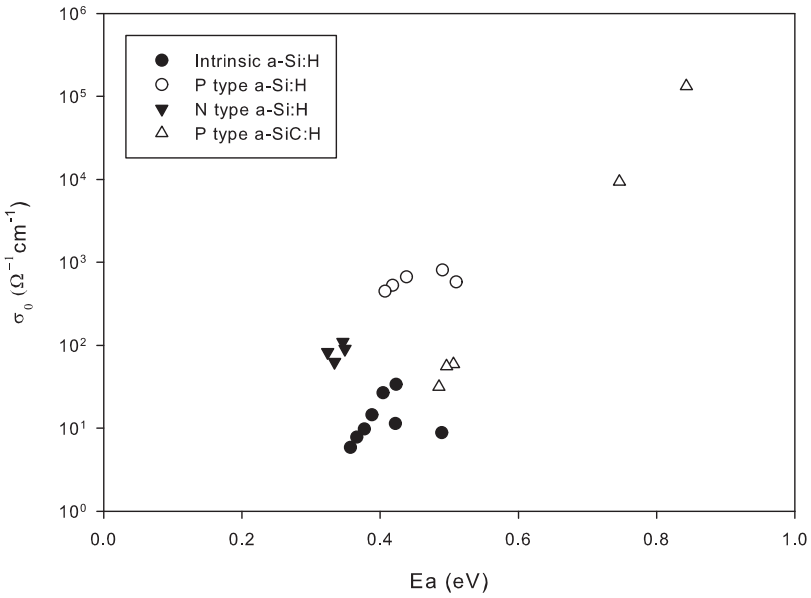

FIGURE 5.13: σ_0 as a function of E_a for all films reported on in this chapter grouped by material type. The a-SiC:H samples extend into the high energy and conductivity region where materials unknown at the time were predicted to lie in 1991 by Street [74, page 236]

The conditions determined as optimum for individual film deposition were used to create nip superstrate cells on TCO/glass substrates at 200C, the cell structure was chosen to match the order of layer deposition required for nip substrate cells. N type a-SiC:H was not included as part of the cell as it was found that the addition of carbon to n type a-Si:H layers did not enhance E_g. The best performing cell was 4.59% efficient which can be contrasted with the 5.57% efficient nip cell created at the higher substrate temperature of 250C (see section 4.12).

To achieve this efficiency at 200C it was necessary to halve the thickness of the absorbing intrinsic layer to ≈130nm. This was because the majority of carriers were generated close to the n and intrinsic layer interface by short wavelength light, requiring holes to travel nearly all of the intrinsic region without recombining. A thicker intrinsic layer would support a larger I_{sc} at 0 or reverse bias but at the expense of low R_{shunt} and high R_s which reduces FF and results in a low conversion efficiency.

The analysis techniques described in this chapter could be translated into a development methodology for a-Si:H cells using any substrate temperature, and it is anticipated that future work will involve further reduction of the substrate temperature to enable use of a wide range of flexible polymer substrates. At these lower temperatures the selection of growth conditions in order to encourage sp^3 bonding of a-Si:H and a well passivated amorphous network is vital to preserve the photoconductivity of intrinsic a-Si:H and create efficient cells.

Chapter 6

Flexible nip substrate cells deposited at 200C

Following the work of the previous chapter, nip cell deposition was transferred from a TCO/glass substrate to flexible substrates. The flexible substrates chosen were 50μm thick Kapton type HN polyimide film and 1mm thick stainless steel polished to a 10nm average radius. (Kapton is the trade name of a polyimide based polymer film manufactured by DuPont). Whilst the steel was not as flexible as the Kapton, it would still bend with the application of a small amount of force. In this sense it was a halfway point for development between the truely flexible Kapton film and rigid TCO coated glass.

Kapton was chosen as a substrate because of its ability to maintain physical and mechanical properties over a wide temperature range. It can withstand temperatures of 400C so a substrate temperature of 200C was not strictly required, but it is still too great for the majority of commercially available polymer films. For example PEN (PolyEthylene Naphthalate) films possess a glass transition temperature of 140C and PET (PolyEthylene Terephthalate) films have a glass transition temperature of 80C. Whilst exceeding these limits will not destroy a polymer film, (the melting point of PEN and PET films is $\approx$ 269C and 250C respectively), depositing onto a substrate that has shifted from a glassy to a soft deformable state will be likely to destroy any thin film device on it when it reverts back upon cooling to room temperature. PEN and PET can withstand higher temperatures than the majority of polymer films which typically melt near 100C. The glass transition temperature of Kapton is 385C and so it is expected to remain stable during deposition at 200C.

Characterisation in this chapter makes extensive use of AFM scans to examine the topography of deposited metal layers, but the technique only became available after deposition work with flexible substrates had ceased. At the time of flexible cell fabrication the surface roughness of deposited metallic back contacts could only be investigated using an optical microscope prior to deposition. Whilst this gave some insight as to back

contact suitability, in hindsight it was no substitute for a more advanced technique. The limitation of back contact deposition techniques to e-beam evaporation is suspected to have caused problems relating to the surface roughness of the metallic back contacts it produced, sputtering would have been a more appropriate deposition method if it had been available at the time.

6.1 Fabrication issues with nip substrate cells

Growth of nip substrate cells differs from the pin superstrate configuration in that either a conducting substrate must be used or a conducting film must be deposited onto a substrate before cells can be created. The surface roughness of this back contact was of large importance because the n type a-Si:H located on top of it was ≈100nm in thickness.

A back contact surface that was too rough would cause breakup of the n type layer disrupting the electric field across the intrinsic region and reducing carrier collection in the region of the roughness peak. In extreme cases a back contact with large surface roughness peaks could shunt an entire cell by contacting both the n and p type regions. Figure 6.1 illustrates these situations.

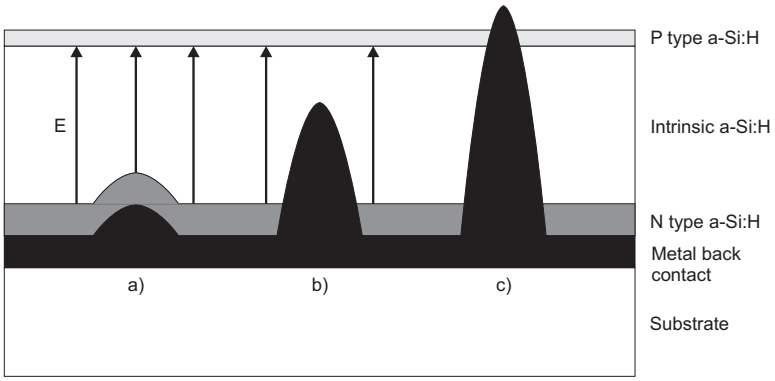

FIGURE 6.1: Fabrication issues due to the surface roughness of a deposited metallic back contact. a) Surface roughness is present but the peak height and gradient of the roughness is such that n type a-Si:H can still cover it conformally with no problems. b) A sharper gradient and larger peak cause disruption of the n layer and therefore the electric field in the location of the metal peak. c) Peak height of the roughness is such that the cell is fully shunted and will operate as a resistor instead of a diode

A similar problem also occurs when the metallic back contact is thinned or not present in an area. Missing material from an evaporated metal back contact was often seen as "pinholes" in the layer under illumination. Pinholes are common when depositing using e-beam evaporation due to heating gradients in the crucible, and a lower working pressure than other deposition techniques making it a line of sight based PVD system.

Thermal gradients in the crucible and material to be evaporated cause non uniform deposition and "splatter" (sometimes also known as spitting) of material in concentrated

areas on the substrate. Hotter material in these areas contracts leading to thickness variations and often pinholes. This problem can be reduced by scanning the crucible with the electron beam to provide a more distributed heating effect but this was not an option with the system that was used. The line of sight nature of e-beam evaporation also means that pinholes can form around dust particles present on the substrate, whereas a technique like PECVD would deposit around them conformally and incorporate them into a coating.

In the worst case pinholes in a back contact could also cause shunted cells depending on the depth of the pinhole and the gradient of its sidewalls. Pinhole formation was found to be a problem with every type of metal back contact that was evaporated, some to a greater extent than others which suggests that heating gradients rather than substrate preparation was the dominant problem.

6.2 Nip substrate cell development on polished stainless steel

Before utilisation of truely flexible substrates, stainless steel polished to a 10nm radius was trialled as a substrate. By removing the back contact deposition as a process step required for a complete cell (the stainless substrate was sufficiently conductive), it was possible to isolate the effects of inverting the cell structure and the ITO top contact from the influence of a potentially too rough evaporated metal back contact. Figure 6.2 shows the topography of a 50μm square area of the polished steel measured using contact mode AFM.

A-Si:H was deposited onto a polished stainless steel substrate to form cells and investigate whether a diode characteristic could be measured. The substrate was cleaned with a 30W hydrogen plasma for 5 minutes before any other gases were introduced to the reactor to remove any oxide and surface contamination present. 25 sccm of silane was present throughout the deposition, with 25 sccm of 1% phosphine mixture and 60 sccm of 1% diborane mixture added to create n and p type a-Si:H. The n layer was deposited for 7 minutes with a thickness target of 100nm, a 10 minute plasma break and gas flush was performed after n layer deposition to minimize intrinsic contamination. Intrinsic a-Si:H was deposited for 10 minutes and 1% diborane mixture was added for a further 3 minutes. RF power and substrate temperature were 40W and 200C.

20mm^2 top contacts of aluminium were evaporated to define cells and IV characteristics were measured to determine if diodes had been successfully formed. Figure 6.3 shows the dark IV characteristics obtained from 4 cells using a linear and logarithmic scale. Excellent agreement is seen between the characteristics which is likely to be due to the small variations in surface roughness present on the substrate.

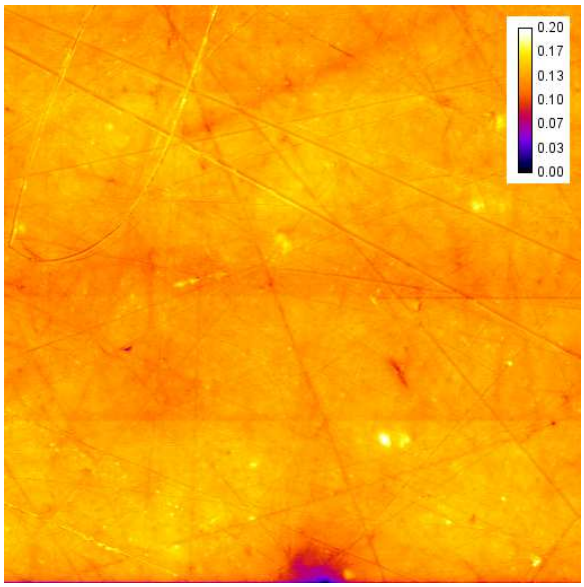

FIGURE 6.2: The topography of a 50μm square area of stainless steel polished to a 10nm radius determined by a contact mode AFM scan. The height scale is given in μm. The majority of features observed are less than 100nm in height which indicates that the polishing was accurate and that the steel should be suitable as a back contact for an nip substrate cell. One defect exists with a peak depth of ≈200nm which could potentially cause problems, but the gradient of the defect appears to be gradual rather than a sharp peak

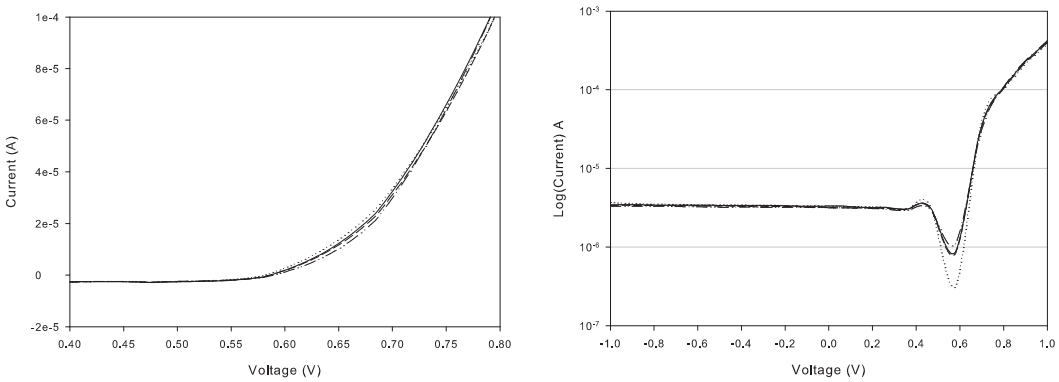

(a) (b)

FIGURE 6.3: Dark IV characteristics of several 20mm^2 nip substrate cells on a polished stainless steel substrate. A small amount of illumination was present as shown by the minimum of the logarithmic current of graph b). There is excellent agreement between the different cells which is probably related to the low surface roughness of the substrate

The deposition method was repeated to produce a second substrate, and 1cm^2 cells were defined using a top contact of sputtered ITO. The ITO was 60nm thick with the thickness chosen to minimize reflection of light at 500nm. Figure 6.4 and Figure 6.5 show the dark and illuminated IV characteristic of the best performing cell using linear and logarithmic current scales. No alteration was made to the illuminated IV characteristic to account for the resistance of the substrate.

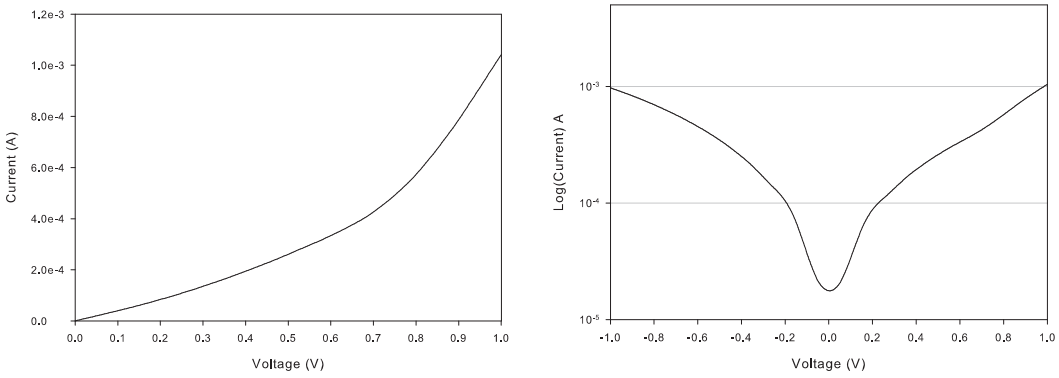

(a) (b)

FIGURE 6.4: The dark IV characteristic of a 1cm^2 nip substrate cell on a polished stainless steel substrate.

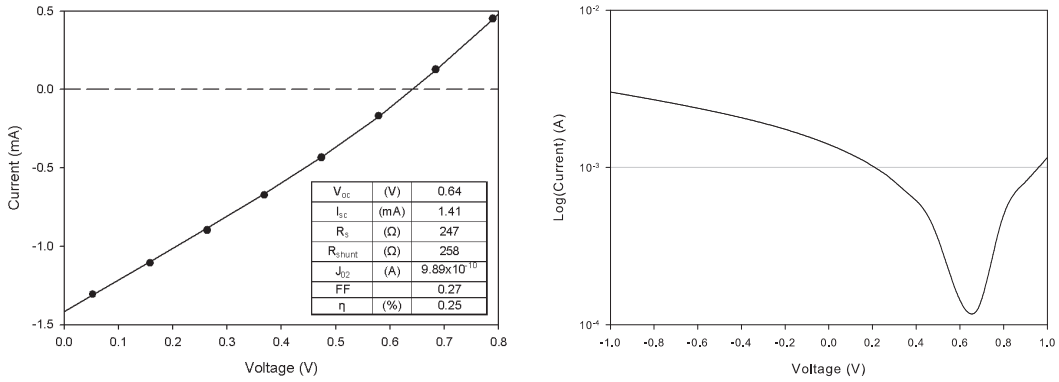

V_{oc}	(V)	0.64
I_{sc}	(mA)	1.41
R_s	(Ω)	247
R_{shunt}	(Ω)	258
J_{02}	(A)	9.89×10^{-10}
FF		0.27
η	(%)	0.25

(a) (b)

FIGURE 6.5: The illuminated IV characteristic of a 1cm^2 nip substrate cell on a polished stainless steel substrate. The circles in graph a) denote measured data points, whilst the solid line is a double diode fit to the data using the parameters seen in the table. The dashed line represents $y = 0$ and is included as a guide to the eye

I_{sc} is low and the parasitic resistances have a strong effect on the IV characteristic, but the cell is photosensitive and operates properly. R_s is very large and is the principle cause of poor FF, carrier collection with increasing forward bias decreases quickly. This would suggest that either field strength over the intrinsic region was weak or that the cell was starved for low wavelength light that would have generated carriers near the p/i

interface that were less likely to recombine. As it is known that the growth conditions used provide effective doping (which V_{oc} agrees with) then it is reasonable to assume that a lack of short wavelength light is the major problem, the low value of I_{sc} correlates with this. Contamination of the a-Si:H with indium during ITO deposition could also have potentially reduced carrier lifetime which would further degrade performance. Incorporation of indium into a-SiC:H has been known to cause p type doping and disorder of the amorphous network [108].

If a lack of light reaching the intrinsic layer is to blame for the low efficiency, then it must have been absorbed in the p type a-Si:H and ITO layers as the intrinsic a-Si:H thickness is known to be sufficient to achieve 5% efficient cells (see table 5.10). The p layer was deposited for slightly less than 3 minutes beause it would take some time for gas partial pressures to stabilise after diborane was introduced to the reactor. The deposition rate of the p type a-Si:H was 0.25nms^{-1} (see table 5.4) and so the layer could have been potentially up to 45nm thick. With knowledge of $\alpha(\lambda)$ for the p type a-Si:H it is possible to estimate absorption in the layer as a function of wavelength and thickness using Beer's law (see equation (3.23)). Figure 6.6 shows the precentage of absorption per wavelength for 4 different p layer thicknesses from 10nm to 40nm.

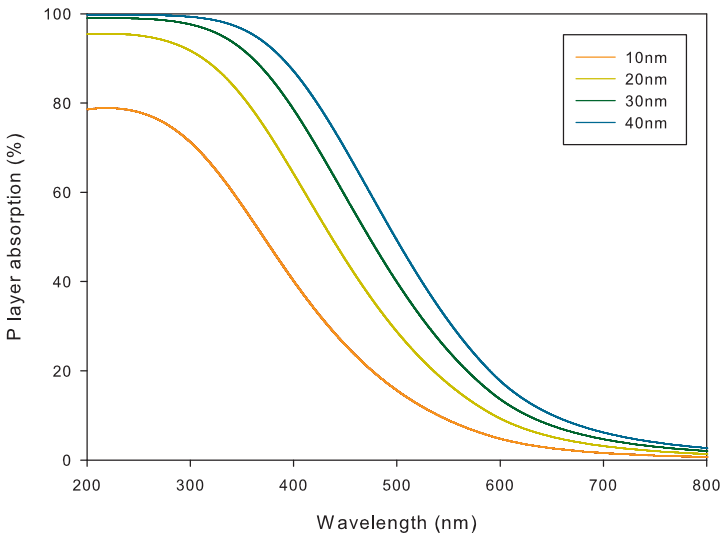

FIGURE 6.6: The percentage of absorption in p type a-Si:H as a function of wavelength and layer thickness, using data for $\alpha(\lambda)$ determined by spectroscopic ellipsometry. It can be seen that increasing the layer thickness past 10nm causes a sharp increase in absorption with the emphasis on lower wavelengths

If it is assumed that all light that is absorbed in the p layer is lost then it is clear that any increase in thickness over 10nm sharply reduces the available photocurrent, especially in the critical region of 400-600nm where the AM1.5 spectrum peaks. Cell performance would improve drastically with optimisation of the p layer thickness, which would only be achievable by inserting a second plasma flush after intrinsic layer deposition and allowing the gas partial pressures to stabilise before recommencing growth.

Work using stainless steel substrates ceased soon after the production of this cell due to project time limitations, but it is expected that if work had continued optimisation of the p layer thickness and the ITO deposition process would have sharply increased cell efficiency in a short amount of time.

6.3 Nip substrate cell development on Kapton

Having shown that the fabrication of functional nip substrate cells on a polished stainless steel substrate was possible at 200C, the stainless steel substrate was replaced with a Kapton film coated with an evaporated metal contact in order to create truely flexible cells. The topography of a 50μm square area of Kapton was investigated using contact mode AFM and is shown in Figure 6.7. The Kapton film is fairly flat, with occasional large and gradual peaks of up to 200nm in height. It is possible that a deposited metal layer could cover these peaks without breaking up and ideally produce a more level surface for a-Si:H deposition.

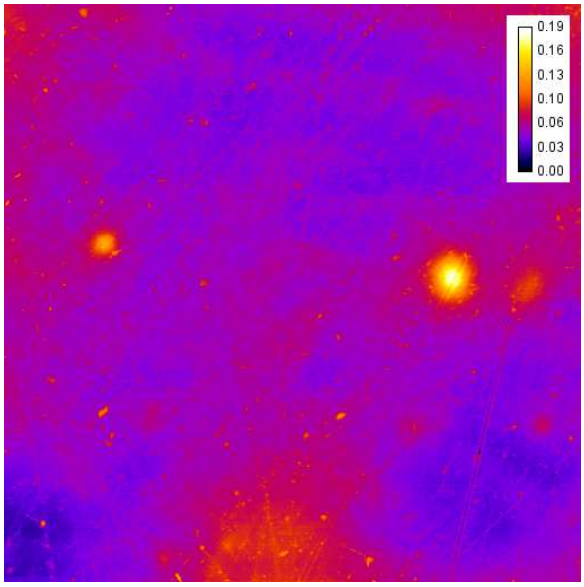

FIGURE 6.7: The topography of a 50μm square area of Kapton determined by a contact mode AFM scan, the height scale is in μm

The first metal to be trialled was chromium due to the low current required to evaporate it and its relative inertness when compared to aluminium. Chromium sublimes when evaporated using an electron beam and depending on the current supplied to the evaporation filament the deposition rate can be extremely quick. Two different deposition rates were investigated using a filament current of 90mA and 110mA. Kapton substrates were cleaned with IPA followed by dust removal using compressed air before evaporation.

The lower current resulted in a conventional deposition rate for e-beam evaporation of 0.2nms^{-1}, whilst the higher power caused the entire crucible of chromium to sublime in

several seconds. Figure 6.8 shows a 50μm square region of each samples topography. The quickly deposited chromium film was scanned using tapping mode AFM due to the sharper features that were found to be present whilst the slowly evaporated chromium film was scanned using contact mode AFM. The sheet resistance of both metal layers was measured using a 4 point probe and was found to be 10$\Omega/\square$ for the quickly evaporated chromium, the slowly evaporated layer was too resistive for a measurement to be made.

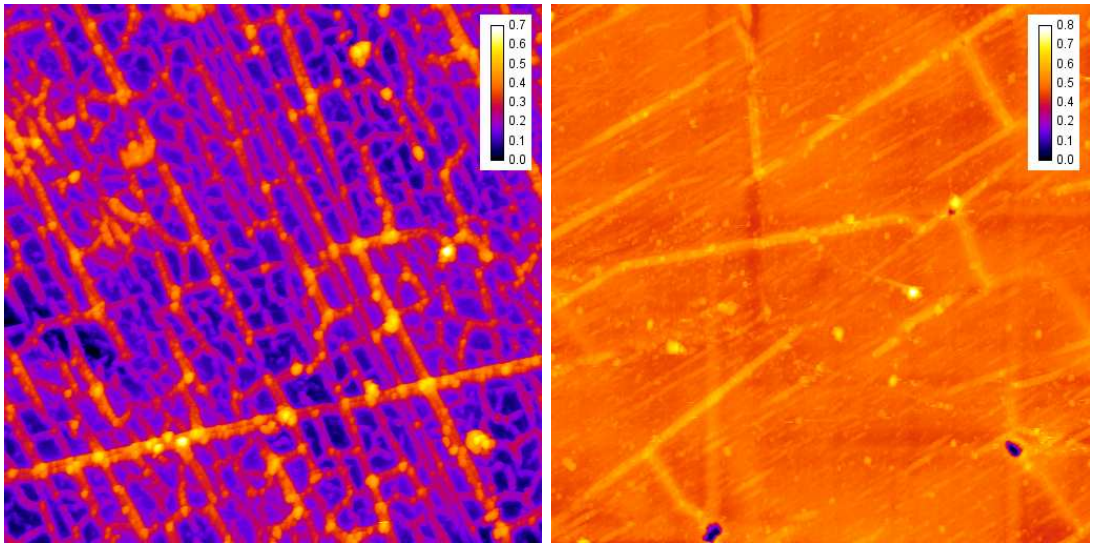

(a) Fast evaporation (b) Slow evaporation

FIGURE 6.8: The topography of a 50μm square area of Chromium deposited in several seconds using 110mA of filament current (fast) and at 0.2nms^{-1} using 90mA of filament current (slow) using tapping and contact mode AFM respectively. The height scale is in μm. Note the sharp peaks of up to 700nm height present in the quickly evaporated film, whilst 2 pinholes can be seen in the the slowly evaporated film

It can be seen that there is a considerable difference between the topography of the chromium films. The film that was rapidly evaporated has a grid like array of sharp peaks that are ≈700nm tall. This made it clearly unsuitable as a base for further a-Si:H deposition. The slowly evaporated chromium film is much flatter but a large density of deep pinholes were present and 2 can be seen in the AFM scan. Further depositions were performed using a variety of cleaning agents and solvents including acetone and distilled water to remove dust and contamination from the Kapton substrate prior to chromium evaporation, but pinhole formation could not be inhibited.

Despite the deficiencies in the electrical and surface roughness properties of both chromium back contacts, nip cells were fabricated on them and aluminium top contacts of varying area were evaporated in order to try and obtain a diode dark characteristic. It was not possible to measure a diode characteristic even using a top contact of several mm^2 or by direct probing of the a-Si:H p layer indicating that shunting of cells was a serious problem even when only a very small active area was defined. Evaporated chromium was concluded to be unsuitable as a back contact.

As an alternative to chromium it was decided to trial a molybdenum back contact. Molybdenum back contacts are popular for use in an nip substrate configuration due to their unreactive and stable nature. Molybdenum was avoided initially due to the difficulty of evaporation, with a melting point of 2617C the graphite crucibles that had been used for previous work were not suitable and there was a possibility that the DC power supply would not be able to supply the filament current required.

The graphite crucibles were replaced with tungsten crucibles and initial tests showed that it was possible to evaporate molybdenum by operating the e-beam DC power supply close to its limit at 450-500mA of filament current. Even when using this beam power (over 1kW) evaporation was slow, often less than 0.1nms^{-1} and run times of 30 minutes or more were required to deposit ≈100nm of molybdenum. This meant that the Kapton substrate would get hot and so metal sheets were placed above it in the evaporation chamber to act as heat sinks. It was found that without heat sinking Kapton substrates would curl and the coverage of molybdenum would be very non uniform.

Figure 6.9 shows the topography of a 50μm square area of molybdenum that was evaporated onto Kapton for 30 minutes. The sheet resistance of the molybdenum layer was 570Ω/□ which was more resistive than expected for a metallic film. The molybdenum would have benefited from being thicker which would probably have grown out more pinhole defects as well. Limits of the e-beam evaporation system meant that longer run times were not possible due to localised heating of the crucible and inefficient use of material.

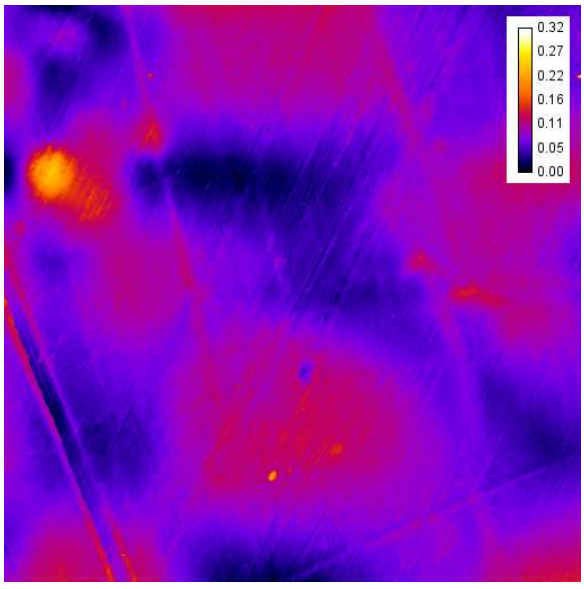

FIGURE 6.9: The topography of a 50μm square area of molybdenum on Kapton determined by a contact mode AFM scan, the height scale is in μm

The surface of the molybdenum mostly consists of gradual shifts in roughness on the order of 20-30μm with peak heights of ≈100nm. One sharper peak is visible in the AFM data but this is probably conformal coating of surface roughness that was present in

the Kapton substrate (see Figure 6.7). Pinholes were present in the molybdenum film but at a lower density than was observed in the chromium films. A variety of substrate cleaning methods prior to evaporation was again employed but to little or no effect.

A-Si:H was deposited onto the molybdenum/Kapton substrate in the same manner as previously described when using a stainless steel substrate. 10mm^2 active areas were defined by aluminium evaporation to form top contacts, and several diode characteristics were measured. Figure 6.10 shows the dark IV characteristics obtained from 4 cells. There is good agreement between the curves but more variation than diodes fabricated on polished stainless steel due to increased substrate surface roughness (see Figure 6.3). The diode action and quantity of devices that were found to be active suggested that cells with an active area of 1cm^2 should be achievable especially if more defects in the evaporated molybdenum could be eliminated.

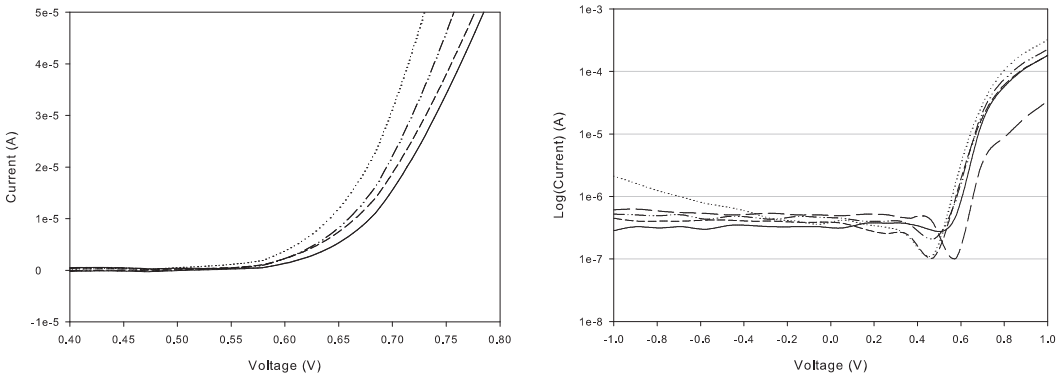

FIGURE 6.10: Dark IV characteristics of several 10mm^2 nip substrate cells on a molybdenum back contact. A small amount of illumination was present as shown by the minimum of the logarithmic current axis of graph b). There is good agreement between the characteristics but more variation is seen than when polished stainless steel was used as a substrate (see Figure 6.3) which is attributed to increased substrate surface roughness

A second series of cells was prepared in the same manner using a molybdenum/Kapton substrate. Aluminium was evaporated to define the top contacts again, but each contact was increased in size to define active areas of 1cm^2 per cell. A diode dark IV characteristic was measured for one of the 1cm^2 area cells and it is shown in Figure 6.11.

A photograph of the cell is shown in Figure 6.12, the 1cm^2 cells can be seen in the center of the substrate and some 10mm^2 cells are located to the rear of the substrate. The IV characteristic could be measured repeatedly when the substrate was allowed to bend to its natural curvature defined by thermal stress between the molybdenum and a-Si:H and then flattened out, further bending destroyed the diode IV characteristic. No problems relating to adhesion of the molybdenum or a-Si:H were encountered, there have been reports of adhesion to Kapton being a problem [109].

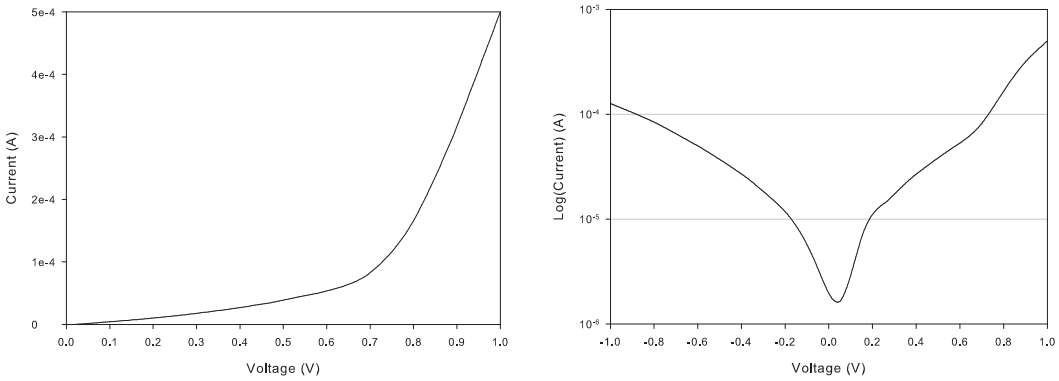

(a) (b)

FIGURE 6.11: The dark IV characteristic of a 1cm^2 nip substrate cell on a molybdenum back contact. The cell that the IV characteristic was measured from is shown in Figure 6.12

FIGURE 6.12: 1cm^2 nip substrate cells deposited on a molybdenum/Kapton flexible substrate. The 6 1cm^2 cells can be seen in the centre of the substrate, with more 10mm^2 cells defined behind them. The curvature of the substrate is due to thermal stress as a result of the mismatch between a-Si:H deposited at 200C and molybdenum at room temperature

The measurement of a dark diode characteristic from a $1cm^2$ area device indicated that despite the issues associated with the surface roughness of the back contact and pinhole formation, the growth of functional and relatively large area cells was possible. Only one of the 6 $1cm^2$ cells was found to operate as a diode, which illustrates how prominent cell shunting due to back contact defects was. Attempts were made to deposit further cells with a transparent top contact of ITO but all were found to be shunted, even when the active cell area was decreased to several mm^2. It is not known why the use of an aluminium top contact was successful whilst an ITO top contact was not, but it is reasonable to assume that it is related to the conditions present during ITO deposition or possibly indium contamination of the a-Si:H.

Fabrication of a functional $1cm^2$ cell on Kapton with a transparent top contact was not successfully achieved before practical work ceased, but by obtaining a dark IV characteristic from a $1cm^2$ cell it was shown that it would have been possible with more time.

6.4 Chapter Summary

Flexible nip substrate cells were successfully created at a temperature of 200C. Polished stainless steel and a flexible polyimide film (Kapton) were chosen as substrates. A $1cm^2$ cell with a transparent ITO top contact was deposited on stainless steel and was found to possess a 0.27% conversion efficiency. Molybdenum was evaporated onto Kapton substrates to form a conducting rear contact, and a $1cm^2$ cell was found to possess a diode IV characteristic when measured in the dark using an aluminium top contact. An illuminated IV characteristic was not obtained with a $1cm^2$ cell on a Kapton/molybdenum substrate and even smaller areas of several mm^2 could not be made to function as diodes when using an ITO top contact. It is still unknown why cells on a steel substrate would function with an ITO top contact whilst cells on a Kapton/molybdenum substrate would not, but the yield of functional cells on stainless steel was also poor suggesting that process improvements using both substrates are possible. These improvements most likely would relate to the properties of the rear contact in nip substrate cells and perhaps further passivation using a conducting diffusion barrier. Zinc oxide is known to be effective in this role because it can be grown with a topography favourable to light trapping and a-Si:H cell growth [110, 111].

The poor cell efficiency obtained using a polished stainless steel substrate can be attributed to unoptimised window layers. The p type a-Si:H film was far too thick for good performance, heavily limiting light available to the intrinsic region and preventing tunneling of carriers from the intrinsic region to the ITO. ITO deposition was optimised as a single material, resistivity and transmission were known to be good but the effects of the ITO/a-Si:H interface and ITO deposition process on cell performance were not

studied and could have been important. These factors could have been part of the reason for large values of R_s.

E-beam evaporation was found to be an unsuitable technique for back contact deposition. Chromium films were either too resistive or too rough, molybdenum films were also quite resistive and a large density of pinhole defects were present in all evaporated films regardless of the cleaning methods used to prepare the Kapton substrate. Non uniform heating of the crucible and the splattering of hotter regions of molybdenum on the substrate that resulted is also suspected to have contributed to pinhole formation. Thicker back contacts could have perhaps grown out a majority of the defects but limitations of the e-beam system with respect to how much molybdenum could be evaporated in one deposition meant that back contact thickness was limited to ≈100nm.

If the process was repeated, ideally either an e-beam system capable of higher power and a more controlled deposition or sputtering would be used to deposit a conducting back contact. Sputtering offers several advantages over e-beam evaporation including higher energies, plasma cleaning of substrates, improved uniformity of deposition due to targets acting less like a point source, and the possibility of subsequently depositing TCO diffusion barriers without breaking vacuum. The finer control of deposition parameters that sputtering would allow should enable the deposition of metallic back coatings onto polymer film substrates with low stress.

It is expected that with a sputtered back contact and a small amount of p type a-Si:H and ITO deposition optimisation, cell efficiency using a flexible substrate could have reached values near previous results obtained using an nip superstrate configuration on a TCO/glass substrate ($> 5\%$).

Chapter 7

Conclusions and future work

A range of a-Si:H thin film solar cells have been successfully fabricated using inductive PECVD. Both superstrate and substrate configurations have been investigated using a variety of substrates and primarily focusing on substrate temperatures of 200C and 250C. Gas flow rates and RF power were among the variables investigated to optimise device performance. In addition to complete cell fabrication the optical and electrical characteristics of the thin films that comprise cells were investigated using spectroscopic ellipsometry and the variation of conductivity with temperature. A custom system for the analysis of thin film conductivity was designed and constructed for this purpose. The optical absorption of amorphous semiconductors was modelled using a Cody-Lorentz oscillator which provided a Kramers-Kronig consistent solution for the complex refractive index from 200-1600nm.

The first phase of work involved verifying the suitability of the newly recommissioned PECVD reactor for the project by investigating the photoconductivity of intrinsic a-Si:H. By varying the silane flow rate, substrate temperature, and RF power peak photoconductivities of almost $10^{-5}\Omega^{-1}cm^{-1}$were measured which agreed with previous measurements [24] and indicated that the deposited a-Si:H was of PV grade.

Once it had been demonstrated that the reactor could produce PV grade a-Si:H, an attempt was made to produce the most efficient single junction a-Si:H pin superstrate cell possible using any growth conditions required. From an initial result of several % refinements were made to the deposition process until a cell was produced that was 8.05% efficient using a substrate temperature of 250C. Illuminated IV characteristics were parameterised using a double diode model which allowed the changes in deposition parameters and cell designs to be quantified. To obtain the reported efficiency it was necessary to alter the pumping scheme of the PECVD reactor and to procure a commercially available Asahi TCO/glass substrate. A p type A-SiC:H window was also included in the cell design by depositing a-Si:H in the presence of methane, this enhanced V_{oc} and the transmission of light to the intrinsic absorbing region.

The final result of this phase of work agreed with some of the best results obtained in the past with pin single junction superstrate cells [38] and approximately a decades worth of a-Si:H research was achieved in 3 months. With more time the cell efficiency could have been improved to near 10% based on past results but diminishing returns and the problem of essentially repeating past research with a new reactor suggested that investigating the optical and electrical properties of a-Si:H and a-SiC:H thin films deposited at a lower than optimal substrate temperature would be more original.

Thin films of intrinsic a-Si:H, a-Si:H doped with diborane and phosphine, and diborane doped a-SiC:H were prepared. Intrinsic a-Si:H films were prepared varying substrate temperatures and RF power whilst doped a-Si:H was investigated by varying the dopant:silane ratio, and p type a-SiC:H was prepared with a varying methane:silane ratio and a constant flow of diborane.

The room temperature conductivity of intrinsic samples was found to be in the order of 10^{-6}-$10^{-7}\Omega^{-1}cm^{-1}$giving a 2-3 decade ratio of dark to light conductivity which agrees with previous measurements of intrinsic a-Si:H [24]. Activation energy measurements revealed the intrinsic material to have a slightly n type characteristic of 0.4-0.5eV which is probably due to E_f being pinned by charged mid gap defects resulting from dangling Si bonds in the amorphous network. No significant variation in the dark conductivity was observed between the intrinsic films, but films grown at 250C did exhibit a smaller optical gap and improved absorption over the 400-800nm wavelength range. It was shown that the relationship between dark conductivity and temperature over the 100-150C range could be modelled by the use of 2 activation energy terms which it is proposed represent the position of E_f relative to E_c and the average trap energy in the localised states beneath E_c. Measurements of E_u obtained by ellipsometry were of a similar magnitude providing support for this model, but it should also be considered that the activation energy of conduction in an amorphous semiconductor can also vary as a function of temperature in amorphous semiconductors due to the thermal release of trapped carriers.

Doped a-Si:H films grown at 200C were found to exhibit room temperature dark conductivity several orders above that of intrinsic a-Si:H indicating that substitutional doping had taken place. E_f was brought to within 0.3eV of E_c and 0.4eV of E_f where it was pinned by localised tail states, agreeing with the classic results of Spear and LeComber [24]. Linear narrowing of E_g and widening of E_u was found to occur as a function of increasing dopant:silane ratio, and this is attributed to the addition of states near E_c and E_v and distortion of the amorphous network via incorporation of dopant atoms. The optimum dopant:silane ratios at 200C were found to not differ from those that were determined by trial and error with previous work with whole cells at 250C, there is little difference between the bonding encouraged by either temperature. It is suspected that a further drop in substrate temperature to $\approx$150C would significantly alter the mechanics and bonding distributions by which dopant atoms and hydrogen are included in an a-Si:H network.

P type a-SiC:H films were found to exhibit a maximum value of E_g (2.3eV) for a methane:silane flow ratio of 1.2. σ_{RT} was found to be 2 orders of magnitude less than p type a-Si:H films, and E_f was brought to within 0.5eV of E_v. The electronic properties of the different films grown by varying the methane:silane ratio were found to follow a Meyer-Neldel relationship demonstrating that the activation energy of conduction was itself a function of temperature. It was found that when the methane:silane ratio was increased beyond the optimum the film doping reverted back towards intrinsic, but remained weakly p type. E_g remained near 2eV. This material may warrant further investigation as Yunaz et al. [112] [113] concluded that the optimum tandem cell structure would utilise a top cell with $E_g \approx$2eV, and it occupies an unusual place in the 2D σ_0 and E_a parameter space (see Figure 5.13).

To conclude work at 200C, nip superstrate cells were fabricated on Asahi U-type substrates. The orientation was chosen to match the order of deposition that would be used to create an nip substrate cell. The cells did not use an a-Si:H window layer as it was found to worsen performance. Using the predetermined ideal deposition conditions for a-Si:H at his temperature the best cell was 4.59% efficient which can be compared to the 5.57% efficient nip superstrate cell grown at 250C. To achieve this figure the intrinsic layer of the cell grown at 200C had to be thinned to ≈130nm in order to enable effective collection of generated carriers.

The final section of work was the transfer of the 200C nip cell process to polished stainless steel and Kapton flexible substrates. This resulted in true substrate orientated cells. Aluminium and ITO top contacts of varying area were deposited to investigate dark and illuminated IV characteristics. A 1cm^2 cell was successfully deposited onto stainless steel resulting in an efficiency of 0.27%. This low figure is attributed to an extremely large R_s of 250Ω, as a result of the p type window layer which was probably far too thick and severely depleted the cell of short wavelength light. With more time the efficiency would have been rapidly raised to a more conventional figure by layer optimisation.

Several metals were trialled as back contacts on the Kapton substrates. Chromium was found to be unsuitable but molybdenum provided a back contact free of sharp surface roughness peaks. Because e-beam evaporation was the only available method of back contact deposition, the thickness of the molybdenum back contact was limited to several hundred nm and was found to be fairly resistive. To address this issue a thick layer of thermally evaporated aluminium was deposited first and then capped with molybdenum to form a diffusion barrier.

Pinholes were a problem in all of the evaporated back contacts, and substrate cleaning prior to deposition was found to have little effect on the pinhole density. It is felt that e-beam evaporation was not an ideal deposition technique and that a more suitable alternative would have been sputtering if for no other reason than the possibility of

much thicker back contacts. Despite this a 1cm^2 cell was successfully fabricated using an aluminium top contact and a dark IV characteristic was obtained. It was not found possible to repeat this process with an ITO top contact but it is unknown as to whether this was due to defects or an incompatibility with the ITO RF sputtering process. It was concluded that when planning a deposition process involving a flexible polymer substrate, great care must be taken to optimise the topography of the rear contact before progressing further.

7.1 Suggestions for future work

The work performed for this project provides a large scope for further investigation with solid and flexible substrates. Cells on flexible substrates were only developed to the point of being functional in the dark on Kapton and yield was low. The process requires optimisation with respect to the metallic rear contact and it is a suggested that the use of sputtering would be more suitable than evaporation. Whilst a thin metallic rear contact could be evaporated initially to enhance conductivity and reflectivity, the use of sputtering to deposit a thicker layer of TCO on top of it would help to passivate defects in the metal film and ensure a topography suitable for further a-Si:H deposition. The development of a process to sputter TCO could also be employed to investigate an intermediate reflecting layer in a tandem cell, and for top contact formation when using a substrate cell orientation. It is anticipated that the efficiency of cells fabricated on polymer film substrates would swiftly rise once issues with the rear contact have been resolved.

Secondly the investigation into low temperature deposition of a-Si:H could be extended to lower temperatures. Use of hydrogen dilution and higher RF powers could compensate for the reduced temperatures, maintaining a doping efficiency in particular is a known issue that would have to be overcome. 100C would be a sensible target as it would enable use of a greater variety of polymer substrates that are cheaper than Kapton. Ideally a process would be possible at room temperature, but PECVD may not be suitable for this.

The deposition of μc-Si and nc-Si was only briefly attempted in this report, but they are very important materials for current and next generation a-Si:H research. Doped μc-Si reduces undesirable absorption of light and intrinsic μc-Si enables the deposition of very stable tandem and triple junction cells with enhanced absorption of long wavelengths compared to a-Si:H single junction cells. Modelling of multiple junction cells using optical constants measured with ellipsometry could provide an estimation of the layer thicknesses required to achieve current matching, which would speed up cell fabrication by providing a starting point for optimisation.

It is hard to predict where the next major advances in a-Si:H cell research will occur, but it is unlikely to be in the form of cells that require more than 3 junctions. A-Si:H and a-SiC:H have optical gaps that are well suited to the role of a top cell in a multiple junction device, whilst μc-Si and a-SiGe:H can provide absorption up to 1.4-1.12eV. This leaves little room for the addition of further junctions unless the trade off of increased V_{oc} balances the loss in I_{sc}, this would imply that I_{sc} was limited by the thickness of one junction. A new alloy of a-Si:H that could be crystallised resulting in excellent electric properties and a low mobility gap (less than 1.12eV), could enhance the efficiency of a triple junction cell when used as a bottom junction. Failing the discovery of new alloys, improvements in light harvesting by improving the optical path length of thin a-Si:H top cells could also raise performance. The replacement of the doped top cell window layer by a suitably doped TCO front contact could also be a method to enhance R_s, FF, and I_{sc} by admitting more light to an absorbing region.

Chapter 8

Appendix A - Publications

8.1 Conference Publications

O. D. Clark, M. Thwaites, and D. M. Bagnall. Towards thin film amorphous silicon Micro-morph cells on flexible substrates. In *PVSAT4*, pages 97–100, Bath, 2008.

M. Banakar, O. D. Clark, and D. M. Bagnall. Variable angle spectroscopic ellipsometry used to optimise thin film silicon and ITO layers. In *PVSAT5*, pages 151–154, Wrexham, 2009.

Bibliography

[1] M. K. Hubbert. *Nuclear Energy and the Fossil Fuels*. Shell Development Co., Exploration and Production Research Division, 1956.

[2] E. Martinot. Renewables 2007: Global status report. Technical report, REN21, 2007.

[3] A. Jäger-Waldau. PV status report 2008. Technical report, European Commission Institute for Energy, 2008.

[4] P. D. Maycock. PV review: World solar PV market continues explosive growth. *Refocus*, 6(5):18–22, 2005.

[5] D. M. Chapin, C. S. Fuller, and G. L. Pearson. A new silicon pn junction photocell for converting solar radiation into electrical power. *Journal of Applied Physics*, 25 (5):676, 1954.

[6] M. A. Green. Recent developments in photovoltaics. *Solar Energy*, 76(1-3):3–8, 2004.

[7] R. N. Bhattacharya, M. A. Contreras, B. Egaas, R. N. Noufi, A. Kanevce, and J. R. Sites. High efficiency thin film CuInGaSe photovoltaic cells using a CdZnS buffer layer. *Applied Physics Letters*, 89:253503, 2006.

[8] X. Wu, R. G. Dhere, D. S. Albin, T. Gessert, C. Dehart, J. Keane, A. Duda, T. J. Coutts, S. Asher, and D. H. Levi. High-efficiency CTO/ZTO/CdS/CdTe polycrystalline thin film solar cells. In *PVSEC 17*, Munich, 2001.

[9] R. C. Chittick, J. H. Alexander, and H. F. Sterling. The preparation and properties of amorphous silicon. *Journal of the Electrochemical Society*, 116:77, 1969.

[10] W. B. Jackson, S. M. Kelso, C. C. Tsai, J. W. Allen, and S. J. Oh. Energy dependence of the optical matrix element in hydrogenated amorphous and crystalline silicon. *Physical Review B*, 31(8):5187–5198, 1985.

[11] K. Winer and L. Ley. Surface states and the exponential valence-band tail in a-Si:H. *Physical Review B*, 36(11):6072, 1987.

[12] W. E. Spear. Drift mobility techniques for the study of electrical transport properties in insulating solids. *Journal of Non-Crystalline Solids*, 1(3):197–214, 1968.

[13] J. M. Marshall, R. A. Street, and M. J. Thompson. Electron drift mobility in a-Si:H. *Philosophical magazine B*, 54(1):51–60, 1986.

[14] K. Ohno, K. Murayama, and A. Matsuda. Hopping transport of electrons and holes at localized band tail states in amorphous hydrogenated silicon and amorphous heavy-hydrogenated silicon. *Japanese Journal of Applied Physics*, 44(7A):4764, 2005.

[15] G. D. Cody, T. Tiedje, B. Abeles, B. Brooks, and Y. Goldstein. Disorder and the optical-absorption edge of hydrogenated amorphous silicon. *Physical Review Letters*, 47(20):1480, 1981.

[16] N. M. Johnson, F. A. Ponce, R. A. Street, and R. J. Nemanich. Defects in single-crystal silicon induced by hydrogenation. *Physical Review B*, 35(8):4166–4169, 1987.

[17] G. Lucovsky, R. J. Nemanich, and J. C. Knights. Structural interpretation of the vibrational spectra of a-Si:H alloys. *Physical Review B*, 19(4):2064–2073, 1979.

[18] D. K. Biegelsen, R. A. Street, C. C. Tsai, and J. C. Knights. Hydrogen evolution and defect creation in a-Si:H alloys. *Physical Review B*, 20(12):4839–4846, 1979.

[19] J. C. Knights and R. A. Lujan. Microstructure of plasma-deposited a-Si:H films. *Applied Physics Letters*, 35:244, 1979.

[20] H. Fritzsche, M. Tanielian, C. C. Tsai, and P. J. Gaczi. Hydrogen content and density of plasma-deposited amorphous silicon-hydrogen. *Journal of Applied Physics*, 50:3366, 1979.

[21] C. Wang and G. Lucovsky. Intrinsic microcrystalline silicon deposited by remote PECVD - a new thin film photovoltaic material. *21st IEEE Photovoltaic Specialists Conference*, 2:1614–1618, 1990.

[22] P. G. Le Comber and W. E. Spear. Electronic transport in amorphous silicon films. *Physical Review Letters*, 25(8):509, 1970.

[23] C. Tsang and R. A. Street. Recombination in plasma-deposited a-Si:H. luminescence decay. *Physical Review B*, 19(6):3027, 1979.

[24] W. E. Spear and P. G. LeComber. Electronic properties of substitutionally doped amorphous Si and Ge. *Solid State Communications*, 33(6):935–949, 1975.

[25] R. A. Street. Doping and the Fermi energy in amorphous silicon. *Physical Review Letters*, 49(16):1187–1190, 1982.

[26] R. A. Street, D. K. Biegelsen, and J. C. Knights. Defect states in doped and compensated a-Si:H. *Physical Review B*, 24(2):969, 1981.

[27] D. L. Staebler and C. R. Wronski. Reversible conductivity changes in discharge-produced amorphous Si. *Applied Physics Letters*, 31:292, 1977.

[28] W. E. Spear, P. G. Le Comber, S. Kinmond, and M. H. Brodsky. Amorphous silicon p-n junction. *Applied Physics Letters*, 28:105, 1976.

[29] H. Fritzsche. Electronic phenomena in amorphous semiconductors. *Annual Review of Materials Science*, 2(1):697–744, 1972.

[30] D. E. Carlson and C. R. Wronski. Amorphous silicon solar cell. *Applied Physics Letters*, 28(11):671–673, 1976.

[31] Y. Uchida, H. Sakai, and M. Nishiura. Interpretation of characteristics in a-Si:H solar cells. *Journal of Applied Physics*, 20:191–194, 1981.

[32] Y. Kuwano, S. Tsuda, M. Ohnishi, H. Nishiwaki, S. Shibuya, S. Nakano, and T. Imai. A new integrated type of a-Si:H solar cell. *Japanese Journal of Applied Physics*, 20(2):213–218, 1981.

[33] Y. Hamakawa, H. Okamoto, and Y. Nitta. A new type of amorphous silicon photovoltaic cell generating more than 2.0V. *Applied Physics Letters*, 35(2), 1979.

[34] G. Nakamura, K. Sato, Y. Yukimoto, and K. Shirahata. Broadening of spectral response width by a-Si:H/a-SiGe:H p-i-n type solar cells. *Japanese Journal of Applied Physics*, 20:227–232, 1980.

[35] D. E. Carlson. Amorphous silicon solar cells. *IEEE Transactions on Electron Devices*, 24(4):449–453, 1977.

[36] H. Haruki, Y. Uchida, H. Sakai, M. Nishiura, and M. Kamiyama. Analysis of conversion efficiency of large area a-Si:H solar cells. *Japanese Journal of Applied Physics*, 21(1):283–288, 1982.

[37] A. Madan, J. McGill, W. Czubatyj, J. Yang, and S. R. Ovshinsky. Metal-insulator-semiconductor solar cells using amorphous Si:F:H alloys. *Applied Physics Letters*, 37:826–828, 1980.

[38] Y. Tawada, H. Okamoto, and Y. Hamakawa. a-SiC:h/a-Si:H heterojunction solar cell having more than 7.1% conversion efficiency. *Applied Physics Letters*, 39: 237–239, 1981.

[39] D. A. Anderson and W. E. Spear. Electrical and optical properties of amorphous silicon carbide, silicon nitride and germanium carbide by the glow discharge technique. *Philosophical magazine*, 35:116, 1977.

[40] A. Catalano, R. V. Daiello, J. Dresner, B. Faughnan, A. Firester, J. Kane, H. Schade, Z. E. Smith, G. Swartz, and A. Triano. Attainment of 10% conversion efficiency in amorphous silicon solar cells. In *16th Photovoltaic Specialists Conference*, pages 1421–1422, San Diego, 1982.

[41] S. Yamazaki, A. Mase, K. Urata, K. Shibata, H. Shinohara, S. Nagayama, M. Abe, T. Hamatani, and K. Suzuki. An amorphous silicon solar cell having a conversion efficiency of 10.50%. *Electron Device Letters, IEEE*, 5(8):315–318, 1984.

[42] S. Guha, J. Yang, P. Nath, and M. Hack. Enhancement of open circuit voltage in high efficiency amorphous silicon alloy solar cells. *Applied Physics Letters*, 49: 218–219, 1986.

[43] Jeffrey Yang, Robert Ross, Ralph Mohr, and Jeffrey P. Fournier. High efficiency solar cells using amorphous silicon and amorphous silicon-germanium based alloys. In *18th Photovoltaic Specialists Conference*, volume 1, pages 1519–1522, Las Vegas, 1988.

[44] N. Fukuda, H. Tanaka, K. Miyachi, Y. Ashida, Y. Ohashi, and A. Nitta. Fabrication of amorphous silicon solar cells with high performance such as fill factor of 0.77 and conversion efficiency of 12.0%. In *18th Photovoltaic Specialists Conference*, volume 1, pages 247–250, Las Vegas, 1988.

[45] Y. Kazama, K. Seki, W. Kim, S. Yamanaka, M. Konagai, and K. Takahashi. High efficiency amorphous silicon solar cells with "delta-doped" p-layer. *Japanese Journal of Applied Physics*, 28(7):1160, 1989.

[46] K. Higuchi, K. Tabuchi, K. Lim, M. Konagai, and K. Takahashi. High-efficiency delta-doped amorphous silicon solar cells prepared by photochemical vapor deposition. *Japanese Journal of Applied Physics*, 30(8R):1635, 1991.

[47] J. Yang and S. Guha. Double-junction amorphous silicon-based solar cells with 11% stable efficiency. *Applied Physics Letters*, 61(24):2917–2919, 1992.

[48] S. Guha, J. Yang, A. Pawlikiewicz, T. Glatfelter, R. Ross, and S. R. Ovshinsky. Band-gap profiling for improving the efficiency of amorphous silicon alloy solar cells. *Applied Physics Letters*, 54:2330–2332, 1989.

[49] A. Shah, E. Vallat-Sauvain, P. Torres, J. Meier, U. Kroll, C. Hof, C. Droz, M. Goerlitzer, N. Wyrsch, and M. Vanecek. Intrinsic microcrystalline silicon (μc-Si:H) deposited by VHF-GD: a new material for photovoltaics and optoelectronics. *Materials Science and Engineering B*, 69(70):219–226, 2000.

[50] R. Fluckiger, J. Meier, H. Keppner, M. Gotz, and A. Shah. Preparation of undoped and doped microcrystalline silicon (μc-Si:H) by VHF-GD for pin solar cells. *Photovoltaic Specialists Conference, 1993*, pages 839–844, 1993.

[51] G. Fischer, S. Dubail, J. A. Anna Selvan, N. Pellaton Vaucher, R. Platz, C. Hof, U. Kroll, J. Meier, P. Torres, H. Keppner, N. Wyrsch, M. Goetz, A. Shah, and K. D. Ufert. The Micromorph solar cell: Extending a-Si:H technology towards thin film crystalline silicon. In *25th IEEE Photovoltaic Specialists Conference*, volume 1, pages 1053–1056., Washington D.C., 1996.

[52] P. Torres, J. Meier, M. Goetz, N. Beck, U. Kroll, H. Keppner, and A. Shah. Microcrystalline silicon solar cells at higher deposition rates by VHF-GD. *Materials Research Society Symposium Proceedings*, 452:883–888, 1997.

[53] H. Keppner, P. Torres, J. Meier, R. Platz, D. Fischer, U. Kroll, S. Dubail, J. A. A. Selvan, N. Pellaton Vaucher, Y. Ziegler, R. Tscharner, C. Hof, N. Beck, M. Goetz, P. Pernet, M. Goerlitzer, N. Wyrsch, J. Veuille, J. Cuperus, A. Shah, and J. Pohl. The micromorph cell: a new way to high efficiency low temperature crystalline silicon thin film cell manufacturing? *AIP Conference Proceedings*, 394:271–281, 1997.

[54] J. C. Knights, R. A. Lujan, M. P. Rosenblum, R. A. Street, D. K. Bieglesen, and J. A. Reimer. Effects of inert gas dilution of silane on plasma-deposited a-Si:H films. *Applied Physics Letters*, 38:331, 1981.

[55] O. Vetterl, F. Finger, R. Carius, P. Hapke, L. Houben, O. Kluth, A. Lambertz, A. Muck, B. Rech, and H. Wagner. Intrinsic microcrystalline silicon: A new material for photovoltaics. *Solar Energy Materials and Solar Cells*, 62(1):97–108, 2000.

[56] J. Meier, S. Dubail, S. Golay, U. Kroll, S. Fa, E. Vallat-Sauvain, L. Feitknecht, J. Dubail, and A. Shah. Microcrystalline silicon and the impact on micromorph tandem solar cells. *Solar Energy Materials and Solar Cells*, 74(1-4):457–467, 2002.

[57] J. Yang, A. Banerjee, and S. Guha. Triple-junction amorphous silicon alloy solar cell with 14.6% initial and 13.0% stable conversion efficiencies. *Applied Physics Letters*, 70:2975, 1997.

[58] J. Yang, B. Yan, G. Yue, and S. Guha. Comparison of hydrogenated amorphous silicon germanium and nanocrystalline silicon for multijunction solar cells: pros, cons, and status. *Photovoltaic Specialists Conference, 2005*, 1:1359–1364, 2005.

[59] R. E. I. Schropp, H. Li, J. K. Rath, and C. H. M. van der Werf. Thin film nanocrystalline silicon and nanostructured interfaces for multibandgap triple junction solar cells. *Surface and Interface Analysis*, 40, 2008.

[60] P. Buehlmann, J. Bailat, D. Domine, A. Billet, F. Meillaud, A. Feltrin, and C. Ballif. In situ silicon oxide based intermediate reflector for thin film silicon micromorph solar cells. *Applied Physics Letters*, 91:143505, 2007.

[61] H. Okaniwa, K. Nakatani, M. Yano, M. Asano, and K. Suzuki. Preparation and properties of a-Si:H solar cells on organic polymer film substrate. *Japanese Journal of Applied Physics*, 21:239–244, 1982.

[62] H. Okaniwa, K. Nakatani, M. Asano, K. Suzuki, M. Yano, M. Hirasaka, and Y. Hamakawa. Hydrogenated amorphous silicon solar cell on organic polymer substrate. *IEICE Transactions, Section E*, 66:34–38, 1983.

[63] T. Yoshida, K. Tabuchi, A. Takano, M. Tanda, T. Sasaki, H. Sato, S. Fujikake, Y. Ichikawa, and K. Harashima. Fabrication technology of a-Si:H/a-SiGe:H/a-SiGe:H triple junction plastic film substrate solar cells. In *28th IEEE Photovoltaic Specialists Conference*, volume 1, pages 762–765, 2000.

[64] K. Tabuchi, S. Fujikake, H. Sato, S. Saito, A. Takano, T. Wada, T. Yoshida, Y. Ichikawa, H. Sakai, and F. Natsume. Improvement of large-area SCAF structure a-Si:H solar cells with plastic film substrate. *26th IEEE Photovoltaic Specialists Conference, 1997*, 1:611–614, 1997.

[65] A. Takano and T. Kamoshita. Light-weight and large-area solar cell production technology. *Japanese Journal of Applied Physics*, 43(no. 12):7976–7983, 2004.

[66] Y. Liu, J. K. Rath, and R. E. I. Schropp. Development of micromorph tandem solar cells on foil deposited by VHF-PECVD. *Surface and Coatings Technology*, 201(22-23):9330–9333, 2007.

[67] M. N. Van den Donker, A. Gordijn, H. Stiebig, F. Finger, B. Rech, B. Stannowski, R. Bartl, E. A. G. Hamers, R. Schlatmann, and G. J. Jongerden. Flexible amorphous and microcrystalline silicon tandem solar modules in the temporary superstrate concept. *Solar Energy Materials and Solar Cells*, 91(7):572–580, 2007.

[68] H. Li, C. H. M. van der Werf, A. Borreman, J. K. Rath, and R. E. I. Schropp. Flexible a-Si:H/nc-Si:H tandem thin film silicon solar cells on plastic substrates with i-layers made by hot-wire cvd. *Physica Status Solidi Letters*, 2(4), 2008.

[69] M. Brinza, J. K. Rath, and R. E. I. Schropp. Thin film silicon nip solar cells deposited by VHF PECVD at 100c substrate temperature. *Solar Energy Materials and Solar Cells*, 2008.

[70] S. A. Filonovich, P. Alpuim, L. Rebouta, J. E. Boure, and Y. M. Soro. Hydrogenated amorphous and nanocrystalline silicon solar cells deposited by HWCVD and RF-PECVD on plastic substrates at 150c. *Journal of Non-Crystalline Solids*, 354(19-25):2376–2380, 2008.

[71] T. Söderström, F. J. Haug, V. Terrazzoni-Daudrix, and C. Ballif. Optimization of amorphous silicon thin film solar cells for flexible photovoltaics. *Journal of Applied Physics*, 103:114509, 2008.

[72] T. Söderström, F. J. Haug, X. Niquille, V. Terrazzoni, and C. Ballif. Asymmetric intermediate reflector for tandem micromorph thin film silicon solar cells. *Applied Physics Letters*, 94:063501, 2009.

[73] M. H. Brodsky, M Cardona, and J. J. Cuomo. Infrared and raman spectra of the silicon-hydrogen bonds in amorphous silicon prepared by glow discharge and sputtering. *Physical Review B*, 16(8):3556, 1977.

[74] R. A. Street. *Hydrogenated Amorphous Silicon*. Cambridge University Press, 1991.

[75] N. M. Johnson, C. E. Nebel, P. V. Santos, W. B. Jackson, R. A. Street, K. S. Stevens, and J. Walker. Stability of hydrogenated amorphous silicon deposited at high temperatures with a remote hydrogen plasma. *Applied Physics Letters*, 59: 1443, 1991.

[76] K. S. Stevens and N. M. Johnson. Intrinsic stress in hydrogenated amorphous silicon deposited with a remote hydrogen plasma. *Applied Physics Letters*, 71: 2628, 1992.

[77] M. Tzolov, F. Finger, R. Carius, and P. Hapke. Optical and transport studies on thin microcrystalline silicon films prepared by very high frequency glow discharge for solar cell applications. *Journal of Applied Physics*, 81(11):7376–7385, 1997.

[78] T. Toyama, Y. Nakano, T. Ichihara, and H. Okamoto. P-type microcrystalline SiC fabricated by rf plasma CVD with 40-MHz excitation. *Photovoltaic Energy Conversion*, 2, 2003.

[79] A. A. Howling, J. L. Dorier, C. Hollenstein, U. Kroll, and F. Finger. Frequency effects in silane plasmas for PECVD. *Journal of Vacuum Science and Technology*, 10(4):1080–1085, 1991.

[80] A. G. Aberle, S. R. Wenham, and M. A. Green. A new method for accurate measurements of the lumped series resistance of solar cells. *Photovoltaic Specialists Conference*, pages 133–139, 1993.

[81] C. Bendel, U. Rudolph, M. Schroder, and E. Kunz. Sensol global A new measurement system for global radiation. *16th European PV conference, Glasgow*, 2000.

[82] A. R. Burgers, J. A. Eikelboom, A. Schonecker, and W. C. Sinke. Improved treatment of the strongly varying slope in fitting solarcell IV curves. *Photovoltaic Specialists Conference*, pages 569–572, 1996.

[83] J. Klein, J. Schneider, M. Muske, S. Gall, and W. Fuhs. Aluminium-induced crystallisation of amorphous silicon: influence of the aluminium layer on the process. *Thin Solid Films*, 451:481–484, 2004.

[84] J. Klein, J. Schneider, M. Muske, R. Heimburger, S. Gall, and W. Fuhs. Aluminium-induced crystallisation of amorphous silicon: parameter variation for optimisation of the process. *photovoltaic Specialists Conference*, pages 1197–1200, 2005.

[85] C. Ornaghi, G. Beaucarne, J. Poortmans, J. Nijs, and R. Mertens. Aluminum-induced crystallization of amorphous silicon: influence of materials characteristics on the reaction. *Thin Solid Films*, 451:476–480, 2004.

[86] M. Zou, L. Cai, H. Wang, and W. Brown. Nano-aluminum-induced crystallization of amorphous silicon. *Materials Letters*, 60(11):1379–1382, 2006.

[87] G. J. Qi, S. Zhang, T. T. Tang, J. F. Li, X. W. Sun, and X. T. Zeng. Experimental study of aluminum-induced crystallization of amorphous silicon thin films. *Surface and Coatings Technology*, 198(1-3):300–303, 2005.

[88] J. C. Manifacier, J. Gasiot, and J. P. Fillard. A simple method for the determination of the optical constants n, k and the thickness of a weakly absorbing thin film. *Journal of Physics (E)*, 9:1002–1004, 1976.

[89] A. M. Goodman. Optical interference method for the approximate determination of refractive index and thickness of a transparent layer. *Journal of Applied Optics*, 17(17):2779–87, 1978.

[90] R. Swanepoel. Determination of the thickness and optical constants of amorphous silicon. *Journal of Physics (E)*, 16(12):1214–1222, 1983.

[91] C. M. Herzinger, B. Johs, W. A. McGahan, J. A. Woollam, and W. Paulson. Ellipsometric determination of optical constants for silicon and thermally grown silicon dioxide via a multi-sample, multi-wavelength, multi-angle investigation. *Journal of Applied Physics*, 83:3323, 1998.

[92] A. S. Ferlauto, G. M. Ferreira, J. M. Pearce, C. R. Wronski, R. W. Collins, X. Deng, and G. Ganguly. Analytical model for the optical functions of amorphous semiconductors from the near-infrared to ultraviolet: Applications in thin film photovoltaics. *Journal of Applied Physics*, 92:2424, 2002.

[93] Y. Hishikawa, S. Tsuge, N. Nakamura, S. Tsuda, S. Nakano, and Y. Kuwano. Device-quality wide-gap hydrogenated amorphous silicon films deposited by plasma chemical vapor deposition at low substrate temperatures. *Journal of Applied Physics*, 69:508, 1991.

[94] R. H. Klazes, M. Broek, J. Bezemer, and S. Radelaar. Determination of the optical bandgap of amorphous silicon. *Philosophical magazine B*, 45(4):377–383, 1982.

[95] Y. Hishikawa, N. Nakamura, S. Tsuda, S. Nakano, Y. Kishi, and Y. Kuwano. Interference-free determination of the optical absorption coefficient and the optical

gap of amorphous silicon thin films. *Japanese Journal of Applied Physics*, 30(part 1):1008–1014, 1991.

[96] P. J. Zanzucchi, C. R. Wronski, and D. E. Carlson. Optical and photoconductive properties of discharge-produced amorphous silicon. *Journal of Applied Physics*, 48:5227, 1977.

[97] M. Stutzmann, D. K. Biegelsen, and R. A. Street. Detailed investigation of doping in hydrogenated amorphous silicon and germanium. *Physical Review B*, 35(11): 5666–5701, 1987.

[98] J. Ristein and G. Weiser. Influence of doping on the optical properties and on the covalent bonds in plasma deposited amorphous silicon. *Solar Energy Materials*, 12(3):221–232, 1985.

[99] M. Gorn, P. Lechner, H. D. Mohring, H. Rbel, B. Scheppat, and N. Kniffler. Refractive index and absorption in boron-doped a-SiC:H using either diborane or trimethylboron as a doping gas. *Philosophical magazine B*, 64(1):101–111, 1991.

[100] R. Martins, A. Maarico, M. Vieira, I. Ferreira, and E. Fortunato. Structure, composition and electro-optical properties of n-type amorphous and microcrystalline silicon thin films. *Philosophical magazine B*, 76(3):249–258, 1997.

[101] A. Hadjadj, P. Stahel, P. R. i Cabarrocas, V. Paret, Y. Bounouh, and J. C. Martin. Optimum doping level in a-Si:H and a-SiC:H materials. *Journal of Applied Physics*, 83:830, 1998.

[102] A. Hadjadj, P. R. Cabarrocas, and B. Equer. Mobility-edge shift during diborane doping in hydrogenated amorphous silicon and hydrogenated amorphous silicon carbide. *Philosophical magazine B*, 80(7):1317–1326, 2000.

[103] R. A. Street. Trapping parameters of dangling bonds in hydrogenated amorphous silicon. *Applied Physics Letters*, 41:1060, 1982.

[104] K. Chew, S. F. Rusli, J. Ahn, Q. Zhang, V. Ligatchev, E. J. Teo, T. Osipowicz, and F. Watt. Gap state distribution in amorphous hydrogenated silicon carbide films deduced from photothermal deflection spectroscopy. *Journal of Applied Physics*, 91:4319, 2002.

[105] W. Meyer and H. Neldel. Beziehungen zwischen der energiekonstanten var epsilon und der mangenkonstanten a in der leitwerts-temperaturformel bei oxydischen halbleitern. *Z. Tech. Phys.*, 12:588593, 1937.

[106] M. Vetter, C. Voz, R. Ferre, I. Martn, A. Orpella, J. Puigdollers, J. Andreu, and R. Alcubilla. Electronic properties of intrinsic and doped amorphous silicon carbide films. *Thin Solid Films*, 511:290–294, 2006.

[107] T. A. Abtew, M. L. Zhang, Y. Pan, and D. A. Drabold. Electrical conductivity and the Meyer Neldel rule: The role of localized states in hydrogenated amorphous silicon. *Journal of Non-Crystalline Solids*, 2008.

[108] N. Saito, Y. Inui, T. Yamaguchi, and I. Nakaaki. Indium doping of a-SiC:H films prepared by reactive magnetron co-sputtering. *Thin Solid Films*, 353(1-2):189–193, 1999.

[109] A. Vijh, X. Yang, W. Du, and X. Deng. Film adhesion in amorphous silicon solar cells. In *Photovoltaic Specialists Conference*, volume 30, pages 329–331, Orlando, FL, 2005. Springer.

[110] J. Yang, B. Yan, and S. Guha. Amorphous and nanocrystalline silicon-based multi-junction solar cells. *Thin Solid Films*, 487(1-2):162–169, 2005.

[111] P. Pernet, R. Felder, M. Goetz, H. Keppner, D. Fischer, and A. Shah. Optimization of amorphous silicon solar cells on polymer film substrates. In *14th EC Photovoltaic Solar Energy Conference*, pages 2339–2342, Barcelona, 1997.

[112] I. A. Yunaz, K. Hashizume, S. Miyajima, A. Yamada, and M. Konagai. Fabrication of amorphous silicon carbide films using VHF-PECVD for triple-junction thin-film solar cell applications. *Solar Energy Materials and Solar Cells*, 2009.

[113] I. A. Yunaz, A. Yamada, and M. Konagai. Theoretical analysis of amorphous silicon alloy based triple junction solar cells. *Japanese Journal of Applied Physics*, 46:1152–1154, 2007.